Multi-Antenna Multi-Frequency Microwave Imaging Systems for Biomedical Applications

By:

Marta GUARDIOLA GARCIA

Advisor:

Prof. Lluís JOFRE ROCA

Thesis submitted to the Universitat Politècnica de Catalunya (UPC) in partial fulfillment of the requirements for the degree of
DOCTOR OF PHILOSOPHY

PhD. Program: Signal Theory and Communications
AntennaLab group

UPC

Barcelona, September 2013

Marta Guardiola
Multi-antenna Multi-frequency Microwave Imaging Systems for
Biomedical Applications

Book cover photograph by: Judith Barrera
Model: Laura Guardiola

A la meva mare i al meu pare,
amb qui comparteixo el 50% dels meus gens.
A la meva germana,
amb qui ara en comparteixo el 100%.
I a en Pau,
amb qui comparteixo el 100% de la meva vida.

ABSTRACT

Medical imaging refers to several different technologies that are used to view the human body in order to diagnose, monitor, or treat medical conditions. Each type of technology gives different information about the area of the body being studied depending on the radiation used to illuminate the body. The current and most-established imaging methods, accounting for x-rays, ultrasounds or magnetic resonance, are ineffective for detecting some diseases at a curable stage. Moreover, they present some drawbacks that limit its use, such as health risk, high price, patient discomfort, bulky apparatus, etc.

In the last decades, active microwave systems are being considered for the internal inspection of light-opaque materials thanks to its capacity to penetrate and differentiate their constituents based on the contrast in dielectric properties with a sub-centimeter resolution. Moreover, they are safe, relatively low-cost and portable. Driven by the promising precedents of microwaves in other fields, an active electromagnetic research branch was focused to medical microwave imaging. The potential in breast cancer detection, or even in the more challenging brain stroke detection application, were recently identified. The initial advantage in terms of significant electric contrast between the lesions and the surrounding tissues was not as important as expected. This fact together with the traditional challenges associated to noise or multipath corruption are the main hurdles limiting its clinical use.

Intensive research in tomographic methods is now devoted to develop quantitative iterative algorithms based on optimizing schemes. These algorithms face a number of problems when dealing with experimental data due to noise or modeling inaccuracies in the direct problem. Primarily focused in robustness, the tomographic algorithm developed and assessed in this thesis proposes a non-iterative and non-quantitative implementation based on a modified Born method. Taking as a reference the efficient, real-time and robust 2D circular tomographic method developed in our department in the late 80s, this thesis proposes a novel implementation providing an update to the current state-of-the-art. The two main contributions of this work are the 3D formulation and the multi-frequency extension, leading to the so-called Magnitude Combined (MC) Tomographic algorithm. First of all, 2D algorithms were only applicable to the reconstruction of objects that can be assumed uniform in the third dimension, such as forearms. For the rest of the cases, a 3D algorithm was required. Secondly, multi-frequency information tends to stabilize the reconstruction removing the frequency selective artifacts while maintaining the resolution of the higher frequency of the band.

This thesis covers the formulation of the MC tomographic algorithm and its assessment with medically relevant scenarios in the framework of breast cancer and brain stroke detection. In

the numerical validation, realistic models from magnetic resonances performed to real patients have been used. These models are currently the most realistic ones available to the scientific community. Special attention is devoted to the experimental validation, which constitutes the main challenge of the microwave imaging systems. For this reason, breast phantoms using mixtures of chemicals to mimic the dielectric properties of real tissues have been manufactured and an acquisition system to measure these phantoms has been created. The results show that the proposed algorithm is able to provide robust images of medically realistic scenarios and detect malignant breast lesions and brain hemorrhages, both at an initial stage.

Keywords - 3D Microwave Imaging, Tomographic Imaging, Diffraction Tomography, Near-Field Imaging, Breast Cancer, Brain Stroke, UWB, Numerical Validation, Experimental Validation.

Acknowledgements

Sempre he trobat que el conte de la caputxeta vermella s'adapta molt bé a una gran quantitat de situacions. És una història amb un objectiu concret, que s'assoleix recorrent un camí, mai mancat d'impediments, ni afortunadament de persones disposades a donar-te un cop de mà. El camí cap al doctorat és una d'aquestes situacions. L'objectiu és clar, assolir el títol de Doctor[1]. Sempre m'he imaginat un doctor com una persona amb cabells blancs i molta experiència, com l'àvia del conte. El camí no és tan clar, és ben bé com un bosc frondós i ple d'esbarzers, que a voltes esgarrapen, però també regalen móres ben gustoses. En aquest bosc, també és molt fàcil perdre's o trobar una romeguera que pot fer que el camí s'allargui considerablement.

Doncs bé, el meu camí va començar un bon dia de fa uns 5 anys. El Prof. Lluís Jofre em fa oferir la oportunitat d'endinsar-me en aquest viatge que em permetria progressar tant a nivell acadèmic com personal, en una temàtica molt rellevant socialment i amb la qual tinc un gran interès particular. La temàtica que s'amaga darrere de cada pas d'aquest camí, és la formació d'imatges utilitzant les microones per aplicacions mèdiques. Aquest objectiu sovint s'ha simplificat i banalitzat a: veure "tetes". I sí, resulta que m'he passat 5 anys bàsicament mirant "tetes".

Aquesta ha estat una de les bromes més recurrents dels companys de viatge que m'han acompanyat en alguna part o en tot el camí. En Pere, l'Òscar, en Sergi, en Txema, en Benji, en Javi, en René, en Jordi Balcells i l'Isaac formaven part de l'equip d'experts en el camí del doctorat, que quan vaig arribar ja donaven els seus últims, o no tan últims, passos. Amb d'altres he compartit incomptables hores de viatge, experiències, cafès i tes i alguna escapada destinada a l'oci. Els més esportistes: en Marc, en Jordi Abril, l'Enrique i en Dani Rodrigo, ens hem posat les malles en més de una ocasió, alguns més estretes que d'altres, per compartir alguns km corrent, encara que els dos últims prefereixen anar sobre rodes. Amb l'Edgar, algunes vegades no ens hem entès, però res que no pugui solucionar una copa de Don Julio. L'Edu Makhoul ens ha fet salivar en varies ocasions amb les seves especialitats síries. I és que el menjar ha estat un element clau, quants dinars i aliments variats del "lloc habitual" hem compartit. Un tiramissu? Challenge accepted!

Durant un temps, vam formar un gran equip amb la Gemma, la Bea i la Irena. El món d'en Beakman i el contenidor d'envasos van ser la nostra inspiració. La Gemma ha estat una gran companya de camí amb qui he compartit, tal i com diu ella mateixa, "feina, accent, gustos i aficions". En un ambient tan fred i impersonal, la Vero sempre hi ha posat la part més humana. Amb la Maria hem fet plans per sobreviure en un món, on encara i lamentablement resten

---

[1] que no vol dir ser metge, sinó Doctor of Philosophy

costums masclistes. I què puc dir d'en Santi, ell és el llenyataire que em venia a salvar quan venia el llop. Sempre atent i disposat a ajudar en qualsevol moment. Encara et dec l'iHam.

Durant quatre mesos vaig recórrer el camí anglès i vaig anar a parar a la Universitat de Bristol. Prof. Ian Craddock welcomed me warmly in such a wet country and he kindly offered me a space in his research group. My desk mate Mantalena made me feel like being in home from the very first time and Tommy was always willing to solve my questions and problems with the simulator. Thank you all for caring about me in those difficult times.

Evidentment durant el camí vaig haver de treballar molt, la major part de temps davant l'ordinador però també al laboratori. L'Albert Aguasca m'ha salvat més d'un cop de l'amputació d'alguna extremitat tallant amb la dremel. En Rubén i l'Albert m'han facilitat enormement la feina de laboratori: gestionar comandes, fer algun cable, antena o circuit. En cas de problemes pràctics, en Joaquim sempre podia aportar una bona solució. En un indret solitari, en Josep sempre tenia "bon material" i elaborava amb gran precisió qualsevol peça tot explicant el proc'es amb "pèls" i senyals. El Prof. Jordi Romeu ha estat molt present en la última part del camí. Formant part de la Càtedra Telefónica-UPC m'he convertit en una espècie de dona-orquestra, fent des de conferenciant experta en xarxes socials fins a productora d'un vídeo per promocionar un hackaton. Agrair-li doncs haver confiat en mi per fer tot aquest ventall de feines. Uff, i la burocràcia! resulta que durant el camí s'ha de fer una muntanya de papers... la Teresa i l'Aynie ho han facilitat extraordinàriament.

I els que m'esperen a casa després del viatge: els meus pares Xavier i Carme, la iaia Nita i la meva germana Laura. Ja saps que "sense tu jo no sóc ningú". Finalment a qui m'acompanya nit i dia, en la vida més quotidiana, però que també em dóna suport en la acadèmica, i sobretot perquè no em deixa de sorprendre amb les seves idees i inquietuds. No canviïs mai Pau.

CONTENTS

1   INTRODUCTION

1.1   Context of the thesis

Medical imaging is considered among the most important medical developments of the past 1000 years according to one of the most prestigious peer-reviewed medical journals in the world [1]. The reason is its unequaled power in providing with "sight and insight" about human disease and physiology. Medical imaging refers to several different technologies that are used to create images of the human body (or parts and function thereof) for clinical purposes (medical procedures seeking to reveal, diagnose, or examine disease) or medical science (including the study of normal anatomy and physiology). Internal imaging of the human body has been possible only in the past century, driven by the discovery of x-rays in 1895. More than 100 years of intense research have paid back with a plethora of improvements in x-ray imaging, as well as the invention of new imaging technologies exploiting other physical properties of biological tissues. The advances achieved for many applications are magnificent, but there is still room for more progresses in the diagnosis and treatment for many of the health major challenges.

In the highly competitive world of medical imaging, a new imaging technology must meet a number of requirements to be considered as such: high sensitivity and specificity, non-invasive and low health-risk, cost-effective (to be widely available and capable of mass screening), involve minimal discomfort to the patient (short screening time, comfortable application) and provide easy to interpret, objective and consistent results. The existing medical imaging systems fulfill the previous requirements to some degree and demonstrate more or less effectiveness depending on the application. Based on the previous definition, the most-established medical imaging technologies include: x-ray-based methods (including computed tomography (CT) and mammography), magnetic resonance imaging (MRI), ultrasounds (US) and nuclear medicine (including planar and single-photon emission computed tomography (SPECT) gamma imaging and positron emission tomography (PET)). Measurement and recording techniques which are not primarily designed to produce images, such as electroencephalography (EEG), magnetoencephalography (MEG) and others, are not seen as forms of medical imaging in this thesis.

In general, imaging systems relay on illuminating an area of the body with a penetrating wave and capturing the signals resulting from the interaction of the illuminating radiation and the tissues with a proper sensor. When interacting with biological tissues, any signal experiment changes. These changes are actually the evidence of some inhomogeneity that can be attributed to the presence of a different tissue or different health conditions within the same tissue. By processing the received signal with an imaging or a reconstruction algorithm, the changes observed in the received signal can be translated to more relevant data for the medical doctors on the conditions of the inspected body area.

Depending on the signal and sensor's nature, it is possible to obtain images based on different properties of the object, i.e. physical, mechanical, electrical or biological, see Figure 1.1. Some details of its internal structure which cannot be detected with a certain technique, can be visualized with another one. This is the reason that motivates the efforts in developing new sensors and appropriate imaging systems exploiting other properties that are not covered by the existing imaging methods.
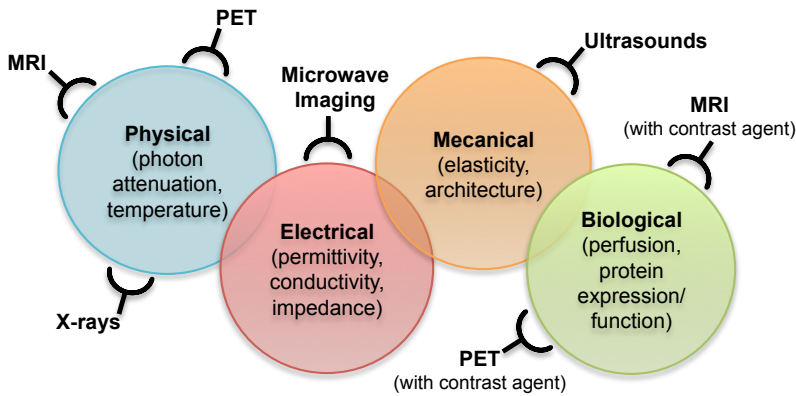
Figure 1.1: Properties of breast tissue exploited by different imaging methods.

1.2   Microwave Imaging for Medical Applications

In this section, microwave imaging for medical applications is introduced. Since nowadays the golden and most renowned standard for screening the human body are x-rays, in the following lines, microwave imaging is presented resorting to an analogy with x-rays.

Active microwave imaging is an imaging modality based on illuminating an object under test with an incident radiation, as it is done in x-ray methods. By measuring the resultant signal with a proper sensor, an image of the distribution of the object properties interacting with the illuminating fields, as a function of position, can be retrieved. In microwave imaging, the sensors are the transmitting and the receiving antennas situated in the vicinity of the object, whereas in traditional radiology the sensor is directly the photographic film.

Whereas both approaches are applied in a similar way, fundamental differences exist in the manner the waves interact with the tissues. While x-ray detectors measure attenuation and provide images representing the tissue density, microwaves interact and represent the dielectric properties (permittivity ϵ and conductivity σ). Each tissue has its own permittivity and conductivity which are different to those of the surrounding tissues. The difference in the dielectric properties of the object and the medium it is embedded in, is referred as contrast. This is actually the principle exploited by microwave imaging and what motivated the researchers to investigate the potentiality of microwave radiation to detect signs of several health problems.

In the case of x-rays, the wavelength is very small compared to the size of the human organs and linear-path-ray-propagation inside the organ can be assumed. However, in microwave region, the wavelength is comparable to the size of the organs, and as a result the wave undergoes multiple disturbances known as scattering. Scattering effects occur whenever propagation waves encounter an alteration in the dielectric properties of the medium which is more pronounced for electrically large or highly contrasted objects. Thus, in the microwave region, the scattering effects cannot be neglected.

Another difference between traditional film radiography and microwave imaging lies on the reconstructed image type. While radiography provides a projected image (P), meaning that the three-dimensional (3D) object characteristics are represented (and superposed) in a two-

3

dimensional (2D) image; microwave imaging has the capability to obtain cross sectional images (S_1 and S_2) known as tomographic images, see Figure 1.2. Typically the x-ray films and digital images are viewed directly by the radiologist, usually with no or minimal additional processing. This is in contrast to microwave imaging (and CT), where reconstruction algorithms are needed to form cross-sectional images. Cross-sectional images are always desirable since reduce the possible shadowing effects when a dense tissue is situated in front of the target.
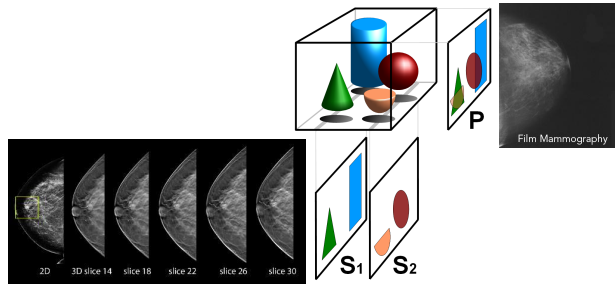
Figure 1.2: Projection (P) and tomographic (S_1 and S_2) images. Detail of several CT slices and a film mammography. Used under a Creative Commons Attribution-ShareAlike license.

Thus, the microwave imaging problem consists on determining the object dielectric properties from a measurement of the received fields, resulting from the interaction between the illuminating field and the object, at a sufficient number of points. In presence of an object, the total received field can be interpreted as the superposition of the scattered field, $\vec{E}^s$, produced by the presence of the object, and the incident field, that is the field that would exist without the object, see Figure 1.3.
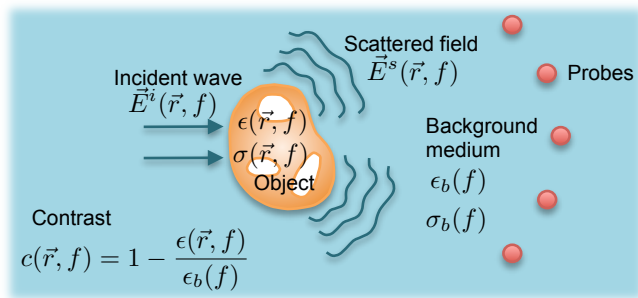
Figure 1.3: The field scattering effect in microwave imaging.

In order to produce a tomographic image using microwaves, the so-called inverse scattering problem has to be solved, where the object's dielectric properties are deduced from the scattered field, $\vec{E}^s$, which is reradiated by the object, and the known illuminating field (incident field $\vec{E}^i$), see Figure 1.3. This results in a non-linear relationship between the scattered field and the dielectric properties of the object,

1.2.1 Advantages

Over the last three decades, microwave imaging has gained interest between the research community for its potential practical clinical use. Firstly, the capacity of microwave to sense and image the dielectric contrast of soft tissues provides a mechanism to identify and determine its physiological or pathological conditions [2]. It has been demonstrated that tissue malignancies, tumors or changes related to the blood supply, such as hypoxia, acute ischemia, and chronic infarction, change the tissue dielectric properties. In terms of safety, microwave systems are non-invasive and do not involve any health risk thanks to the low-power non-ionizing radiation. Thereby, they may be safe enough to be used in mass screening or treatment without restrictions. Finally, and thanks to a mature microwave technology, it is possible to implement cost-effective and portable devices, which could be widely available even in primary care trust or in under-developed countries.

1.2.2 Challenges

The major hurdles limiting the patient use of microwave imaging systems are fundamental. They stem from the very nature of the microwave field and its interaction with the living tissues. They have to be dealt when designing the acquisition apparatus and the imaging algorithm which have to be enough robust to avoid the degradation of the image quality and detection capability.

1.2.2.1 Resolution, frequency and penetration

The resolution is a gauge of image quality that measures the smallest detail represented in the image. It is also defined as the smallest distance between two small close objects that can be clearly discerned in an image. If the two objects are so close that the distance is below the system resolution, they will appear as a single object in the image. The resolution depends strongly on the shortest wavelength (or equivalently to the frequency range) contained in the illuminating wave through the so called diffraction limit. The diffraction limit of most imaging approaches based on far-field measurements is about a half or a quarter of a wavelength. The shorter the wavelength, the smaller the shape details captured by the image, the better the resolution. However, a short wavelength also means smaller penetration depth. The relation between frequency, wavelength and penetration along the electromagnetic (EM) spectrum particularized for medical imaging is sketched in Figure 1.4.

In tissue sensing, this triple trade-off between resolution, wavelength (or equivalently frequency) and penetration, is generally found in an optimal frequency range between 2 and 8 GHz [3]. The upper part of the range leads to to resolutions up to 1 cm and penetration depths of 2 cm in case of fatty tissues or as low as 4 mm in muscle [4, 5], which can be regarded as insufficient for some imaging applications. Nevertheless, the literature shows several examples of super-resolution [6] achieving resolutions as small as 1/30 of a wavelength. This is possible since near-field measurements pick up evanescent field information form the target (scatterer) and such information is not subject to the diffraction limit. The same behavior is also achieved by using image reconstruction methods based on non-linear optimization schemes[1]. Hence, in

---

[1]In section 1.4.1 a brief explanation on non-linear reconstruction methods is given
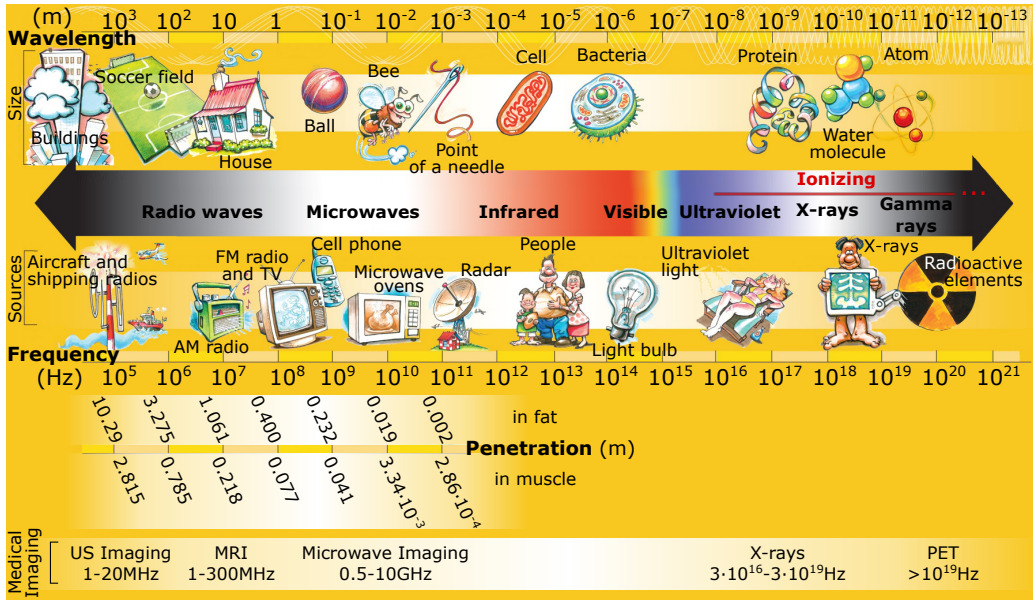
Figure 1.4: EM spectrum. Relation between frequency, wavelength and penetration. Note that penetration depth only applies to the microwave region.

near-field measurements, super-resolution mechanism may allow to reduce the frequency and increase the penetration depth while keeping the resolution.

1.2.2.2 Interaction with living tissue

Biological organs are intrinsically heterogeneous, lossy and can be in motion. The motion of the imaged object during measurement, due to the breath, nerves, medical conditions, etc., reduces the sensitivity and the resolution of the imaging procedure. In breast imaging, motion can be reduced by compressing the breast between plates, hemispherical cups, etc. or using prone positioning (lying face down with the abdomen against the examination table). Organs consist of a large number of tissues and thus are very heterogeneous. Moreover the different structures have a size comparable to the wavelength producing significant scattering at the interfaces. Due to the high water content, they present a considerable conductivity which attenuates the signal and limits the penetration depth. To make matters worse, the shapes and dielectric properties vary from one person to another and change over time in the same individual.

1.2.2.3 Towards clinical systems

Finally, in terms of implementation, while the community is quite good at imaging numerical anthropomorphic models, the translation to the clinic has really been the problem. The biggest issues with getting a system working had been acquiring the data above the noise floor and without multi-path corruption. Other issues which have to be considered prior to a clinical use are the screening duration or even a non-bulky implementation.

1.3   Medical applications of microwave imaging

Microwaves are used in the medicine field for both imaging and sensing for diagnosis and treatment processes. As a diagnosis tool, microwaves, and in particular UWB radar, showed potential in monitoring human vital signs such as respiration, heart beat [7], etc. In the framework of medical imaging, microwaves have the capacity to reconstruct an image of the spatial distribution of the dielectric properties of organs and tissues aimed to diagnose health conditions. Classical applications of microwave imaging include: imaging of thermal changes related to some disease or hyperthermia treatments [8], imaging of extremities [9], imaging of the blood flow to diagnose acute ischemia [10], imaging of water accumulation for detecting cerebral or pulmonar edema [11] or urinary incontinence [12]. More recent microwave medical imaging applications are focused on brain stroke detection [13, 14], bone health monitoring (osteoporosis) [15] and the most recurrent breast cancer detection [16–18, J1].

Regarding the treatment methods based on microwaves, hyperthermia (or thermotherapy) [19] and ablation [20] are cancer treatments that involve heating tumor cells within the body. Hyperthermia proposes to elevate the temperature of a certain body area to a temperature of about 42-45°C as s function of time, while ablation uses higher temperatures (> 50°C) to produce the direct destruction of some tumors. Research in hyperthermia began over a hundred years ago, when doctors first noticed that high heat, such as that resulting from a fever, killed cancer cells and shrank tumors. Today hyperthermia is used as an adjunct to radiation therapy and chemotherapy in clinic, but the research continues towards improving the confinement of the dose of heat to the cancerous tumor and reducing the dose of microwave radiation. Apart from cancer treatment, other applications of hyperthermia include: prostatic hyperplasia, heart ablation and balloon angioplasty [21].

This thesis is focused in microwave imaging for the diagnosis of breast cancer detection, but also its potentiality in brain stroke detection will be inspected. The reasons for this choice will be explained in the remaining of this section, but they are both reinforced by the important incidence rates of both diseases, as shows Figure 1.5.
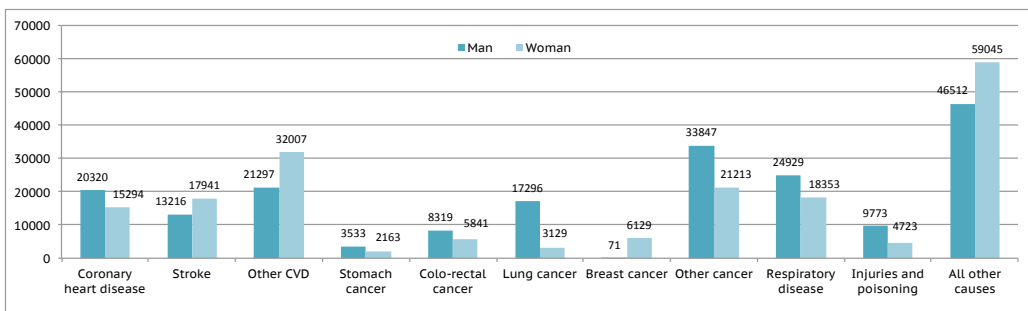
Figure 1.5: Total number of deaths by cause and sex in 2012 in Spain [22].

1.3.1 Breast cancer

1.3.1.1 The breast cancer burden

Spanish statistics report breast cancer as the most common non-skin-related malignancy and the leading cause of death from cancer among women [23]. In Catalunya, 1 in 9 women will develop breast cancer throughout her life, which represents an incidence rate of 83.9 cases/100 000 inhabitants/year. In Spain, the incidence rate is lower (50.9 cases/100 000 inhab./year) due to the lesser level of global industrialization. Similar rates to Catalunya are observed in Northern Europe (82.5 cases/100 000 inhab./year) and United States (99.4 cases/100 000 inhab./year) [24]. Breast cancer represents the 29% of all the tumors detected in Spanish women. In absolute numbers, it accounts for 22 000 new breast cancers detected each year, the vast majority between 45 and 65 year-old women. Due to the aging of the population and the increasingly early diagnosis, the number of cases is growing at a rate of 1-2% per year.

Early detection is, up to now, the best hope for reducing the burden of this disease. X-ray mammography and self-examination of the breast, are now the mainstays for early detection of breast cancer. Many developed countries introduced preventive mass screening mammography programs which are credited for part of the recent reduction in breast cancer mortality [25]. In Spain the survival rate after 5 years of breast cancer is 79,4%, very close to that of the global European rate of 80,3%. However, in many under-developed countries, the detection is fairly low compared to developed countries. Therefore, an economical imaging system with high sensitivity and specificity must be found to solve global mortality from breast tumors.

1.3.1.2 Current breast cancer detection techniques

X-ray mammography, in spite of being the golden standard for breast cancer screening, is not perfect. Mammography cannot eliminate all deaths from cancer because it does not detect all types of cancer, including some that are detected by physical examination. It is particularly ineffective in women with dense breast tissue due to shadowing effects, which is especially common in young woman, leading to increased rates of false-positive findings. The result is a relatively large number unnecessary biopsy (60-85% of lesions detected by mammography are benign) and the preventable emotional distress of patients about the possibility of having breast cancer. Table 1.1 shows that while a 25-30% decrease in breast cancer mortality among women between ages of 50-70 involved in mammographic screening is observed, a lesser benefit is seen among women ages 40 to 49 [26]. This is the reason why in United States, the U.S. Preventive Services Task Force (USPTSF) revoke the recommendation to start screening using mammography at the age of 40 instead of 50, and why the majority of mass screening programs worldwide begin at the age of 50, causing serious controversy on the benefit of mammography on young people [27]. These concerns are more relevant when the young patient presents a specific risk factor, who in grounds of age, tend to have a faster average cell growth rate. In this case, tumors may develop too quickly to be identified at an early or curable stage using the standard screening intervals, meaning that it may need to be conducted more frequently and effectively. The ionizing radiation character of x-rays clashes with this necessity. Even though the radiation is kept on minimal levels in today's mammography equipment, there is still a small risk of radiation-induced breast cancer especially associated to repeated exposure [28]. From the patient's point of view, during the mammogram the breast is compressed to to increase the

Age	Probatility	Mortality reduction
<30	1 out of 2525	16-18%
30-40	1 out of 217	16-18%
40-50	1 out of 50	25-30%
50-60	1 out of 24	25-30%
60-65	1 out of 14	25-30%
65-70	1 out of 14	55%*
70-75	1 out of 10	55%*
75-80	1 out of 10	No reduction*

Table 1.1: Probability of breast cancer depending on the age and mortality reduction thanks to x-ray mammography. *Lack of data for this age group from randomized clinical trials.

image quality and keep it still. This procedure may involve discomfort and even pain in case of sensitive breasts.

The current limitations of mammography have been driving forces behind the efforts to improve this technique and other diagnostic tools and to develop additional novel methods for medical imaging. Accordingly, other imaging technologies, particularly non-ionizing modalities such as MRI and US are being used to provide additional diagnostic specificity over x-ray mammography alone. MRI offers higher sensitivity but at the expense of high cost and low specificity which can lead to overdiagnosis. Therefore MRI is not currently used for breast cancer screening except for high risk cases. Ultrasound is being used to evaluate lumps that are hard to see or characterize on a mammogram, but provides a poor specificity. Additional tools such as PET are increasingly used for being the most accurate single imaging technique for visualizing the spread of tumors or its response to therapy. Table 1.2 shows a comparative summary of the performance of the current medical imaging technologies particularized for breast cancer detection.

To date, no single imaging method appears to offer a satisfactory tradeoff between all the requirements for a medical imaging tool mentioned in section 1.1 for early stage breast cancer detection. In order to improve the performance, combining some of the aforementioned modalities to take profit of the strenghts of each technique seems a good solution and was investigated in [29]. According to this study, the highest sensitivity, 99.4% was achieved when mammography, clinical examination and MRI were combined. However, in this case the specificity dropped to only 7%. Therefore, a combination of the current detection modalities is not sufficient to enhance the detection quality, reduce cost and time, increase safety and reduce discomfort. These limitations motivated the researchers globally to investigate new alternative detection techniques exploiting other properties of body tissues such as microwave imaging.

	Mammography	CT	Ultrasounds	MRI	PEM
Use	Mass screening. Image bone, soft tissue and blood vessels all at the same time. Shadowing due to dense tissues	To determine and image distant metastasis in a single exam	Evaluate lumps found in mammography. Not suitable for bony structures	Young women with high risk. Images small details of soft tissues	Functional imaging of biological processes. To image metastasis or response to theraphy
Sensitivity	67.8%	91%	83.0%	94,4%	61.0%
Specificity	75.0%	93%	34.0%	26,4%	80.0%
Health risk	Ionizing radiation	Ionizing radiation, allergic reaction to contrast agent	No	Pacemakers, allergic reaction to contrast agent	Ionizing radiation, radioactive tracers injection
Invasive	No	No	No	No	No
Comfort	Breast compression	Claustrophobia	Yes	Claustrophobia	Claustrophobia
Operator dependency	Result interpretation	-	Exploration, result interpretation	-	-
Time	a few sec	5 min	10-20 min	40-60 min	90-240 min
Cost	86$	1200-3200$	100-1000$	1200-4000$	3000-6000$
Image type	Projection	Tomographic	Tomographic	Tomographic	Tomographic

Table 1.2: Performance comparison between the most used breast cancer screening methods: X-ray mammography, X-ray CT, US, MRI [29] and PEM [26, 30]. Sensitivity and specificity values depend strongly on the type of cancer and on the breast composition. The values included in the table are averaged.

1.3.2 Brain stroke

1.3.2.1 The brain stroke burden

Cerebrovascular accidents or brain strokes occur due to a loss of blood supply to a part of the brain caused by a blood clot (ischemic stroke) or bleeding (hemorrhagic stroke) [22]. Cerebrovascular disease affected more than 15 million people in the world in 2002. After a stroke, 10% of patients recover almost completely, 25% recover with minor impairments, 40% experience moderate to severe impairments requiring special care, 10% require care in a nursing home or other long-term care facility and 15% die shortly after the stroke. In terms of mortality, stroke by itself is the the second most common single cause of death in the European Union (EU), accounting for over 460,000 deaths in EU each year. Around one in every twelve men (8%) and one in ten women (11%) die from this disease. While hemorrhagic strokes represent only around 15% of the cases, it is the most deadly, with more than 37% fatality rate within 30 days. Ischemic strokes represent the 85% of cases and a 7.6% result in death within 30 days. In a period of a year after their first stroke, a 22% of men and 25% of women will die. Of the stroke survivors, approximately half will suffer permanent disability and a 14% of people have another stroke within a year and a 25% within 5 years. Figure 1.6 the stroke statistics in Catalunya.

This tough statistics obviously represent a important health burden but also an economical one. Stroke is estimated to cost the EU economy over 38 billion Euros a year. Of the total cost of stroke, arround 50% is due to direct health care costs (representing around 9% of the total health care expenditure across the EU), 22% to productivity losses and 29% to the informal care of people with stroke.
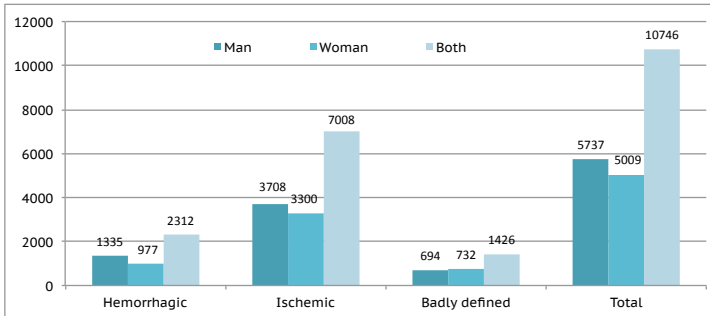
Figure 1.6: Total number of patients hospitalized with a diagnosis of CVD in 2002 by type and sex in Catalunya [31].

1.3.2.2   Current brain stroke detection techniques

The main issue when a patient arrives at a hospital with stroke symptoms is to differentiate between bleeding and ischemic strokes. Both present similar symptoms but radically different treatment. A delayed or wrong diagnosis definitely may cause important after-effects. In case of ischemic strokes, the treatment, usually consisting of administering thrombolytics, has to be given within 3 hours of the onset of the symptoms and requires a firm diagnosis. This is currently so difficult that only 2-5% of patients could benefit from thrombolytic treatment. The main reason is that stroke is primarily detected with CT, which is only available in hospitals that are not always close to the patient. Other brain imaging methodologies include MRI an functional MRI, having the drawback of high cost; PET and SPECT which are also costly and require radioactive tracers; and EEG and MEG that suffer from poor and spatial resolution.

Current and future trends focus on investigating into new neuro-imaging approaches or combining them into new multi-modal methods [32]. Ongoing research into non-ionizing and non-invasive methods considers microwave imaging as a potential tool for stroke detection as a first line method thanks to a relatively economical and portable implementation.

1.4   State of the art of microwave imaging for medical applications

This section starts with a brief timelined description of the evolution of microwave imaging for medical applications with the aim of giving a historically-reasoned perspective of the problem. Next, a more detailed explanation of the recent developments organized in the 2 main topics (imaging algorithms and imaging systems) is presented.

Active microwave imaging for medical applications arose as an attempt to extend the knowledge of optical image reconstruction to the so-called "long waves" or microwave frequencies. Microwave holography was firstly proposed in mid 1960s motivated by the ability to penetrate optically opaque materials and the recent advances in microwave technology. A hologram is created when the whole information: amplitude, frequency, and phase of the signal is used in the reconstruction procedure. By doing so, one can see the depth of the image, which is absent in regular optical camera images or in film x-rays. The reason is that a camera records only the intensity (square amplitude) of light at a given frequency (for which the film is sensitive), whereas holography also records the phase that contains the depth, or the third dimension. The underpinning principle in microwave holography is to consider a reference wave[2] and a straightforward 2-stepped algorithm based on back-propagation of the received electric field [33]. This approach faced a number of technical and theoretical problems and did not provide images with enough quality for the requirements of medical applications, but rather for radar target identification, radio wave propagation or antenna diagnosis [34].

Later on, the so-called tomographic methods[3] were presented as a promising alternative to holography for cross-sectional or three-dimensional reconstruction of geometrically complicated biosystems [35]. The major contribution of tomographic methods was to relate the measured scattered fields with the object function or contrast profile, and form an estimate of the object's dielectric properties. To do so, one have to solve a non-linear inverse scattering problem which requires some regularization or approximation, at that time addressed using first-order diffraction tomography based on Born or Rytov aproximations. Imaging the dielectric properties of penetrable objects (in particular the refraction index) turned to be much more powerful in distinguishing tissues than the former visualization of the surface reflectance provided by microwave holography. [34].

This opened the door to microwave imaging for biomedical applications, specially when Larsen and Jacobi in the late 1970s obtained two-dimensional images of the internal structure of canine kidneys from the transmission coefficients between two antennas moved in parallel. It was the first time that sufficient penetration and resolution was reached to clearly distinguish various tissues. This was, in part, possible thanks to the wave impedance matching provided by a coupling or matching liquid, in that case, water [36]. This liquid was used as an interface between the antenna and the object to smooth the change in the dielectric properties seen by the wave as it propagates. It would prevent from large reflections in the object surface that may avoid the propagation inside the organ. From those results, microwave imaging for medical applications gained interest among the research community. Significant contributions were done under the UPC-Supélec collaboration during 1980s, establishing a complete theoretical and experimental imaging platform with the microwave circular scanner [9] and the planar camera [37] respectively, see Figure 1.7.

Soon, the limitations of diffraction tomography in retrieving quantitatively the dielectric properties of electrically large or highly contrasted objects came to light [38]. For this reason, the first inverse scattering iterative schemes were proposed [39, 40]. Again, the evolution of tomographic methods was truncated due to the huge computational cost of the iterative problem [41].

---

[2]This is the incident field that would have existed at the acquisition aperture if the target were not present

[3]The word tomography, originally referring to the representation of the imaged body in slices, is now attributed to a type of algorithm. However, all microwave imaging typologies (radar and holography) can produce tomographic images thanks to the coherent acquisition of the fields.

(a) Circular Scanner [9]   **(b)** Planar camera [37]
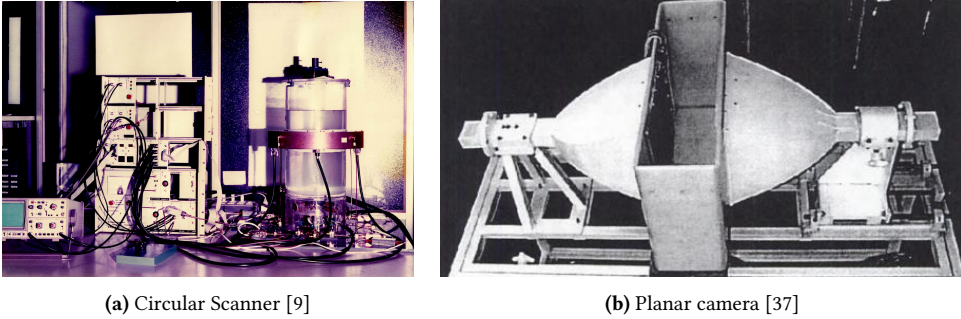
Figure 1.7: Experimental microwave imaging systems developed during late 1980s.

After more than 20 years of developments and powered by the significant progress in computers, measurement equipment and numerical techniques, in early 2000s microwave imaging for biomedical applications stirred researcher's interest again. This time, to the existing tomographic methods, another approach exploiting the principles of radar synthetic focusing, was considered. Radar-based or confocal methods seek to identify regions of strong backscatter which, in turn, could be associated to the presence of a contrast in dielectric properties [16]. At the same time, tomographic methods made a step forward to 3D multi-frequency systems. Accordingly, first tomographic methods acquired mono-frequency data on a single plane by an array of sensors, typically circular, which surrounded the imaged object [9]. As a result the 2D image represented a slice of the object. With this method, no vertical discrimination was achieved (in the direction perpendicular to the acquisition plane), meaning that only the objects that can be assumed uniform in vertical direction could be correctly imaged. Subsequently, the array was scanned vertically, acquiring and processing the data separately for each position [42]. Thus a stack of 2D images, derived from the data acquired on a single plane, was obtained. This method provided a 3D representation of the object but entailed a number of problems since the 3D images were not produced simultaneously processing all the available data [43]. In view of the inherent limitation of the 2D methods, the recent 3D tomographic methods process all the available data at once to produce 3D images. Also, multi-frequency algorithms stirred the interest of some researchers for the power to stabilize the solution of iterative methods and improve image quality [44].

1.4.1 Imaging Algorithms

Currently, the large amount of work done in the field of active microwave imaging algorithms for medical applications fall in two large groups: tomographic methods and radar imaging, see Figure 1.8. Whereas the staring point of both types of algorithms is common, they differ on the information that is reconstructed from this data. In both approaches the measured fields are acquired from a number of antennas surrounding the object under test. The acquisition must be done alternatively activating each antenna as a receiver to be able to differentiate each signal. Generally, the same antennas are also used to generate the field that illuminates the object.

13
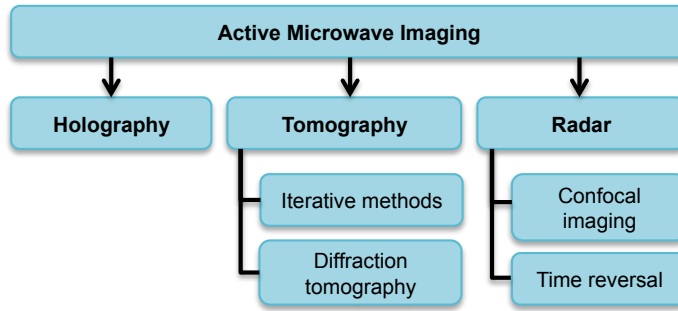
Figure 1.8: Summary of the microwave imaging methods proposed for medical applications.

1.4.1.1   Radar Imaging

Radar or confocal imaging exploits the principles of radar synthetic focusing, which are widely used in remote sensing, land-mine detection and underground surveillance [45]. The goal is to identify regions of strong backscatter similar to conventional radars. The success of the reconstruction depends crucially on acquiring as many scattered responses as possible at as many angles of illumination as possible. If a significant scatterer or target is present, all scattered signals may content its signature in addition to other undesired signals (clutter and noise).

Hence, prior to the application of the algorithm, the desired signal must be extracted from the measured data. For instance, in breast tumor detection the desired signal is the tumor response and the clutter includes reflections from the skin, breast tissues, antennas, structural parts of the imaging system, etc. Several strategies are used to this aim, generally based on windowing [46] or on the subtraction of two consecutive measurements, one presenting a small change into the scenario [44, 47]. Another strategy aimed to remove the considerable amount of reflection from the signature of the internal structures is to identify the outer surface of the breast [48].

The focusing algorithm is the classical Delay-And-Sum (DAS) or bifocusing algorithm. It consists on forming every image point by means of the synthesis of two focused groups of antennas (transmitters and receivers). The received signals from all the antenna pairs are numerically weighted by a focusing operator so as to be focused on a unique point. This numerical focusing operator restores the amplitude and phase changes suffered by a wave in its way to and from every scattering point in the object. The weighted signals corresponding to the same focusing point and all the antenna combinations are then added together coherently. This process is repeated for each focusing point [44]. Only the focusing points corresponding to a point where the object is present will be added constructively and will present a higher magnitude in the final image. Another interesting approach on the processing of backscattered pulses is presented by the time-reversal algorithms [49]. The final image will consist of a 3D energy intensity map, where the regions of large backscatterer indicate the presence of a contrast in dielectric properties.

In the framework of breast cancer detection, the capacity of radar approach to identify tumors is conditioned by an accurate reconstruction of its shape. Apart from tumors, other breast structures, such as fibroglandular tissue, present high contrast and thus strong backscattering

comparable to that of the tumor. Accordingly, since the presence of a spot in the radar image the is not sufficient to identify malignant tumors, irregular and non-symmetric shapes may be key factors to indicate the presence of malignant tumors [50].

1.4.1.2 Microwave tomography

The underlying idea of microwave tomography is to reconstruct the dielectric profile of the object under test (i.e. relative permittivity and conductivity). In this case the dielectric contrast between malignant and healthy tissues is the mechanism in which the detection is based. For a more detailed description about the dielectric properties of breast tissues the reader is referred to the next chapter.

The procedure aimed to retrieve the dielectric properties from the measured scattered field involves to solve an inverse scattering problem which is non-linear and generally ill-posed (the inversion of the solving matrix is not too stable and noise or measurement errors may lead to different solutions). As explained before, the first approach to this problem was addressed by using first-order approximations (Born or Rytov [51]) leading to the so-called diffraction tomography. Born approximation assumes that the field inside the object can be approximated to the incident field (without considering the scattering produced by the presence of the object). This approach has been widely used in biomedical imaging field [9, 34]. By doing so, the problem is linearized and the dielectric properties of the object could be retrieved. When Born approximation is not accomplished [38], the quantitative performance of the algorithm is degraded and only qualitative results are obtained, in a similar manner to that of radar images.

Iterative optimization schemes were then proposed to obtain a general exact reconstruction of the dielectric properties. The first step is the discretization of the imaged volume or surface into distinct cells as is depicted in Figure 1.9. For each individual cell, a initial guess of its dielectric properties, ϵ_0, σ_0, is assumed based on *a priori* information. At each iteration, the forward and the inverse scattering problem are solved until the optimization of a cost functional is reached. The first step is to compute the forward problem to obtain the scattered field $(\vec{E}_i^s)$ produced by the dielectric profile retrieved in the previous iteration due to a certain illuminating field. The subtraction between the measured, $\vec{E}_m^s$, and the computed field, define the error function also known as cost functional. The aim is to determine the dielectric properties of each cell through the minimization of the cost functional. In the minimization process, the dielectric properties of each cell are changed by small increments, $\Delta\epsilon_0$, $\Delta\sigma_0$, and the error value is re-calculated. The dielectric properties of the scenario are then updated and successively refined images are obtained. This process continues until the error converges to a small value.

The previous lines provide a generic description about the iterative process as an introduction to the reader. Nevertheless, this process can be conducted in a more sophisticated manner by the existing inverse scattering approaches. Several optimization methods have been utilized in microwave medical imaging such as Newton-Kantorwich [41], gradient methods [52], Gauss-Newton inversion [53], Born iterative method [54], contrast source inversion [55] and global optimization methods [56].
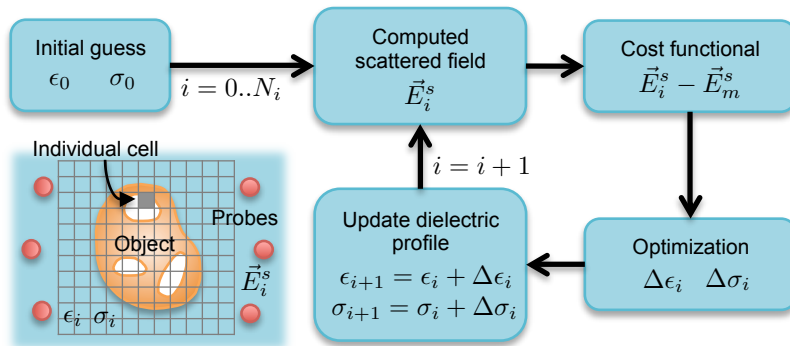
Figure 1.9: Scheme of a generic iterative tomographic process.
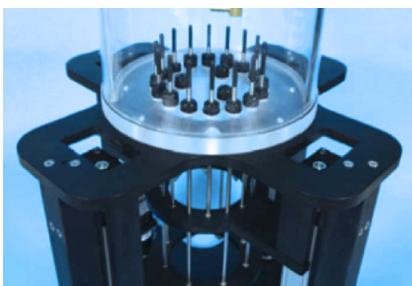
(a) Antenna array of 32 monopoles

(b) Photograph of the system in the clinic

Figure 1.10: Clinical cylindrical microwave breast imaging system [57].

1.4.2 Imaging Systems and Clinical Trials

The first near-field microwave imaging system used in clinical trials for breast cancer detection was developed at Dartmouth College [42], see Figure 1.10. The system consisted of a circular antenna array of 32 monopoles operating in the frequency range 300-1000 MHz. The antenna array was positioned in a tank filled with saline solution to act as coupling medium between the antennas and the breast. The patient lay in prone position with the breast hanging, through an opening in the table, into the tank where the antennas were immersed. The antenna array is moved vertically, in 1-cm steps, through a mechanical jack to acquire measurement from the chest level down to the nipple. A microwave switching system was used to select which antenna transmits the power from the microwave source and which antenna sends its received power to the receiver. This system, in conjunction to an iterative tomographic algorithm, was used in clinical trials in [18, 57, 58].

Another ultra-wideband microwave imaging system for breast cancer detection was developed by the University of Bristol [17], see Figure 1.11. The system consists of a multistatic radar operating at 4.5-10 GHz. The hemispherical prototype employed 31 cavity-backed patch antennas arranged in a 3D conformal hemispherical geometry connected with coaxial cables to

(a) Hemispherical array of 60 antennas   (b) Photograph of the system
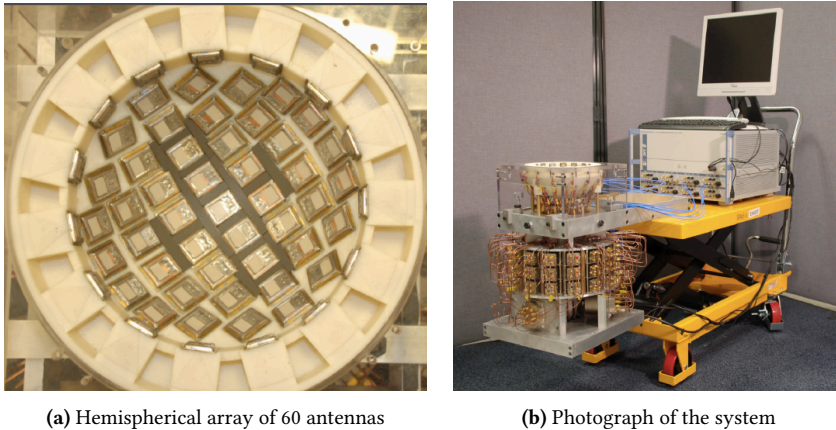
Figure 1.11: Microwave hemispherical multistatic radar breast imaging system [61].

a custom-built network of electromechanical switches. The bank of switches selects all possible pairs of antennas within the array and connects them to a vector network analyzer (VNA). The VNA performs the radar measurement in the frequency-domain that is transformed into time-domain in a post-reception step. This system was used in preliminary clinical trials [59]. Poor results for some of the patients showed that there was a lack of repeatably due to slight patient movement during the scan. Later on, with the aim of improving immunity to clutter and decreasing scan times, a new prototype of 60 antennas was presented [60]. Different ceramic cups and a paraffin based coupling medium were used to match the patient's breast inside the antenna array. [61] describes the initial clinical trials conducted with this system on 95 patients still showing some problems due to the breast fitting in the antenna array.

In the framework of brain stroke detection, the group of Chalmers University developed a 10 triangular patch antenna array mounted inside a bicycle helmet working in the frequency range 0.1 GHz to 3.0 GHz [14]. As matching medium, plastic bags filled with the matching liquid were placed between the helmet and the patient's head. The system uses two different algorithms aimed to distinguish between bleeding and non-bleeding strokes. The first is a full dielectric reconstruction method using inverse algorithms for microwave tomography. The second is not an imaging algorithm but a classifier based on calculated subspace distances in the measured data and a training set of data from patients with known diagnosis. With the last algorithm several clinical experiments were conducted [62].

1.5   Concluding remarks

Considering all the above mentioned, microwave imaging, join a set of valuable features, i.e. low health risk, portability, low cost and comfortable application, that are not provided by any of the current imaging methods. Reviewing the weaknesses of x-rays and the other methods in terms of imaging performance, the superiority of microwave imaging is arguable and in any case needs for more research, above all focused into ensuring the robustness of the method to experimental or clinical measurements.

Depending on the algorithm used for microwave imaging, a different result is achieved. In general, iterative tomographic methods succeed in imaging numerical breast models, but only a few have demonstrated to be robust enough to deal with experimental data [58]. Traditionally, data acquisition issues related to multi-path or noise corruption were the main hurdles towards clinical use. The major advantage of this methodology is that, in principle, the resolution is not diffraction limited and the major disadvantage stem from the EM forward model. Accordingly, the reconstruction is relatively slow, specially for full 3D geometries, and the fidelity of the model is sometimes questionable. In fact, in order to reduce the computational burden, most forward models currently used, assume one or more simplifications such as: sensors and structure invariant in one direction (to reduce the problem to a 2D one), sensors radiating like point sources or sensors measuring the field at one point. Such models have limited validity and may compromise the convergence of the algorithm which cannot be guaranteed.

Instead radar methods do not require to solve the inverse scattering problem and are inherently 3D and broadband. This approach has been widely investigated for its simplicity, robust signal processing and short computation time. First clinical trials [61] demonstrate the level of maturity achieved, however being limited to qualitative results and relatively contrasted scenarios.

Currently, non-iterative imaging methods based on diffraction tomography [J1, J3] or even holography [63] are being proposed again for medical applications. Several new features, such as multi-frequency, are now added aimed to enhance the image quality. While the computational cost of iterative algorithms is progressively less restrictive, the sensitivity to noise and the difficulty to model realistic scenarios in the forward problem, turn to be important limiting issues specially when thinking about a future clinical application. Holographic and diffraction tomography methods, instead, feature real time performance, versatility, and robustness to measurement noise. The limitation of qualitative reconstruction of the dielectric profile is arguable in the sense that the dielectric properties of the targeted tissue and the surrounding tissues may be so similar that can be confused, e.g. the dielectric properties of tumors and fibroglandular tissue. Thus the reconstructed exact dielectric properties might not be an ultimate criterion to identify injuries or disease, and other characteristics such as the shape can be useful.

1.6   Objectives of the Thesis

The encompassing objective of this doctoral thesis is to formulate and validate a tomographic algorithm for medical imaging using microwave radiation. Under this aim, a lot of work has been reported during the past 30 years, but once reviewed the state of the art seems reasonable to prioritize robustness in spite of having to renounce to a quantitative performance. This is the basic idea under the Magnitude Combined Tomographic algorithm that will be developed and assessed in this work according to the following specific goals:

- Formulate a 3D microwave tomographic algorithm for medical applications exploiting multi-view and multi-frequency information. With robustness as a prerequisite, a modified Born-based tomographic algorithm will be pursued, taking as a reference the previous experience of our department [8]. The aim is to maintain the advantages of the basis algorithm: quasi-real time, simple implementation and low noise sensitivity. Further work will explore the possibility to obtain quantitative reconstructions by adding an iterative process.

- Validate the algorithm with realistic and medically relevant simulations in the framework of breast cancer and brain stroke detection. Combine the visual inspection and the use of metrics to observe and quantify the reconstruction performance. The intermediate work includes the familiarization with the dielectric tissue characterization methods, brain and breast numerical models and electromagnetic simulation software.

- Validate the algorithm with experimental measurements in a non-controlled environment. Only a few 3D tomographic methods reported satisfactory results with non-canonical experimental measurements, due to their low robustness to noise, multipath or interferences. This work includes the design and building of the whole acquisition system and the manufacturing of the human organs and tissues models (phantom).
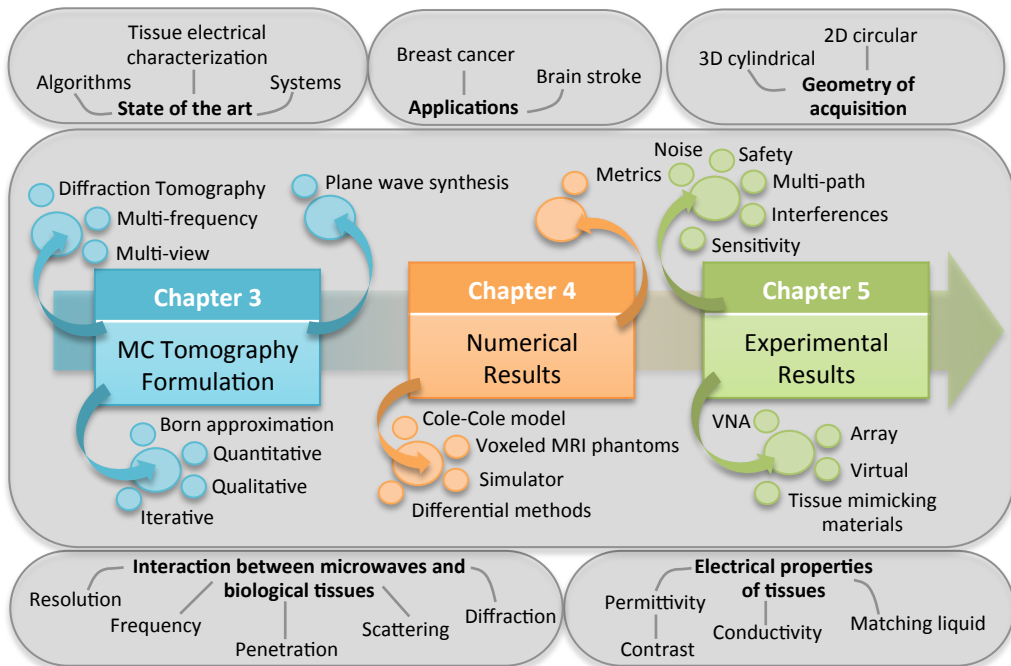
Figure 1.12: Objectives and outline of the thesis.

1.7   Outline and Organization of the Thesis

This doctoral dissertation is organized in six chapters, including the present chapter, which introduces microwave medical imaging, presents a comprehensive and detailed analysis of the state-of-the-art and defines the main goals of this work.

Chapter 2 describes the behavior of the materials when they are illuminated with an electromagnetic field. A special focus is given to biological tissues, and in particular, to the two driven applications of this thesis: breast cancer and brain stroke detection. From this study, the main mechanisms that enable the tissue differentiation, detection and characterization are derived. The information compiled in this chapter is the basis of microwave imaging and is essential to

contextualize the ideas, designs, mechanisms and procedures presented in the following chapters.

The three subsequent chapters contain the main contributions of this doctoral research. Each of these three chapters addresses one of the three objectives previously detailed as represented in Figure 1.12.

- Chapter 3 addresses the algorithm formulation starting from the original 2D circular tomographic method. To state the geometric independence of the basis algorithm, first of all, the generic algorithm is presented and then is particularized for 2D circular and 3D cylindrical acquisition geometries. The multi-frequency combination is performed using the Magnitude Combined method. Finally a frequency stepped method is proposed to keep the quantitative performance of the reconstruction.

- Chapter 4 collects the numerical results for both 2D and 3D algorithms in the framework of breast cancer and brain stroke detection. Increasingly realistic and complex models are considered ranging from the canonical ones to the voxeled MRI-derived phantoms.

- Chapter 5 covers the experimental work of the thesis. The construction of the acquisition system is performed step by step in parallel to the evolution of the algorithm. The ultimate goal is to reconstruct a realistic 3D phantom composed by tissue mimicking materials. Finally, a design for an arrayed experimental system is proposed.

The document is concluded in chapter 6 summarizing the main results presented along the document and enumerating the future research lines.

2

ELECTROMAGNETIC MODELING OF HUMAN TISSUES

W HEN an EM wave encounters a discontinuity in its propagation path, due to the presence of an object or scatterer, the wave experiments a change. Reciprocally, the EM field also produces electric changes into the internal structure of the scatterer. All this changes will depend actually on the molecular structure of the scatterer, that can be modeled by means of its electrical properties.

The aforementioned phenomena constitute the basis of the so-called direct and inverse scattering problems. The direct scattering problem consists of retrieving the scattered field resulting from the illumination of a known object by a given incident field. The prerequisite is an accurate modeling of the electrical properties of the object. On the other hand, the inverse scattering problem starts from the measured scattered fields and the aim is to retrieve the electrical properties of the unknown object. Both problems are treated in this thesis, the direct scattering problem is used to evaluate the proposed imaging algorithm, which in turn consists of solving the inverse scattering problem.

The direct scattering problem and the modeling of dielectric properties of human tissues are extensive research topics. In consequence, this chapter does not pretend to be an intensive review on this area, instead an introductory step prior to focus on the inverse problem.

2.1 EM waves in matter

The Maxwell's equations are the theoretical basis describing the propagation of EM fields in matter along the three dimensional axes [64, 65]. Assuming time-harmonic fields (time variations of the form $e^{j2\pi ft}$), the Maxwell's equations take the form:

$$\nabla \times \vec{E}(\vec{r}, f) = -j2\pi f \mu(\vec{r}, f)\vec{H}(\vec{r}, f) \tag{2.1}$$

$$\nabla \times \vec{H}(\vec{r}, f) = \vec{J}(\vec{r}, f) + j2\pi f \epsilon(\vec{r}, f)\vec{E}(\vec{r}, f) \tag{2.2}$$

$$\nabla \cdot \vec{D}(\vec{r}, f) = \rho(\vec{r}) \tag{2.3}$$

$$\nabla \cdot \vec{B}(\vec{r}, f) = 0 \tag{2.4}$$

The relationship between electric and magnetic field intensity vectors $(\vec{E}, \vec{H})$ and displacement vectors $(\vec{D}, \vec{B})$ is stated by means of the dielectric properties of the medium: the permittivity ϵ and magnetic permeability μ.

$$\vec{D}(\vec{r}, f) = \epsilon(\vec{r}, f)\vec{E}(\vec{r}, f) \tag{2.5}$$

$$\vec{B}(\vec{r}, f) = \mu(\vec{r}, f)\vec{H}(\vec{r}, f) \tag{2.6}$$

In a linear, heterogeneous and isotropic medium ϵ and μ are scalars not depending on the field intensities and varying along the coordinate axis $\vec{r}$ and frequency f. Assuming a source-free ($\rho = 0$) and lossy medium ($\sigma \neq 0$), the conduction current density can be expressed as $\vec{J} = \sigma \vec{E}$ with the conductivity σ in S/m. Some authors [65] write 2.2 directly in terms of the complex equivalent permittivity $\epsilon_{eq}(\vec{r}, f) = \epsilon(\vec{r}, f) - j\frac{\sigma(\vec{r}, f)}{2\pi f}$.

$$\nabla \times \vec{H}(\vec{r}, f) = \sigma(\vec{r}, f)\vec{E}(\vec{r}, f) + j2\pi f \epsilon(\vec{r}, f)\vec{E}(\vec{r}, f) = j2\pi f \left(\epsilon(\vec{r}, f) - j\frac{\sigma(\vec{r}, f)}{2\pi f} \right) \vec{E}(\vec{r}, f) \tag{2.7}$$

The complex permittivity describes the dielectric properties that influence the reflection of EM waves at the interfaces and the attenuation of wave energy within materials. This magnitude is often expressed in relative terms (compared to free-space)

$$\epsilon^*(\vec{r}, f) = \frac{\epsilon_{eq}(\vec{r}, f)}{\epsilon_0} = \epsilon'(\vec{r}, f) - j\frac{\sigma(\vec{r}, f)}{2\pi f \epsilon_0} = \epsilon'(\vec{r}, f) - j\epsilon''(\vec{r}, f) \tag{2.8}$$

where $\epsilon_0 = 1/(36\pi) \cdot 10^{-9}$ F/m is the permittivity of free space. The real part, ϵ', is referred as the dielectric constant and represents the stored energy when the material is exposed to an electric field, while the dielectric loss factor, ϵ'', which is the imaginary part, influences the energy absorption and attenuation due to the ohmic losses of the material. Another parameter of interest in dielectrics is the tangent loss angle defined as:

$$\tan \delta = \frac{\epsilon''(\vec{r}, f)}{\epsilon'(\vec{r}, f)} \tag{2.9}$$

For a perfect dielectric $\tan \delta = 0°$, while $\tan \delta = 90°$ denotes a perfect conductor.

2.2 Dielectric properties of biological tissues

Matter is composed of charged particles that are affected by the application of external fields (electric and magnetic fields produced by other charges). When an EM field encounters an object, the field excites a movement of the electric charges composing the object. Depending on its structure at cellular and molecular level, the movement can range from a free motion of electrons (conductors) to a slight shift between positive and negative charges (dielectrics or insulators). In case of dielectrics, the electric charges move forming electric dipoles aligned according to the illuminating field. At macroscopic level, the capacity of dielectrics to polarize, or in other words, the easiness of formation of such dipoles, is measured using the concept of permittivity. Hence the permittity determines how an electric field affects a dielectric medium, but also, how the field itself is affected by the presence of a dielectric.

Biological tissues are essentially dielectrics. The behavior of biological tissues at microwave frequencies is determined by the electro-chemical behavior of cells and their cellular structure. In particular, they present a permeability similar to the vacuum and a permittivity highly correlated to the water, which accounts for a 70% of its mass on average. The ability of the polar molecules to align with the electric field is described by dielectric relaxation theory. The polarization does not occur instantaneously, thus the associated time constant is called the relaxation time. One simple relaxation model is the Debye model:

$$\epsilon^*(f) = \epsilon_\infty + \frac{\epsilon_s - \epsilon_\infty}{1 + j2\pi f\tau} \tag{2.10}$$

The Debye model has been extensively used for modeling the frequency dependence of the complex permittivity of polar materials such as water. ϵ_s and ϵ_∞ are respectively, the relative permittivity at infinite and zero frequencies. The complex permittivity is modelled as a lossy resonant circuit. Since this effect is contracted by the thermal agitation, when the electric field is interrupted, the alignment relaxes exponentially at a rate τ^1 [66].

Dielectric data from biological tissues commonly exhibits relaxation behavior that is far broader than the simple Debye type. This could arise from the superposition of several relaxation processes. As a result, the permittivity decreases when frequency increases in different steps called dispersions. These dispersions are not produced instantaneously, and are characterized by the corresponding relaxation phenomena. In biological systems, there are four relaxation regions [67]. Each relaxation occurs in a specific frequency range and allows to identify different phenomena. At the frequencies employed in the present work, the γ is the main dispersion, see Figure 2.1. The γ-dispersion, also called orientation polarization, is located at GHz region, and it is due to the polarization dipoles, fundamentally free water molecules. Accordingly, the data from biological tissues can be fitted nicely by a modified form of Debye model known as the Cole-Cole function [67]. This model takes into account the dispersion of the relaxation constant of the material called α.

$$\epsilon^*(f) = \epsilon_\infty + \frac{\epsilon_s - \epsilon_\infty}{1 + (j2\pi f\tau)^{(1-\alpha)}} \tag{2.11}$$

To enable a more wideband performance, the relaxation constant and the permittivity values

---

[1]Note that the position dependence ($\vec{r}$) has been removed from the permittivity formulation. In general we assume that the phantoms are composed by the aggregation of a finite number of homogeneous tissues. Each one of these homogeneous tissues is modeled with unique Cole-Cole formula.

ϵ_s and ϵ_∞ can be divided into several regions by adding intermediate values.

$$\epsilon^*(f) = \epsilon_\infty + \sum_n \frac{\epsilon_n - \epsilon_{n+1}}{1 + (j2\pi f\tau_n)^{(1-\alpha_n)}} + \frac{\sigma}{j2\pi f\epsilon_0} \tag{2.12}$$

The last term accounts for the losses due to the ionic conductivity σ. This equation was successfully assessed between 10 Hz and 100 GHz [68]. More recently, [69] demonstrated that a the single-pole Cole-Cole model is sufficient to fit the dielectric properties of biological tissues between 0.5 and 20 GHz.

$$\epsilon^*(f) = \epsilon_\infty + \frac{\epsilon_s - \epsilon_\infty}{1 + (j2\pi f\tau)^{(1-\alpha)}} + \frac{\sigma}{j2\pi f\epsilon_0} \tag{2.13}$$
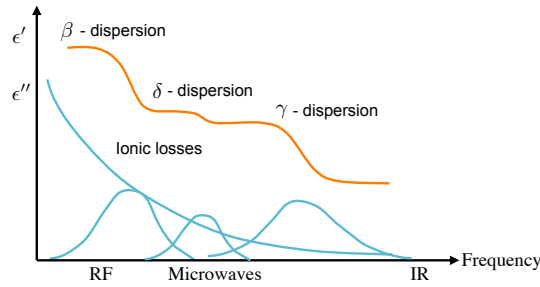
Figure 2.1: Ideal representation of dielectric constant and loss factor spectra in biological tissue [70].

Up to this moment, the theoretical basis of tissue characterization has been stated. This theory models correctly the frequency dependent dielectric properties of different biological tissues mainly characterized by its water content. Depending on the water content, human tissues can be divided into two main groups: materials with high and low water content. Muscle, liver, kidney, brain, skin, lung and blood compile the first group. Fat and bone may be included in the second group. Accordingly, the dielectric constant of these tissues ranges from 5 (bones and fat) to more than 50 (body fluids including blood, muscle or kidney). A summary of the dielectric properties obtained with Cole-Cole models for different human tissues at 3 GHz is presented in Table 2.1.

Apart from the variability between different tissues, the complex permittivity changes within the same tissue. Cole-Cole models (2.11) include basically the frequency dependence (dispersion), but there are other effects that are not actually modeled for various reasons:

- Temperature: all the studies assume a certain temperature during the measurement that ranges between 19°C and 28°C *in-vitro* and around 37°C *in-vivo*.

- *in-vivo* and *in-vitro* measurements: permittivity and conductivity values tend to decrease very rapidly when the tissue is excised (less than 5 min, being almost stable between 5 min. and 5 h. after resection) due to changes in blood flow, water content and the interruption of the metabolism [71]. This effect is more noticeable in low water content tissues (such as adipose) [72]. Current reference studies on dielectric properties of body tissues [4,67–69,73] are based on measurements on excised tissues. [72] states that *ex-vivo* measurements did not consider the variation in the dielectric properties of living tissues,

Tissue	% Water	ϵ'	σ(S/m)
Gray matter	89	48	2.2
White matter	87	35	1.5
Blood	83	57	3.0
Lung	82	47	0.2
Heart	80	54	2.7

Tissue	% Water	ϵ'	σ(S/m)
Kidney	77	51	2.9
Liver	76	42	2.1
Muscle	75	52	2.1
Bone	12	11	0.5
Fat	8	5	0.1

Table 2.1: Approximate dielectric constant and conducitivty of human tissues related to its water content at 3 GHz [4, 5, 67, 68].

but also anticipated that the difference in the dielectric properties between *in-vivo* and *ex-vivo* was in the range of 20% to 39% depending on the frequency.

- Variability between individuals: the shapes and electrical parameters differ significantly from one person to another. Moreover they change over time in a given person due to various reasons (age, accidental or therapeutic irradiation, pathological conditions, etc.) [74].

- Physiological and pathological conditions: any change in the tissue affecting its water content, produce strong variations in the complex permittivity. This is the basis of the detection principle in microwave imaging [69]. It has been demonstrated that tissue malignancies, blood supply, hypoxia, acute ischemia, and chronic infarction, change tissue dielectric properties [13, 75, 76].

2.2.1 Normal and malignant breast tissues

Before proceeding with the dielectric characterization of breast cancer, it is worth commenting, at this point, the anatomy of the breast and the types of breast cancer. This is to ensure that the breast phantoms that will be used later on for the evaluation of the reconstruction algorithm is realistic and of interest to the medical community.

Breasts are modified sudoriferous glands which produce milk in women. Externally, each breast has one nipple surrounded by the areola. Internally the breast contains a number of mammary glands mainly distributed within 30 mm of the base of the nipple. These are drained to the nipple by 4-18 lactiferous ducts forming a complex network similar to the tangled roots of a tree. The remainder of the breast is composed of connective tissue (collagen and elastin), adipose tissue (fat) and ligaments. The ratio of glands to adipose tissue ranges from 1:1 in non-lactating women to 2:1 in lactating women, see Figure 2.2.

There are many different types of breast cancer, each named by the part of the breast where the cancer cells begin to grow. Ductal carcinoma is the most common type and begins in the cells of the ducts. Lobular carcinoma is another type of breast cancer that starts in the lobules. If a tumor remains within the duct or lobule it is known as carcinoma in situ accounting for the 60% of the diagnosed cases, whereas if a tumor spreads outside the duct or the lobule is known as infiltrating or invasive carcinoma. Invasive carcinoma can be regional, if only has spread to surrounding tissue or nearby lymph nodes, or distant, if it has metastasized (spread)
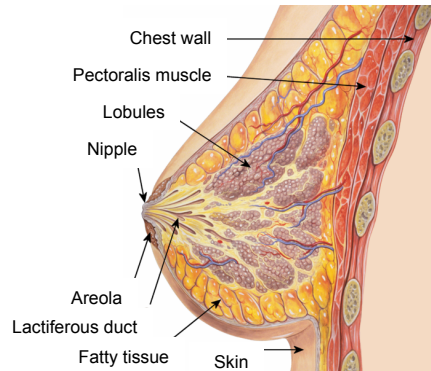
Figure 2.2: Normal breast anatomy scheme. ©Patrick J. Lynch, used under a Creative Commons Attribution-ShareAlike license: http://creativecommons.org/licenses/by-sa/3.0/

to distant organs. Regional carcinomas represent the 33% of the diagnosed cancers and distant carcinomas account for the 5% of cases [77].

Doctors diagnose and classify breast cancer according to stages (stages 0 to IV). In order to determine the stage of breast cancer the oncologist considers 3 important factors: tumor size, nodal status and metastasis [77]:

- Stage 0: ductal or lobular carcinoma in situ is very early stage breast cancer that has not spread beyond the duct or lobule.

- Stage I: tumor is 2 cm or smaller and has not spread outside the breast. Tumors smaller than 2 cm represent 75 cases in 100 000 women.

- Stage II: no tumor found in the breast but cancer is found in the axillary lymph nodes, or the tumor is 2-5 cm (can be spread to the axillary lymph nodes) or larger than 5 cm but confined to the breast. Tumors between 2.1 and 5 cm represent 35 cases in 100 000 women.

- Stage III: the tumor has spread to tissue near the breast and may have spread to lymph nodes within the breast, under the arm, beneath the collarbone or near the neck. Tumors bigger than 5 cm represent 7 cases in 100 000 women.

- Stage IV: tumor has spread to other organs of the body, most often the bones, lungs, liver or brain.

Stages 0, I and II are considered to be early breast cancer. In this stages the survival rates are significantly higher (93%, 88% and 77%) than those of III and IV stage being 53% and 15% respectively [78].

Apart of the tumor size, another important indication is the tumor shape. The importance of the tumor shape lies on the fact that benign tumors tend to have irregular nonsymmetrical contours. Therefore detecting the shape of the tumor can help to diagnose its malignant or benignant nature.

In spite of having a very heterogeneous composition, the location of the breast outside the high-loss thoracic wall and the low-loss adipose-dominating internal breast tissue, initially make breast cancer detection a good candidate for microwave imaging. Due to the potentiality

of microwave imaging for breast tumor detection, extensive literature on the dielectric properties of breast tissues exist since the beginning of the 80s [75, 76, 79]. The conclusion from these measurements was that a significant contrast between malignant and normal breast tissues of approximately 4:1 in relative permittivity and between 4-8:1 in conductivity existed in the microwave regime. The initial significant contrast between normal and malignant breast tissues was one reason for microwaves to quickly become a subject of intense research worldwide in a quest for a new modality for early-stage breast cancer detection. More recent measurement campaigns showed that the contrast between the tumor and normal breast was slightly overestimated. By considering *in-vivo* tissues, instead of *ex-vivo* samples, this contrast seems to be close to 2:1 in permittivity and 3:1 in conductivity, according to the reconstructed images from a clinical tomographic breast imaging prototype [42]. These studies also indicate that while contrasts between malignant and fatty breast tissue may be as large as 10, those between malignant and healthy fibrogladular tissues can be as low as 10% in both permittivity and conductivity [18, 57, 69, 72, 73]. This finding is important since most breast tumors appear in the fibroglandular tissue (about a 58%) that includes milk ducts and the fibers that support the breast. This also implies that signature of the tumor is substantially reduced in younger women where the fibroglandular portion of the breast is significant. However, in older women the fibroglandular portion of the tissue is considerably reduced and, therefore, microwave imaging has more potential in older women than in younger women [80].

Three main approaches were proposed to overcome the low contrast limitation: the first consists of using a hybrid imaging modality, the second is to administer contrast agents in the microwave range and the third consists of exploiting differential methods. Examples of hybrid imaging include the combination of microwave with acoustic imaging [81] or microwave with MRI [82]. Contrast agents account for the inoculation of microbubbles [83] or carbon nanotubes [84] that may accumulate in the lesion and increase its contrast. Finally, differential methods relay on the comparison of two consecutive measurements, one before and one after administering the contrast agent or producing any change into the target. Actually, this approach reconstructs the difference between both measurements. By doing so, only the parts that experienced a change in its dielectric properties will be visible in the reconstructed image [J1].

Recently, Lazebnik *et. al.* issued the need of an extended large scale characterization of the dielectric properties of female breasts. As a result, the major platform of breast tissue models for microwave imaging was presented [85]. It consists of an online repository of anatomically realistic numerical breast phantoms derived from MRI images of patients in prone position. The numerical phantoms are classified according to their radiographic density as follows: almost entirely fat (<25% glandular), scattered fibroglandular (25-50%), heterogeneously dense (51-75%) and very dense (>75%). Each phantom is comprised of a 3D grid of cubic voxels of 0.5 mm^3. The breast model incorporates the structural heterogeneity of normal breast tissue and its realistic dispersive dielectric properties based on [69, 73]. In this large scale study, the dielectric properties of normal, benign, and malignant tissue were measured *ex-vivo*. The study involved 354 normal breast tissue specimens from healthy patients (breast reduction) and 319 tissue specimens from cancer surgeries over a frequency range from 0.5 to 20 GHz. The conclusion of this study was that the normal breast tissues can be classified into three different groups depending on the adipose content: 0-34% adipose, 35-84% adipose and 84-100% adipose. By using this classification they obtained much more stable results, where the age dependency and the *in-vivo/ex-vivo* differences seem to be lower than expected. Figure 2.3 shows the 3D view of
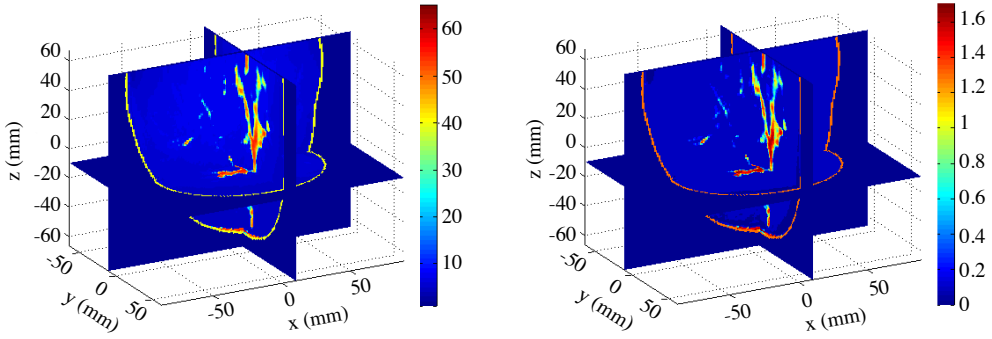
(a) Relative permittivity of a MRI-derived voxeled breast model [85] at 2 GHz.

(b) Conductivity of a MRI-derived voxeled breast model [85] at 2 GHz

0-30% adipose breast tissue
31-84% adipose breast tissue
84-100% adipose breast tissue
tumor
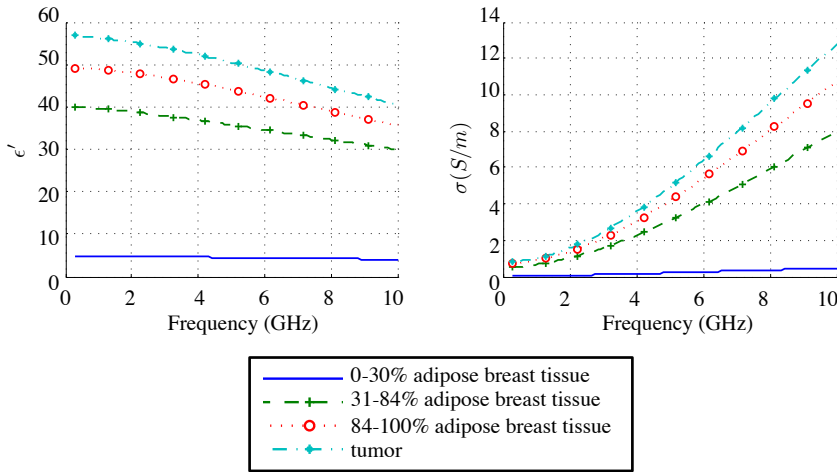
(c) Relative permittivity and conductivity of the malignant and normal breast tissues between 0.5 and 10 GHz [69, 73].

Figure 2.3: Dielectric properties of brain tissues.

the voxeled breast model and the values of the permittivity and conductivity of the main breast tissues over the 0.5-10 GHz band.

2.2.2 Brain tissues

Similarly to breast tumor detection, stroke detection can be addressed by using microwave imaging to visualize the presence of bleeding inside the brain tissues. Microwaves have the ability to distinguish a blood accumulation from the surrounding brain tissues thanks to its high permittivity and losses. In this way hemorrhagic strokes may be differentiated from the ischemic strokes.

The brain is located and protected inside the bony skull which is externally covered by

the scalp. Inside the skull, the brain is covered and protected by three layers of tissue called meninges. The space between the two most internal layers is full of a fluid called cerebrospinal fluid (CSF) which bathes and cushions the brain, see Figure 2.4.

The brain itself is composed of the cerebrum, the cerebellum, and the brainstem as shows Figure 2.4. The cerebrum is the largest part of the brain and is composed of right and left hemispheres. It performs higher functions like interpreting touch, vision and hearing, as well as speech, reasoning, emotions, learning, and fine control of movement. The cerebellum is located under the cerebrum. Its function is to coordinate muscle movements, maintain posture, and balance. The brainstem includes the midbrain, pons, and medulla. It acts as a relay center connecting the cerebrum and cerebellum to the spinal cord. It performs many automatic functions such as breathing, heart rate, body temperature, wake and sleep cycles, digestion, sneezing, coughing, vomiting, and swallowing. The surface of the cerebrum has a folded appearance called the cortex. The cortex contains about 70% of the 100 billion nerve cells. The nerve cell bodies color the cortex gray-brown giving it its name, gray matter. Beneath the cortex are long connecting fibers between neurons, called axons, which make up the white matter. The brain communicates with the body through the spinal cord and twelve pairs of cranial nerves 2.4. Hemorrhage, or bleeding, occurs when a blood vessel breaks, either from trauma
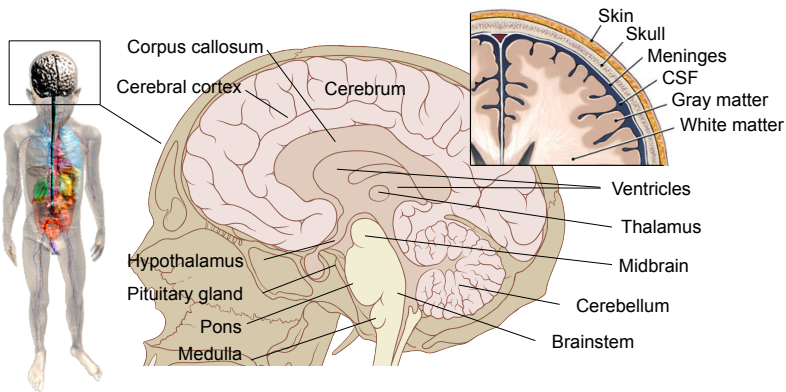
Figure 2.4: Normal brain anatomy: main brain parts and protective layers. ©Patrick J. Lynch, used under a Creative Commons Attribution-ShareAlike license: http://creativecommons.org/licenses/by-sa/3.0/

or excess internal pressure. Intracerebral hemorrhage affects vessels within the brain itself, while subarachnoid hemorrhage affects arteries at the brain's surface, just below the protective arachnoid membrane. Intracerebral hemorrhages represent about 10% of all strokes, while subarachnoid hemorrhages account for about 7%. Hemorrhage into the lower brain region (i.e., pons) carries a grave prognosis, with 55% mortality and 24% dependency in survivors. Hemorrhage into other locations may have a much better prognosis for survival and independence. Concerning the hemorrhage size, patients with a hemorrhage size of 60 cubic centimeters (cc), have an estimated 30-day mortality rate of 91%. Patients with a hemorrhage volume of 30 cc or more were severely disabled at 30 days. In this thesis, the hemorrhage will be modeled as a blood sphere, thus a 60 cc lesion would be represented with a sphere of 24 mm in radius and a 30 cc lesion with a sphere of 12 mm. Thus we will be interested in detecting lesions smaller

than 12 mm in radius to ensure a better prognosis.

Unlike breast tissues, brain was not object of intense research in the field of microwave imaging. Only a few examples can be found in the literature [13, 62] and are very preliminary. However the rapid increase and public acceptance of modern mobile communication equipment in recent years was a matter of public health concern. Thus the RF exposure levels, specially in the head area, began to be controlled using specific absorption rate (SAR) measurements during the mobile phone usage. Therefore several studies were conducted towards obtaining accurate values of the dielectric properties of living human head tissues in the frequency range from 800 to 2450 MHz [86]. Other studies cover a wider frequency range, and thus are more suitable for microwave imaging, ones are specific to brain tissues [87], or extensive human tissue repositories [4, 5, 67, 68]. Also anatomically realistic whole-body human models exist. A very complete one is Virtual Family from IT'IS fundation that consists of several full human computer-aided design (CAD) models with up to 84 different tissues and organs including the brain. All the models are represented as a 3D CAD objects (not voxels), hence allowing to be meshed at arbitrary resolutions [88]. Figure 2.5 shows a 3D view of the voxeled brain model extracted from [88] in which the dielectric properties of the main brain tissues are included [5].

2.3   The direct scattering problem

This section is devoted to the calculation of the diffraction produced by the illumination of a dielectric object leading to the so-called direct scattering problem. The understanding of the direct problem is a crucial point for the retrieval of the reciprocal problem, which is the inverse scattering problem.

The propagation of the EM energy in a medium is defined by a differential equation that can be derived form the Maxwell's equations namely wave equation. Applying the rotational to equation (2.1) and introducing equation (2.2) in the second term then:

$$\nabla \times \nabla \times \vec{E}(\vec{r}, f) = -j2\pi f \mu(\vec{r}, f)(\vec{J}(\vec{r}, f) + j2\pi f \epsilon(\vec{r}, f)\vec{E}(\vec{r}, f)) \tag{2.14}$$

Using the identity $\nabla \times \nabla \times \vec{E} = -\nabla^2 \vec{E} + \nabla(\nabla \cdot \vec{E})$, then

$$\nabla^2 \vec{E}(\vec{r}, f) + k^2 \vec{E}(\vec{r}, f) = j2\pi f \mu_0 \vec{J}(\vec{r}, f) - \nabla(\nabla \cdot \vec{E}) \tag{2.15}$$

where $k = 2\pi f \sqrt{\mu_0 \epsilon(\vec{r}, f)}$ is the wavenumber in the medium that depends on the frequency f and the position $\vec{r}$. μ can be approximated to that of the vacuum $\mu_0 = 4\pi \cdot 10^{-7}$ H/m for nonmagnetic materials such as biological tissues[2]. Since the permittivity of the medium depends on the position, the divergence of the field

$$\nabla \cdot \vec{E} = \epsilon \vec{E} \cdot \nabla(1/\epsilon) = -\vec{E}\frac{\nabla \epsilon}{\epsilon} \tag{2.16}$$

has to be considered. The divergence contains the gradient of the permittivity and thus will produce changes into the polarization of the field. However the polarization effects can be

---

[2]Note that the position and the frequency dependence of the wavenumber is not indicated to simplify notation

(a) Relative permittivity of a MRI-derived voxeled brain model [88] at 2 GHz.

(b) Conductivity of a MRI-derived voxeled brain model [88] at 2 GHz

(c) Relative permittivity and conductivity of the main brain tissues between 0.5 and 10 GHz [5].
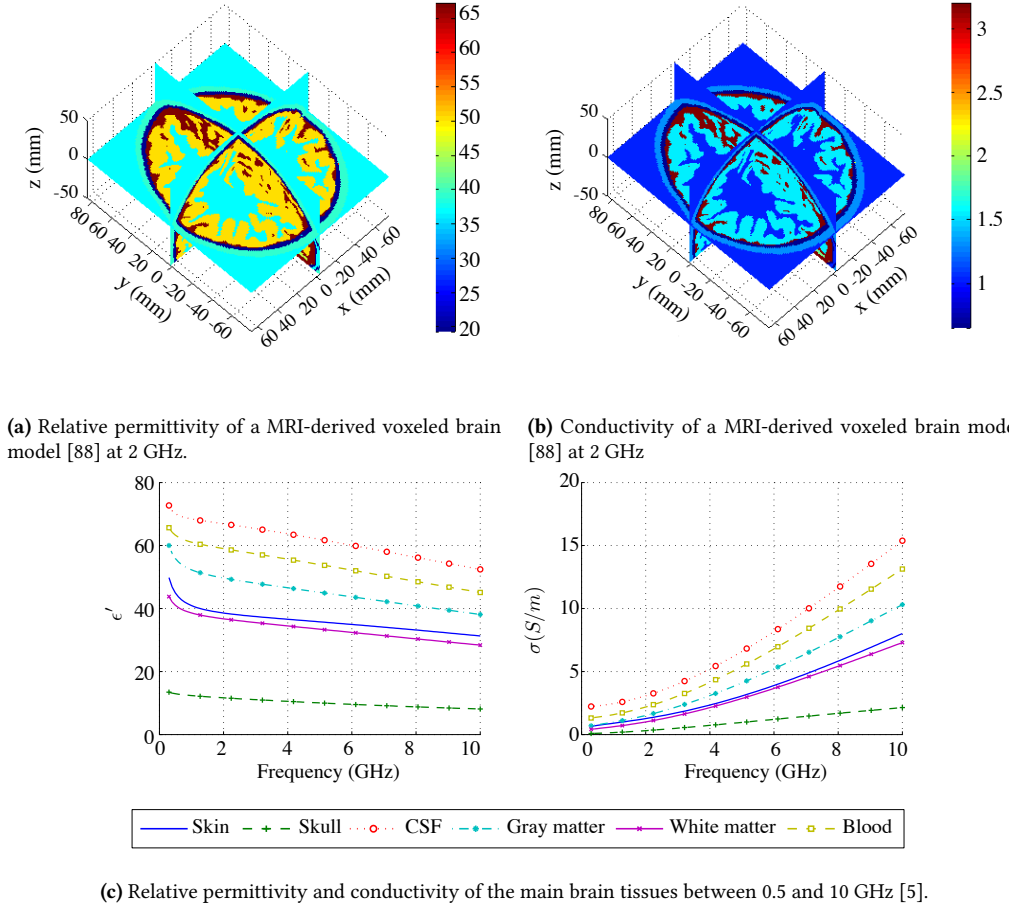
Figure 2.5: Dielectric properties of brain tissues.

ignored if the wavelength is much smaller than the correlation size of the inhomogeneities in the object.

$$\nabla^2 \vec{E}(\vec{r}, f) + k^2 \vec{E}(\vec{r}, f) = j2\pi f \mu_0 \vec{J}(\vec{r}, f) \tag{2.17}$$

Assuming that an object is immersed in a homogeneous medium of permittivity ϵ_b, namely background medium, the last term of the wave equation can be related to the excitation produced by the induced currents in the object.

$$\nabla^2 \vec{E}(\vec{r}, f) + k_b^2 \vec{E}(\vec{r}, f) = j2\pi f \mu_0 \vec{J}_{eq}(\vec{r}, f) \tag{2.18}$$

These induced currents can be defined as the currents that when applied to an homogeneous medium of permittivity ϵ_b produce the same field distribution as the original problem. The expression of the induced currents can be easily derived from the Maxwell's equations in a source-free area

$$\nabla \times \vec{H}(\vec{r}, f) = j2\pi f \epsilon(\vec{r}, f) \vec{E}(\vec{r}, f) = \vec{J}_{eq}(\vec{r}, f) + j2\pi f \epsilon_b(f) \vec{E}(\vec{r}, f) \tag{2.19}$$

31

$$\vec{J}_{eq}(\vec{r}, f) = j2\pi f(\epsilon(\vec{r}, f) - \epsilon_b(f))\,\vec{E}(\vec{r}, f) = -j2\pi f\epsilon_b(f)c(\vec{r}, f)\vec{E}(\vec{r}, f) \qquad (2.20)$$

c is the contrast function of the object with respect to the background medium defined as:

$$c(\vec{r}, f) = 1 - \frac{\epsilon(\vec{r}, f)}{\epsilon_b(f)} \qquad (2.21)$$

Then the wave equation can be expressed as:

$$\nabla^2 \vec{E}(\vec{r}, f) + k_b^2 \vec{E}(\vec{r}, f) = k_b^2 c(\vec{r}, f)\vec{E}(\vec{r}, f) \qquad (2.22)$$

The electric field $\vec{E}(\vec{r}, f)$, sometimes called total field by some authors, can be considered as the superposition of two components: the incident field $\vec{E}^i$ existing in the homogeneous background medium without the object, and the scattered field $\vec{E}^s = \vec{E} - \vec{E}^i$ produced by the induced currents in the object. Since the incident field satisfies the homogeneous wave equation, $\left(\nabla^2 + k_b^2\right)\vec{E}^i(\vec{r}, f) = 0$, (2.22) can be written as:

$$\nabla^2 \vec{E}^s(\vec{r}, f) + k_b^2 \vec{E}^s(\vec{r}, f) = k_b^2 c(\vec{r}, f)\vec{E}(\vec{r}, f) \qquad (2.23)$$

By solving 2.23 for a point source located at $\vec{r}'$, $\delta(\vec{r} - \vec{r}')$, the general solution for an arbitrary source can be inferred.

$$\left(\nabla^2 + k_b^2\right)G(\vec{r} - \vec{r}', f) = -\delta(\vec{r} - \vec{r}') \qquad (2.24)$$

The solution of equation (2.24) is given by the Green's function, that in $\mathbb{R}^3$ takes the form:

$$G(\vec{r} - \vec{r}', f) = \frac{e^{\pm jk_b|\vec{r} - \vec{r}'|}}{4\pi|\vec{r} - \vec{r}'|} \qquad (2.25)$$

and in $\mathbb{R}^2$ depends on the Hankel function of second kind:

$$G(\vec{r} - \vec{r}', f) = \frac{1}{4j}H_0^{(2)}(k_b|\vec{r} - \vec{r}'|) \qquad (2.26)$$

Thanks to the linearity of the wave equation and using Green's theorem [89], the scattered field can be expressed as the convolution of the excitation with the Green's function:

$$\vec{E}^s(\vec{r}, f) = -k_b^2 \int_{v'} c(\vec{r}', f)\vec{E}(\vec{r}', f)G(\vec{r} - \vec{r}', f)d\vec{v}' \qquad (2.27)$$

This equation is confirmed everywhere and in particular inside the imaging domain v'. By considering the total field, $\vec{E}$, as the superposition of the incident field, $\vec{E}^i$, and the scattered field, $\vec{E}^s$, the integral formulation for the total field is obtained.

$$\vec{E}(\vec{r}, f) = \vec{E}^i(\vec{r}, f) - k_b^2 \int_{v'} c(\vec{r}', f)\vec{E}(\vec{r}', f)G(\vec{r} - \vec{r}', f)d\vec{v}' \qquad (2.28)$$

This two coupled equations constitute the starting point of methods for solving the direct scattering problem aimed to calculate $\vec{E}^s$ from the knowledge of the dielectric properties of the object or the contrast, c, and $\vec{E}^i$.

2.3.1 Solving the direct scattering problem

In general, equation (2.28) cannot be solved analytically since $\vec{E}^s$ appears also inside the integral (in the total field, $\vec{E}$). For the calculation of the scattering produced by the highly heterogeneous and complicated biological stuff, nowadays numerical methods are used. Nevertheless, before the advent of the cost-effective and powerful computers, different approximation methods were studied.

2.3.1.1 Analytic solution

Only in cases where the object has a very simple geometry, equation (2.28) can be solved analytically in one of the usual coordinate systems. This is the case of the scattering by metallic cylinders and wedges in cylindrical coordinates and the scattering by metallic spheres in spherical coordinates [64]. A more interesting case in the framework of this thesis, is the scattering by a dielectric cylinder in a cylindrical coordinate system. For the full derivation of this expression, the reader is referred to the appendix A.

2.3.1.2 First order approximations

First order approximations, and in particular Born approximation, allow to formulate the scattered field in explicit form and they will be the basis of the inverse problem solution proposed in this thesis. First order approximations are based on the hypothesis of weak scattering objects producing small perturbations on the incident field. Two main methods are commonly used to approximate the integrand of (2.27) namely Born and Rytov approximations [51].

Born approximation assumes that the scattered field is negligible in front of the incident field inside the object, $\vec{E}^s(\vec{r}, f) << \vec{E}^i(\vec{r}, f)$, thus, $\vec{E}(\vec{r}, f) \simeq \vec{E}^i(\vec{r}, f)$ and (2.28) can be expressed as:

$$\vec{E}(\vec{r}, f) \simeq \vec{E}^i(\vec{r}, f) - k_b^2 \int_{V'} c(\vec{r}', f)\vec{E}^i(\vec{r}', f)G(\vec{r}, \vec{r}')d\vec{v}' \tag{2.29}$$

Rytov approximation assumes a smooth phase change of the total field with respect to the incident field. For this reason the total field is defined as $\vec{E}(\vec{r}, f) = e^{\phi(\vec{r}, f)}$ where $\phi(\vec{r}, f) = \phi^i(\vec{r}, f) + \phi^s(\vec{r}, f)$. Analogously to Born approximation, Rytov approximation assumes that $\phi^s(\vec{r}, f)$ can be neglected in front of $\phi^i(\vec{r}, f)$, then:

$$\vec{E}(\vec{r}, f) \simeq \vec{E}^i(\vec{r}, f)e^{\phi^s(\vec{r}, f)} \tag{2.30}$$

where:

$$\phi^s(\vec{r}, f) = -\frac{k_b^2}{\vec{E}^i(\vec{r}, f)} \int_{V'} c(\vec{r}', f)\vec{E}^i(\vec{r}', f)G(\vec{r}, \vec{r}')d\vec{v}' \tag{2.31}$$

Both approximations lead to similar formulation but their applicability range is different. Born approximation produces a better estimation of the scattered amplitude for large deviations in the dielectric contrast for objects small in size. On the other hand, the Rytov approximation gives a more accurate calculation of the scattered phase for large-sized objects with small deviations in contrast.

	FDTD	FEM	MoM
Description	Approximating continuous derivatives with finite (or discrete) differences.	Based on connecting simple element equations over many small subdomains (finite elements) to approximate a more complex equation over a larger domain. No direct discretization but uses variational formulation or weighted residuals.	Approximating the problem by a system of linear equations by expanding the unknown currents into basis functions weighted by a set of testing functions.
Domain	Time	Frequency	Time or Frequency
Equations	Differential	Differential	Integral
Pros	Very simple algorithm, easy modeling of arbitrarily complicated shapes and materials, wideband.	Usefull in complex inhomogeneous structures.	General and accurate.
Cons	Waveform deformation and grid anisotropy, blocked approximation of curved surfaces, grid termination problem.	Grid termination problem.	High computational cost due to the matrix inversion.

Table 2.2: Summary of the main features of FDTD, FEM and MoM numerical methods.

2.3.1.3 Numerical methods

Numerical methods are aimed to solve the direct scattering problem by discretizing the space in cells and solving Maxwell's equations at each point in the grid. Discretization consumes computer memory, and solving the equations takes significant time. Large scale problems face memory and CPU limitations. Typical formulations involve either time-stepping through the differential equations over the whole domain for each time instant (finite difference time domain (FDTD)); or through banded matrix inversion to calculate the weights of basis functions when modeled by finite element method (FEM); or calculating integrals when using method of moments (MoM), see Table 2.2.

Choosing the right technique for solving a problem is important, as choosing the wrong one can either result in incorrect results, or results which take excessive time to compute. When simulating realistic biological stuff, the organ is commonly divided in a grid of small cubes or voxels. Each voxel has an homogeneous complex permittivity that models the electrical properties of the tissue occupying the volume of the voxel. Due to the former and the interest in using multi-frequency illumination, Finite Difference Time Domain (FDTD) method is more appro-

priate [90]. FDTD is a widely used numerical method when solving inhomogeneous problems with different dielectric materials. It starts form Maxwell's equations in differential form and solves the direct problem in time domain in a discretized and limited spatial region. This region has to be well delimited by perfect magnetic layer (PML) boundaries that absorb completely all the reflections, thus simulating free space. The smaller the discretization, the more accurate the solution is.

Several commercial electromagnetic simulation software packages exist, which often include more than one solver. In the framework of this thesis a freely available FDTD software package namely MEEP [91] and CST EM simulation software, will be used to perform the simulations for the assessment of the reconstruction algorithm.

2.4   Concluding remarks

This chapter has stated the theorethical and practical framework for solving the direct scattering problem devoted to obtain the scattered field resulting from the illumination of the object under test with a certain incident field.

A preliminary step to calculate the direct problem is to model the dielectric properties of the human tissues. This can be accurately done using Cole-Cole models which take into account the frequency dispersive character of biological tissues.

The direct scattering problem does not have an analytic solution except from very canonical geometries. For a general solution one have to resort to numerical methods. The most suitable method for the simulation of human organs and tissues, specially when they are discretized in voxels, is the FDTD. Several commercial EM simulation programs exist that implement this method. In the following chapters MEEP simulation software will be used for the 2D simulations and CST studio for the 3D simulations.

This thesis is focused into breast cancer and brain stroke detection. Both represent significant medical challenges which can benefit from the microwave technology to improve the current diagnosis process. For a realistic and medically relevant simulation of brain and breast tissues, the main characteristics of both organs and the particular diseases were studied. One of the main potentials of microwave imaging is in the early detection field, thus the considered lesions must be the typical ones for this stage. In breast cancer detection, the tumor should be confined into the breast volume and not bigger than 2 cm. Also, for a realistic representation, the tumor, it should be placed in contact or inside fibroglandular tissue. With respect to brain stroke, we will focus on detecting the bleeding stroke. According to the statistics, the commonest type of hemorrhage is the intracerebral, meaning that the bleeding will be inside of the gray or the white brain matter. Being able to detect a hemorrhage smaller than 12 mm in radius (if assumed spherical) the after-effects of the stroke are reduced.

3

MAGNITUDE COMBINED TOMOGRAPHY FORMULATION

As explained in the first chapter, the inverse scattering problem (or the imaging problem), has been historically addressed using two different methodologies. The first strategy is implemented by radar methods and consists of using focusing operators based on delay-and-sum algorithms (section 1.4.1.1), the second seeks to invert the integral equation that relates the total measured field with the current sources leading to the so-called inverse scattering or tomographic methods (section 1.4.1.2).

The algorithm developed in this thesis, namely Magnitude Combined Tomography, is based on previous work carried out in AntennaLab departament on tomographic imaging algorithms for 2D cylindrical geometries [92,93]. That algorithm implemented a computationally efficient diffraction tomographic method based on Born approximation.

More recent publications such as [43] demonstrated that 2D algorithms are not valid for imaging 3D geometries, except the case where the object can be assumed uniform in the third dimension. In relevant medical cases, such as breast cancer detection or brain stroke, 2D algorithms cannot be used anymore. Thus, in this thesis, the previous algorithm is extended to 3D performance.

Aimed to improve the image quality, multi-frequency information will be included. The well-known problem of residual phase errors associated to the Born approximation in highly contrasted or relatively large objects is addressed by using an only-magnitude multi-frequency combination, as will be shown in the following pages.

3.1 Inverse scattering based on Born approximation

Magnitude Combined Tomography is based on the inversion of the integral equation 2.28 using a modified Born approximation method. This technique leads to a spectral algorithm that fills the angular spectrum in a specific manner that will be explained below by the so-called Fourier diffraction theorem.

3.1.1 Fourier diffraction theorem

Using the definition of induced current, equation 2.20, the scattered field defined as equation 2.27 can be expressed as the convolution between this current and the Green's function:

$$\vec{E}^s(\vec{r}, f) = -j2\pi f\mu_0 \int_{v'} \vec{J}_{eq}(\vec{r}', f) \cdot G(\vec{r} - \vec{r}', f) d\vec{v}' \tag{3.1}$$

To deconvolute the currents, the inverse Fourier transform can be used. This operator allow to translate a magnitude from the spatial domain of the fields and currents to the spectral domain $\vec{K}$.

$$\vec{E}^s(\vec{r}, f) = -j2\pi f\mu_0 G(\vec{r}, f) * \vec{J}_{eq}(\vec{r}, f) \xrightarrow{\mathscr{F}} \tilde{E}^s(\vec{K}, f) = -j2\pi f\mu_0 \tilde{G}(\vec{K}, f)\tilde{J}_{eq}(\vec{K}, f) \tag{3.2}$$

Then the spectrum of the scattered field can be expressed as:

$$\tilde{E}^s(\vec{K}, f) = -j2\pi f\mu_0 \tilde{J}_{eq}(\vec{K}, f)\frac{1}{|\vec{K}|^2 - k_b^2} \tag{3.3}$$

The last term of equation 3.3 is the spectrum of the Green's function, $\tilde{G}(\vec{K}, f)$. Note that when $|\vec{K}| = k_b$ the Green's function has a singularity. As demonstrated in [38] only those waves on the region where the Green's function is singular will be propagated. Thus the spectrum of the scattered field will only contain the information of the spectrum of the currents when $|\vec{K}| = k_b$. In 2D, this region is a circumference of radius k_b, whereas in 3D is a sphere of the same radius.

Let us assume now that a plane wave directed to $\hat{r}_T$ illuminates a dielectric object.

$$\vec{E}^i(\vec{r}, f) = e^{-jk_b\hat{r}_T \cdot \vec{r}} \xrightarrow{\mathscr{F}} \tilde{E}^i(\vec{K}, f) = 4\pi^2 \delta(\vec{K} - k_b\hat{r}_T, f) \tag{3.4}$$

For weak scattering objects $\vec{E}(\vec{r}, f) \simeq \vec{E}^i(\vec{r}, f)$, that is Born approximation the induced current can be expressed as:

$$\vec{J}_{eq}(\vec{r}, f) \simeq -j2\pi f\epsilon_b(f)c(\vec{r}, f)\vec{E}^i(\vec{r}, f) \tag{3.5}$$

and its Fourier transform as[1]:

$$\tilde{J}_{eq}(\vec{K}, f) \simeq -\frac{j2\pi f\epsilon_b(f)}{4\pi^2}\tilde{C}(\vec{K}, f) * \tilde{E}^i(\vec{K}, f) = -j2\pi f\epsilon_b(f)\tilde{C}(\vec{K} - k_b\hat{r}_T, f) \tag{3.6}$$

Thus, the Fourier transform of the equivalent current and the object's dielectric contrast are defined through the equations:

$$\tilde{J}_{eq}(\vec{K}, f) = \mathscr{F}\left[\vec{J}_{eq}(\vec{r}, f)\right] = \iiint_{v'} \vec{J}_{eq}(\vec{r}, f)e^{j\vec{K}\vec{r}} d\vec{v}' \tag{3.7}$$

$$\tilde{C}(\vec{K} - k_b\hat{r}_T, f) = \mathscr{F}\left[c(\vec{r}, f)\right] = \iiint_{v'} c(\vec{r}, f)e^{j(\vec{K} - k_b\hat{r}_T, f)} d\vec{v}' \tag{3.8}$$

---

[1]The Fourier transform of $\vec{A}$ is denoted as $\tilde{A}$

From equations 3.3 and 3.6, it can be derived that a plane wave illumination directed to $\hat{r}_T$ gives information of the object's contrast spectrum only on the contour of a circumference (2D) or on the surface of a sphere (3D) of radius k_b and centered at $k_b\hat{r}_T$, see Figure 3.1.

Repeating the process for different illumination directions (multi-view), the center of the circumference or circle rotates on the surface of a circumference or sphere of k_b in radius. In this way the whole angular spectrum domain can be eventually covered. Nevertheless, it will be always a low-pass filtered version of the original with a cut-off frequency of $2k_b$. This is the reason for the resolution limit of approximately half a wavelength ($\lambda_b/2 = \frac{1}{2f\sqrt{\mu_0\epsilon_b}}$).

From equation 3.3 it can be also derived that by changing the frequency of illumination and consequently $k_{b,i}$, where i indicates the different frequencies, the radius of the circumferences or spheres changes. Thus, multi-frequency is a complementary way to multi-view to fill the angular spectrum. Multi-view tends to provide a better longitudinal resolution, whereas multi-frequency, improves the transverse resolution. Hence, the convenience of combining both strategies to reach a maximum longitudinal and transverse image resolution, see Figure 3.1.
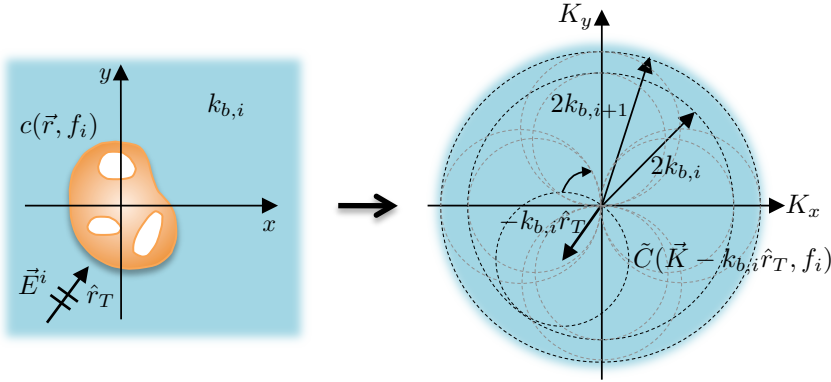

Figure 3.1: 2D spectrum of the dielectric contrast. For a plane wave illumination the spectrum of the dielectric contrast is sampled on a circumference of radius $k_{b,i}$ centered at $-k_{b,i}\hat{r}_T$. For different directions of incidence, $\hat{r}_T$, the sampling domain rotates and for different frequencies, f_i, the radius changes.

3.1.2 Generalization to arbitrary geometries using the reciprocity theorem

The previous section showed that a region of the spectrum of the currents, or equivalently a region of the spectrum of the object's dielectric contrast, could be obtained from the spectrum of fields. However this formulation is restricted to the case of having a plane wave illumination. In a realistic measurement scenario, it is not always possible to have enough space to produce a plane wave at the object vicinity. Thus non-bulky compact systems are normally used, where far field conditions are not accomplished. This section shows how the reciprocity theorem allows to calculate the object's dielectric contrast spectrum directly from a measurement of the near-field by an arbitrary acquisition surface.

Let as consider a typical measurement situation, such as depicted in Figure 3.2, where the
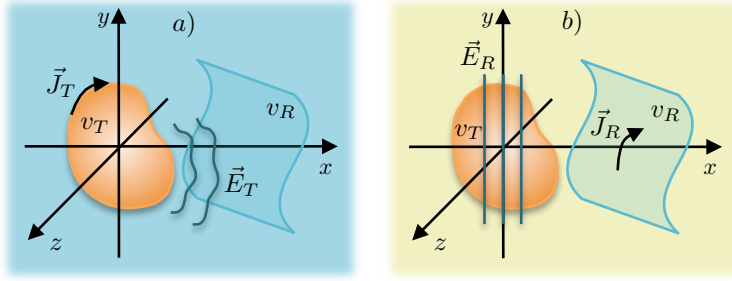
Figure 3.2: Reciprocity theorem. In a) the currents $\vec{J}_T$ produce a field $\vec{E}_T$ which is measured in v_R. In the reciprocal situation b), the former measurement region acts as a source when it is excited by the currents $\vec{J}_R$ that produce in a source-free region (v_T) a plane-wave field $\vec{E}_R$.

current, $\vec{J}_T$ produce the field $\vec{E}_T$ that is measured in v_R. The reciprocity theorem (equation 3.9) allows to eventually link the induced current on the object, $\vec{J}_T$, and the scattered field, $\vec{E}^s$, measured along an arbitrarily shaped antenna. To do so, in the reciprocal situation, the former measurement region, v_R, acts as a source when it is excited by the currents $\vec{J}_R$ that produce in a source-free region (v_T) a plane-wave field $\vec{E}_R$.

$$\int_{v'_R} \vec{J}_R \cdot \vec{E}_T \, d\vec{v}'_R = \int_{v'_T} \vec{J}_T \cdot \vec{E}_R \, d\vec{v}'_T \tag{3.9}$$

Where,

$$\vec{E}_R(\vec{r}, f; \hat{r}_R) = e^{-jk_b\hat{r}_R\vec{r}}\hat{r}_R \tag{3.10}$$

and $\vec{J}_T$ is the electric current on the object induced by a plane wave incident field propagating along the direction $\hat{r}_T$, $\vec{E}^i(\vec{r}, f; \hat{r}_T) = e^{-jk_b(f)\hat{r}_T\vec{r}}\hat{r}_T$. Under Born approximation and according to equation 3.5, $\vec{J}_T$ can be expressed as:

$$\vec{J}_T(\vec{r}, f; \hat{r}_T) \simeq -j2\pi f\epsilon_b(f)c(\vec{r}, f)\vec{E}^i(\vec{r}, f; \hat{r}_T)\hat{r}_T = -j2\pi f\epsilon_b(f)c(\vec{r}, f)e^{-jk_b\hat{r}_T\vec{r}}\hat{r}_T \tag{3.11}$$

Replacing equations 3.10 and 3.11 into 3.9:

$$\int_{v'_R} \vec{J}_R(\vec{r}, f; \hat{r}_R) \cdot \vec{E}_T(\vec{r}, f; \hat{r}_T) \, d\vec{v}'_R =$$

$$-\int_{v'_T} j2\pi f\epsilon_b(f)c(\vec{r}, f)e^{-jk_b(\hat{r}_R+\hat{r}_T)\vec{r}}(\hat{r}_R \cdot \hat{r}_T) \, d\vec{v}'_R \tag{3.12}$$

The second integral in equation 3.12 takes the form of the shifted Fourier transform of $c(\vec{r}, f)$, similarly to equation 3.6. Then, the spectrum of the object's dielectric contrast responds to:

$$\tilde{C}(-k_b(\hat{r}_R + \hat{r}_T), f) = -\frac{1}{j2\pi f\epsilon_b(f)} \int_{v'_R} \vec{J}_R(\vec{r}, f; \hat{r}_R) \cdot \vec{E}_T(\vec{r}, f; \hat{r}_T) \, d\vec{v}'_R \tag{3.13}$$

Let us suppose that all the currents are vertical and directed to the z-axis. Hence, the currents $\vec{J}_R$ can be expressed as:

$$\vec{J}_R(\vec{r}'_R, f; \hat{r}_R) = I_R(\vec{r}'_R, f; \hat{r}_R)\hat{z} = I_{z,R}(\vec{r}'_R, f; \hat{r}_R) \tag{3.14}$$

where $I_{z,R}(\vec{r}'_R, f; \hat{r}_R)$ is the complex amplitude of the current distribution at a position $\vec{r}'_R$ along the antenna surface, that, when acting as a transmitter, produces a plane wave that propagates in the direction $\hat{r}_R$.

When equation 3.14 is introduced in 3.12, due to the scalar product in 3.12, only the z-component of $\vec{E}_T$ remains, allowing the use of the scalar formulation without loss of generality, leading to:

$$\tilde{C}(-k_b(\hat{r}_R + \hat{r}_T), f) = -\frac{1}{j2\pi f \epsilon_b(f)} \int_{v'_R} I_{z,R}(\vec{r}'_R, f; \hat{r}_R) \cdot E_{z,T}(\vec{r}'_R, f; \hat{r}_R) \, dv'_R \qquad (3.15)$$

The field $\vec{E}_{z,T}(\vec{r}'_R, f; \hat{r}_R)$ produced by an incident plane wave towards $\hat{r}_T$, can be inferred in the same way. If the interaction between the incident field and the object is linear, it is possible to synthesize $\vec{E}_{z,T}$ by weighting the measured scattered field $E^s(\vec{r}'_T, f, \vec{r}'_R)$ by the current distribution coefficients that produce a plane wave towards $\hat{r}_T$

$$E_{z,T}(\vec{r}'_R, f; \hat{r}_R) = \int_{v'_T} I_{z,T}(\vec{r}'_T, f; \hat{r}_T) \cdot E^s(\vec{r}'_T, f, \vec{r}'_R) \, dv'_T \qquad (3.16)$$

Finally, introducing equation 3.16 in 3.15, the final expression for the spectrum of the object's dielectric contrast is obtained.

$$\tilde{C}(-k_b(\hat{r}_R + \hat{r}_T), f) = -\frac{1}{j2\pi f \epsilon_b(f)} \int_{v'_T} \int_{v'_R} E^s(\vec{r}'_T, f, \vec{r}'_R)$$
$$\cdot I_{z,R}(\vec{r}'_R, f; \hat{r}_R) I_{z,T}(\vec{r}'_T, f; \hat{r}_T) \, dv'_T dv'_R \quad (3.17)$$

3.1.3 Plane wave generation

The previous formulation is general for an arbitrary acquisition surface. However, in a realistic situation, the acquisition surface is not continuous, rather than this, it consists of an array of N probes arranged in a certain geometry. To obtain a proper scanning for imaging purposes, for a given transmitting position (n^{th}-array element), $\vec{r}'_{T_n}$, the scattered field is measured at the remaining points over the acquisition surface, $\vec{r}'_{R_m}$ ($n \neq m$). This procedure is successively repeated changing the transmitting position until the completion of $N(N-1)$ acquisitions.

Concerning the shape of the acquisition surface, what ultimately defines it is the expression of the I coefficients. In this case, I coefficients represent the amplitude of the current distribution to apply at each antenna on the array to produce a z-polarized plane wave that propagates inside the array in a direction $\hat{r}$. When the incident field is a cylindrical wave, an incident plane wave can be always synthesized as a superposition of cylindrical waves generated by the line sources $I_z(\vec{r}'_n, f; \hat{r})$ located at $\vec{r}'_n$ on the cylindrical antenna. These coefficients are the responsible to produce a plane wave as a weighted superposition of the waves emanating from the probes arranged in a certain geometry. Depending on the geometry, the coefficients will correspond to different expressions. If the geometry is canonical, such as circular, cylindrical or spherical, I can be always expressed in a close form. Otherwise, if the geometry is not canonical, the synthesis of plane wave illumination can not be, in general, solved analytically. In this last case, since the wave is not needed to be synthesized in the whole space, but inside
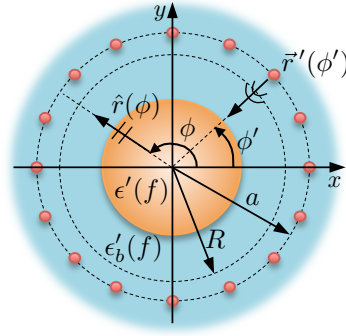
Figure 3.3: Plane wave synthesis in a circle of radius R centered in a circular array of radius a composed by N_ϕ angularly equispaced probes immersed in a background medium of relative permittivity $\epsilon_b'(f)$.

the antenna region, the so-called focusing operators can be used [94]. In this thesis, circular and cylindrical arrays will be used. Both are the commonest acquisition surfaces for 2D and 3D geometries respectively according to the literature [9, 42, 95, J3]. Moreover, they offer a good compromise between algorithm efficiency and ergonomics to the shape of the imaged objects, in this case the breast and the brain.

3.1.3.1 Plane wave generation for 2D circular geometries
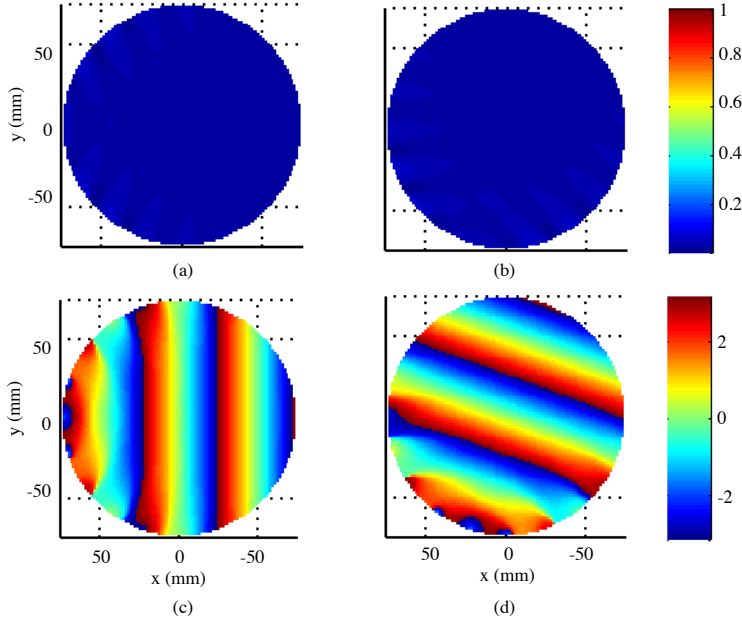
Figure 3.3 shows the geometry for the 2D plane wave synthesis problem. It consists of a circular array of N_ϕ both transmitting and receiving antennas of radius a inside a background medium of relative permittivity $\epsilon_b'(f)$. The ith-array element, placed at $\vec{r}_i' = a\cos\phi_i' \cdot \hat{x} + a\sin\phi_i' \cdot \hat{y}$ is excited with a current $I_z(\phi_i', f; \phi)$ that produces a plane wave directed to $\hat{r} = \cos\phi \cdot \hat{x} + \sin\phi \cdot \hat{y}$ inside the circular region of radius a.

For this scenario, the current coefficient to be applied to each probe, and in particular to the ith-array element, responds to the following expression:

$$I_z(\phi_i', f; \phi) = -\frac{1}{\pi^2 f \mu_0 a} \sum_{|n|>0}^{k_b a} \frac{j^{-n}}{H_n^{(2)}(k_b a)} e^{jn(\phi-\phi_i')} \tag{3.18}$$

The full derivation of the current coefficients can be found in Appendix B.

Figure 3.4 shows the result of the synthesized plane wave inside the circular array of antennas for two directions of incidence. For this purpose, the current distribution has been discretized and the field inside the array has been computed as the superposition of the radiated fields of a circular array of infinitesimal dipoles. The ring has a radius $a = 75$ mm and is composed by $N_\phi = 20$ probes. The frequency of illumination is 2 GHz and the relative permittivity of the background is $\epsilon_b' = 10$.

Figure 3.4: Amplitude and phase of the synthesized plane wave in a circular array for two different plane wave directions. (a) Plane wave amplitude for $\phi = 0°$, (b) plane wave amplitude for $\phi = 70°$, (c) plane wave phase for $\phi = 0°$, (d) plane wave phase for $\phi = 70°$.

3.1.3.2 Plane wave generation for 3D cylindrical geometries

Figure 3.5 shows the geometry for the plane wave synthesis problem with a cylindrical array of both transmitting and receiving antennas. The array is composed by N_z, $2a$-diameter rings of N_ϕ angularly equispaced antennas and it is immersed inside a background medium of relative permittivity $\epsilon'_b(f)$. From this arrangement, a plane wave directed to $\hat{r} = \sin\theta\cos\phi \cdot \hat{x} + \sin\theta\sin\phi \cdot \hat{y} + \cos\theta \cdot \hat{z}$ can be synthesized by exciting each array element, marked as ij, placed at $\vec{r}'_{ij} = a\cos\phi'_{ij} \cdot \hat{x} + a\sin\phi'_{ij} \cdot \hat{y} + z'_{ij} \cdot \hat{z}$, with the proper current amplitude weights expressed as:

$$I_z(z'_{ij}, \phi'_{ij}, f; \theta, \phi) = -\frac{1}{2\pi^2} e^{jk_{b,z}z'_{ij}} \sum_{|n|>0}^{k_{b,\rho}a} j^{n+1} e^{jn(\phi - \phi'_{ij})} \frac{1}{\sin\theta H_n^{(2)}(k_{b,\rho}a)} \frac{\delta(\rho'_{ij} - \rho)}{\rho'_{ij}} \hat{z} \quad (3.19)$$

being $k_{b,z} = k_b\cos\theta$ and $k_{b,\rho} = k_b\sin\theta$.

From equation 3.19, it can be observed that for the generation of vertically z-polarized plane waves, only vertical currents, I_z, are needed. This means that the acquisition array can be simply composed by z-oriented probes. This fact is in agreement with the previous decision on using only vertical currents for generating z-polarized plane waves.

Again, in the Appendix B, the full derivation of the current coefficients for both z and ϕ-polarized plane waves, can be found. Note that the coefficients are obtained for an ideal electric probe. That is the reason why dipole-like antennas, which are the antennas having the most
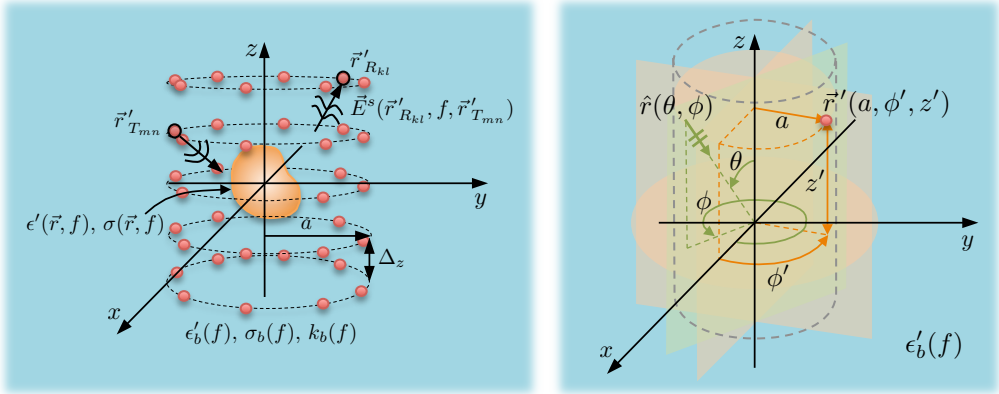
Figure 3.5: Plane wave synthesis in a cylindrical array composed by N_z $2a$-diameter rings of N_ϕ angular equidistant elements, both transmitters and receivers, separated a distance Δ_z in the vertical direction immersed in a background medium of relative permittivity $\epsilon'_b(f)$.

similar performance to that of a ideal probe, are used in the experimental system as array elements.

Figure 3.6 shows the result of the synthesized plane wave inside the cylindrical array of antennas for two directions of incidence. The cylindrical array has a radius $a = 75$ mm and a length $l_z = 240$ mm. The number of antennas along ϕ is $N_\phi = 20$ and along z is $N_z = 25$. The frequency of illumination is 2 GHz and the relative permittivity of the background is $\epsilon'_b = 10$.

3.1.4 Algorithm implementation

Using the expressions obtained in the previous section, equation 3.17 is particularized for circular and cylindrical arrays. As said, the shape of the acquisition surface plays an important role from the implementation point of view. Accordingly, for canonical acquisition geometries, such as circular or cylindrical, the spectral formulation reduces to exponential base functions allowing the implementation via fast Fourier transform (FFT), which is much more efficient.

3.1.4.1 2D circular algorithm's implementation

For a circular acquisition surface acting both as a transmitter (T) and a receiver (R), equation 3.17 can be expressed as:

$$\tilde{C}(-k_b(\phi_T + \phi_R), f) = -\frac{(2\pi)^2 a^2}{j2\pi f \epsilon_b(f)} \int_0^{2\pi} \int_0^{2\pi} E^s(\phi'_T, f, \phi'_R)$$
$$\cdot I_{z,R}(\phi'_R, f; \phi_R) I_{z,T}(\phi'_T, f; \phi_T) \, d\phi'_T \, d\phi'_R \quad (3.20)$$
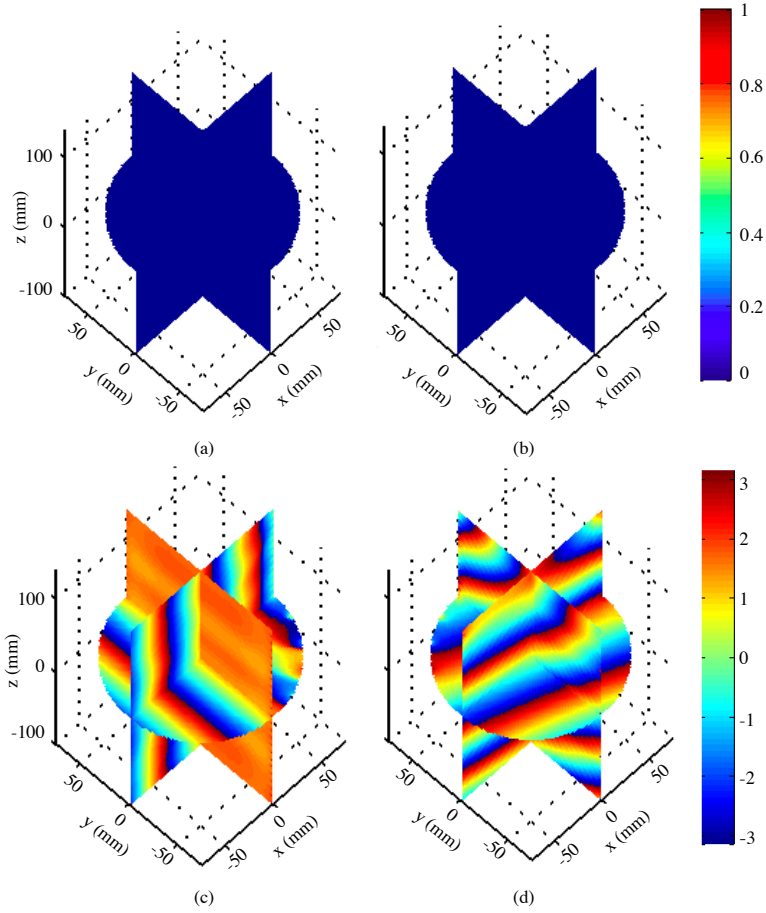
Figure 3.6: Amplitude and phase of the synthesized plane wave in a cylindrical array for two different plane wave directions. (a) Plane wave amplitude for $\theta = 90°$, $\phi = 0°$, (b) plane wave amplitude for $\theta = 45°$, $\phi = 70°$, (c) plane wave phase for $\theta = 90°$, $\phi = 0°$, (d) plane wave phase for $\theta = 45°$, $\phi = 70°$.

If instead of a circular antenna, a circular array of N_ϕ z-oriented dipole-like antennas, such as depicted in Figure 3.3, is considered and introducing equation 3.18:

$$\tilde{C}(-k_b(\phi_T + \phi_R), f) = \frac{16j}{2\pi f k_b^2 \mu_0} \sum_{i=0}^{2\pi} \sum_{j=0}^{2\pi} E^s(\phi'_{T_j}, f, \phi'_{R_i}) e^{-jn\phi'_{T_j}} e^{-jm\phi'_{R_i}}$$

$$\cdot \sum_{|m|>0}^{k_b a} \sum_{|n|>0}^{k_b a} \frac{j^{-(m+n)}}{H_m^{(2)}(k_b a) H_n^{(2)}(k_b a)} e^{jn\phi_T} e^{jm\phi_R} \quad (3.21)$$

Equation 3.21 can be efficiently implemented with an FFT algorithm. The first pair of summations can be interpreted as the Fourier transform of the scattered field, $\hat{E}^s(m, n)$. Then, the

spectrum of the dielectric contrast can be calculated as the inverse Fourier transform of the remaining terms:

$$\tilde{C}(-k_b(\phi_T + \phi_R), f) = IFFT\left[\frac{16j}{2\pi f k_b^2 \mu_0} \frac{j^{-(m+n)}\tilde{E}^s(m, n)}{H_m^{(2)}(k_b a)H_n^{(2)}(k_b a)}\right] \tag{3.22}$$

To obtain the dielectric contrast profile of the object, $c(\vec{r}, f)$, it just remains to calculate the inverse Fourier transform of $\tilde{C}$ and remap it into a rectangular reconstruction grid. The algorithm has been implemented using Matlab®. Figure 3.7 shows the algorithm's flow diagram.

3.1.4.2 3D cylindrical algorithm's implementation

Similarly to the 2D circular case, equation 3.17 is now particularized for a 3D cylindrical acquisition surface:

$$\tilde{C}(-k_b(\phi_T + \phi_R), f) = -\frac{(2\pi)^2 a^2}{j2\pi f \epsilon_b(f)} \iint_0^{2\pi} \iint_{-\infty}^{\infty} E^s(z_T', \phi_T', f, z_R', \phi_R')$$
$$\cdot I_{z,R}(z_R', \phi_R', f; \phi_R) \cdot I_{z,T}(z_T', \phi_T', f; \phi_T)\, \phi_T'\, d\phi_R'\, dz_T'\, dz_R' \tag{3.23}$$

Let us suppose that the cylindrical surface is composed by N_z $2a$-diameter rings of N_ϕ angular equidistant elements, both transmitters and receivers, separated a distance Δ_z in the vertical direction, as shows Figure 3.5. The array elements are dipole-like antennas producing a current directed to the z-axis. Note that the position of the antennas in the cylindrical coordinate system depends on the azimuthal angle ϕ' and the coordinate z'. Considering the previous and introducing equation 3.19 to 3.24:

$$\tilde{C}(-k_b(\phi_T+\phi_R), f) = -\frac{(2\pi)^2 a^2}{j2\pi f \epsilon_b(f)}\left(\frac{1}{2\pi^2}\right)^2 \sum_{i=0}^{2\pi}\sum_{j=0}^{2\pi}\sum_{k=-\infty}^{\infty}\sum_{l=-\infty}^{\infty} E^s(z_{T_{ij}}', \phi_{T_{ij}}', f, z_{R_{kl}}', \phi_{R_{kl}}')$$

$$e^{jk_{b,z_T}z_{T_{ij}}'} e^{jk_{b,z_R}z_{R_{kl}}'} \cdot \sum_{|m|>0}^{k_{b,\rho_T}a}\sum_{|n|>0}^{k_{b,\rho_R}a} \frac{j^{m+1}j^{n+1}e^{jm(\phi_T-\phi_{T_{ij}}')}e^{jn(\phi_R-\phi_{R_{kl}}')}}{\sin\theta_T \sin\theta_R H_m^{(2)}(k_{b,\rho_T}a)H_n^{(2)}(k_{b,\rho_R}a)} \tag{3.24}$$
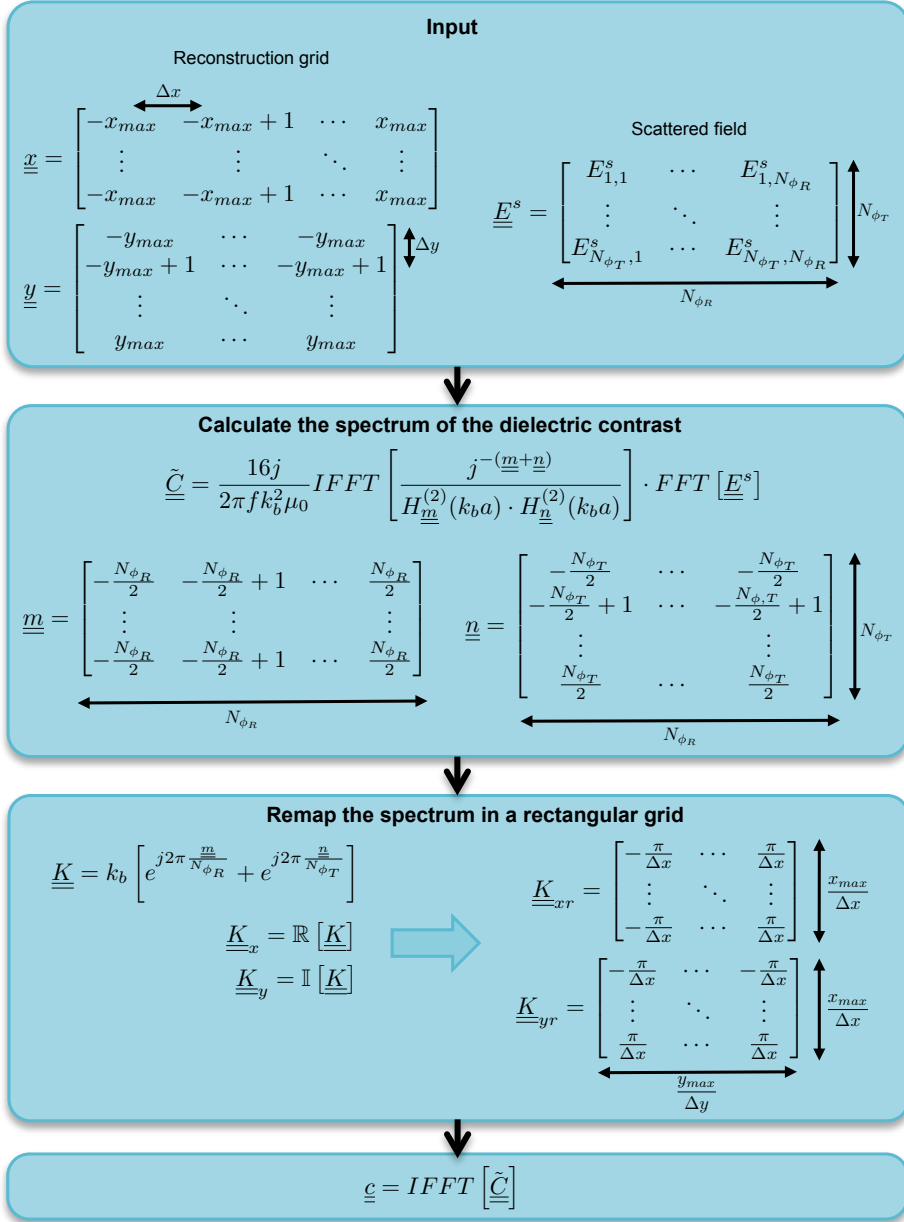
In terms of implementation with Matlab®, in this case, the algorithm implements the formula 3.24 as shows the flow diagram in Figure 3.8.

3.2 Practical considerations

To go from the merely theoretical algorithm formulation to the implementation of the experimental system, a number of practical considerations have to be taken into account.

3.2.1 Operating frequency choice and its implications on resolution, penetration and sampling in spatial domain

The choice of the operating frequency is a challenging issue which determines the quality of the reconstruction in terms of resolution and attenuation. The resolution is in the order of half a

Input

Reconstruction grid

$$\underline{\underline{x}} = \begin{bmatrix} -x_{max} & -x_{max}+1 & \cdots & x_{max} \\ \vdots & \vdots & \ddots & \vdots \\ -x_{max} & -x_{max}+1 & \cdots & x_{max} \end{bmatrix}$$

$$\underline{\underline{y}} = \begin{bmatrix} -y_{max} & \cdots & -y_{max} \\ -y_{max}+1 & \cdots & -y_{max}+1 \\ \vdots & \ddots & \vdots \\ y_{max} & \cdots & y_{max} \end{bmatrix} \updownarrow \Delta y$$

Scattered field

$$\underline{\underline{E}}^s = \begin{bmatrix} E^s_{1,1} & \cdots & E^s_{1,N_{\phi_R}} \\ \vdots & \ddots & \vdots \\ E^s_{N_{\phi_T},1} & \cdots & E^s_{N_{\phi_T},N_{\phi_R}} \end{bmatrix} \updownarrow N_{\phi_T}$$

$$\underleftrightarrow{N_{\phi_R}}$$

Calculate the spectrum of the dielectric contrast

$$\underline{\underline{\tilde{C}}} = \frac{16j}{2\pi f k_b^2 \mu_0} IFFT \left[\frac{j^{-(\underline{\underline{m}}+\underline{\underline{n}})}}{H^{(2)}_{\underline{\underline{m}}}(k_b a) \cdot H^{(2)}_{\underline{\underline{n}}}(k_b a)} \right] \cdot FFT \left[\underline{\underline{E}}^s \right]$$

$$\underline{\underline{m}} = \begin{bmatrix} -\frac{N_{\phi_R}}{2} & -\frac{N_{\phi_R}}{2}+1 & \cdots & \frac{N_{\phi_R}}{2} \\ \vdots & \vdots & & \vdots \\ -\frac{N_{\phi_R}}{2} & -\frac{N_{\phi_R}}{2}+1 & \cdots & \frac{N_{\phi_R}}{2} \end{bmatrix}$$

$$\underleftrightarrow{N_{\phi_R}}$$

$$\underline{\underline{n}} = \begin{bmatrix} -\frac{N_{\phi_T}}{2} & \cdots & -\frac{N_{\phi_T}}{2} \\ -\frac{N_{\phi_T}}{2}+1 & \cdots & -\frac{N_{\phi,T}}{2}+1 \\ \vdots & & \vdots \\ \frac{N_{\phi_T}}{2} & \cdots & \frac{N_{\phi_T}}{2} \end{bmatrix} \updownarrow N_{\phi_T}$$

$$\underleftrightarrow{N_{\phi_R}}$$

Remap the spectrum in a rectangular grid

$$\underline{\underline{K}} = k_b \left[e^{j2\pi \frac{\underline{\underline{m}}}{N_{\phi_R}}} + e^{j2\pi \frac{\underline{\underline{n}}}{N_{\phi_T}}} \right]$$

$$\underline{\underline{K}}_x = \mathbb{R}\left[\underline{\underline{K}} \right]$$

$$\underline{\underline{K}}_y = \mathbb{I}\left[\underline{\underline{K}} \right]$$

$$\underline{\underline{K}}_{xr} = \begin{bmatrix} -\frac{\pi}{\Delta x} & \cdots & \frac{\pi}{\Delta x} \\ \vdots & \ddots & \vdots \\ -\frac{\pi}{\Delta x} & \cdots & \frac{\pi}{\Delta x} \end{bmatrix} \updownarrow \frac{x_{max}}{\Delta x}$$

$$\underline{\underline{K}}_{yr} = \begin{bmatrix} -\frac{\pi}{\Delta x} & \cdots & -\frac{\pi}{\Delta x} \\ \vdots & \ddots & \vdots \\ \frac{\pi}{\Delta x} & \cdots & \frac{\pi}{\Delta x} \end{bmatrix} \updownarrow \frac{x_{max}}{\Delta x}$$

$$\underleftrightarrow{\frac{y_{max}}{\Delta y}}$$

$$\underline{\underline{c}} = IFFT \left[\underline{\underline{\tilde{C}}} \right]$$

Figure 3.7: Flow diagram of the reconstruction algorithm for 2D circular acquisition geometries. All the arithmetic operations of this diagram are element-by-element.

wavelength and the attenuation has an impact on the penetrability in the imaged tissue. For this reason, the operating frequency choice is a compromise between resolution and attenuation, that also influences the number of antennas and the array's characteristics.
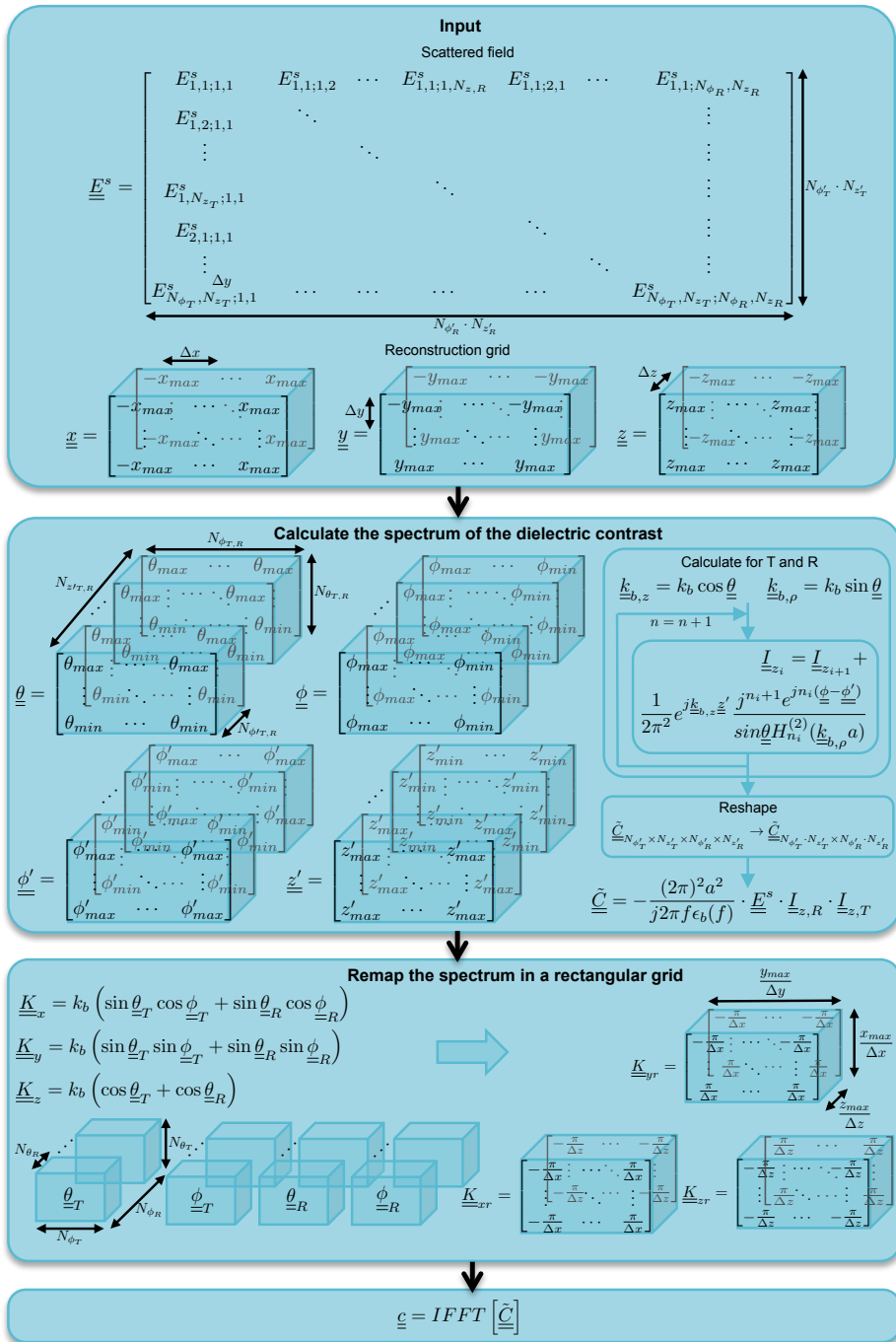
Figure 3.8: Flow diagram of the reconstruction algorithm for 3D cylindrical acquisition geometries. All the arithmetic operations of this diagram are element-by-element.

Circular		**Linear**	
$N_\phi \geq \frac{2\pi a}{\lambda_b/2} = 2\frac{2\pi f_{max}\sqrt{\epsilon_b'}}{c_0}a$		$N_z \geq \frac{l_z}{\lambda_b/2} = 2\frac{l_z f_{max}\sqrt{\epsilon_b'}}{c_0}$	

Table 3.1: Sampling criteria for spatial domain. f_max refers to the maximum frequency of illumination, a is the radius of the circular array and l_z the length of the linear array.

In medical diagnostics, the goal for microwave imaging systems is a sub-centimeter resolution in order to detect early stage lesions. For low-loss small bodies [3] the use of frequencies between 2 and 8 GHz is suggested. However for medium or big size average water content biological tissues, the range between 2 and 4 GHz seems to offer a better compromise with sufficient resolution [96], as shows Figure 3.9.
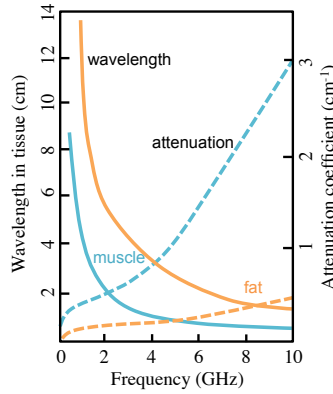
Figure 3.9: Trade-off between resolution and attenuation depending on the operating frequency [3].

By defining the maximum frequency of the illuminating field, the minimum number of antennas is also set. Accordingly, from the electromagnetic modal expansion of the fields scattered by an object when it is illuminated by an incident field, a minimum number of views has to be defined to avoid loss of information. The maximum separation between array elements is determined by the well-known Nyquist spatial sampling criteria to $\lambda_b/2 = \frac{c_0}{f\sqrt{\epsilon_b'}}$. Table 3.1 shows the minimum number of views for a circular geometry of radius a (N_ϕ) and for a linear array of length l_z (N_z). Moreover, it can be observed that for a circular array, the minimum number of views is also equal to the number of coefficients of the cylindrical mode expansion of the scattered field, that is $k_b a$, [64, 97]. From this point, for a given antenna radius and length, the number of antennas is calculated according to Table 3.1 if not stated otherwise.

3.2.2 3D cylindrical algorithm's non-idealities

3.2.2.1 Linearly polarized antennas

The impact of using only the vertical (z-oriented) currents in the reconstruction procedure, is scarcely noticeable when reconstructing objects of size comparable to the wavelength in the background medium. However, this effect can be observed when reconstructing very thin objects having horizontal orientation, that is, objects oriented in a perpendicular plane to z-axis. In this case a loss of intensity in the reconstructed image can be observed. Figure 3.10 shows the 3D cylindrical reconstruction of the contrast magnitude of a a 90 mm-long cylinder immersed in a medium of $\epsilon'_b = 34$ which is rotated $0°$, $45°$ and $90°$ around $\hat{y}$ axis at 2 GHz. The cylindrical array of $l_z = 250$ mm in length and $a = 75$ mm in radius is composed by 12 rings of 32 antennas. The input data for the reconstruction (the scattered field) has been obtained using the CST simulation software. The first row corresponds to a cylinder of 10 mm in diameter and the second one to cylinder of 1 mm in diameter. For the thinner one, a loss of intensity combined with a shortening of the cylinder can be observed as it rotates. However, when the thickness increases, this effect is practically negligible.
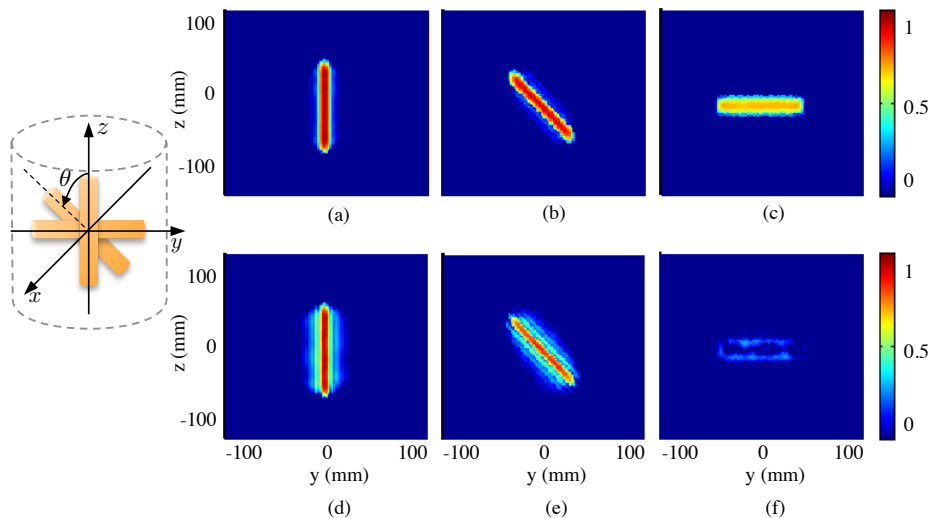
Figure 3.10: YZ plane of the reconstruction of the normalized dielectric contrast magnitude using 3D MC tomography. The imaged object is a cylinder of permittivity $\epsilon'_c = 50$ of 2 different diameters immersed in a medium of $\epsilon'_b = 34$ at 2 GHz. The cylinder is rotated an angle θ around x axis. (a) Diameter=10 mm, $\theta = 0°$, (b) diameter=10 mm, $\theta = 45°$, (c) diameter=10 mm, $\theta = 90°$, (d) diameter=1 mm, $\theta = 0°$, (e) diameter=1 mm, $\theta = 45°$, (f) diameter=1 mm, $\theta = 90°$.

3.2.2.2 Finite cylinder length

In the case of cylindrical acquisition geometries, due to the limited extent of the cylindrical measurement surface in the $\hat{z}$-direction, there is a certain truncation error, which is translated to a deterioration of the synthesized plane wave expressed by equation 3.19. In order to quan-

tify the synthesized plane wave error in terms of electric field, it is convenient to define the following error function [98].

$$T(\vec{r}) = \frac{|\vec{E} - \vec{E}_{pw}|^2}{|\vec{E}_{pw}|^2} \tag{3.25}$$

where $\vec{E}$ refers to the electric field of the synthesized plane wave and $\vec{E}_{pw}$ is the theoretical plane wave electric field expressed as $\vec{E}_{pw}(x, y, z) = e^{-jk_b(\sin\theta\cos\phi\cdot x + \sin\theta\sin\phi\cdot y + \cos\theta\cdot z)}$. Figure 3.11 shows the plane wave error function for vertical polarization and different θ angles. The cylindrical array has a radius $a = 75$ mm and a length $l_z = 240$ mm. The number of antennas along ϕ is $N_\phi = 20$ and along z is $N_z = 25$. The frequency of illumination is 2 GHz and the relative permittivity of the background is $\epsilon_b' = 10$. It can be observed that the closer θ is to $0°$, or equivalently to $180°$, the less accurate the plane wave is. Degraded plane waves may produce artifacts in the reconstruction. In order to prevent it happening, in the algorithm, the polar direction of the synthesized plane wave, θ, should be limited. As a criteria of limitation, the validity angle is considered, see Figure 3.12.

$$\tan\theta_v = \frac{l_z - l_{zo}}{2(a - a_o)} \tag{3.26}$$

This limitation will produce an extra smoothing of the reconstruction. Otherwise, the inclusion of degraded plane waves will produce artifacts in the image that may lead to positive false detections.
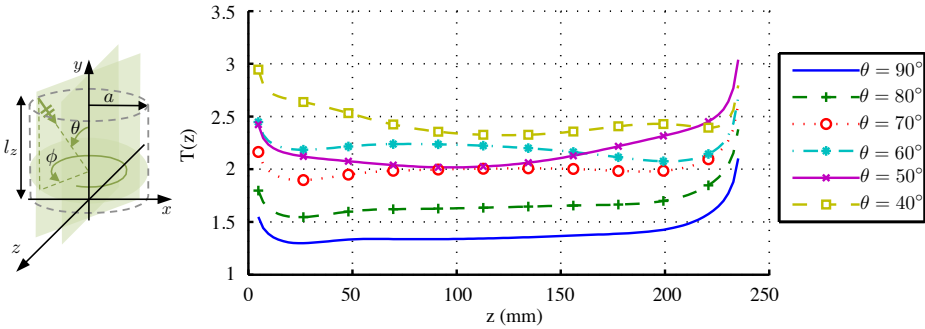
Figure 3.11: Plane wave error function for vertical polarization and different θ angles ($\phi = 0°$).
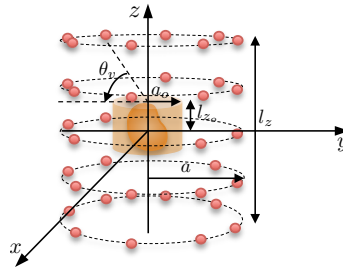
Figure 3.12: Plane wave validity angle.

51

3.2.3 Born approximation

As shown in section 2.3.1.2, the reconstruction algorithm here presented, relays on Born approximation linearize the wave equation and be able to invert this relation between the object and the scattered field. The necessary approximation for this purpose limit the range of objects that can be quantitatively imaged to those that do not severely change the incident field. For instance, an object having a substantially different permittivity with respect to the background, but being electrically small, produces an internal field with small changes in the magnitude but preserving a pretty similar phase to that of the incident field. In this case, the Born approximation might be valid. Instead, objects of several wavelengths in size, might produce phase changes of 180° or more, that will violate the approximation. In this section, the effects of these approximation for changes in the dielectric contrast, object size and frequency is shown by means of computer simulations.

The first-order Born approximation is valid only when the magnitude of the scattered field is smaller than that of the incident field. If the object is a cylinder of constant permittivity, it is possible to express this condition as a function of the object size (radius a) and relative permittivity ϵ'_c. Assuming a plane wave incident field propagating in the direction $k_b \cdot \hat{r}$ that encounters a relatively large object, the field inside the object will not be given by $\vec{E}_c(\vec{r}, f) \neq Ae^{jk_b \cdot \hat{r}}$, but instead will be a function of the change in refractive index, which is related to the change in permittivity as $\Delta n = \sqrt{\Delta \epsilon'}$. Along a ray through the center of the cylinder and parallel to the direction of propagation of the incident plane wave, the field inside the object becomes a slow (or fast) version of the incident wave of the form $\vec{E}_c(\vec{r}, f) = Ae^{j(\sqrt{1+\Delta\epsilon})k_b \cdot \hat{r}}$. Since the wave is propagating through the object, the phase difference between the incident field and the field inside the object is approximately equal to the integral of the change in refractive index through the object. Therefore, the total phase shift produced by a cylinder is approximately

$$\Delta\varphi = 4\pi\Delta n \frac{a}{\lambda_b} = \frac{4\pi f a \sqrt{\epsilon'_c}}{c_0} \tag{3.27}$$

where λ_b is the wavelength of the incident wave. This relationship is clearly shown in Figure 3.13, where a canonical scenario consisting of an infinitely large dielectric cylinder of radius a and relative permittivity ϵ'_c placed in a circular array of antennas immersed in air, is reconstructed using the 2D circular algorithm. Figure 3.13(a) shows the reconstructed phase evolution with respect to frequency for the central point of the reconstructed dielectric contrast when the permittity of the cylinder changes and Figure 3.13(b) when the cylinder radius changes.

A quantitative study of the error in the reconstruction based on Born approximation can be performed based on the work presented in [38]. As a measure of error, a relative mean square error of the object contrast function integrated over the entire plane is used. If the actual object contrast function is $c(\vec{r}, f)$ and the reconstructed object contrast function is $c'(\vec{r}, f)$, then the mean squared error (MSE) is

$$MSE = \frac{\iint \left[c(\vec{r}, f) - c'(\vec{r}, f)\right]^2 d\vec{r}}{\iint \left[c(\vec{r}, f)\right]^2 d\vec{r}} \tag{3.28}$$

To evaluate the error, two sets of simulations of a single infinitely large uniform cylinder were performed using MEEP simulation software. The cylinder was centered in a circular array of 64 antennas of radius 80 mm immersed in air at 10 GHz. For each simulation, the scattered field
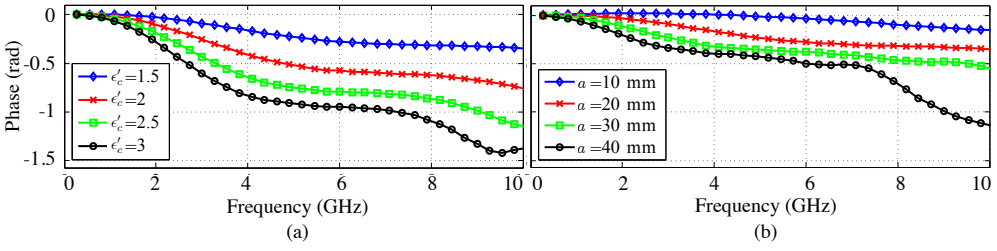
Figure 3.13: Evolution of the phase of the reconstruction of a centered cylinder with respect to the frequency. (a) Cylinder of $a = 20$ mm and $\epsilon'_c = 1.5, 2, 2.5$ and 3 and (b) cylinder of $a = 10, 20, 30$ and 40 mm and $\epsilon'_c = 1.5$.

was calculated for a particular radius and permittivity and it was reconstructed using the 2D circular algorithm. Figure 3.14(a) shows the MSE for cylinders of radius (r_c) 1, 2 and 3 λ_b and 50 different refractive indexes ($n_c = \sqrt{\epsilon'_c}$) ranging from 1.01 to 1.25. The exact contrast value was computed according to 2.21. Figure 3.14(b) shows the MSE for cylinders of refractive index 1.01, 1.25 and 1.5 and 50 radii between 1 and $10\lambda_b$. By comparing both figures, it can be seen that Born approximation performs better for relatively contrasted objects, rather than for electrically large objects. For objects of few wavelengths in radius, the error in the Born reconstruction increases gradually when the contrast increases. Instead, for low-contrasted objects, the error is relatively constant until a threshold is reached and then increases more rapidly. In Figure 3.14(a) for the cylinders or radius $2\lambda_b$ and $3\lambda_b$, this breakpoint occurs approximately at a phase shift arround 0.7π, according to equation 3.27. Thus a criteria for the validity of the Born approximation is that the product of the radius of the cylinder in wavelenghts and the change in refractive index must be less than 0.175 [38].

Since the body organs and tissues have a size of the order of a few wavelengths, when Born approximation is useful in medical imaging, the error committed is such that, in general, an absolute quantitative retrieval of the dielectric properties is not possible, but the geometry is well preserved, as it will be shown in next chapters.

3.2.4   Execution time

One of the strengths of this algorithm is to provide a numerically efficient implementation in terms of Fast Fourier Transform. This allows a real time performance if the number of antennas is not excessive, such as the case of the 2D circular acquisition geometry. For the 3D cylindrical case, the management of a larger amount of data requires a longer execution time of about 30 seconds for each frequency of illumination. Further speed improvements can be achieved by optimizing the code.

3.3   Multi-frequency extension

In the previous section, it has been shown that the effects of Born approximation are funda-mental to the reconstruction process and limit the range of objects that can be quantitatively
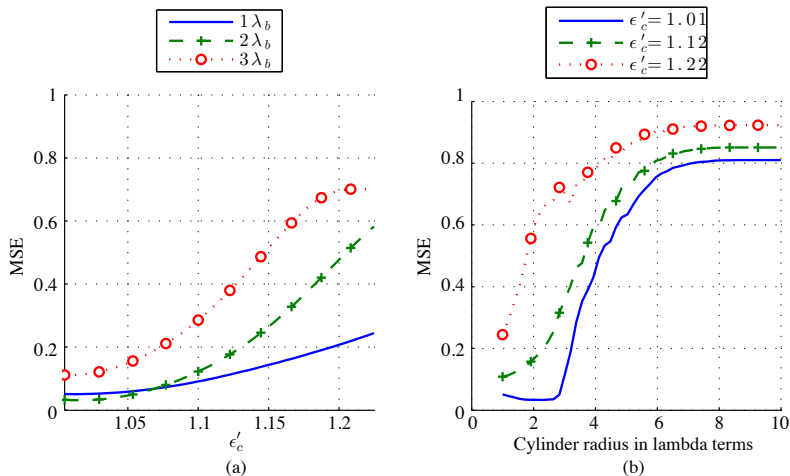
Figure 3.14: MSE of the Born based reconstruction of a cylinder of different radius and relative permittivity immersed in air. (a) MSE as a function of the refractive index for cylinders of radius 1, 2 and 3 λ_b, (b) MSE as a function of radius for cylinders of refractive index 1.01, 1.12 and 1.22.

reconstructed. Conversely, the experimental limitations are caused because it is only possible to collect a finite amount of data. Up to the limit in resolution caused by evanescent waves, it is possible to improve a reconstruction by collecting more data. This is the underpinning argument for collecting multi-frequency information in microwave imaging methods. Multi-frequency is increasingly used in microwave imaging pursuing an improvement of the algorithm performance with respect to the mono-frequency case [96]. As shown in Figure 3.14, Born approximation produces a residual phase error in the reconstruction that increases with the electrical size and contrast of the object, while the magnitude information remains correct [99]. Thus, the multi-frequency extension has to be carefully chosen in order to enhance the features of interest without having destructive interference between them. The most straight-forward attempt is to perform a coherent[2] combination of the images at different frequencies. In this case and before combining the different frequency image pixels, a flat, or almost flat, phase slope must be ensured, or equivalently that the maximum phase error inside the object is bounded to a certain value. According to the evolution of the phase represented in Figure 3.13, the coherent frequency combination can only be applied when the scenario consist of a low-contrasted or electrically-small object, which generally, is not the case of medical imaging. To be applicable, some extra information is needed in order to compensate such a phase slope. Here, the so-called Magnitude Combined (MC) strategy is proposed, that consists on the summation of only the magnitude of each individual frequency image pixel.

$$c_{MC}(\vec{r}) = \sum_{f_i=f_{min}}^{f_{max}} |c(\vec{r}, f_i)| \tag{3.29}$$

This is essentially the same process occurring in an optical camera were the intensity of each pixel is added over all frequencies. In the spectral domain, when combining multiple frequencies (represented by spectral spheres of different radius) with multiple views (represented by

---

[2]Coherent combination consists of the summation of both magnitude and phase.

rotating spectral spheres), a wider and denser mesh of points is obtained, as represented in Figure 3.1, reverting in a much more robust reconstructed image.

In order to ensure an optimal use of multi-frequency information, the frequency step Δf between the images at different frequencies should be lower than $\Delta f < \frac{c_0}{4a\sqrt{\epsilon'_b}}$. Notice that whereas the frequency step is only dependent on the object size, the angular sampling (Table 3.1) decreases when frequency increases.

Following with the single cylinder reconstruction, the convenience of the multi-frequency extension can be clearly seen. Figure 3.15 shows the reconstruction of a cylinder of 15 mm in radius and relative permittivity ϵ'_c immersed in a background of relative permittivity ϵ'_b=10. The circular antenna array of radius 75 mm is composed by 128 antennas and the reconstruction is performed between 3-10 GHz using 3 different frequency combination methods: mono-frequency, coherent multi-frequency combination and MC multi-frequency. As explained before, since the absolute quantitative performance is lost in the multi-frequency combination, the reconstructed dielectric contrast represented in the figures is normalized to the same maximum value and plotted between 0 and 1 in linear scale. Under low contrast scenarios, see Figure 3.15(a), frequency and spatial scannings are partially equivalent and hence a single frequency and dense angular sampling may be equivalent to a dense frequency sampling combined with a reduced number of views. For this reason, the multi-frequency extension of the algorithm, Figures 3.15(c) and 3.15(d), do not provide any advantage with respect to the mono-frequency approach, Figure 3.15(b). Under high contrast conditions as shown in Figure 3.15(e) the advantages of the multi-frequency extension comes to light. While mono-frequency, Figure 3.15(f), and coherent multi-frequency combination, Figure 3.15(g), approaches fail in obtaining an accurate reconstruction, MC, Figure 3.15(h) recovers the size, position and shape of the cylinder and its internal uniformity. In particular, higher frequencies give information about contours and small details and lower frequencies contribute to the reconstruction of smoother parts. Notice also, that the mono-frequency reconstruction is clearly affected by a Moiré pattern that disappears in the MC image. The reason of this effect, can be explained by the strong frequency dependence of the interaction between the illuminating fields and the object, which become apparent in Figure 3.15(b). Instead, when a continuous frequency spectrum is employed for the exploration, a reduction of the resonant character of the reconstruction is observed.

3.4   Concluding remarks

This chapter has formulated the imaging algorithm for 2D circular and 3D cylindrical acquisition geometries. The algorithm takes advantage of the quasi-real time, robust and straightforward implementation of the well-known Born-based reconstruction methods [93]. To these methods, two main modifications were needed to deal with medical imaging. From one hand, the extension to 3D was necessary to screen objects that cannot be assumed uniform in the third dimension. Accordingly, the results of the previous Born-based methods were restricted to cross-sectional images of body parts such as arms or legs. Nonetheless, for other more medically relevant cases, such as breast tumor detection or brain stroke, the capacity to discriminate in the third dimension is crucial and 2D methods are not valid any more. From the other hand, a method for combining multi-frequency data has been added, pursuing an improvement of the algorithm performance with respect to the mono-frequency case in terms of resolution and robustness to frequency-selective artifacts. The well-known problem of residual phase errors as-
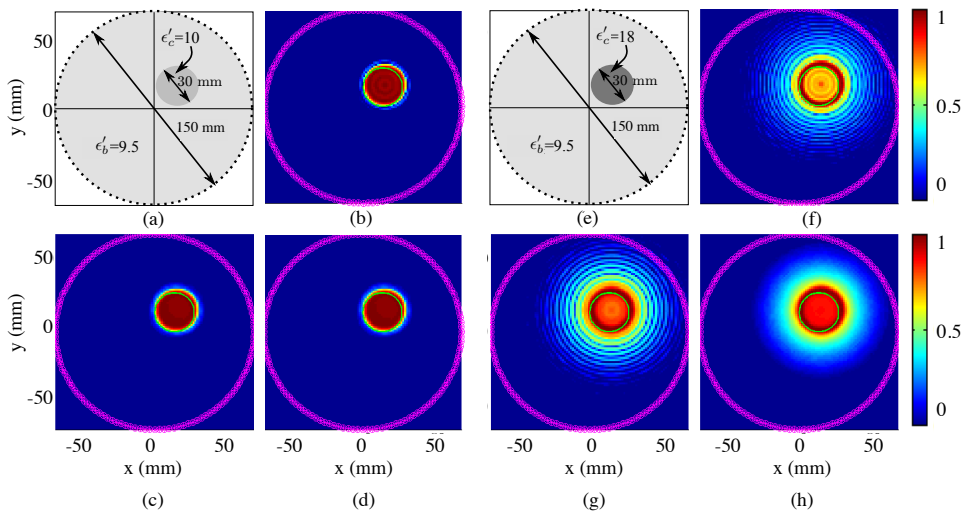
Figure 3.15: Reconstruction of a cylinder of 15 mm in radius and relative permittivity ϵ'_c immersed in a background of relative permittivity ϵ'_b=10. The circular antenna array of radius 75 mm is composed by 128 antennas. The reconstruction is performed between 3-10 GHz using 3 different frequency combination methods. (a) Low-contrasted scenario geometry, (b) low-contrasted mono-frequency reconstruction, (c) low-contrasted coherent multi-frequency reconstruction, (d) low-contrasted MC multi-frequency reconstruction, (e) highly-contrasted scenario geometry, (f) highly-contrasted mono-frequency reconstruction, (g) highly-contrasted coherent multi-frequency reconstruction, (h) highly-contrasted MC multi-frequency reconstruction. In these images, the position of the antennas is indicated by means of asterisks and the contour of the object under investigation with a green trace.

sociated to the Born approximation in highly contrasted or relatively large objects is addressed by using an only-magnitude multi-frequency combination.

Before proceeding with the algorithm validation, several practical considerations have to be taken into account.

- The trade-off between resolution and penetration depending on the operation frequency leads to an optimal frequency range between 2 and 4 GHz for medical imaging purposes. The operating frequency also impacts on the minimum number of views (or antennas) in the acquisition array. The existence of redundancy in the spectral domain, specially when multi-frequency information is used, relaxes the sampling requirement in the angular domain slightly, allowing to reduce the number of antennas. Accordingly, if the number of antennas is kept bounded to a reasonable amount, the advantage in terms of simplicity and speed of MC algorithm is clear compared to iterative methods.

- The 3D cylindrical reconstruction algorithm formulation considers only vertical currents on an infinitely large cylinder. The effects of both non-idealities have been shown with canonical simulations, reporting a negligible effect of using only vertical currents when the object has a certain radius. The cylinder truncation produces a degradation of the synthesized plane waves. The effect of this on the reconstruction, can be mitigated by restricting the plane wave angles between 45° and 135°.

- Born approximation limits the range of objects that can be quantitatively imaged to those having a product between radius in wavelengths and refractive index smaller than 0.175. Otherwise the reconstruction of the contrast is qualitative keeping the same progressiveness as the original contrast profile.

The initial strengths provided by the basis Born-based algorithm have been preserved. The proposed MC tomographic algorithm is still simple and for a typical 3D cylindrical antenna arrangement for breast inspection has a total run time of 30 seconds per frequency. The subsequent chapters will address the reconstruction of realistic phantoms to demonstrate its robustness.

4
NUMERICAL RESULTS

I N this chapter the numerical validation of the algorithms formulated in previous chapter will be issued covering breast cancer detection and brain stroke detection applications. Regarding the algorithms, the 2D circular and the 3D cylindrical MC tomographic methods will be used to reconstruct biological objects. The most suitable configuration in terms of number of probes, background medium and imaging strategy, will be studied. The algorithms will be also validated in relation to reconstruction quality, and in particular regarding the smallest detectable object, robustness to internal inhomogeneity of the imaged object and quantitative performance.

Concerning the applications, breast and brain phantoms, ranging from very simplified models to realistic magnetic resonance (MR) derived voxeled phantoms, will be imaged. The ultimate voxeled phantoms will also consider the real complex permittivity values of all the existing tissues and the variability along the operating frequency range.

4.1   2D circular results

This section is devoted to the preliminary assessment of the 2D circular Magnitude Combined (MC) tomographic algorithm for medical applications. For this purpose, cross-sectional images of both simplified and realistic MRI-derived breast models are obtained using the 2D circular MC reconstruction algorithm. Even though 2D methods are not applicable to medical imaging for several reasons explained before, it is a good platform to validate the algorithm, since most of the results can be extrapolated to 3D. Moreover, 2D reconstructions, and above all 3D simulations, consume significantly less time compared to 3D, thus allowing to perform parametric studies. Accordingly, in this section, a set of parametric, simple but representative simulations in the framework of breast cancer detection will performed and reconstructed. This is addressed in the first part of this section, to determine the dielectric properties of the background medium, the smaller detectable tumor and the robustness of the algorithm to inhomogenity inside the breast. All this studies will be very useful for the design of more realistic simulations later on in this chapter. Still for the simplified breast model, a set of relevant testing scenarios will be defined devoted to reveal the detection limitations of the algorithm.

Finally, the preliminary work towards conferring quantitative performance to the MC tomographic algorithm is presented. The so-called Frequency Differential Linearized (FDL) technique proposes a frequency stepped iterative scheme to avoid the effects when Born approximation is not accomplished while keeping its advantages in terms of robustness and simplicity.

A step forward towards more realistic models can be done by using voxeled phantoms. These phantoms are created by dividing the breast into small uniform voxels having the dielectric properties of the tissue occupying that space. The models are extracted from MRI images taken from real patients. In the final part of the section, the results of the 2D FDL method will be compared to the 2D MC method using voxeled breast models.

4.1.1   Simulation software

2D simulations are performed with MEEP [91, 100]. It is a free simulation software developed by Massachusetts Institute of Technology (MIT) based on FDTD time domain numerical method. The advantages of MEEP in this particular application, apart from its versatility and simplicity, are given by the fact that it is a time-domain technique. When a short pulse is used as a source, the response of the system over a wide range of frequencies can be obtained with a single simulation. It is also very appropriate to model realistic organs and tissues because allows the user to specify the material at all points within the computational domain. The major inconvenient is that it requires the entire computational domain to obtain a result of the whole structure, and the grid spatial discretization must be sufficiently fine to resolve both the smallest electromagnetic wavelength and the smallest geometrical feature in the model, leading to very large computational domains and thus very long solution times. The grid termination with PML also contributes to increase the simulation domain since a gap larger than $\lambda_b/4$ must be kept between the scenario and the boundaries.

The transmitting antennas are modeled as infinite wires of current which generate a Gaussian pulse of pulse half-duration σ=30 ps. This parameter is calculated to ensure an almost flat behavior over the desired frequency band (2-4 GHz). The receivers are ideal probes which measure the received signal in an interval of time. As a result, it produces two vectors corre-

sponding to the transient response, one in the presence of the object, and the other without the object. By subtracting the second measurement from the first, the scattered field is obtained.

4.1.2   Simplified breast phantoms

The simplified breast phantom consists of a circular homogeneous body 45 mm in radius containing a 8 mm radius tumor inside, as depicted in Figure 4.1. A 3 mm thick layer covering the breast tissue emulates the skin. The complex permittivity values used in the phantom are summarized in Table 4.1. The permittivity value for the uniform breast tissue was taken from [69,73] and correspond approximately to the average values of the different normal breast tissue groups. It could be classified as a very dense breast, since it has a very low fat content. The reason to use such a dense breast tissue, is to avoid, at this stage, the strong permittivity mismatching with respect to the skin. Accordingly, the skin effect will pose a lot of difficulty in detecting the tumor, up to a point that it could mask the effect of the variables of interest of the parametric study. A solution to deal with the important permittivity mismatching between the addipose-dominated breast tissue and the skin, will be given later on in this chapter. Another effect that has been neglected in these simulations is the frequency dispersion of the dielectric properties. The acquisition system consists of a circular array of 128 antennas of 75 mm in radius operating at a frequency range between 0.3 and 10 GHz, Table 4.2.

As explained in section 3.3, since the absolute quantitative performance is lost in the multi-frequency combination, from this point, the reconstructed dielectric contrast will be normalized to the maximum value and plotted between 0 and 1 in linear scale.
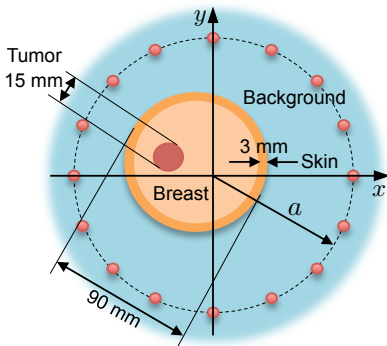
Figure 4.1: Geometry of the 2D simplified numerical breast phantom composed by a uniform breast tissue covered by a skin layer. A small circular tumor is placed inside the breast tissue.

Tissue	ϵ'	σ
Skin	37	0.44
Breast	34	0.64
Tumor	54	0.97

Table 4.1: Complex permittivity of normal breast tissue, skin and tumor.

Param.	Value
a	75 mm
N_ϕ	128
f	0.3-10 GHz

Table 4.2: Main parameters of the simulation of the 2D simplified breast phantoms.

4.1.2.1   Need of a background medium

The skin acts as a first shield of the body against microwave radiation. The subsequent layers of fat, muscle, etc., that present substantial different averaged complex permittivities, add to

the rejection of the microwave power through reflection and dissipation (conversion to heat). One approach to effectively couple the microwave signal into the tissue, is the immersion of the antenna and the imaged organ in a background medium, referred to as coupling liquid. The advantage of this approach is that organs or body parts of various sizes can be accommodated by the same acquisition setup. The antenna performance is more predictable since it is affected mostly by the known matching liquid and less by the unknown imaged organ. The disadvantages include the waste of power due to spillover, reflections, liquid losses and maintenance of the liquid (without bubbles, contamination, etc.). Another approach, that will not be investigated in this thesis, is the design of microwave antennas which can couple the power directly into the tissue, i.e., by way of direct contact with the tissue [101].

Nevertheless, due to the layered structure of the human body, the background medium is not able to simultaneously match all layers of tissues. In this case, the commonest strategy is to match the dielectric properties of the most abundant tissue in the imaged volume. For instance, for the breast screening scenario depicted in Figure 4.1, the background medium is matched to the breast tissue. In this way, not only the tumor, but also the rest of the tissues, will appear in the reconstructed image with an intensity depending on the dielectric contrast with respect to the matching liquid.

Matching the dielectric properties, commonly refers to match the real part of the permittivity, since signal reflection due to a change of media is governed by the change in refraction indexes on the interface. When jumping to experimental, in many systems, it is often desirable to have a lossy background medium in order to reduce the reflections on the tank walls containing the system. Nevertheless, the losses cannot be arbitrarily large, given the also-lossy nature of biological tissue. Accordingly, if the addition of both losses exceed the whole system sensitivity, the detection of the tumor would be impossible. Thus, in many cases both real and imaginary parts of the permittivity of the background medium and the medium to be imaged are matched. This is also a way to keep the background permittivity to a moderate value, which is also convenient for implementation reasons. A moderate background medium permittivity does require neither an excessively fine discretization in the direct problem, nor a large number of probes in the acquisition system (both depending on the background medium wavelength).

In order to know more quantitatively which is the permitted deviation of permittivities between the breast tissue and the matching media, a set of simulations doing a sweep of the matching medium permittivity between 5 and 45 is presented in Figures 4.2 and 4.3. It can be observed that some evidence of the tumor is present in all the reconstructions, being clearly detectable (3 dB higher than the surrounding) when the permittivity of the matching medium is between 35 and 24. A more quantitative value is given by the fractional permittivity variation defined as follows

$$FPV = \frac{\epsilon'_{b,max} - \epsilon'_{b,min}}{\epsilon'_{breast}} \cdot 100 \qquad (4.1)$$

where $\epsilon'_{b,max}$ and $\epsilon'_{b,min}$ are the maximum and minimum matching medium relative permittivities and ϵ'_{breast} is the breast tissue relative permittivity. This leads to FPV=32.3%. Alternatively, the maximum allowed percent contrast (defined as $c = |1 - \frac{\epsilon'_{breast}}{\epsilon'_b}| \cdot 100$ can be calculated. For the upper permittivity threshold ($\epsilon'_{b,max}$ =35) the maximum permitted contrast is 3%, while for the lower permittivity threshold ($\epsilon'_{b,min}$ =24) the maximum permitted contrast is higher (42%). Thus, according to these results, when a perfect permittivity match between the background and the object is not possible, it is always better to have a matching media permittivity lower
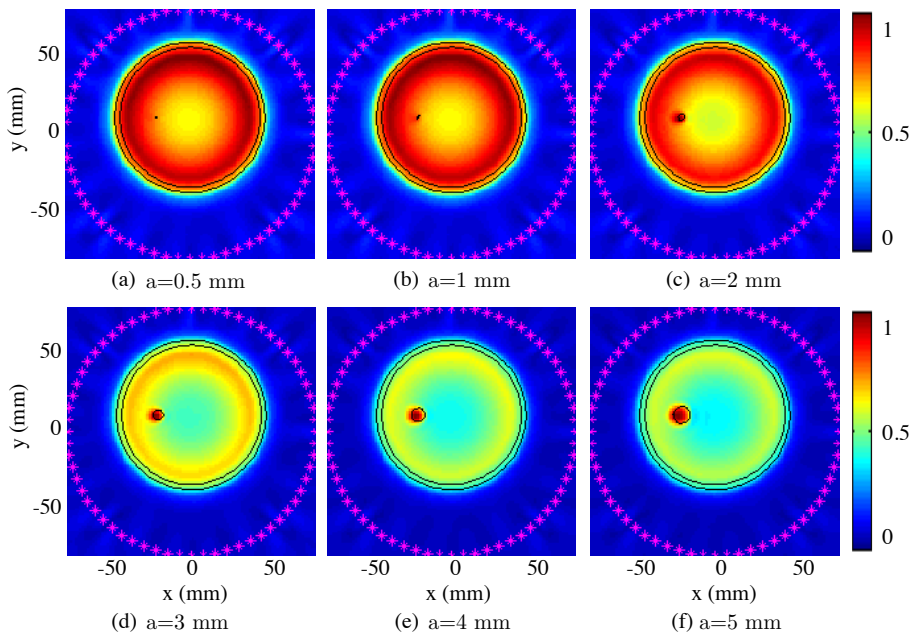
than the object permittivity.
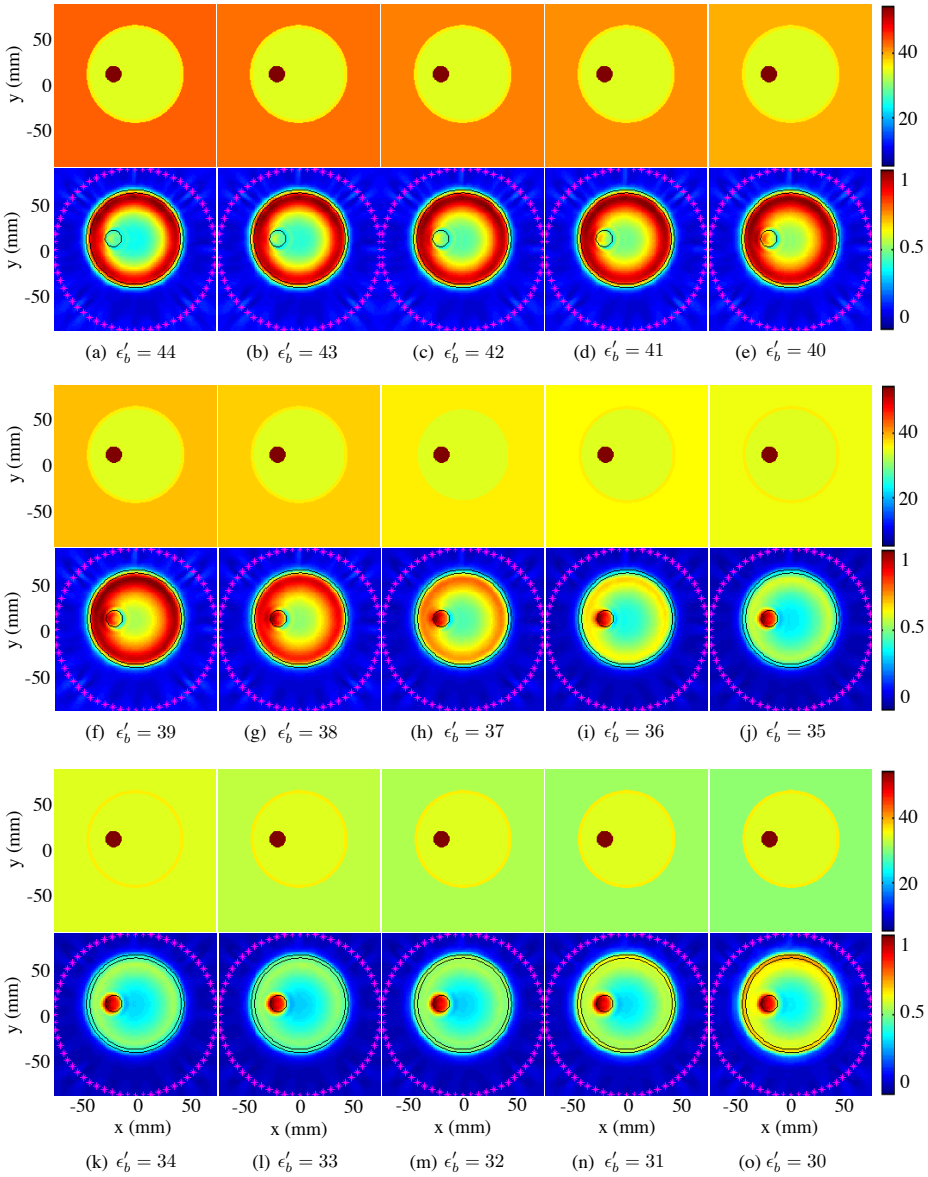
Figure 4.2: Original permittivity profile and 2D MC reconstruction of the simplified numerical breast phantom. A sweep of the matching liquid relative permittivity is performed between $\epsilon'_b = 44$ and 30 with $\sigma_b = 0.1$. The breast phantom is as shows Figure 4.1 with the dielectric properties of Table 4.1.

Another important observation, is that a centered circular artifact tends to appear when the breast is not well-matched, which can be interpreted as false positive detection. Thus the
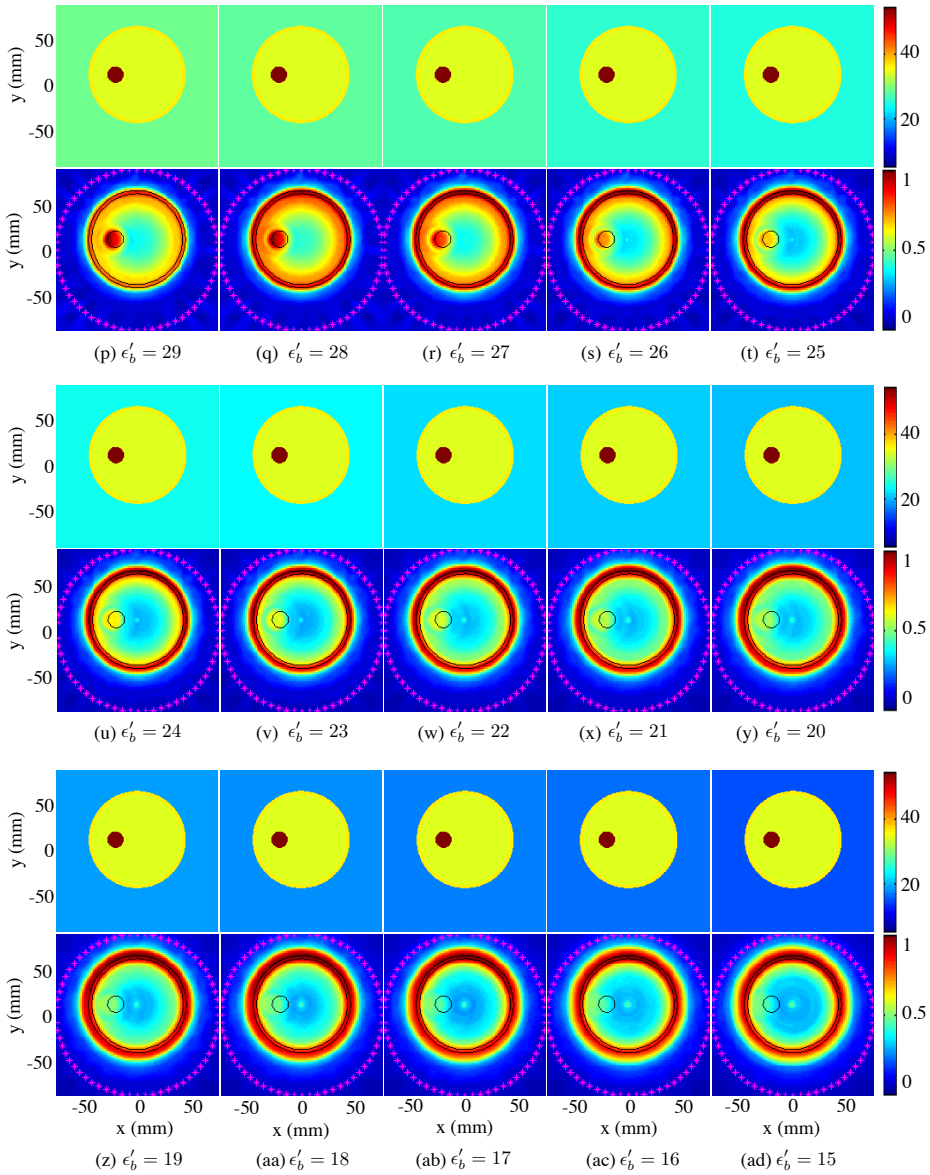
Figure 4.3: Continuation of Figure 4.2. Original permittivity profile and 2D MC reconstruction of the simplified numerical breast phantom. A sweep of the matching liquid relative permittivity is performed between $\epsilon'_b = 29$ and 15 with $\sigma_b = 0.1$. The breast phantom is as shows Figure 4.1 with the dielectric properties of Table 4.1.

importance of a proper permittivity matching.

4.1.2.2 Early stage tumor detection capability

Another important issue for medical applications is the capability of detecting early stage lesions. In case of breast cancer, early stage detection is of vital importance to prevent from metastasis processes or mastectomy (clinical removal of one or both breasts, partially or completely) which is the most recurrent operation in patients presenting a tumor larger than 5 cm that does not shrink very much with chemotherapy.

To test the capability of MC tomography to detect small breast tumors, a set of simulations sweeping the radius of the tumor between 0.5 mm and 5 mm, using a background medium matched to the skin ($\epsilon'_b = 34$) is reconstructed using 2D MC algorithm between 0.5 and 4 GHz, see Figure 4.4. The tumor begins to appear from a radius of 1 mm, being clearly visible from 2 mm.

Figure 4.4: 2D MC reconstruction of the simplified numerical breast phantom doing a sweep of the tumor radius between $a = 0.5$ mm and 5 mm. The breast phantom is as shows Figure 4.1 with the dielectric properties of Table 4.1, the matching liquid has a relative permittivity $\epsilon'_b = 34$ and $\sigma = 0.1$.

4.1.2.3 Robustness to inhomogenity

Breast is a very inhomogeneous tissue, and thus, it is important that reconstruction algorithms could be robust to some variations within the tissue. As has been reported in [102], random variations of 10% around the nominal dielectric properties of breast tissues can be considered typi-

cally. Figure 4.5 present the reconstruction results of the inhomogeneous breast with tumors of increasing radius. It is the same phantom as the previous simulations but replacing the homogeneous breast tissue for an inhomogeneous tissue composed by 4×4 mm^2 voxels. Each voxel has a random permittivity ranging from $\epsilon^*_{inhom} = \epsilon^*_{hom} - 0.1 \cdot \epsilon^*_{hom}$ to $\epsilon^*_{inhom} = \epsilon^*_{hom} + 0.1 \cdot \epsilon^*_{hom}$, that is a ±10% variation in both real and imaginary parts of the permittivity. The results are represented in the second row of Figure 4.5. The third row of Figure 4.5 shows the results for a ±30% variation in both real and imaginary parts of the permittivity with respect to the nominal value. Comparing these images to the previous reconstructions, it can be observed that the algorithm is robust to a ±10% inhomogenity since no significant differences can be observed with respect to Figure 4.4. However when the contrast of the inhomogeneity increases up to a ±30%, the detection performance is deteriorated since the inhomogeneity becomes visible. This performance is clearly influenced by the size of the inhomogeneity. Since in this case the inhomogeneity is represented as 4×4 mm^2 squares, when its permittivity becomes comparable to that of the tumor, it will be also visible in the image. Thus the tumor must be bigger than the inhomogeneity to be distinguishable (tumor radius bigger than 2 mm).

In a real breast scenario, the inhomogeneity is produced by the different breast constituents (fat, glands, etc.), but also by the inhomogeneity within the same tissue. The inhomogeneity within the same tissue will be comparable to the ±10% case, since the contrast and the size of the inhomogeneity will not be large enough to produce visible changes in the image. Conversely, the different breast constituents will be large masses (comparable or even bigger than the tumor) that could have high permittivities (comparable to the breast in case of glands). In this last case, the inhomogeneity will appear in the image unless a subtraction mechanism is applied as will be shown later on in this chapter.

4.1.3 Relevant scenarios for breast imaging

Once the performance of the algorithm was tested with simplified parametric models, now, still simple but more medically relevant phantoms will be studied. From this point, the skin permittivity matching problem is addressed by considering an adipose-dominated breast tissue, $\epsilon'_{breast} = 10$. Since the background medium is matched to the breast tissue a strong mismatching between the skin and the background exist. 4 different breast phantoms of increasing complexity where defined as summarized in Table 4.4. Scenario 1, namely simple model, consists of a uniform breast tissue with an embedded tumor. Scenario 2, namely multi-layer and multi-target 1 (MLMT 1), is the same as 1 but includes an external skin layer and the inclusion of a glandular tissue close to the tumor. Scenario 3, namely multi-layer and multi-target 2 (MLMT 2), is the same as 2 but the tumor is completely embedded in glandular tissue. Scenario 4, namely compressed, is aimed to determine if compressing the breast offers any advantage with respect to the non-compressed case. The acquisition system consists of a circular array of $a = 75$ mm in radius composed by $N_\phi = 64$ antennas operating between 0.5 and 4 GHz, see Table 4.3.

Figure 4.6 shows the results corresponding to the previous 4 scenarios using the 2D circular MC reconstruction algorithm. The second and third rows, Figure 4.6(b) and (c), present the results of the conventional imaging without skin removal for the whole and the upper part of the frequency range respectively. In view of the results, it can be concluded that it is very important to have a good matching in all the interfaces between the phantom's layers. The high permittivity of the skin and the subsequent low permittivity breast fatty tissue, produce
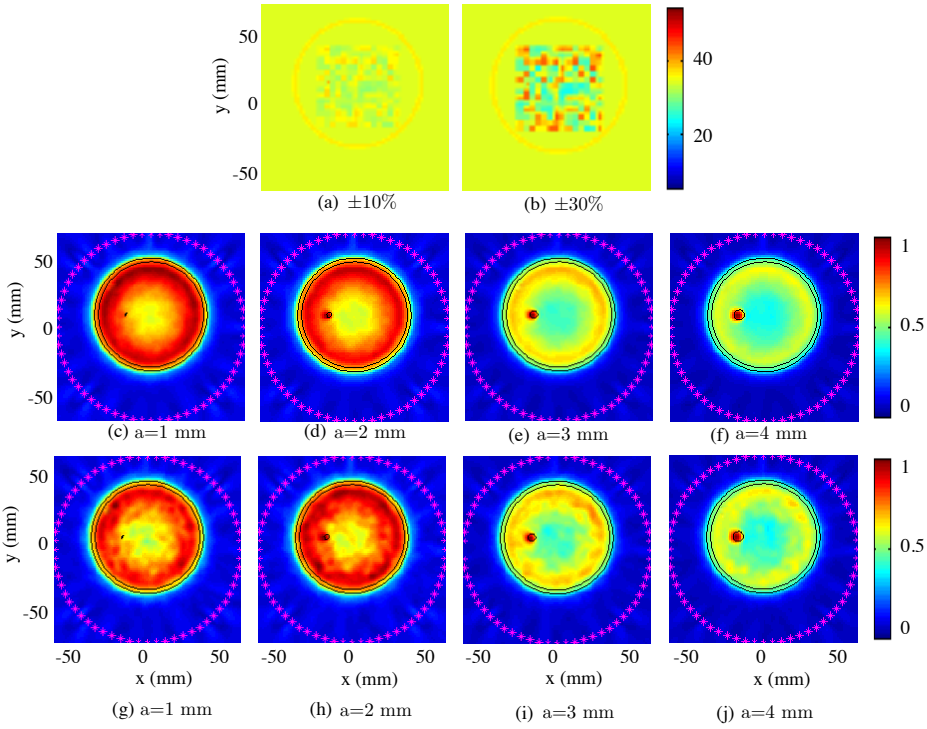
Figure 4.5: 2D MC reconstruction of the simplified numerical breast phantom doing a sweep of the tumor radius between $a = 1$ mm and 5 mm for two different percentages of inhomogeneity in the breast tissue. The breast phantom is as shows Figure 4.1 with the dielectric properties of Table 4.1, the matching liquid has a relative permittivity $\epsilon'_b = 34$ and $\sigma = 0.1$. (a) permittivity profile of the $\pm 10\%$ inhomogeneous breast tissue, (b) permittivity profile of the $\pm 30\%$ inhomogeneous breast tissue, (c) tumor of 1 mm in radius, $\pm 10\%$ inhomogeneous breast tissue, (d) tumor of 2 mm in radius, $\pm 10\%$ inhomogeneous breast tissue, (e) tumor of 3 mm in radius, $\pm 10\%$ inhomogeneous breast tissue, (f) tumor of 4 mm in radius, $\pm 10\%$ inhomogeneous breast tissue, (g) tumor of 1 mm in radius, $\pm 30\%$ inhomogeneous breast tissue, (h) tumor of 2 mm in radius, $\pm 30\%$ inhomogeneous breast tissue, (i) tumor of 3 mm in radius, $\pm 30\%$ inhomogeneous breast tissue and (j) tumor of 4 mm in radius, $\pm 30\%$ inhomogeneous breast tissue.

such a strong reflection that can even mask the tumor response completely depending on the frequency. Accordingly, for the lower frequencies, the skin layer is less important in terms of the wavelength and thus it can be penetrated, however the resolution is poor. If a higher resolution is needed skin removal techniques may be desirable to compensate the detrimental effect of the skin layer [103]. Using MC algorithm, this technique is implemented as a differential reconstruction, where the scattered field of a reference scenario is subtracted from the scattered field of the complete breast phantom. The reference scenario is synthesized as follows. First, the skin surface of the breast is detected. Next, starting from a uniform image of complex permittivity equal to the background, a uniform skin permittivity is assigned to the image pixels detected at the previous step and to the surrounding pixels in order to create a 2-mm-thick skin layer. Finally, the internal part of the skin is filled with a uniform average breast tissue. The

Parameter	Value
a	75 mm
N_ϕ	64
f	0.5-4 GHz
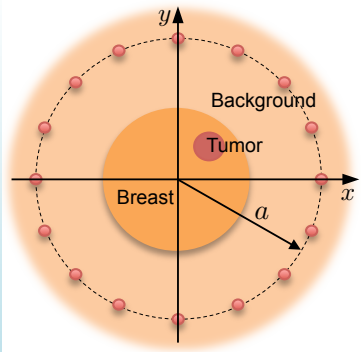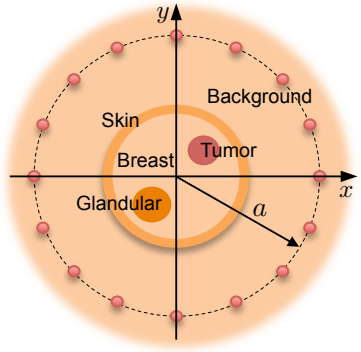
Table 4.3: Main parameters of the simulation of the 2D relevant breast scenarios.

results after applying this process are shown in Figure 4.6(d) and 4.6(e). It can be observed, that in the simple and in the MLMT 1 models, the tumor is clearly detected, even when skin removal is not used. However, the two last phantoms (MLMT 2 and compressed) are very challenging cases. Both can be even worse than realistic cases because the tumor is completely inside the glandular tissue and both tissues are circular. In real cases, although the tumor is commonly inside fibroglandular tissue, it is not as homogeneous and continuous and thus the tumor is more visible for the illuminating signals. Despite the difficulty, there is still evidence of the tumor presence for both the lower (4.6(d)) and the higher (4.6(e)) frequency bands, but the shape and size of the breast constituents are not accurately reconstructed. For the higher frequency band, since the penetration capability is reduced, only the contours of the tumor and glandular tissues are retrieved. Also, when the glandular tissue is really close to the skin layer, an artifact appears on the skin (Figures 4.6(d) MLMT1 and MLMT2). Finally, the breast compression strategy (last column) do not seem to give a clear advantage using MC algorithm since the sharp breast edges resulting from the compression produce a strong backscattering that prevail in front of the tumor.
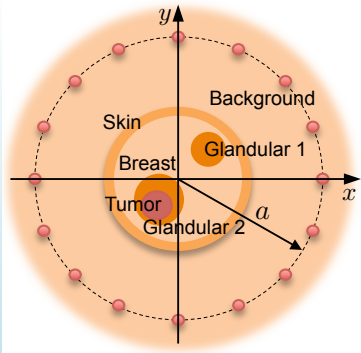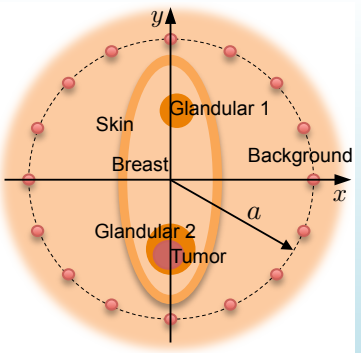
For a more quantitative evaluation of the results, four different metrics are defined devoted to measure the algorithm performance in terms of tumor response and spatial accuracy. The signal to clutter ratio (SCR) measures the tumor response compared to the clutter and the signal to mean ratio (SMR) measures the tumor response compared to the neighboring tissues. The position accuracy (PA) quantifies the accuracy in determining the tumor location and the full width half maximum (FWHM) the size accuracy. The metrics definition is included in Appendix C. Table 4.5 summarizes the results of the metrics. f_1 refers to the whole frequency band (0.5-4 GHz), f_2 to the frequency band between 3.5-4 GHz and S indicates that frequency removal was applied. The metrics results are in agreement with the conclusions extracted with the visual inspection of the reconstructions. The best performance is obtained for the simple model. While, in general, the best spatial resolution, quantified by FWHM and PA, is obtained for the higher frequency band, the best performance against clutter (SMR) is obtained when the whole band is combined. This trends confirms that the choice of the frequency band is a crucial issue above all when the phantom becomes more complicated.

4.1.4 Frequency Differential Linearized technique (FDL): towards quantitative performance

MC tomography was primarily interested in the robustness and efficiency of the algorithm. As it has been shown, the algorithm takes advantage of the simplicity of a modified-Born method to retrieve a quasi-real time qualitative reconstruction of the contrast in permittivity. In this

Tissue	ϵ'	σ	Diameter (mm)	ϵ'	σ	Diameter (mm)
Background	10	0.5	-	10	0.5	-
Skin	-	-	-	35	1	100
Breast	6.12	0.11	96	6.12	0.2	96
Glandular	-	-	-	42	1.11	40
Tumor	55.3	1.57	20	55.3	1.57	20

Tissue	ϵ'	σ	Diameter (mm)	ϵ'	σ	Diameter (mm)
Background	10	0.5	-	10	0.5	-
Skin	35	1	100	35	1	100
Breast	6.12	0.11	96	6.12	0.11	96
Glandular 1	42	1.11	40	42	1.11	40
Glandular 2	21.8	0.5	45	21.8	0.5	45
Tumor	55.3	1.57	20	55.3	1.57	20

Table 4.4: Relevant scenarios of increasing complexity for breast tumor detection.
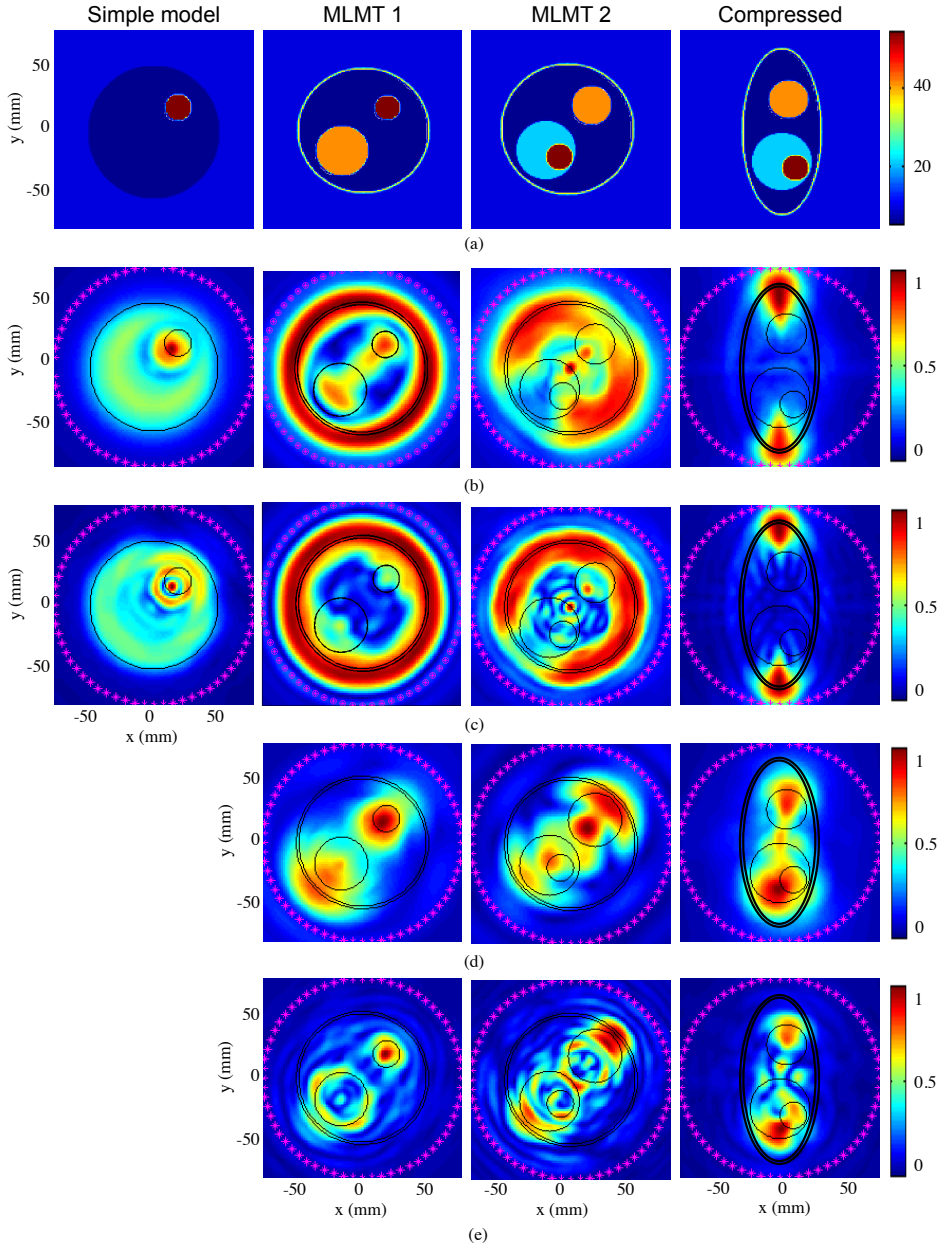
Figure 4.6: 2D MC reconstruction results of the relevant scenarios shown in Table 4.4. (a) Relative permittivity profile, (b) absolute reconstruction at 30 frequencies over the 0.5-4 GHz band, (c) absolute reconstruction at 5 frequencies over 3.5-4 GHz band, (d) reconstruction with skin removal at 30 frequencies over the 0.5-4 GHz band and (e) reconstruction with skin removal at 5 frequencies over 3.5-4 GHz band.

	Simple model		MLMT 1				MLMT 2		Compressed	
	f_1	f_2	f_1	f_2	Sf_1	Sf_2	Sf_1	Sf_2	Sf_1	Sf_2
SCR	9.80	9.82	6.52	7.19	8.30	9.10	7.53	8.89	7.94	6.62
SMR	5.81	5.47	2.32	0.65	6.15	7.46	5.81	5.69	5.90	4.12
FWHM	12	6	12	7.5	21	6	24	13.5	9	7.5
PA	6.36	6.36	0	2.12	0	0	10.81	6.18	7.07	6.80

Table 4.5: Metrics for the 2D relevant breast scenarios.

section we propose to improve the reconstruction quality of the previous algorithm towards a quantitative performance. Hence, the so-called FDL technique is based on the use of the extra information available with the emerging multi-frequency measuring techniques [CA1]. The proposed technique consists on combining the simplicity and robustness of the linear reconstruction Born-based techniques with the accuracy of the iterative methods. Figure 4.7 shows the flow-chart of the FDL algorithm. The starting point is a broadband measurement of the
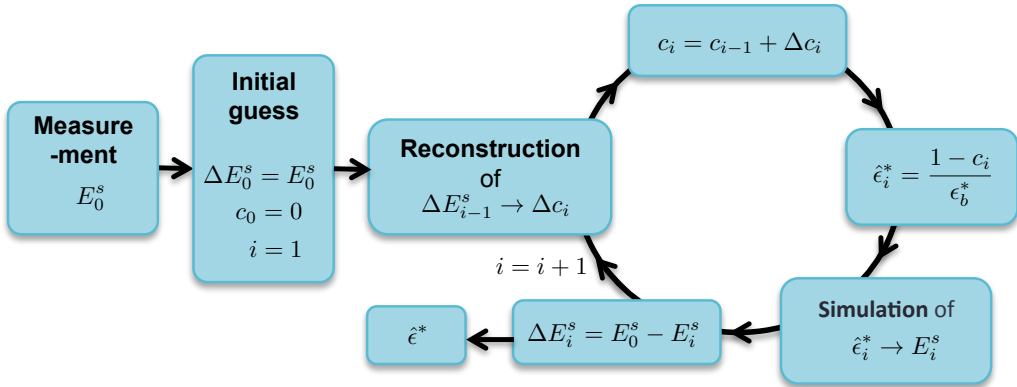
Figure 4.7: Flow-chart of the FDL technique.

scattered field denoted as E_0^s and a initial guess of the scene. Initially, a uniform background is assumed, meaning that no foreknowledge is required, thus contributing to the algorithm robustness. Notice that the scenario has to be discretized in cells. The size of the cells was taken according to the requirements of the simulator as $\lambda_b/10$ which is approximately 1 mm. In the first step of the FDL algorithm, the differential scattered field is reconstructed using the 2D circular reconstruction algorithm for the lowest frequency of the band. The differential scattered field of the first iteration ($i = 1$), $\Delta E_0^s = E_0^s$, is calculated as the subtraction between the measured scattered field and the reference scattered field measured for a uniform background without the object. The idea is to start the reconstruction process for a low frequency such that the requirement for small product between electrical size and contrast may be accomplished and thus it could be linearly treated without committing any error. In the next step, the contrast of each cell is updated adding the reconstructed contrast obtained in the previous step, $c_i = c_{i-1} + \Delta c_i$. Then, the permittivity of the scenario is estimated from the contrast as

$\hat{\epsilon}_i^* = \frac{1-c_i}{\epsilon_b^*}$ and it is simulated using CST EM simulation software. Finally the differential field, $\Delta E_i^s = E_0^s - E_i^s$, is calculated as the subtraction between the measured field and the simulated field. Subsequently this process is repeated for the next frequency till the algorithm converges, that is the simulated field is very similar to the measured field. Note that by using a differential approach in the reconstruction, a low contrasted scenario is obtained at each iteration, which again accomplishes Born approximation. In this way the quantitative performance of the algorithm may be preserved.

Figures 4.8 and 4.9 are devoted to show the improvement towards a quantitative performance of the FDL iterative algorithm with respect to the previous MC algorithm. Let us suppose a scenario consisting of an infinite cylinder along z-axis of 40 mm in radius and a permittivity of 50. The cylinder is immersed in a background medium of 33 in permittivity. The aquisition system is a circular array of 8 cm in radius composed by 64 evenly distributed antennas around the cylinder, operating at a frequency range between 0.15 and 1.5 GHz. Since the electrical size of the object is going to increase with frequency, at a certain point, Born approximation will start to fail. For such a geometry, this occurs at approximately 1 GHz. Figure 4.8(b) shows the 2D circular reconstruction at a single frequency of 0.15 GHz (the smallest frequency of the range of interest). The magnitude represented is now the real part of the permittivity. For such a low frequency, the information of the lower part of the spectrum, that represents the smother parts of the object is obtained. In this low-resolution image, the cylinder is not well delimited but it is a good starting point for the iterative scheme, since Born approximation is accomplished. Figures 4.8(c), 4.8(d) and 4.8(e) correspond to the reconstruction of the same object at a 0.79, 1.15 and 1.5 GHz respectively. Increasingly better resolution is obtained, however at 1.15 GHz Born approximation begins to fail and thus a degradation of the reconstruction is observed. The degradation is revealed as a reduction of the reconstructed permittivity on the center of the cylinder which seems hollow. Subsequently, Figure 4.8(f) presents the reconstruction using MC method that combines the magnitude of the images obtained at 20 frequencies over the frequency range between 0.15 and 1.5 GHz. It an be observed that MC succeeds in reconstructing the geometry, preserving the uniformity of the cylinder, but still the exact value of the permittivity is not correct. Figures 4.8(g) and 4.8(h) present the reconstructions obtained with FDL technique. Figure 4.8(g) uses 1 iteration at each frequency over the same frequency range as in the MC reconstruction. A similar performance to MC method is obtained, meaning that more iterations are recommended. Finally, Figure 4.8(h) shows that by using 6 iterations at each frequency, the exact value of the permittivity is retrieved.

4.1.4.1   Voxeled breast phantom results

The technique has been applied to test-bed anthropomorphic breast models extracted from MR images available at [85]. From the data supplied in the repository, 2D breast models have been extracted by considering a slice of the actual phantoms. In particular, a cross section corresponding to slice number 120 of the model classified as class 1 numerical phantom 1 (mostly fatty, ID number 071904) has been selected [69, 73]. The considered phantom has been discretized into 1 mm^3 voxels. Figure 4.10(a) shows the relative permittivity profile of the phantom containing a tumor of 5 mm in diameter, glandular tissue and non-uniform fatty tissue surrounded by a 2 mm-thick skin layer at 2 GHz. Table 4.6 summarizes the relative permittivity and conductivity values of the breast model constitutents at 2 GHz. A matching medium with permittivity $\epsilon_b' = 4.6$ is used to ensure a maximum transmitted signal into the breast.
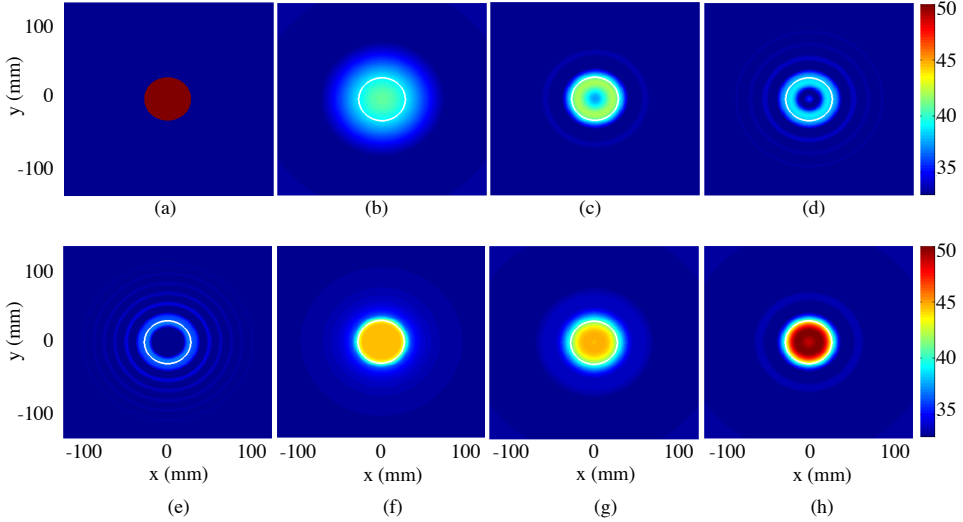
Figure 4.8: 2D circular reconstructions of an infinitely large cylinder of 40 mm in radius and permittivity 50 immersed in a background medium of permittivity $\epsilon'_b = 33$. (a) Geometry, (b) reconstruction at 0.15 GHz (c) reconstruction at 0.79 GHz, (d) reconstruction at 1.15 GHz, (e) reconstruction at 1.5 GHz, (f) MC reconstruction, (g) FDL reconstruction 1 iteration per frequency and (h) FDL reconstruction 6 iterations per frequency.
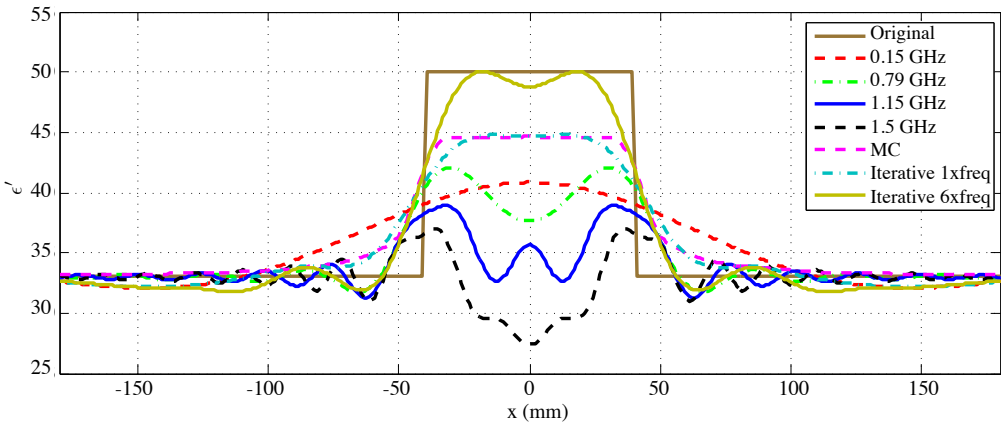
Figure 4.9: Longitudinal cut of the 2D circular reconstruction of an infinitely large cylinder of 40 mm in radius and permittivity 50 immersed in a background medium of permittivity 30 using different methods and configurations.

At the current stage of development, the losses and the frequency dispersion are not considered in the model. The measurement system consists of a $a = 90$ mm in radius antenna ring with $N_\phi = 32$ evenly spaced transmitting and receiving probes. The frequency range has been

selected between 1-4 GHz, see Table 4.7.

Tissue	ϵ'	σ
Background	5	0
Skin	39	1.3
Fat	2-7	0-0.1
Transitional	8-37	0.2-0.9
Fibroglandular	38-60	1-1.7
Tumor	55	1.6

Parameter	Value
a	90 mm
N_ϕ	32
f	1-4 GHz

Table 4.6: 2D voxeled breast average complex permittivities at 2 GHz [5, 69].

Table 4.7: Main parameters of the simulation of the 2D voxeled breast model.

As performed in the last section, in order to penetrate inside the breast, it is necessary to estimate the breast surface to reduce the skin effect. To do so, a 2 mm-thick uniform skin layer of relative permittivity 38 is assumed. Figure 4.10(b) shows the reconstruction of the permittivity after 16 iterations (1 per frequency). It can be observed that the tumor and the fibroglandurar tissue are detected. Regarding the quantitative estimation of the permittivity, it is slightly underestimated (44 instead of 55 for the tumor and a maximum of 38 instead of a maximum of 54 for the fibroglandular tissue). Notice that this is a very initial work and more improvements are needed to avoid the underestimation of the permittivity values and the correct retrieval of the imaginary part of the permittivity.
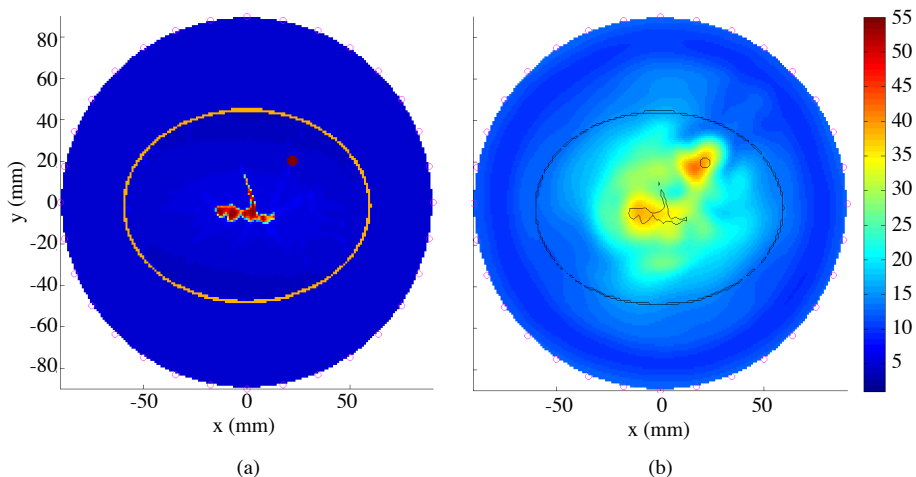
Figure 4.10: 2D FDL reconstruction of the MRI-derived voxeled mostly fatty breast phantom. (a) Original relative permittivity profile at 2 GHz, (b) 2D MC reconstruction after 16 iterations (1 per frequency) between 1-4 GHz.

4.2   3D cylindrical results

As said, 3D reconstruction algorithms where pursued for the purpose of providing a correct reconstruction for general objects not necessarily uniform in one direction as required for the 2D algorithms. To exemplify this fact, a canonical scenario consisting of a 90 mm-diameter isolated centered sphere of $\epsilon'_{s1} = 2.19$ with the inclusion of a smaller sphere of 16 mm in diameter and $\epsilon'_{s2} = 5.5$, all immersed in air, is simulated and reconstructed using both 2D and 3D algorithms. In Figure 4.11(b) the reconstruction of the aforementioned scenario using the 2D MC algorithm is compared to the result of the corresponding 3D version, Figure 4.11(c). Again the plots represent the normalized dielectric contrast in linear scale. It can be observed how 2D and 3D algorithms are able to image the small sphere when reconstructing the cut at $z = -40.8$ mm (center of the small sphere). However, when reconstructing the plane $z = 0$ mm, where the small sphere is not present, the image recovered by the 2D algorithm shows reminiscences of it, while for the 3D algorithm it is not visible, as expected. This states the capability of the 3D MC to provide vertical discrimination and localize precisely embedded objects in general scenarios. In contrast, 2D algorithms are restricted to cases where vertical uniformity can be assumed.
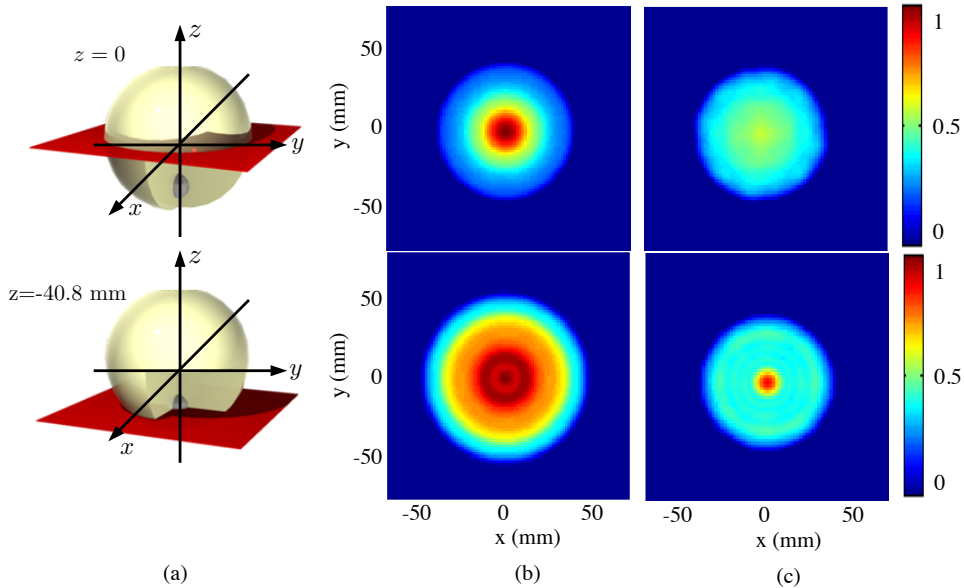
Figure 4.11: 3D cylindrical MC reconstruction of an isolated sphere of relative permittivity $\epsilon'_{s1} = 2.19$ with the inclusion of a smaller sphere of $\epsilon'_{s2} = 5.5$ in air. (a) Geometry, (b) 2D MC reconstruction, (c) 3D MC reconstruction.

This section is devoted to the assessment of the 3D cylindrical MC algorithm for medical applications and in particular for breast tumor and brain stroke detection. For this purpose, both simplified and realistic MRI-derived breast models are reconstructed using the 3D MC algorithm.

4.2.1 Simulation software

3D simulations are performed using both FEKO EM simulation software and CST microwave studio. The frequency domain solver based of the method of moments of FEKO was used to simulate the simple models, while the time domain solver of CST was more suitable for the complex voxeled models. The method of moments was used for its accuracy, easy integration with Matlab and because it allowed to obtain a fast single frequency simulation which was very convenient for testing purposes. However the matrix inversion of voxeled phantoms composed by a large amount of different tissues may require hundreds of GB of memory, becoming unsolvable with MoM. In those cases, CST time domain solver was used.

4.2.2 Simplified breast and brain models

The goal of this section is to give an initial idea of the potential of 3D MC algorithm to deal with 3D models of breast and brain organs before proceeding with realistic voxeled models. With these simple models, the most convenient array configuration in terms of number of antennas will be investigated. While the number of elements in the circular array is completely defined by the Nyquist sampling criteria given a certain radius, in the cylindrical array not. Similarly to circular arrays, in cylindrical arrays, the number of antennas in each ring and the separation between the elements along the cylinder main axis ($\hat{z}$-direction) are completely defined. However, the extension of the cylinder has to be determined empirically depending on the system parameters.

4.2.2.1 Breast cancer detection

Regarding breast tumor detection scenario, a simplified model consisting of an hemispherical breast attached to the chest wall with the inclusion of a 8 mm in radius spherical tumor, is considered [CA8]. The breast phantom is composed by a 3 mm-thick skin layer and a uniform low-adipose breast tissue to reduce the skin effect, as done in previous section, see Figure 4.12. An external medium of $\epsilon'_b = 34$ is used to match the permittivities. Regarding the dielectric properties, they are essentially the same as in the 2D parametric studies, but in this case, the complex permittivity frequency dispersion was taken into account in the model. The complex permittivity values for each breast tissue depending on the frequency were calculated using Cole-Cole models as explained in section 2.2, using the coefficients provided in [69, 73]. The corresponding values for the breast model constituents are represented in Figure 4.13 and summarized in Table 4.9. The acquisition system consists of a cylindrical array of antennas of $a = 75$ mm in radius composed by N_z rings separated $\Delta_z = 15$ mm of $N_\phi = 36$ elements each, see Table 4.8. The separation between elements along $\hat{\phi}$ and $\hat{z}$-directions was calculated using the expressions of 3.1. As explained before, the number of antennas along the cylinder main axis, or more explicitly the length l_z, has to be determined. Here we are primarily interested in having the minimum number of antennas that still produce a good quality reconstruction and thus, correct plane waves. A reduction in the number of antennas can be accomplished by

optimizing the variables appearing in the following equations

$$N_\phi = 2 \frac{2\pi f \sqrt{\epsilon_b'}}{c_0} a \tag{4.2}$$

$$N_z = 2 \frac{f \sqrt{\epsilon_b'}}{c_0} l_z \tag{4.3}$$

by:

- Reducing l_z.
- Reducing a with the limitation of the radius of the phantom (a_o), $a > a_o$.
- Reducing ϵ_b'. However the background must be matched to the breast tissue to ensure penetration.
- Reducing f which also reduces the resolution.

The previous options indicate that the most feasible way to reduce the number of antennas is optimizing l_z. Figure shows the 3D MC imaging results for different cylinder lengths l_z. As explained in section 3.2.2.2, the truncation of the cylinder produces a detrimental effect on the synthesized plane waves quality. In order to avoid artifacts in the reconstruction, poor quality plane waves must not be included in the imaging process. This can be done by limiting the synthesized plane waves polar direction of propagation, θ. According to the definition of validity angle, equation 3.26, the quality of the plane waves is better when the relation between l_z and the object size along the cylinder axis l_{z_o}, is large. For the particular case of the simplified breast, cylinder lengths between $l_z = 50$ mm and $l_z = 300$ mm with $\delta_z = 15$ mm, are studied leading to validity angles between $\theta_v = 4.7°$ and $60.2°$.
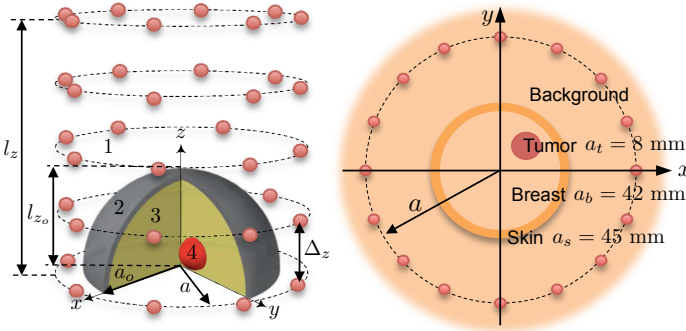
Figure 4.12: Geometry of the 3D simplified numerical breast phantom and the acquisition system.

Parameter	Value
a	75 mm
N_ϕ	36
Δ_z	15 mm
N_z	1-21
f	0.5-2 GHz

Table 4.8: Main parameters of the simulation of the 3D simplified breast model.

Figure 4.14 shows the 3D MC imaging results for different number of vertical levels N_z. For each case, two cuts are plotted: the upper one is the XY cut and the lower one is the XZ cut. These figures show the normalized magnitude of the dielectric contrast in linear scale between 0 and 1. In view of the results, it can be stated that the reconstruction is accurate when the number of vertical levels N_z is larger than 4 ($l_z > 60$ mm). This means that the acquisition cylinder must exceed the imaged object, but it is not needed to be excessively larger. With more
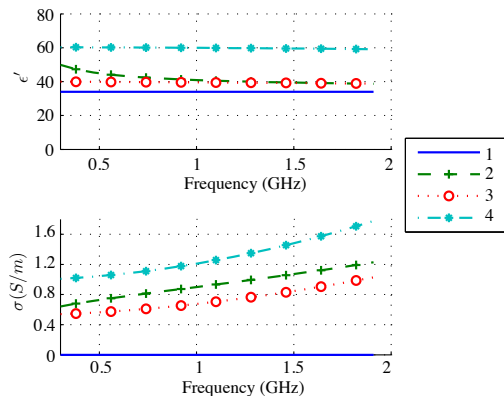
Figure 4.13: Permittivity and conductivity of the 3D simple breast model: 1. background medium, 2. skin, 3. breast tissue, 4. tumor [5,69].

Tissue	ϵ'	σ	$|c(\vec{r})/c_{max}|$
Background	34	0	0
Skin	40	0.9	0.34
Breast	39	0.67	0
Tumor	60	1.21	1

Table 4.9: Simplified breast model complex permittivity at 1 GHz.

than 4 levels of antennas, the reconstruction do not change noticeably. $N_z = 5$ means a total cylinder length of $l_z = 60$ mm leading to a total number of antennas of $N_z \cdot N_\phi = 180$. For this case, the position and size of the tumor is well detected in both XY and XZ planes and the breast volume is correctly represented. Due to the cylinder truncation, the resolution along z-axis is not as good as the resolution of XY plane. Figure 4.10 summarize the metrics results. As expected the metrics improve as the number of vertical levels increase. For $N_z = 3$ and 4 the full width half maximum (FWHM) could not be calculated since the reconstructed contrast of the tumor never decrease to less than the half of the maximum value. See Appendix C for a detailed description of the metrics.

N_z	1	2	3	4	5	6	7	8
SCR	-0.17	5.23	2.83	4.43	6.48	6.41	7.14	7.60
SMR	1.52	2.91	2.29	2.72	3.83	6.48	7.56	7.94
FWHM	12	10.61	-	-	13.82	11.71	10.61	10.61
PA	0.71	2.83	0.71	0.71	0.71	0.71	0.71	0.71

Table 4.10: Metrics for the 3D simple breast model.

4.2.2.2 Brain stroke detection

The aim in brain stroke detection is in fact to detect hemorrhagic brain stroke. This is to detect a blood mass inside the brain. By doing so, in an event of stroke, the bleeding stroke could be differentiated from ischemic stroke and the correct treatment administered to the patient. A simplified brain model is considered as a first approach to the problem. It consists of a semi-spherical body (equivalent to the upper part of the head) composed by several layers accounting
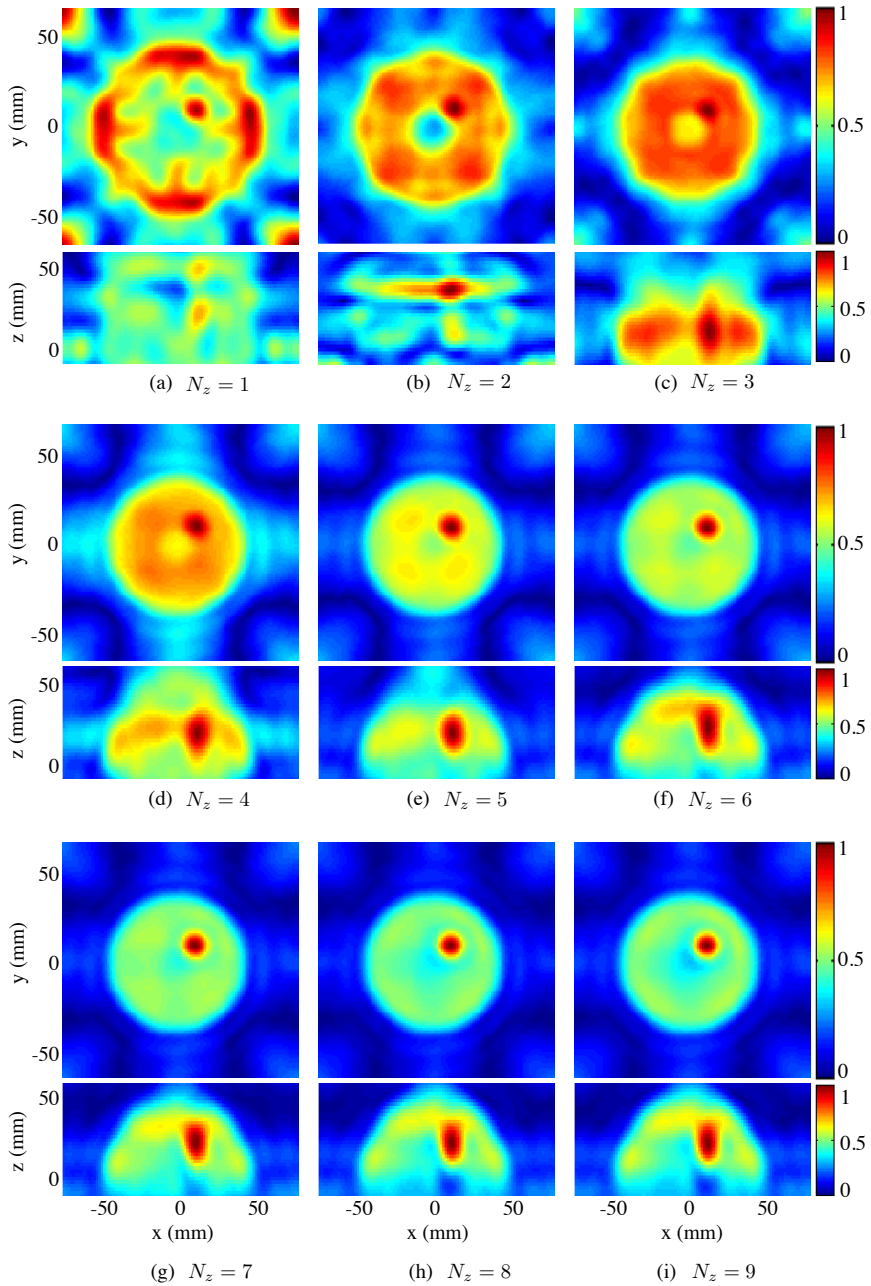
Figure 4.14: 3D MC dielectric contrast reconstruction of the simplified breast phantom using different cylinder lengths l_z.

for the skin, the skull and the brain itself. The brain includes the two hemispheres of white matter covered by a layer of gray matter. The hemorrhage is simulated as a sphere of blood inserted inside the white matter, see Figure 4.15 [CA10]. The dielectric and physical properties of the brain model over the frequency are plotted in Figure 4.16 and summarized in Table 4.12. Additionally, an external matching medium of $\epsilon_b' = 40$ is used in order to reduce the contrast with skin and brain white and gray matter. The acquisition system consists in a cylindrical array of antennas of $a = 110$ mm in radius composed by $N_z = 25$ rings separated $\Delta_z = 10$ mm of $N_\phi = 32$ elements each, see Table 4.11.
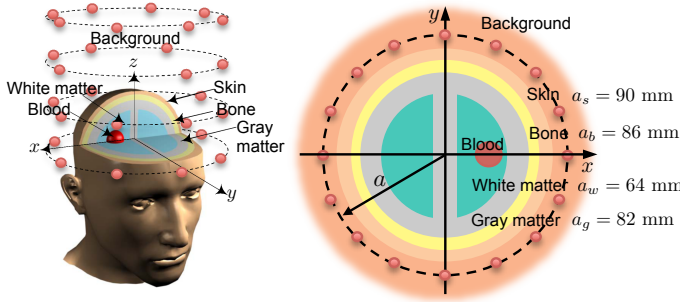
Figure 4.15: Geometry of the 3D simplified numerical brain phantom and the acquisition system.

Parameter	Value
a	110 mm
N_ϕ	32
Δ_z	10 mm
N_z	25
f	0.3-1 GHz

Table 4.11: Main parameters of the simulation of the simplified brain model.
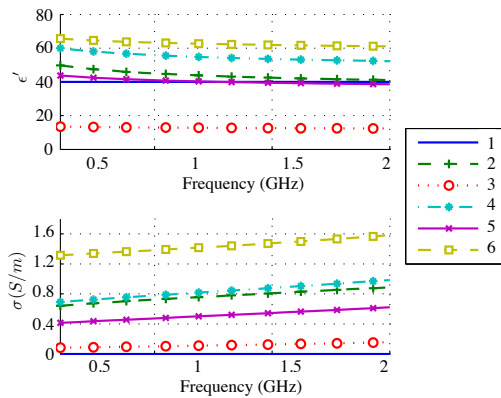
Figure 4.16: Permittivity and conductivity of the simple brain model: 1. background medium, 2. skin, 3. bone, 4. gray matter, 5. white matter, 6. blood [5].

Tissue	ϵ'	σ	$|c(\vec{r})/c_{max}|$
Background	40	0	0
Skin	41	0.88	0.0357
Bone	12	0.15	1
Gray matter	62	0.98	0.429
White matter	38	0.62	0.071
Blood	61	1.58	0.75

Table 4.12: Simplified brain model complex permittivity at 1 GHz.

Figure 4.17 shows the reconstruction of the simple brain phantom without losses. Figure 4.17(a) represents the XY plane, while Figure 4.17(b) shows the 3D view. The 3D view is always represented in this thesis through the 3 main planes intersecting at the center of the target (the stroke in this case). It can be observed that despite of being a more challenging application

due to the significant dielectric contrast between the successive layers, MC algorithm obtains a correct reconstruction. The image allows to differentiate the two brain hemispheres and shows the layered structure of the model. The spherical hemorrhage is detected preserving its position and size. Nevertheless, when the losses are considered, the transmitted field is more attenuated than the reflected one and becomes masked. When this occurs, the border of the brain appear very highlighted in the reconstructed image, while the internal structures are not visible, see Figure 4.18(a). To mitigate this effect to a certain extent, the signals captured when the receiver is situated in front of the transmitter can be canceled, since they enclose essentially information about the reflection. In particular, the angular gating consists multiplying the scattered field measured when the transmitter and the receiver are facing each other and the surrounding measurements by a window. In this case the window is the convolution between a Hanning and rectangular window of 7 samples in length. This window is inverted before the multiplication to have zeros in the central element and ones at both ends. This produces better results than just canceling (set to zero) the desired value. Figure 4.18(b) shows the reconstruction with angular gating, where actually the penetration is enhanced, being unfortunately still insufficient to recover the internal structures. However, the presence of a blood injury can be sensed thanks to the apparition of a dark spot at three o'clock on the border.

When interested into functional monitoring, differential imaging may be a solution to obtain reliable images of the evolution of a intracerebral blood hemorrhage. The subtraction of successive measurements taken at different times provides a low contrast scenario and allows to monitor the evolution of the bleeding. This is a very important issue because many hemorrhages stop spontaneously within the first hour. But bleeding can continue until the accumulated fluid disturbs or compress other brain structures, at which point is too late to drain the hematoma and avoid coma or death. This is implemented doing the subtraction between the scattered field measured at a certain time and a reference scattered field measured previously. This will be the data input of the reconstruction algorithm. Figure 4.19 shows the results of differential imaging. Figure 4.19(a) corresponds to a initial situation (hemorrhage of 5 mm in radius) and Figure 4.19(b) presents a growing hemorrhage of 15 mm in radius. For the first image, the reference measurement is a healthy brain and for the second one, the measurement with a stroke of 5 mm in radius.

Table 4.13 presents the metrics results for the reconstruction of the simple brain without losses and for the differential reconstruction of the brain with a 15 mm stroke. As it can be observed in the reconstructed images, the performance of the differential reconstruction is very accurate for such a simplified phantom, up to a point that no clutter is measured. The negative signal to mean ratio (SMR) value of the lossless model is because the maximum of the reconstruction is not due to the tumor. See Appendix C for a detailed description of the metrics.

	Lossless	Differential
SCR	3.25	∞
SMR	-0.46	21.02
FWHM	15.4	15
PA	3.41	0.52

Table 4.13: Metrics for the 3D simple brain model.
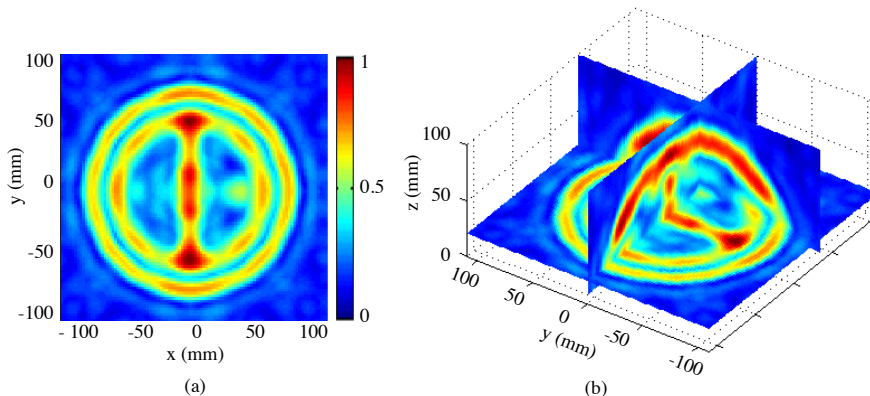
Figure 4.17: 3D MC reconstruction of the simple breast phantom without losses. (a) XY plane of the 3D cylindrical MC reconstruction, (b) 3D view.
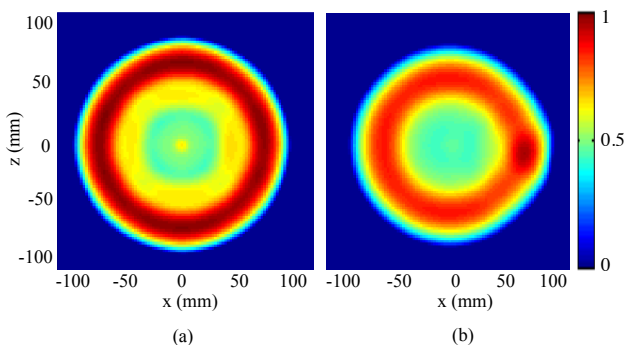
Figure 4.18: 3D MC reconstruction of the simple head phantom with losses. (a) XY plane of the 3D cylindrical MC reconstruction method, (b) XY plane of the 3D cylindrical MC reconstruction method with gating.

4.2.3 Voxeled breast and brain models

4.2.3.1 Breast cancer detection

Nowadays most of the advanced works on microwave imaging of the breast relay on the University of Wisconsin repository of 3D anthropomorphic breast models derived from MR images [85]. From the data supplied by the database, 3D models composed by 1 mm^3 voxels were extracted. For this study [CA4], we selected two different breast typologies, namely mostly fatty and scattered fibroglandular. The first may belong to a old woman, while the second may correspond to a younger woman. The tumor is modeled as a sphere of 5 mm of radius inserted in the vicinity of fibroglandular tissue. The complex permittivity values were calculated according to [85]. The acquisition system is a cylindrical array of both transmitting an receiving probes composed by $N_z = 10$ rings separated $\Delta_z = 10$ mm along z-axis. Each ring of radius
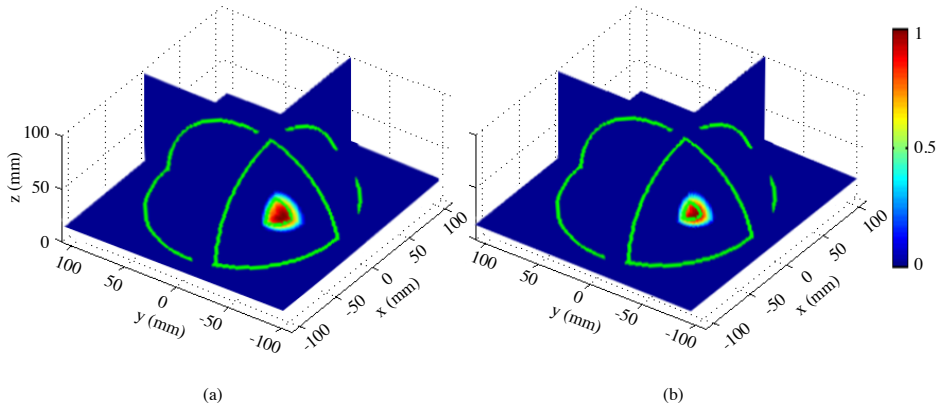
Figure 4.19: Differential 3D MC reconstruction of the simple head phantom with losses. (a) Hemorrhage of 15 mm in radius, (b) hemorrhage of 5 mm in radius.

$a = 90$ mm contains $N_\phi = 32$ angularly equispaced antennas, see Figure 4.20 and Table 4.14. The antennas and the breast model are immersed in a background medium with a complex permittivity similar to the breast fat average permittivity $\epsilon'_b = 5$. When reconstructing human organs composed by an internal volume surrounded by an external layer (skin) with substantial different average complex permittivities, the external medium is not able to simultaneously match both types of tissues. In these cases, it is a well-known practice to use a subtracting technique to compensate the effect of the skin layer, as explained previously in section 4.1.3. To give an idea of the order of magnitude of the permittivities and contrasts existing in such a breast models, Table 4.15 shows the complex permittivity and the magnitude of the dielectric contrast normalized to the maximum permittivity of the model for the main breast constituents at 2 GHz. The last column of the table is included to make the interpretation of the imaging results easier.
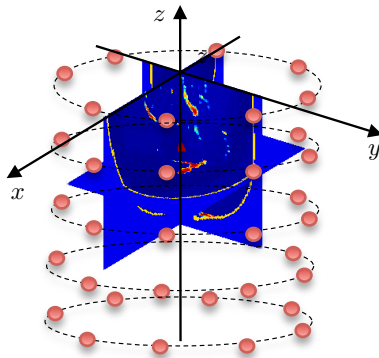
Figure 4.20: Geometry of the 3D MRI-derived voxeled breast phantom and the acquisition system.

Parameter	Value
a	90 mm
N_ϕ	32
Δ_z	10 mm
N_z	10
f	2-4 GHz

Table 4.14: Main parameters of the simulation of the voxeled brain model.

Tissue	ϵ'	σ	$|c(\vec{r}, f)/c_{max}|$
Background	5	0	0
Skin	39	1.3	0.618
Fat	2-7	0-0.1	0-0.036
Transitional	8-37	0.2-0.9	0.036-0.582
Fibroglandular	38-60	1-1.7	0.582-1
Tumor	55	1.6	0.909

Table 4.15: 3D voxeled breast average complex permittivities at 2 GHz [5, 69].

Mostly Fatty Breast   As a first example, class-1 numerical breast phantom 1 (mostly fatty, ID number 071904) has been selected as a healthy breast model [85]. To the previous phantom, a 5 mm tumor was inserted, configuring the full phantom, as depicted in Figure 4.21(a). Figures 4.21(b) and (c) show the reconstruction of the full phantom and the healthy phantom respectively and 4.21(d) show the differential reconstruction obtained by subtracting the scattered field measured for the healthy phantom to the scattered field of the full phantom. All the figures have been normalized to the same maximum contrast value. The white lines indicate the contours of the skin and the fibroglandular tissue of the original model, and the contour in black places the tumor. In this complex case, since the magnitude of the contrast exhibited by the tumor and the fibroglandular tissue are essentially the same, there is no mechanism to avoid the apparition of the fibroglandular tissue in the full phantom image, Figure 4.21(b). It can be observed that the tumor is clearly detected, as well as the larger glands. Concerning the tumor, a slight displacement is observed, specially along the z-axis due to the limited extend of the antenna array in this direction.

Scattered Fibroglandular Breast   The second example deals with class-2 numerical breast phantom 3 (scattered fibroglandular, ID number 010204). Again, a 5 mm spherical tumor was added in the vicinity of the glandular area, see Figure 4.22(a). Figure 4.22(b) shows that even if the considered phantom is more complex than the previous one, due to the higher amount of fibroglandular tissue, the proposed approach allows to reconstruct the tumor and the breast internal structures, this time, however, with a more noticeable shift.

Concerning the metrics, the usual ratios have been calculated showing better results for the mostly fatty breast. When the differential approach is used (full-healthy), the quality in terms of tumor response improves substantially with respect to the full reconstruction since the clutter and the neighboring tissues disappear. Due to the important contrast exhibited by the fibroglandular tissues (close to the tumor contrast), the signal to mean ratio (SMR) of the full phantom is very low and thus not very significant. For this reason, an additional ratio has been defined. The so-called full to healthy ratio (FHR) compares the mean value in two different volumes in the image. The FHR_{tumor} compares a volume with tumor with another one without tumor, and the $FHR_{no\ tumor}$ compares the same volume without tumor with another volume without tumor, as explained in Appendix C. For the mostly fatty breast, $FHR_{tumor} = 2.50$ and $FHR_{no\ tumor} = 0.97$. The results show that the tumor is clearly detected (over a 3 dB
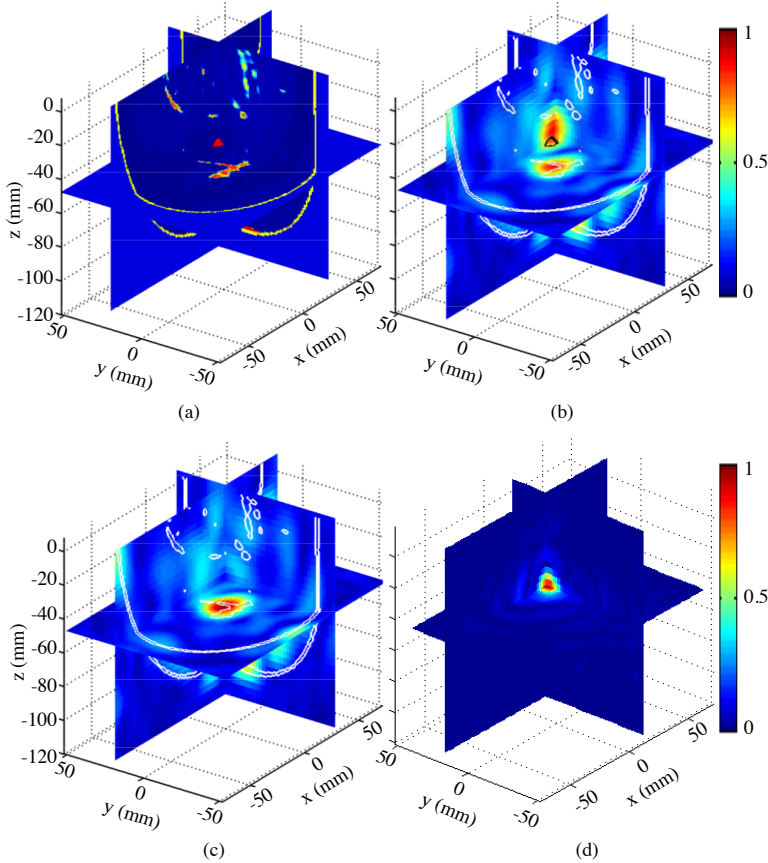
Figure 4.21: 3D MC reconstructions of the MRI-derived voxeled moslty fatty breast phantom. (a) Original normalized dielectric contrast, (b) normalized dielectric contrast of the full phantom, (c) normalized dielectric contrast of the healthy phantom, (d) normalized dielectric contrast of full-healthy phantoms (differential reconstruction).

threshold compared to the healthy case) without producing important disturbances to the rest of the breast. For the scattered fibroglandular breast, the FHR results are are slightly worse than the previous ones, but the detection is still over a 3 dB threshold. See Appendix C for a detailed description of the metrics.

4.2.3.2 Brain stroke detection

The voxeled brain model was extracted from an enhanced anatomical model of a 6 year male child from the Virtual Family [88]. The model is based on MR images of healthy volunteers. It is composed by 9 different materials representing the different brain tissues: grey matter, white matter, blood, cerebellum, CSF, skin, muscle, nerve and bone, as shown in Figure 4.23. The dielectric properties of the brain tissues at each frequency were taken from the Gabriel database [5] and are summarized in Table 4.18. To simulate a hemorrhage a blood sphere of
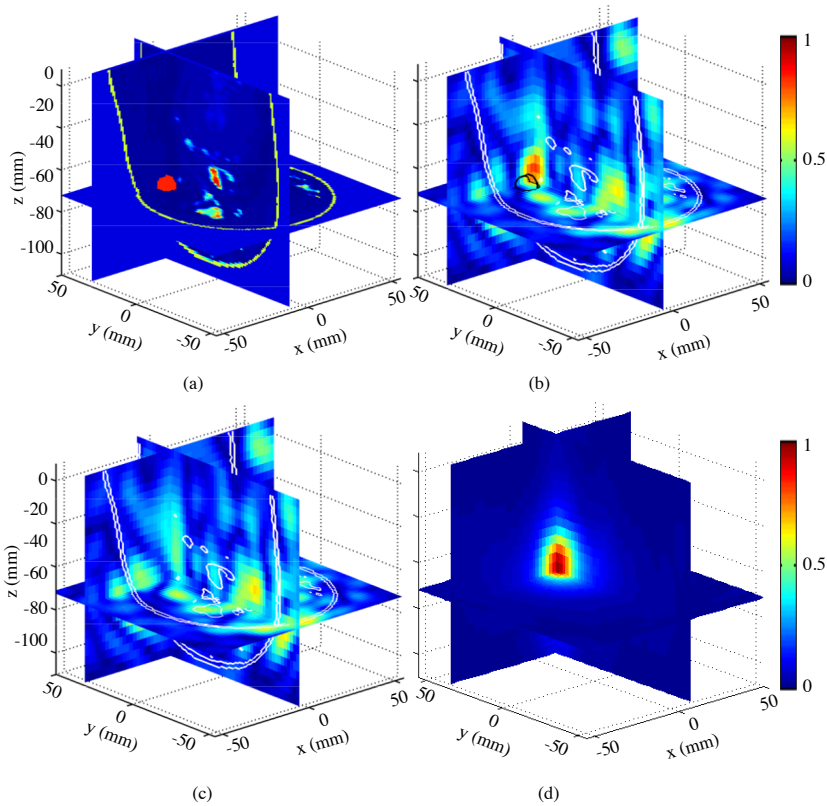
Figure 4.22: 3D MC reconstructions of the MRI-derived voxeled scattered fibroglandular breast phantom. (a) Original normalized dielectric contrast, (b) normalized dielectric contrast of the full phantom, (c) normalized dielectric contrast of the healthy phantom, (d) normalized dielectric contrast of full-healthy phantoms (differential reconstruction).

	Full Fatty	Full-healthy Fatty	Full Fibro.	Full-healthy Fibro.
SCR	8.97	16.99	5.96	19.47
SMR	4.18	11.09	4.91	12.94
FWHM	12	8	6	8
PA	2.83	4.47	5.10	3.16
FHR$_{tumor}$	2.50	-	2.20	-
FHR$_{notumor}$	0.97	-	1.03	-

Table 4.16: Metrics for the 3D voxeled breast model.

5 mm^3 was included inside white matter. The background medium was selected to match the predominant tissue in the brain that is the white matter, leading to $\epsilon_b' = 40$ [CA3]. The scanning system consists of both transmitters and receivers placed along the surface of a cylinder of $a = 110$ mm in radius, composed by $N_z = 25$ rings of $N_\phi = 55$ probes separated $\Delta_z = 10$ mm along z-axis, as summarized in Table 4.17. The operating frequency range was selected between 1 and 2 GHz for its good compromise between penetration and resolution inside the brain. Due to the huge computational cost involved in the simulation of brain, which is much bigger than the breast, the simulation time was reduced by relaxing the discretization. Accordingly, the brain model was simplified by creating uniform voxels of 4 mm^3.
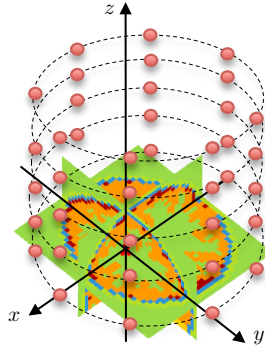
Figure 4.23: Geometry of the 3D voxeled brain phantom and the acquisition system.

Parameter	Value
a	110 mm
N_ϕ	55
Δ_z	10 mm
N_z	25
f	1-2 GHz

Table 4.17: Main parameters of the simulation of the voxeled brain model.

Tissue	ϵ'	σ	$|c(\vec{r}, f)/c_{max}|$
Background	40	0	0
Skin	38	1.26	0.069
Bone	11	0.31	1
Muscle	53	1.45	0.448
Nerve	30	0.91	0.345
Cerebellum	45	1.82	0.172
CSF	67	3.07	0.931
Gray matter	49	1.51	0.310
White matter	36	1.00	0.138
Blood	59	2.19	0.655

Table 4.18: 3D voxeled brain average complex permittivities at 2 GHz [5].

As done in 3D brain simplified model, a differential imaging strategy has to be used in or-

der to penetrate the successive highly contrasted layers of the breast. Figures 4.24(a)-(f) show the dielectric properties and the reconstructed normalized dielectric contrast for a differential mono-frequency reconstruction at 1 and 2 GHz. The differential technique consists on the subtraction of the measured scattered field for a brain with a 5 mm^3 blood hemorrhage and the measured scattered field of a healthy brain. It can be observed that even with a single frequency it is possible to obtain a correct geometrical reconstruction. Figure 4.24(g) demonstrates that by using MC multi-frequency technique, the image quality improves with respect to the mono-frequency case. In particular it can be observed that the small artifacts surrounding the blood spot have been canceled and the image is more uniform. Note also that the resolution of the MC image is basically the same obtained for the highest frequency of the band. Table 4.19 summarizes the results of the metrics and corroborates the trends observed visually. See Appendix C for a detailed description of the metrics.

	1 GHz	2 GHz	MC
SCR	19.96	10	11.25
SMR	9.85	10.61	9.98
FWHM	8.6	6.6	8.8
PA	9.01	7.61	9.15

Table 4.19: Metrics for the 3D voxeled brain model.

4.3 Concluding remarks

This chapter addressed the numerical assessment of the algorithms formulated in previous chapter. The first part was devoted to study the performance of 2D circular MC algorithm. Given the limitation of 2D algorithms to uniform objects in the third dimension, the 2D validation, was aimed to study several issues that could be easily extrapolated to 3D. Accordingly for a simplified breast phantom, a set of parametric studies were performed to determine the best background medium, the minimum detectable tumor size and the robustness to inhomogeneity.

- Regarding the matching medium, the strategy that reported better results was to match the real part of the permittivity of the most abundant tissue in the imaged organ. The imaginary part should be small in order to reduce the losses. In the final image, a bad matching was translated in the apparition of a central artifact and the highlighting of the breast surface. From the parametric study could be concluded that if the matching was not perfect, it is always better to use a lower permittivity background medium, however this has a detrimental effect on the resolution.

- The smallest detectable tumor was 2 mm in radius, below the diffraction limit. This was possible thanks to the data redundancy provided by the multi-view and multi-frequency combinations.

- Since the breast tissue is not homogeneous, a $\pm 10\%$ and a $\pm 30\%$ random inhomogeneity was added leading to an increment in the internal breast artifacts comparable to the tumor response when it was smaller than the size of the inhomogeneity.
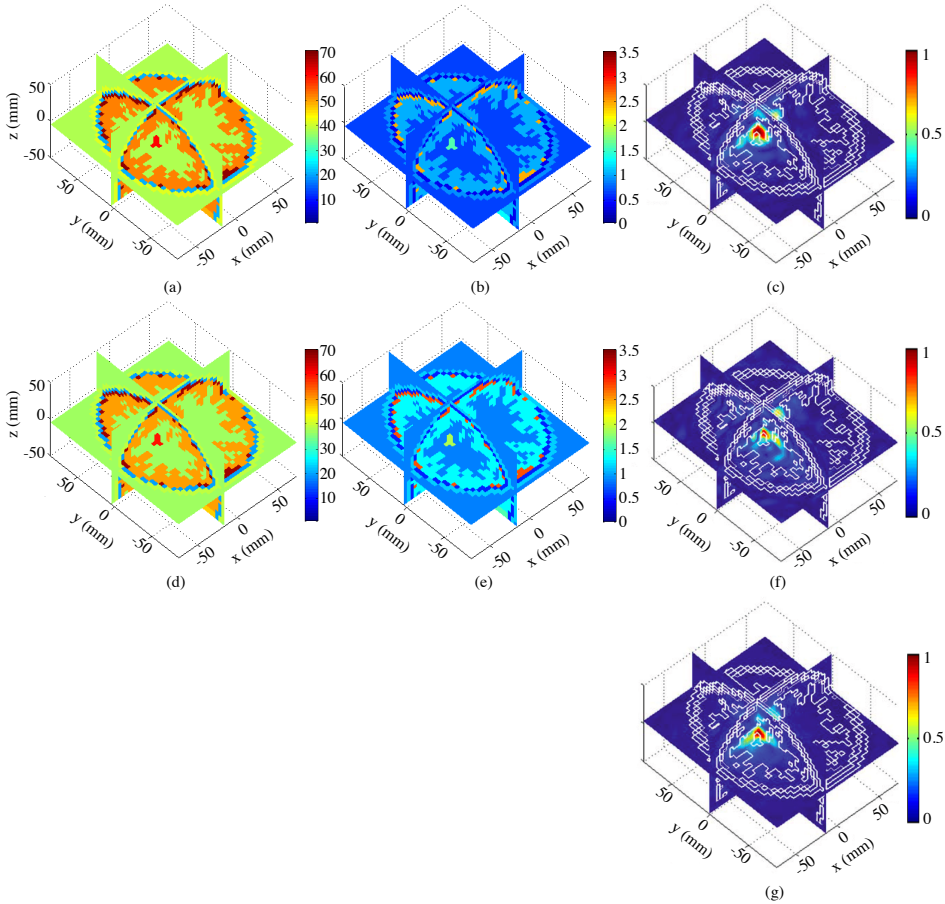
Figure 4.24: Dielectric properties and MC reconstruction of the 3D voxeled brain phantom. (a) Relative permittivity at 1 GHz, (b) conductivity at 1 GHz, (c) 3D reconstruction of the normalized dielectric contrast at 1 GHz, (d) relative permittivity at 2 GHz, (e) conductivity at 2 GHz, (f) 3D reconstruction of the normalized dielectric contrast at 2 GHz, (g) 3D MC reconstruction of the normalized dielectric contrast between 1-2 GHz.

Next, more relevant breast phantoms of increasing complexity were reconstructed. The main problems observed were due to the skin layer and the existence of glandular tissue close or surrounding the tumor. Skin produced problems due to its large dielectric contrast with respect to that of the matching medium (matched to the adipose-dominated breast tissue). Thus, skin subtraction techniques were proposed reporting good results. Concerning the glandular tissue, its inclusion had different effects depending on its location with respect to the tumor and the skin. When it was very close to the skin, it produced artifacts that illuminate the skin contour at the vicinity. When the tumor was completely inside glandular tissue, it was not possible to discriminate between the tumor and the glandular tissue responses but the tumor was still sensed.

Still for the 2D system, the so-called FDL technique was presented aimed to provide quantitative performance to the simple and computationally efficient MC algorithm using a frequency stepped iterative scheme. At the current stage of development, it is able to reconstruct quantitatively the real part of the permittivity with a fair accuracy.

For the 3D cylindrical system, simple but also realistic voxeled breast and brain models were reconstructed. The study of simple models was aimed to determine the system parameters, specially the minimum number of antenna rings along the main cylinder axis. The conclusion is that the acquisition cylinder must exceed the imaged object, but beyond this point the reconstruction does not change significantly.

Brain stroke detection is obviously a very challenging application given the layered structure with really different contrasts combined with the existence of highly lossy liquids inside the brain. If losses were not considered, a bleeding volume inside the most internal brain layer could be detected. However, when losses were considered it was not possible with a direct approach. Instead, a differential technique must be used, consisting on subtracting two consecutive measurements having a change in the blood volume. By doing so, the change in the bleeding was sensed and thus appeared in the image.

The same trends were observed when reconstructing realistic MR derived voxeled breast and brain phantoms considering also the frequency dispersion of the complex permittivity. For the breast phantom, the skin subtraction was needed to be able to penetrate and detect the tumor. For the brain phantom, the skin subtraction was not enough and a differential approach had to be used. This differential approach consisted of subtracting the measurement of the brain state at a particular moment, to a previous measurement in the same conditions, but containing a change in the bleeding volume. Also, due to the higher losses of the brain constituents, the frequency range used to reconstruct the brain was lower than that of the breast, since higher frequencies were not able to penetrate the brain. Finally a detection quality ratio was defined and the results of the voxeled breast phantom were quantified showing a detection over the 3 dB threshold.

5

EXPERIMENTAL RESULTS

T HE last chapter collects the experimental work carried out during the thesis. The evolution of the experimental systems is parallel to that of the algorithms presented in the previous chapter. This work was envisaged as an experimental validation of the algorithm, rather than as a proposal of a clinical-ready scanning system. The main objective of this chapter is to demonstrate the algorithm robustness to real measurements in terms of noise, interference and multipath corruption. Accordingly, a virtual array approach based on a single transmitting and receiving antenna that are moved thanks to a automatic positioning system is used. By doing so, the system is more flexible and can be easily changed and upgraded. At the same time the algorithm evolve, more complex experimental systems were build: with more degrees of freedom, matching liquid, etc. The same trend also applied to the phantoms: from the uniform cylindrical phantoms to breast mimicking ones.

The first part of the chapter is devoted to the 2D experimental systems using air and water as background medium. The second part deals with the 3D cylindrical systems. The chapter ends with a design proposal of an arrayed system devoted to reduce the acquisition time considerably.

5.1 Microwave imaging system components

The essential parts of an experimental system for active microwave imaging are the acquisition system and the signal generation and reception. The acquisition system consists of an array of sensors which can be either real (when all the sensors exist simultaneously) or virtual (when the different sensors are emulated by the movement p.e. of a unique sensor). Depending on this, a multiplexing system to select the active antenna from the array, or otherwise, a positioning system to move the unique antenna following the measurement surface, are needed for the transmitting and receiving ends. For the signal generation and reception a VNA is used. The whole measurement procedure is remotely and automatically controlled by a computer running Matlab scripts. Figure 5.1 shows the block diagram of a generic active microwave imaging system.
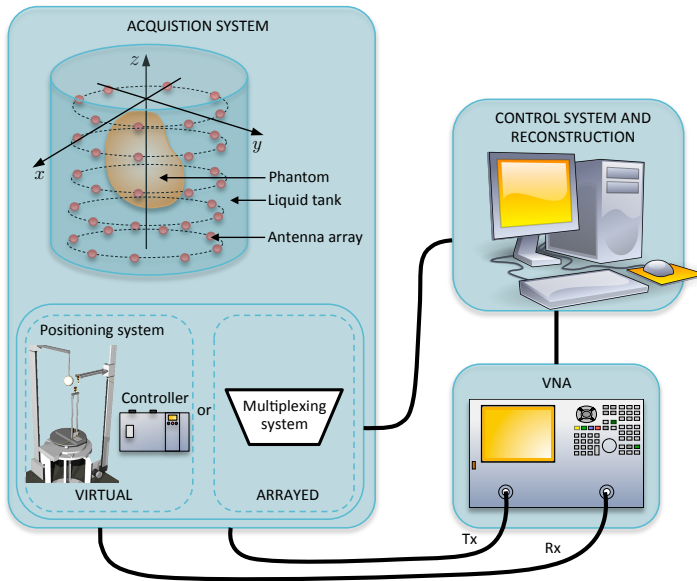
Figure 5.1: Block diagram of the experimental system for active microwave imaging.

5.1.1 Acquisition system

Generally, each experimental imaging system is designed to operate with a certain imaging algorithm. In the case of radar systems, the geometry of acquisition is not limited for the algorithm and thus it could be adapted to the shape of the imaged body. For instance, in breast cancer detection, the hemispherical is the most optimal arrangement, since it allows to illuminate and sense from all the possible directions [47]. Conversely, in tomography, the commonest array arrangement is the planar and circular (2D) or cylindrical (3D), that unlike hemispherical geometries does not pose difficulties due to the polarization change depending on the antenna position. These geometries are illustrated in Figure 5.2. Regarding the implementation of the system, both real and virtual arrays of antennas (the array is composed by only one trans-

(a) monostatic planar surface acquisition [16, 105]

(b) bistatic planar surface acquisition [63]

(c) hemispherical multistatic sensor array [47, 60]

(d) monostatic cylindrical scan [95]

(e) cylindrical tomography [9, 42]

(f) cylindrical tomography with virtual array [J3]
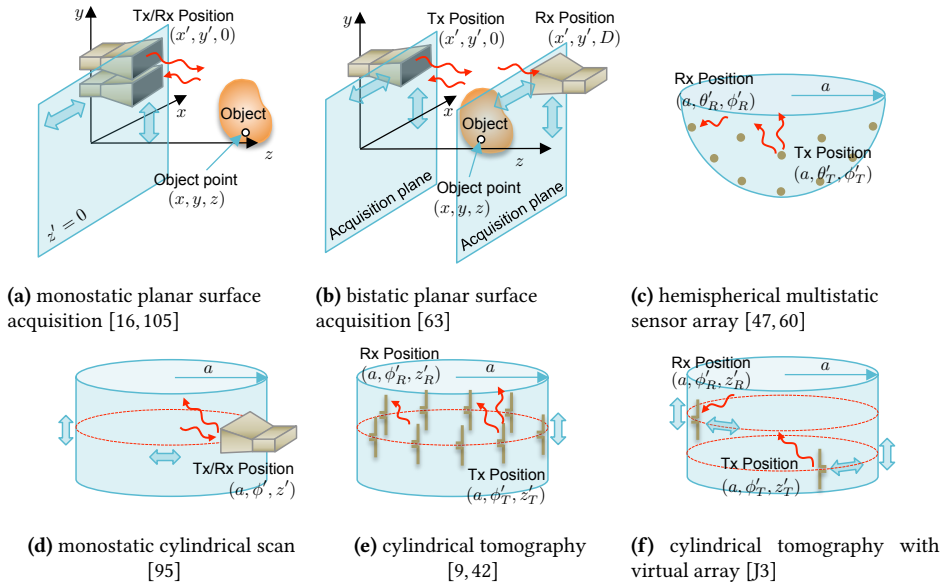
Figure 5.2: Illustration of acquisition surfaces used in microwave imaging of the breast.

mitting and one receiving antennas that are moved at all the sensing points) can be used, see Figure 5.2. Moreover, contacting and non-contacting strategies (the antennas are just on the skin or are separated a certain distance) have been proposed. Contacting systems [101], would be more similar to ultrasound applicators, where the medicine professional guides manually the antenna on the desired area. This system is operator-dependent but does not require matching liquid. Non-contacting systems consist of an array of a certain shape placed in a container full of matching liquid. The antennas are not in contact with the inspected body, that is immersed in the liquid and surrounded by the array. The use of a matching liquid could lead to several challenges such as maintenance or perturbations in the liquid during the measurement. Another original contribution is an intermediate solution between the previous two. In consists of a fixed array of a certain geometry that thanks to an aspiration system allows to put the inspected body in full contact with all the array elements [104].

5.1.1.1 Arrayed system

This system consists of an array of antennas conveniently governed by a multiplexing mechanism with a predefined switching sequence. The multiplexing system is aimed to forward a single RF input signal to one of many RF output lines connected to the antennas. For the receiving end, the multiplexing system directs the signal received by one of many antennas to a single RF output. This approach faces a number of challenges such as coupling between elements, limited size of each element; but permits a real time performance, and thus was the basis of the first clinical trials [17, 42].

5.1.1.2 Virtual array

The virtual antenna array approach consists of moving independently a transmitting and a receiving antenna by means of a computer controlled positioning system [106–108]. This avoids the coupling between the antennas and the complexity of the multiplexing system, however it is no suitable for a real time system due to the prolonged duration of the measurement. For these reasons, the virtual array approach is used in this chapter for the validation of the algorithms. The goal is not to provide a clinical-ready system, but a flexible assessment platform for the algorithms developed in this thesis. Such a positioning system is composed by moving stages and the controllers.

Moving stages Two concentric but independent rotary stages are needed for synthesizing a circular array for both the transmitting and receiving antennas, see Figure 5.3. The main features of the rotary stages RT-5-10 from Newmark Inc. [109] are summarized in Table 5.1. For the cylindrical array, two additional linear stages are required. The linear stage is a custom-built device resulting from the assembly of a ZSH87/2 stepper motor from Phytron [110] and a 1.5 m linear stage from item.

Feature	Rotary stage	Linear stage
Repeteability	0.0014°	-
Resolution	0.0001°	0.04 mm
Accuracy	0.017°	-
Gear ratio	72:1	60:26
Motor	Nema 17	ZSH87/2
Maximum load	45.46 Kg	-
Maximum input speed	$30°/s$	-
Travel	360°	1.5 m
Maximum current	1.2 A	2 A

Table 5.1: Most relevant technical features of rotary and linear stages.

(a) (b)
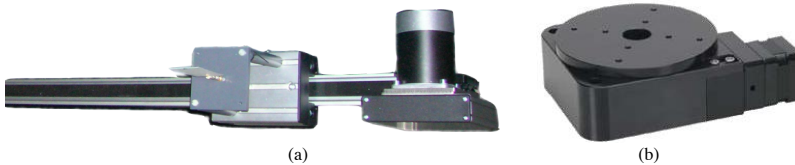
Figure 5.3: Detail of the (a) linear stage, (b) rotary stage.

The most important parameter of the moving stages is the positioning accuracy. Since for each position of the transmitting antenna, the receiver has to move at all the measurement

points, a small error in the positioning, is translated to a large cumulative error at the end of the measurement. Since the algorithm assumes a fixed antenna configuration, a non-accurate antenna positioning during the measurement produces important artifacts in the reconstruction. A common criteria is to define a minimum required accuracy of $\Delta_x < \lambda/100$, which for a maximum frequency of 4 GHz leads to $\Delta_x = 0.043$ mm. Regarding the linear stage, the only available parameter is the resolution (0.04 mm), that is slightly lower than Δ_x. In terms of mechanical displacements, resolution stands for the minimum incremental step produced by the motors, instead, accuracy stand the difference between a commanded position and the actual position. Since accuracy is normally worse than the resolution a set of preliminary imaging tests were performed to ensure the applicability of the linear stage reporting good and repeatable results [111]. For a rotary stage, the criteria of $\Delta_x < \lambda/100$ corresponds to $\Delta_{phi} < \frac{c_0}{100af_{max}}$. If Δ_{phi} should be lower than the accuracy (0.017°), this leads to a maximum radius of the circular array of 2.5 m, which is enough for medical imaging purposes.

Controllers The controllers GCD 93-70 are stand-alone devices that interface with the moving stages. From a instruction given by a computer they generate the proper pulsed signals to manage the step-by-step motors of the moving stages.

5.1.1.3   Probe antennas

The probe antennas are an essential part of an imaging system. They have decisive influence on the limitations of the system, particularly on its sensitivity. There is a large body of literature concerning the design of probe antennas for breast imaging with microwaves and a detailed discussion is not going to be given here. Typical performance measures include: impedance match, radiation efficiency, focusing ability or object coverage, small size, dual independent linear polarization and isolation from nearby interference. Several antenna types have been proposed such as dipole antennas [112], dielectric resonator antennas [113], patch antennas [114, 115], slot antennas [115], Vivaldi antennas [116] and horn antennas [117, 118].

The antennas used for the measurements presented in this thesis are planar elliptical dipoles (they could be also introduced as quasi-monopoles). They are composed by two radiant elliptic elements fed by a coplanar waveguide (CPW) from the lower part. The illuminating signal generated by the network analyzer comes through a coaxial cable, which is connected to the CPW via subminiature version A (SMA). The lower arm, which has been retreated forming an ellipse around the CPW, plays the ground plane effect and acts as a balun. Figure 5.4 shows a detail of the antenna with the most important dimensions. This antenna is commonly used in UWB applications since provides a good matching that varies gently over the bandwidth of interest and a horizontal radiation pattern almost omnidirectional at all frequencies. This can be clearly seen in Figure 5.5 that presents the E and H-planes, the polarization plot[1] and the evolution of the S_{11} parameter over the frequency.

---

[1]The polarization plot presents the hole sphere in a unique circle where the center of the circle corresponds to the north pole of the sphere and the south pole has been expanded and corresponds to the perimeter of the circle. Then, θ angle increases according to a radius from the center of the circle ($\theta = 0°$) to the edge ($\theta = 180°$), and ϕ varies along the circumference between 0° and 360°.
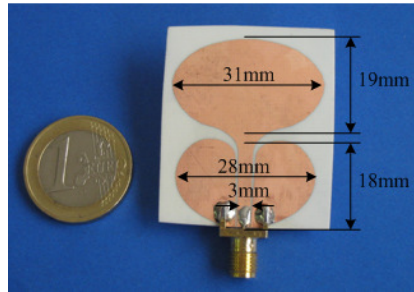
Figure 5.4: Planar elliptical dipole antenna.

5.1.1.4 Tissue mimicking materials and matching liquids

Having a good permittivity matching between the imaged object and the antennas is crucial as showed in 4.1.2.1. In the experimental work carried out in this thesis, both simple low permittivity phantoms and more realistic human-mimicking phantoms were studied. For the first experiment, no matching medium was used since the contrast with air was moderate and does not produce significant alterations to imaging result. For the second, a matching liquid was required.

For non-contacting screening systems, which is the case of this thesis, the matching liquid is contained in a tank where the antennas and the phantom are also immersed. Thus, a liquid matching medium is desirable. Research into matching liquids is normally linked to that of tissue mimicking materials to create phantoms, which is actually what is willing to match.

Early studies on tissue mimicking mixtures were focused in a particular application and they were only valid for a very restricted frequency band (narrowband). In [119], high-water content tissues were modeled with a mixture of TX-150 (a gelling agent), polyethylene powder, water and sodium chloride (NaCl) at frequencies between 13.5-2450 MHz. Bini et. al. [120] used polyacrylamide gel as the chief ingredient to obtain a material with optical transparency and gel-like mechanical properties, however having very limited shelf life. These materials involve complicated fabrication methods as well as chemicals that may be difficult to obtain. [121] used a dough containing flour, oil and a saline solution to model low water-content tissues at 451 MHz. Subsequently [122] and [123] introduced the gelatin-based materials to simulate high-water content tissues from 10 to 50 MHz. Gelatin-based materials are very attractive for its low-cost, ease of fabrication and molding capacity. The main challenge is to achieve long-term stability.

The above materials would be difficult to use in a wideband application since a different material composition would be required for every frequency band of interest. With the advent of broadband systems, research on tissue mimicking materials was focused on broadband tissue simulants. By varying the relative proportions of the ingredients a family of tissues, ranging from the adipose- to the water-dominated tissues, could be simulated. In [124], different mixtures of corn-syrup were used and [125] proposed a mixture of surfactant Triton X-100 and deionized water. The major drawback of these mixtures for building phantoms is that they are liquids. Consequently, they must be poured into thin containers that do not disturb the signal significantly and have a certain shape. For this reasons, liquid mediums were normally used for 2D measurements, where simply very thin capped tubes could be used as containers [125]. Re-
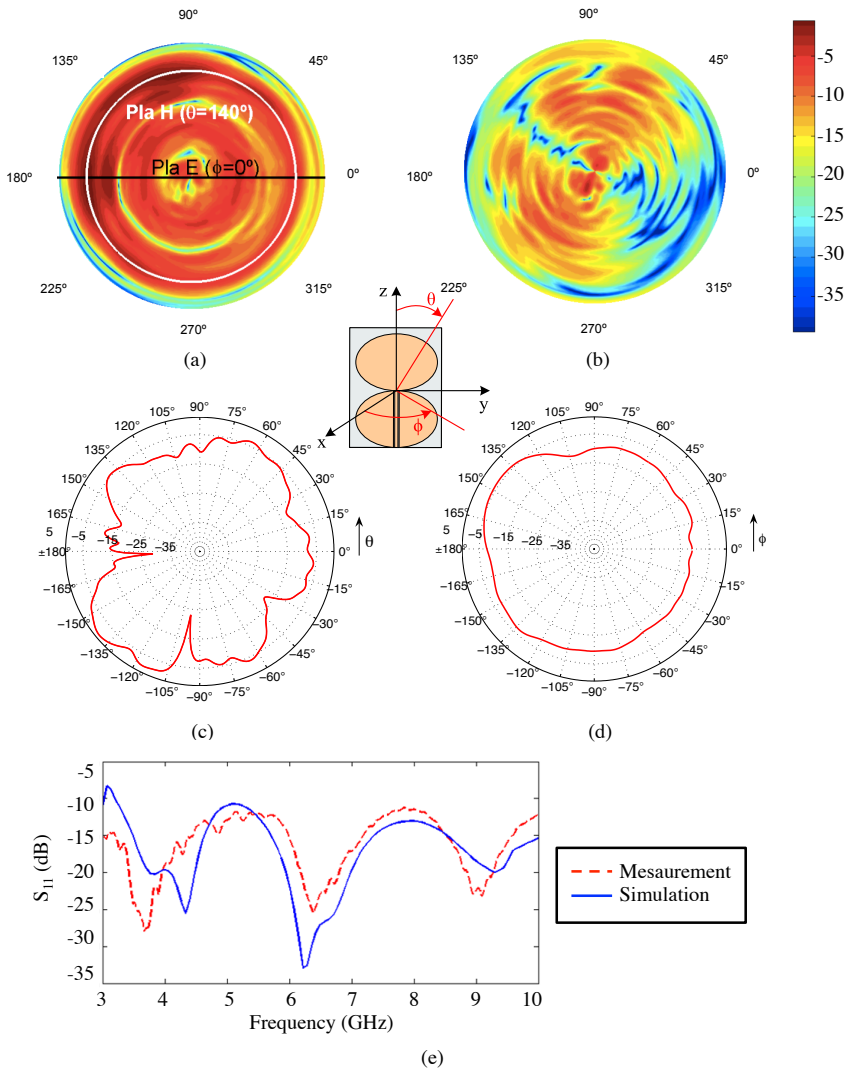
Figure 5.5: Performance of the planar elliptical dipole antenna. (a) E_θ at 3 GHz, (b) E_ϕ at 3 GHz, (c) E-plane at 3 GHz, (d) H-plane at 3 GHz, (e) S_{11}.

cently, the trend on tissue mimicking materials is to produce gelatin-based materials that can be molded directly after preparation and they keep the same shape when removed from the mold. Accordingly, in [126], the authors succeeded in creating a single polyacrylamide gel material covering the frequency range between 500 MHz and 3 GHz. [127] presents a solid conductive plastic that simulated the dielectric properties of muscle from 300 to 900 MHz that could be molded into any arbitrary shape. More recently, Lazebnik et. al. [128] proposed a sophisticated wideband breast phantom based on a mixture of kerosene and safflower oil together with P-toluic acid and n-propanol, deionized water, surfactant and formaldehyde. Based on this, a very similar recipe was proposed in [129] and [130].

As explained before, depending on the system geometry, i.e. 2D, 3D, etc., different phantoms and matching mediums are considered. Hence in this thesis, the exact phantom and matching liquid composition will be explained in detail inside the section corresponding to each experiment.

5.1.2   Types of signals

The microwave measurements can be carried out either in the frequency domain or in the time domain. The frequency-domain measurements are typically S-parameter frequency sweeps in a wide band performed using a VNA. Both the magnitude and phase information are available for the reconstruction process. The time-domain measurement use short pulses that can be generated in several ways. One alternative is to use the time-domain option of the VNA (where the pulse responses are synthesized from wide-band frequency sweep measurements using the inverse Fourier transform). Chirp-radar measurements with custom built hardware [131] or high-speed oscilloscopes and arbitrary waveform generators [132] are also considered.

Microwave imaging setups can also be differentiated on the basis of weather they acquire reflected or transmitted scattered fields, or both. This is also related to the antenna configuration i.e. monostatic, bistatic or multistatic. Traditionally, radar imaging utilizes reflected signals (backscatterer), where often the same antenna is used to transmit and receive (monostatic radar), see Figure 5.2d. Conversely, some medical imaging modalities, and not only based on microwave signals, use transmitted signals such as film x-rays. However, radar-based systems used in microwave imaging, incorporate sensor arrays, since a single backscatterer is insufficient to image the complex living tissues [102], see Figure 5.2c [17]. This is also the case of the most tomographic systems [9, 42] (Figures 5.2e and 5.2f). Notice that for a circular or cylindrical antenna array, except for the diametrically opposed antennas, both transmitted and reflected scattering parameters are captured. Hence they are commonly called bistatic systems, rather than systems working in transmission or in reflection.

The system addressed in this thesis, works in frequency domain and processes both transmitted and reflected scattering parameters, as will be shown later on in this chapter. An Agilent PNA E8362B is used for this measurements. Before the measurement, the system is calibrated using the Thru Reflect Line (TRL) method to cancel the effects of the long cables and transitions used in the measurement. For each reconstruction, two consecutive measurements are taken. The first consists in a full measurement, that is a measurement of the complete scenario, the second, namely empty measurement, is the same as the full measurement but without the presence of the object under test. In this way, the scattered field can be obtained by subtracting the full and the empty measurements. Moreover, by doing so, all the effects which are common in both measurements, such as reflections with nearby objects or with the own acquisition system, are canceled.

5.1.3   Sensitivity, noise and safety assessment

Before proceeding with the experimental validation of the algorithm, three main issues have to be considered: the system sensitivity, the permitted noise floor and the compliance of safety exposure levels.

The sensitivity study consists on determining the minimum level of received power that

will arrive to the receiving antenna given a certain input power. Establishing a typical VNA sensitivity of -85 dBm, the minimum permittivity contrast can be calculated leading to $\epsilon_b' \cdot |c(\vec{r}, f)| = 0.0013$. Such a small contrast indicates that the sensitivity will not be the limiting issue in the measurements, since in the worst scenario the contrast between tumors and the surrounding tissue is of the order of 10%. Appendix D shows the detailed calculation.

In the experimental measurements, the desired signal will be contaminated by noise. Up to now, the noise was not considered in the simulations. However before proceeding with the measurements, it is worth determining which is the theoretical permitted noise floor to obtain a correct reconstruction. To this aim, a simulation with an additive noise power to produce a certain signal to noise ratio (SNR) is performed and then reconstructed. The results obviously will depend on the simulated scenario. For a realistic scenario such as the 3D voxeled mostly fatty breast (section 4.2.3.1), which is one of the most demanding cases, the minimum permitted SNR is -10 dB when working with the differential field (full - empty measurement). Such a small vaule is thanks to the antenna gain given by the large amount of antennas that configure the acquisition array. When using the absolute field (full measurement) instead of the differential field, the minimum SNR increases up to 50 dB. This means that the sensitivity of the VNA must be larger than -60 dBm (for an input power of 0 dBm) to obtain a reconstruction free of noise corruption. As said, the VNA with a typical sensitivity of -85 dBm is suitable for the measurements. Appendix D includes the full derivation of the minimum SNR.

Regarding the safety regulations with respect to the maximum exposure levels, the SAR is calculated and compared to the maximum level established by the IEEE Standard C95.1. To do so, a simplified breast phantom illuminated by a half-wavelength dipole with an input power of 0 dBm at 2 GHz is simulated. The results indicate that the maximum SAR level (1mW/kg) is far below the limit established by the standard (10W/kg). Appendix D shows the simulation results with more detail.

5.2   2D experimental results

This section is devoted to the 2D circular experimental imaging system. The first part comprises the construction of the measurement system based on a virtual array approach. The system works in air, thus limiting the range of objects that can be imaged to those having a small contrast with air. Thus, considering air as background medium, the permittivities of the phantom constituents will be scaled to obtain similar contrasts as real breasts. Moreover, the phantoms must be electrically large and uniform in the z direction to be treated as 2D without committing a significant error. Finally the phantom will be measured and reconstructed using 2D circular MC algorithm.

The second part of the section deals with the introduction of a matching liquid. For this first experiment, water is used for being inexpensive and easily obtainable. Again, such a high permittivity medium limits the objects that can be penetrated to those having a comparable permittivity to that of the water. Since obtaining a material with such a high permittivity is difficult, this part is only focused on the detection and the correct determination of the object shape and position. To this aim, two different systems will be used. One is the modified version of the former system to fit a big water container where the antennas and the object will be immersed. The second is an arrayed system housed at Chalmers University of Technology in Sweden. With both systems simple 1 rod or 2 rods scenarios will be reconstructed using

the 2D magnitude combined algorithm. The results will be compared to those obtained by the iterative time domain inversion algorithm developed at Chalmers [133]. This study was performed during a collaborative work with Chalmers University. [CA6] includes the results obtained that are reproduced herein.

5.2.1 2D circular measurements in air

5.2.1.1 Acquisition system

In order to deal with general non-centered non-symmetric 2D objects, the rotary system has to provide two degrees of freedom allowing the independent rotation of the transmitting and receiving antenna. This is achieved using two high-resolution rotary stages that share the same rotating axis; the object under test and the receiving antenna are rotated concentrically and independently while the transmitting antenna remains in a fixed location, see Figure 5.6. This configuration allows to synthesize two circular virtual arrays for the transmitting and the receiving antennas. Each virtual antenna array is composed by $N_\phi = 128$ measurement points uniformly distributed along a circumference of 75 and 90 mm in diameter, for the receiver and transmitter respectively, completely surrounding the object under test. Table 5.2 summarizes the system main parameters. By capturing the received signal in all measurement positions provided by the combined movement of the receiver and the object, a complete 2D cross-sectional slice of the object can be obtained.
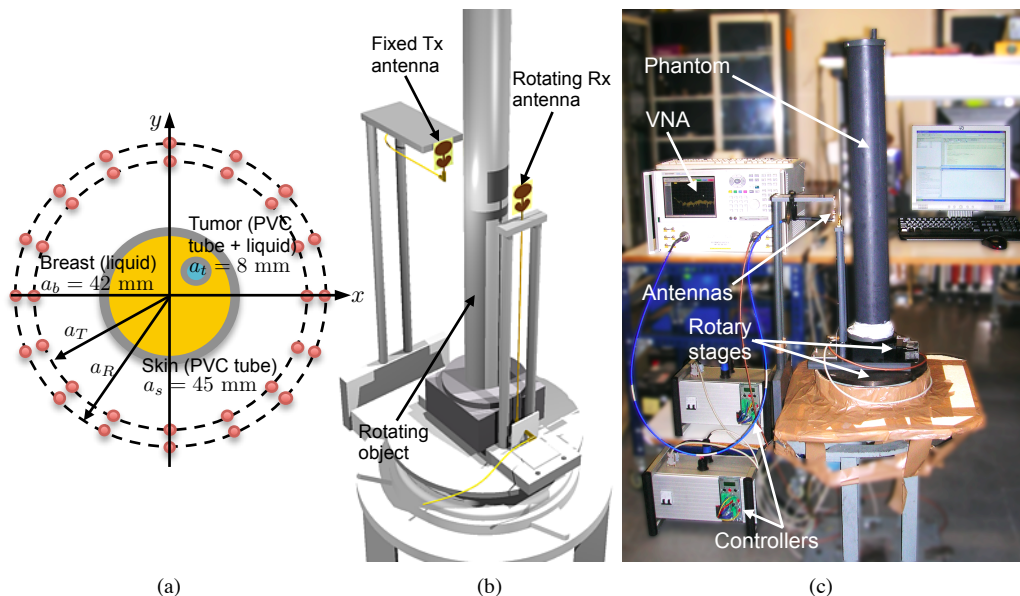
Figure 5.6: 2D circular experimental system in air. (a) Cross-sectional slice of the system, (b) scheme of the acquisition system, (c) photograph of the whole measurement system.

Parameter	Value
a_T	75 mm
a_R	90 mm
N_ϕ	128
f	3-10 GHz

Table 5.2: Main parameters of the 2D circular experimental system in air.

5.2.1.2 Phantom

The phantom built for this system uses easy-to-find household materials such as water and sunflower oil. Since all the ingredients are liquid, a holding structure is needed. To this aim, a 3 mm thick PVC tube of 45 mm in radius is used. At the same time it holds the breast mimicking liquid, the PVC tube emulates the skin. Inside this tube, another thinner PVC tube of 8 mm of radius and 1 mm of thickness, was placed to contain the liquid corresponding to the tumor, see Figure 5.6(a). Two different scenarios are considered. In the first, the larger tube is left empty and the thinner is filled with water. In the second, the larger tube is filled with sunflower oil and the thinner with water. Furthermore, the particular mechanization of the phantom allows to use a set of privileged positions for the breast as well as the tumor, allowing a total of six different configurations. The materials used for the phantom compared with the real values are summarized in Table 5.3.

Tissue	Composition	ϵ'	σ	$|c(\vec{r}, f)/c_{max}|$	Real $|c(\vec{r}, f)/c_{max}|$
Background	Air	1	0	0	0
Skin	PVC	2.7	0.025	0.021	0.34
Breast	Air	1	0	0	0.34
	Sunflower oil	2.5	0.017	0.018	
Tumor	Water	83.4	2.90	1	1

Table 5.3: Complex permittivities of the phantom constituents for the 2D circular measurements in air at 3 GHz [66].

5.2.1.3 Results

First scenario: Air breast, water tumor The first scenario consists of a non-centered hollow PVC tube with a thinner PVC tube filled with water placed inside the first. Figure 5.7(a) shows the geometry of the first scenario and Table 5.3 summarizes the dielectric properties. Figures 5.7(b) and 5.7(c) show the 2D MC reconstructions, corresponding to the numerical simulation of the scenario and the measurement. A very good agreement between measurements and simulations is reported demonstrating the robustness of the algorithm to experimental issues such as noise and multi-path corruption. Note that the measurements were performed in

the laboratory, not in a protected environment such as an anechoic chamber.
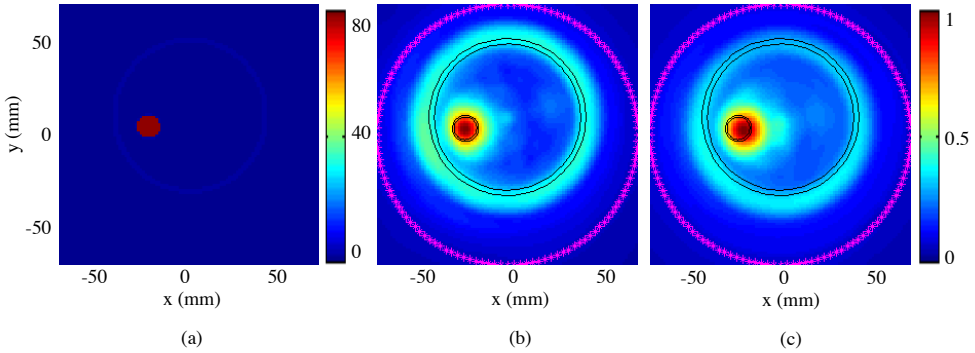
Figure 5.7: MC reconstruction of the air breast + water tumor measured with 2D circular experimental system in air. (a) Original permittivity profile, (b) 2D MC reconstruction of the simulation, (c) 2D MC reconstruction of the measurement.

Second scenario: Oil breast, water tumor In this case the arrangement of the scenario is the same as the previous one, but the PVC tube was filled with sunflower oil, refer to Table 5.3 for the dielectric properties of the phantom and to Figure 5.8(a) for a sketch of the scenario. Note that this phantom is more similar to the real breast in terms of normalized contrast. Figures 5.8(b) and 5.8(c) show the MC reconstruction of the simulation and the measurement of the second scenario respectively. Two main conclusions can be derived from these images. Firstly, the presence of the oil inside the larger tube produces a displacement of the tumor. This is due to the supposition of a uniform media equal to the background made by the algorithm. This effect is obviously more noticeable when the contrast between the background and the object is large, in this case as important as 1.5 in absolute values. Hence the importance of using a matching media of higher permittivity than air. Secondly, the measurement reconstruction is not as neat as the simulation. This could be attributed to a measurement inaccuracy such as an imperfect antenna alignment or to the stepper motor tolerance. To this effect, one should add the dynamic range reduction of the received signal with respect to that of the previous scenario due to the oil losses.

Table 5.4 summarizes the results of the metrics for the two scenarios considered in this section. The aforementioned degradation of the tumor positioning and the smaller contrast between the breast tissue and the tumor is clearly reflected in all the ratios. See Appendix C for a detailed description of the metrics.

5.2.2   2D circular measurements with matching liquid

Two different imaging setups are considered in this section exploiting the arrayed and the virtual array approach respectively. The first is from Chalmers University of Technology and the second is a modification of the system used in the previous experiment to permit water immersion of the antennas and the object [CA6].
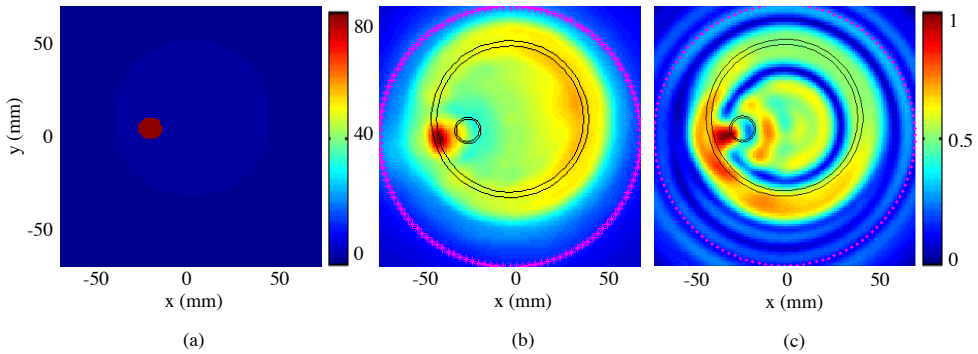
Figure 5.8: MC reconstruction of the oil breast + water tumor measured with 2D circular experimental system in air. (a) Original permittivity profile, (b) 2D MC reconstruction of the simulation, (c) 2D MC reconstruction of the measurement.

	Air breast	Oil breast
SCR	11.25	5.67
SMR	9.31	5.08
FWHM	10.5	9
PA	3.19	9.53

Table 5.4: Metrics for the 2D measurements in air: Signal to clutter ratio (SCR), signal to mean ratio (SMR), full width half maximum (FWHM) and positioning accuracy (PA).

5.2.2.1 Real antenna array

The Chalmers experimental system is shown in Figure 5.9 and the system main parameters summarized in Table 5.5. It consists of a circular array of $N_\phi = 20$ identical monopole antennas evenly distributed on a $a = 100$ mm in radius circle and mounted on a ground plane inside a tank. The measurements are made in deionized water. A VNA is used to measure the transmission and reflection coefficients at a large number of discrete frequencies between 0.1 and 4 GHz. To be able to control the measurement sequence, a 2:32 switch multiplexer module was used to automatically connect and disconnect the transmitting and receiving antennas to the VNA. The measurements are obtained using Gaussian pulses (center frequency of 0.5 GHz and FWHM of 0.5 GHz).

Time Domain Inversion Algorithm (TDA)   The Time Domain Inversion Algorithm is based on minimizing a cost functional F for each point of the discretization grid using a conjugate-gradient optimization scheme. F is essentially the difference between the measured data E^m

103
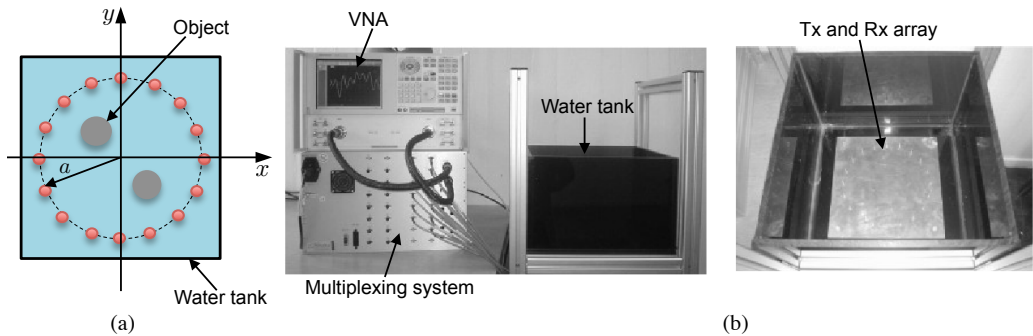
Figure 5.9: Arrayed 2D circular experimental setup housed at Chalmers University of Technology. (a) 2D sketch of the system, (b) photographs of the whole system and detail of the acquisition part.

Parameter	Value
a	100 mm
N_ϕ	20
f	0.1-1 GHz

Table 5.5: Main parameters of the 2D arrayed circular experimental system in water.

and the theoretical value E^s obtained via FDTD numerical simulation,

$$F(\vec{r}) = \int_0^T \sum_{i=1}^{N_\phi} \sum_{j=1}^{N_\phi} \left(|E^s(\vec{r}'_{R_j}, t, \vec{r}'_{T_i})| - E^m(\vec{r}'_{R_j}, t, \vec{r}'_{T_i})|^2 \right) dt \qquad (5.1)$$

where $\vec{r}'_{T_i}$ and $\vec{r}'_{R_j}$ refers to the position of the transmitting and receiving element respectively. In the reconstruction procedure, an initial complex permittivity distribution is assumed in order to compute the first field distribution E_0^s. If no *a-priori* information is available, it is set equal to a uniform background. In each iteration, the gradients are derived considering a small increment in the permittivity and conductivity profile, and the corresponding change in the functional is derived by means of a perturbation analysis [134]. Once the gradients have been updated, the optimization condition is evaluated. Successively improved images are obtained and the process is iterated until the convergence of the cost functional is reached.

5.2.2.2 Virtual antenna array

To allow the immersion of the phantom in a matching liquid, the 2D circular measurement setup in air, explained in section 5.2.1, was modified. The transmitter is in a fixed position while the receiver rotates thanks to a rotary stage fixed upside down on the top structure of the setup. A deionized water tank is placed on a big rotary stage and the object under test is fixed on it, thus rotating jointly. The combined rotation of all the elements synthesize two circular virtual arrays of $N_\phi = 64$ elements with radius $a_T = 135$ mm and $a_R = 100$ mm for the transmitter and the receiver respectively. The antennas and the connectors are protected with a thin plastic bag to

prevent water leakages. A VNA is used to measure the transmission and reflection coefficients between 0.1 and 1 GHz. A computer allows to control remotely the measurement acquisition and the positioning system. Figure 5.10 and Table 5.6 show the system main features.
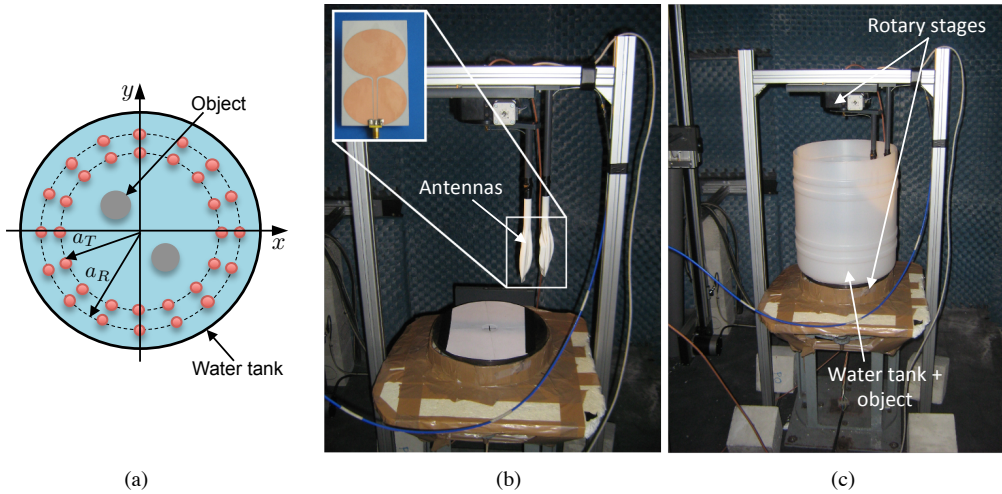
Figure 5.10: Virtual 2D circular experimental setup housed at UPC. (a) 2D sketch of the system, (b) photographs of the whole system and detail of the acquisition part.

Parameter	Value
a_T	135 mm
a_R	100 mm
N_ϕ	64
f	0.1-1 GHz

Table 5.6: Main parameters of the 2D arrayed circular experimental system in water.

5.2.2.3 Results

Three different scenarios are considered in this section. The first two scenarios are measured with the Chalmers system, while the last scenario is measured with the UPC system. The permittivity of the materials used for building the phantoms is summarized in Table 5.7. The Chalmers measurements were reconstructed using both the MC and TDA algorithms, while the UPC measurements only could be correctly reconstructed with MC. The reason for this is due to the sensitivity of TDA to the antenna modeling. Accordingly, the error committed when approximating the monopole antennas of Chalmers system to infinitely large current filaments, was smaller than that of approximating the UWB planar dipoles used in the UPC system. While both algorithms assume 2D interactions in the reconstruction algorithm, TDA also makes this assumption in the forward scattering problem solver in each step of the iterative process.

Component	Composition	ϵ'	σ	$|c(\vec{r}, f)/c_{max}|$
Background	Deionized water	77	0.05	0
Container	Deionized water + ethanol	55	0.12	0.296
Rod	PVC	2.7	0.025	1

Table 5.7: Complex permittivities of the phantom constituents for the 2D circular measurements in water at 1 GHz [66].

Deionized water and ethanol mixture in a plastic container The first scenario consists of a cylindrical plastic container filled with a mixture of deionized water and ethanol as shows Figure 5.11. Figures 5.11(c) and 5.11(d) present the relative permittivity and conductivity reconstructions using TDA. While the permittivity reconstruction is clean and quite accurate in terms of shape and magnitude, the conductivity reconstruction presents more artifacts and the magnitude is not accurately retrieved. As for the results using MC, Figure 5.11(e), here, the normalized contrast in linear scale is represented as usual. It can be observed that the shape and size is reconstructed with better precision than TDA, however it is limited to a qualitative estimation of the contrast. TDA provides a more detailed information of the object under test at expenses of higher reconstruction time. TDA required 10 iterations on a grid of 4 mm followed by 10 additional iterations on a grid of 2 mm to obtain the reconstructions. Conversely, MC provides a qualitative but real time reconstruction (20 sec. per frequency for this arrangement).

Deionized water and ethanol mixture in a plastic container + PVC rod The second scenario, see Figure 5.12, contains the target used in the previous scenario and an additional PVC rod of 10 mm in radius separated 20 mm from the first. This is a more challenging scenario, since another object is placed in the vicinity of the previous one. Using TDA, while the relative permittivity reconstruction is quite accurate, Figure 5.12(c), the algorithm fails with the conductivity, Figure 5.12(d). Concerning MC, it obtains a correct geometric reconstruction, as shows Figure 5.12(e). Moreover, the reconstructed contrast of the thinner rod is lower than that of the thicker rod, meaning that although the reconstructed contrast is not correct in quantitative terms, it is almost correct in relative terms.

2 PVC rods The third scenario includes two PVC cylinders of 8 mm in radius separated 50 mm, as shows Figure 5.13. It is similar to the previous, but now, non of the cylinders is centered. The results presented in Figure 5.13(c) are obtained using MC algorithm. A central artifact appears in the reconstruction because the repeatability of the measurment is not perfect. Accordingly, the rotation of the antenna in the water tank and also the rotation of the own tank, produces random disturbances on the water that cannot be canceled during the system calibration. In spite of this unwanted effect, the two rods are properly detected and placed. Nevertheless, the rod which is more distant to the center is reconstructed differently. It is possibly due to the proximity of the rotating antenna to this rod, which produce stronger disturbances on this rod than on the other one.

Table 5.8 summarizes the results of the metrics for the three scenarios considered in this section for the MC tomography reconstructions. For the second and third scenario, two sets of
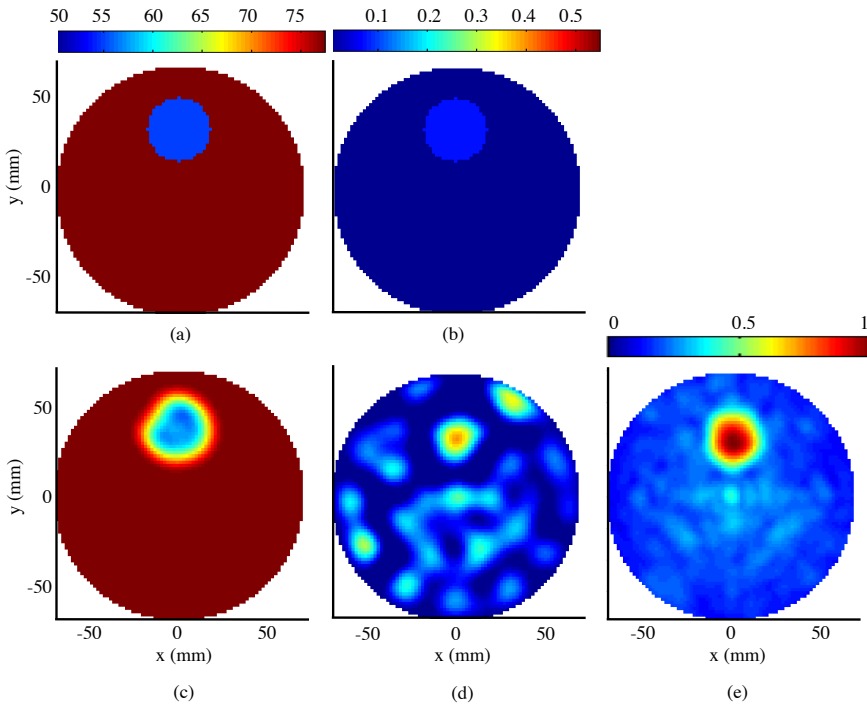
Figure 5.11: MC reconstruction of a deionized water and ethanol phantom in deionized water. (a) original relative permittivity, (b) original conductivity, (c) reconstructed relative permittivity with TDA, (d) reconstructed conductivity with TDA, (e) reconstructed normalized contrast with MC.

results are presented since the scenario contains two targets. The higher ratios of the arrayed system in terms of clutter (SCR), target response (SMR) and spatial accuracy (PA) indicate the better performance of this type of systems. See Appendix C for a detailed description of the metrics.

	Water container	Water container + PVC rod		2 PVC rods	
		Container	Rod	Upper rod	Down rod
SCR	13.01	13.98	7.21	8.24	5.80
SMR	15.21	16.38	9.61	13.21	10.78
FWHM	12	10	8	8	8
PA	4	2	2.83	2.23	4.47

Table 5.8: Metrics for the 2D measurements in water.
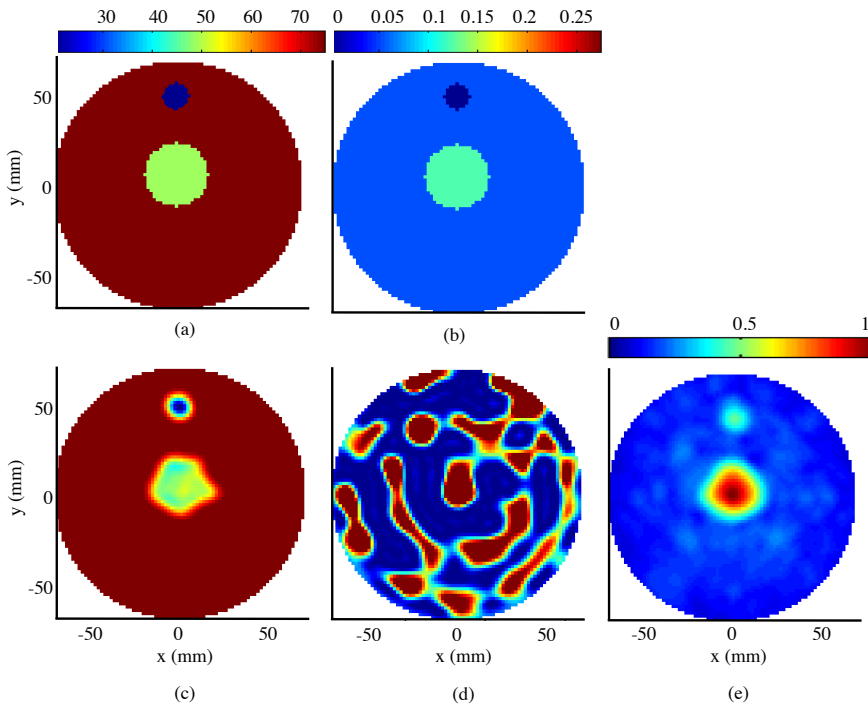
Figure 5.12: MC reconstruction of a deionized water and ethanol phantom + PVC rod in deionized water. (a) original relative permittivity, (b) original conductivity, (c) reconstructed relative permittivity with TDA, (d) reconstructed conductivity with TDA, (e) reconstructed normalized contrast with MC.

5.3   3D experimental results

Analogously to the previous section, the aim of this section is to assess the capability of the MC algorithm to deal with experimental data, this time for the 3D cylindrical geometry. Similarly to 2D, a virtual array approach is pursued. However, actually, the main drawback is the enormous measurement time consumed by the moving stages, since two more degrees of freedom are needed. For this reason, in the first part of the section, a quasi-cylindrical measurement system having 3 degrees of freedom (2 rotation + 1 linear) is built. This preliminary system does not consider matching liquid either. Hence, only low-contrasted objects with revolution symmetry could be imaged. However the measurement time will be significantly reduced, which is essential for a practical system assessment.

After the preliminary system assessment, the second part of the section will be devoted to implement a more sophisticated system with a full cylindrical sampling (4 degrees of freedom) and allowing liquid immersion. With this system, more realistic breast phantoms will be measured. Nevertheless, this system is still not suitable for practical clinical use due to the mechanical scanning. A more realistic arrayed prototype will be designed in the last part of the chapter and the preliminary assessment will be presented.
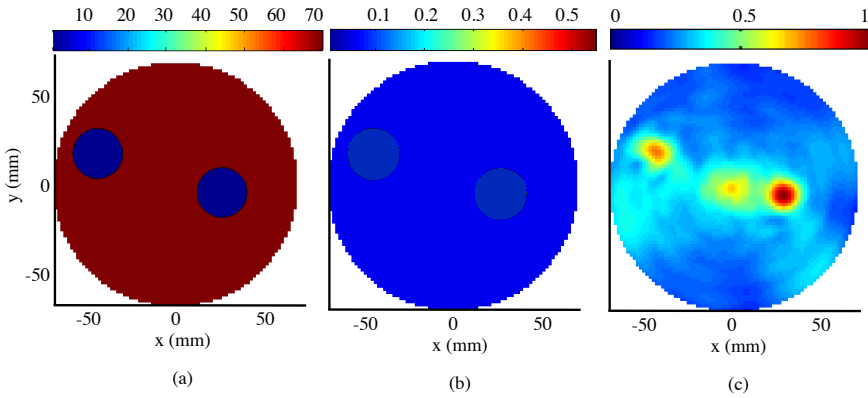
Figure 5.13: MC reconstruction of two PVC rods. (a) Original relative permittivity, (b) Original conductivity, (c) reconstructed normalized contrast with MC.

5.3.1 Quasi-cylindrical measurements

5.3.1.1 Acquisition system

A cylindrical sampling is accomplished by constructing two independent virtual arrays, one for the transmitting antenna and the other for the receiving antenna. By limiting the imaged phantoms to those having revolution symmetry around z-axis, the measurement setup complexity is reduced from 4 degrees of freedom to 3. Then the system will be composed by 2 vertical linear stages and a single horizontal rotary stage. One linear stage is used to move the phantom up and downwards, the rotary stage confers movement to the receiving antenna, and the other linear stage moves the transmitting antenna up and downwards. The remaining measurement points needed to complete two cylindrical arrays are obtained by symmetry. A VNA generates the illuminating field and collects the received signal. Finally a computer is used to remotely and automatically control the positioning system and the VNA, see Figure 5.14. Each virtual antenna array is composed by N_z=25 rings of a_T=90 mm and a_R=75 mm in radius respectively containing N_ϕ=32 equidistant antennas. Each ring is separated Δ_z=10 mm in the vertical direction. Table 5.9 summarizes the system main parameters.

5.3.1.2 Phantom

The phantom consists of a 1 mm in radius metal sphere lodged into a 40 mm in radius paraffin sphere fixed with a PVC rod. Since the object is assumed to be perfectly symmetric, a very accurate manufacturing is required. The manufacturing process is detailed in the following lines. First of all a spherical mold was half filled with liquid paraffin. Before a complete hardening of the paraffin, the metal sphere was placed exactly at the center. Finally the mold was filled to the top with more liquid paraffin. A nylon screw was placed across the filling hole of the mold with the screw head upside down immersed in the paraffin. By doing so, the phantom can be screwed to a PVC rod which was firmly fixed to the measurement system. Table 5.10 summarizes the dielectric properties of this phantom.

109

(a) (b) (c)
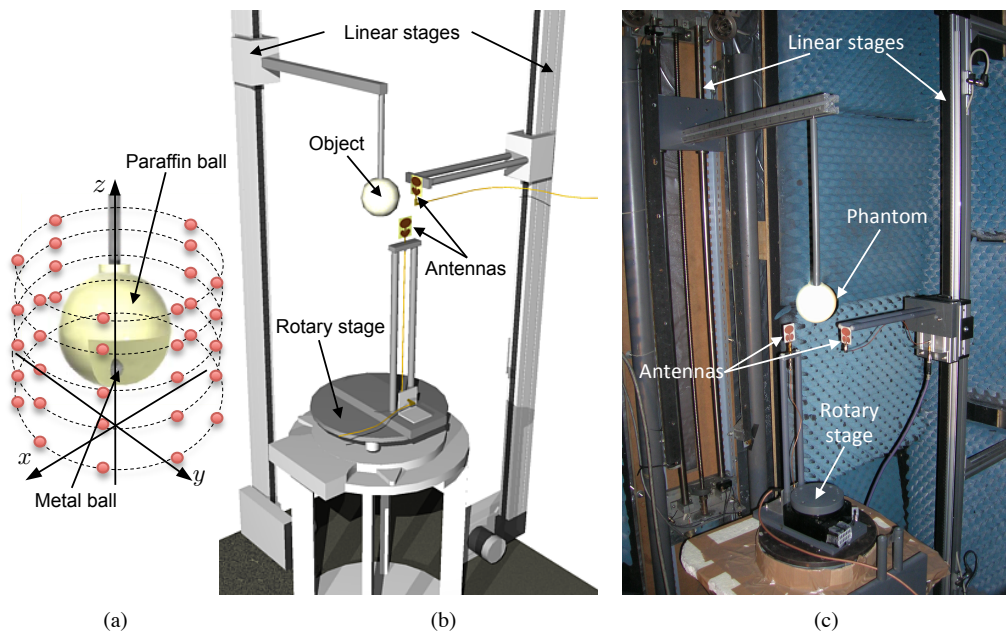
Figure 5.14: Quasi-cylindrical experimental system. (a) Sketch of the system, (b) photographs of the whole system and detail of the acquisition part.

Parameter	Value
a_T	90 mm
a_R	75 mm
N_ϕ	32
N_z	25
Δ_z	10 mm
f	3-10 GHz

Table 5.9: Main parameters of the quasi-cylindrical experimental system.

Component	Composition	ϵ'	σ	$|c(\vec{r}, f)/c_{max}|$
Background	Air	1	0	0
Big ball	Paraffin	2.19	$7.3 \cdot 10^{-5}$	0.7
Rod	PVC	2.7	0.025	1

Table 5.10: Complex permittivities of the phantom constituents for the 2D circular measurements in water at 1 GHz [66].

5.3.1.3 Results

Figure 5.15 present the imaging results from the measurement of the phantom described in the previous lines. The 3D representation, Figure 5.15(b), shows an accurate representation of the contour of the phantom preserving its shape and size along all directions. At the upper part of the phantom, the PVC fixing rod appears very highlighted. Inside the paraffin ball, the smaller sphere is clearly detected at the correct position. Table 5.11 presents the metrics. Such a high values for the signal to clutter ratio (SCR) and signal to mean ratio (SMR) demonstrate the quality of the reconstruction in terms of tumor response. In terms of spatial accuracy, the shift of the tumor position is only of 2.5 mm. See Appendix C for a detailed description of the metrics.

(a)   (b)
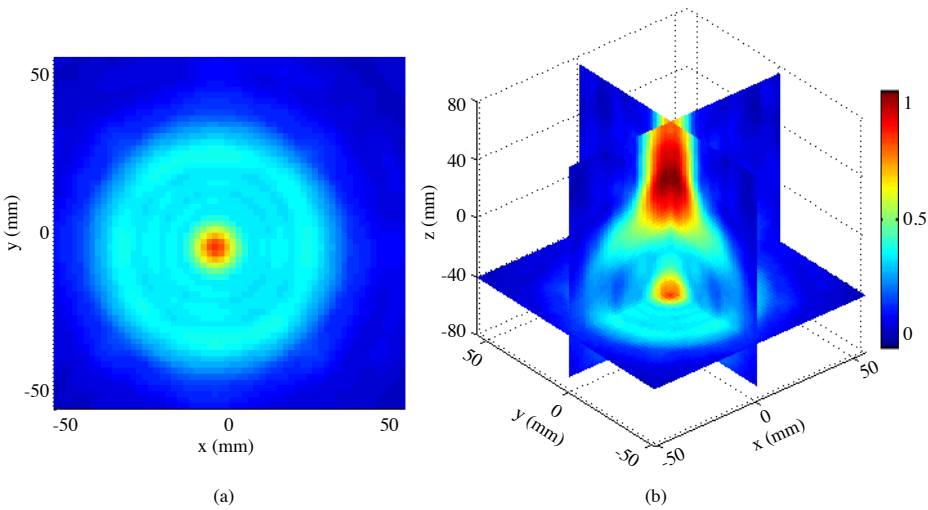
Figure 5.15: MC reconstruction of a metallic ball inside a paraffin ball with the quasi-cylindrical system. (a) XY plane of the 3D cylindrical MC reconstruction, (b) 3D view.

	Paraffin phantom
SCR	18.09
SMR	10.58
FWHM	7.21
PA	2.54

Table 5.11: Metrics for the quasi-cylindrical measurements.

5.3.2 Cylindrical measurements

5.3.2.1 Acquisition system

A further step towards an experimental system for realistic applications is done herein. The previous experimental setup was modified by adding another rotary stage, thus having 4 degrees of freedom. In this way, general objects can be scanned without any symmetry supposition. Also the system was rearranged to allow the phantom immersion in a matching liquid tank. As before, the cylindrical sampling is obtained by constructing two independent virtual arrays, one for the transmitting antenna and the other for the receiving antenna. Now, the system is composed by 2 vertical linear stages and 2 horizontal rotary stages. One linear stage is used to move the phantom up and downwards. Attached to this linear stage, a rotary stage is placed upside down holding the object under test. Hence the object can be rotated and moved up and downwards. One of the antennas is attached to the other vertical linear stage. Finally, on a big rotary stage situated at the lower part of the system, the matching liquid tank is placed. The other antenna is placed in the liquid tank and rotates jointly with it. This antenna is fed with a coaxial cable that passes through the tank thanks to a waterproof screw. The linear stage range of movement must be calculated to ensure that the antennas are always inside the liquid during whole the measurement. Another issue to be considered is the importance of keeping the matching liquid still and free of perturbations. To ensure this point, the big rotary stage moves very smoothly and the measurement is performed only when the liquid is calmed. A VNA generates the illuminating field and collects the received signal. Finally a computer is used to remotely and automatically control the positioning system and the VNA, see Figure 5.16. Each virtual antenna array is composed by N_z=7 rings of a_T=90 mm and a_R=90 mm in radius respectively containing N_ϕ=32 equidistant antennas. Each ring is separated Δ_z=20 mm in the vertical direction. Table 5.12 summarizes the system main parameters.

One of the most limiting parts of the system is the selection of the number of levels (or l_z). The image quality will depend on the accuracy of the synthesized plane waves, which at its turn, require some extra antenna levels beyond the bounds of the object under test (see section 3.2.2.2). An excessive number of antennas leads to enormous measurement duration (in the order of several days) due to the motor movements. Thus, the number of antennas is always a compromise between image quality and measurement run time. A set of parametric simulations with the wax and metal phantom (as section 5.3.1) were reconstructed varying the number of levels N_z and l_z keeping Δ_z fixed. The conclusion was that a minimum of $N_z = 4$ levels were required. However, the measurement indicate that the number of levels should be increased up to $N_z = 7$. This is possibly due to measurement inaccuracies such as the motion of the matching liquid, noise, etc. Thus, the measurement always benefit from an extended redundancy.

5.3.2.2 Phantom

This system was built with the aim of reconstructing realistic breast phantoms. To do so, the system had to incorporate a matching liquid tank and allow a complete cylindrical scanning. In this case, sunflower oil was used to match the breast fat, which is the majority breast constituent. The realistic breast phantom is composed by mixtures of chemicals that mimic the dielectric properties of the real human tissues. The glandular and the tumor tissue materials

(a)   (b)
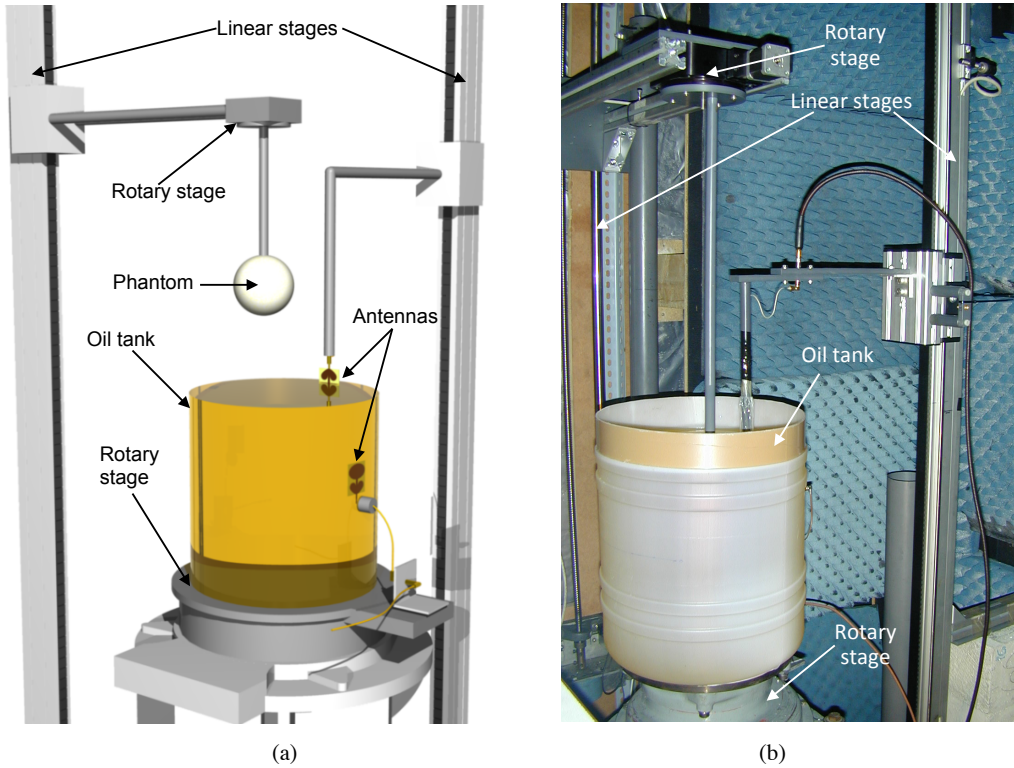
Figure 5.16: Cylindrical experimental system. (a) Sketch of the system, (b) photographs of the whole system and detail of the acquisition part.

Parameter	Value
a_T	75 mm
a_R	95 mm
N_ϕ	32
N_z	7
Δ_z	20 mm
f	0.5-7 GHz

Table 5.12: Main parameters of the cylindrical experimental system.

were obtained according to the recipe proposed in [130]. These materials have a gel-consistency and are gelatin-like when harden, and thus can be molded. While this materials have a good characteristics for a quick measurement, they do not seem very suitable for being immersed in oil several days. Thus, for the fatty tissue, which has to be in direct contact with oil, a more solid material such as plaster was chosen. Plaster was previously proposed to electrically model

113

the fatty tissue ($\epsilon'_f = 5.1$, $\sigma_f = 0.15$ at 2 GHz.) [94]. The glandular tissue and tumor mixtures present a complex permittivity of $\epsilon'_g = 24$, $\sigma_g = 3.5$ and $\epsilon'_t = 52$, $\sigma_t = 11.5$ respectively at 2 GHz.

To create the phantom, first of all, the plaster mix was poured into a cylindrical mold until was filled half way. Before it was completely hard, a 20 mm in diameter spherical hole for the tumor and 3 smaller holes for the glands, were caved into the plaster. Then the tumor mimicking material was created and poured inside the spherical hole. When the tumor material became solid (about 8 hours), more plaster mix was poured on it to completely fill the mold. To incorporate the glands, which have approximately conical shape with the narrower part of the cone being closer to the nipple, three pencils were anchored in the small holes performed on the plaster before pouring for the second time. When the plaster was half solidified the pencils were moved in circles to create cones. Once the fat phantom hardens, the pencils were removed and the liquid gland mixture was poured into the conical hole, see Figure 5.17. The recipes for the tumor and gland tissues are included in Apendix F. The skin layer was not included in the phantom because we assume that a skin subtraction method was used. As done with the previous wax and metal phantom, a nylon screw was fixed on the top of the phantom for its assembly with the system.

Figure 5.17: Tissue mimicking phantom manufacturing process.

5.3.2.3 Results

Preliminary results were obtained using the previous wax and metal phantom. This time, since the system allows a complete cylindrical scanning, the phantom was placed 10 mm off-center. Figure 5.18 shows the MC reconstructions between 1-4 GHz. Since the permittivity of the wax and the oil are very similar, the contour of the ball is very diffuse. For the same reason, the PVC fixing stick does not appear in the image. The inner metallic ball is clearly detected. A slight lengthening along $\hat{\phi}$-direction can be observed due to the oil rotation.

In view of the successful previous reconstruction, the realistic breast phantom built with tissue mimicking materials is measured. Figure 5.19 shows the MC reconstructions between 1-4 GHz. Figure 5.19(b) presents the XY plane where the tumor is clearly detected, again with a slight lengthening along $\hat{\phi}$-direction. This time since the permittivity of the plaster is higher than the paraffin, the contour of the breast is more visible. The glands are also detected as can be observed in the 3D view and the YZ plane (Figure 5.19(a) and Figure 5.19(c)). As expected, the reconstructed contrast of the tumor is higher than that of the glands.

The results of the metrics are summarized in Table 5.13. The preliminary paraffin phantom

shows better results than the realistic phantom above all in position accuracy (PA) and signal to mean ratio (SMR). This is because the presence of the glads that produce more scattering. The remaining metrics are quite similar since the image quality is limited by the experimental system accuracy, which is affected by the rotation of the antennas in the oil tank. Note that the calculation of the clutter in the signal to clutter ratio (SCR) does not consider the glands as clutter, since they represent real masses not an image artifact. See Appendix C for a detailed description of the metrics.
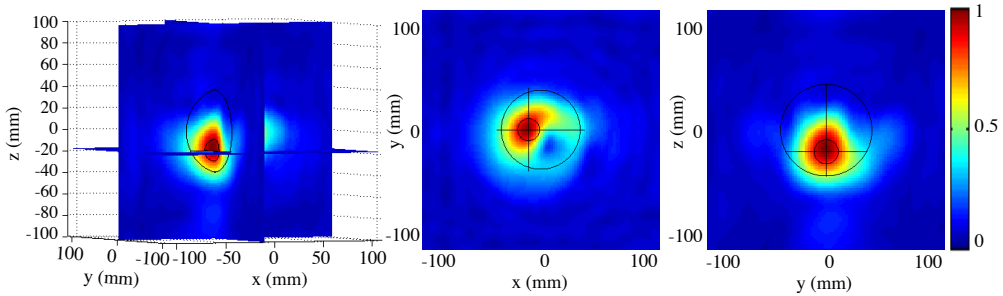
Figure 5.18: MC reconstruction of a metallic ball inside a paraffin ball with the 3D cylindrical system. (a) 3D view, (b) XY plane, (c) YZ plane.
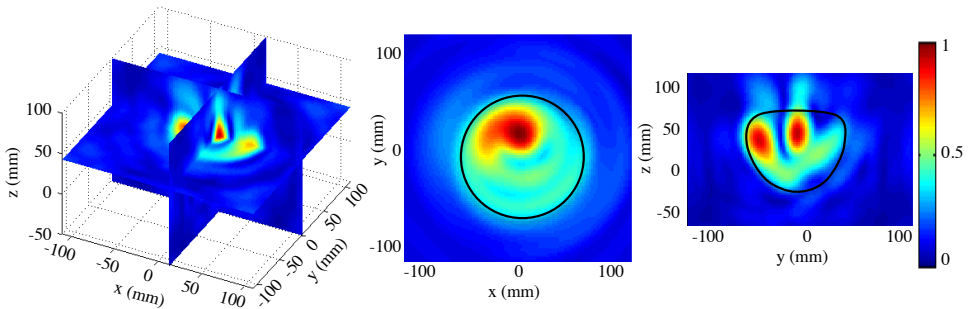
Figure 5.19: MC reconstruction of a breast phantom including fat, fibroglandular tissue and a 10 mm in radius tumor with the 3D cylindrical system. (a) 3D view, (b) XY plane, (c) YZ plane.

5.3.3   Towards a compact and real-time cylindrical system

In this section, the design of a 3D cylindrical arrayed system for microwave tomography is presented. Unlike the previous systems, in the current setup, vertical movements are replaced by real antenna arrays aimed to reduce the acquisition time by a factor N_z^2 [CA9]. The system is as depicted in Figure 5.20. The cylindrical sampling is accomplished by the combined action of the multiplexing and the positioning system. In particular, the object under test is placed at

	Paraffin + metal	Realistic breast
SCR	9.2	6.02
SMR	7.53	5.50
FWHM	17.21	17.49
PA	3.83	6.80

Table 5.13: Metrics for the 3D cylindrical measurements.

the center of a rotary stage that is mounted on another rotary stage attached to the transmitting array. Both rotary stages share the same rotating axis. The rotating array is in a fixed position and remains still during the whole measurement. Each array element is connected to a specific multiplexing circuit that selects a pair of transmitting and receiving elements at a time. A 2-port VNA generates and collects the illuminating and measured signals and a computer controls the whole measurement and stores the data.

The system requirements are mainly imposed by the imaging algorithm and the body under test. The considerations regarding frequency band, number of antennas, separation between elements and polarization are common with the previous systems. However the arrayed configuration imposes additional requirements such as low cross-polarization and low coupling between antenna elements. A non-bulky and narrow array is also desirable to prevent important shadowing when an array passes behind the other due to the rotation. Finally a compact and low-complexity feeding network is needed to avoid problems with cables during the rotation. Appedix E details the design process of the arrayed acquisition system.
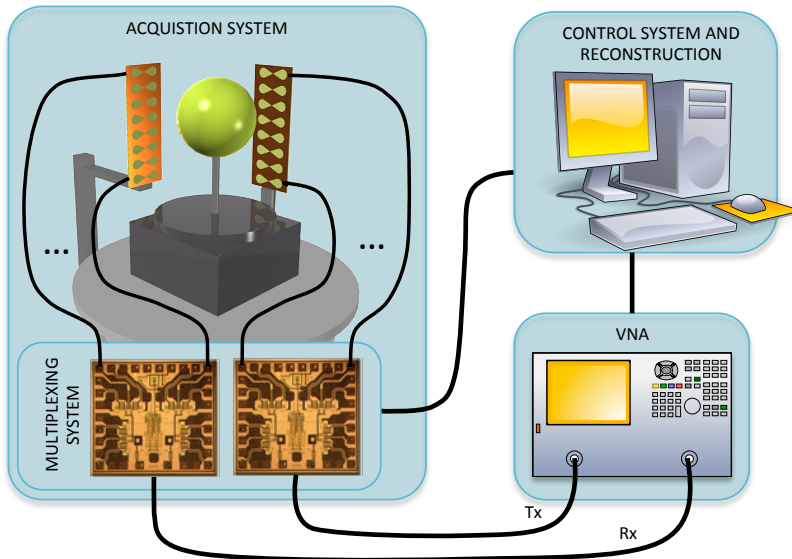
Figure 5.20: Block diagram of the arrayed experimental system for microwave imaging for medical applications.

The preliminary experimental array validation is presented next. The idea is to measure a known field with the 8-element array to evaluate the accuracy of the array as a field probe. The known field is generated by a ridged horn antenna which is situated at a distance d from the array. In the first experiment d is set to 1.5 m to ensure far field conditions. Thus, the measured field at all the array elements must have almost the same amplitude and present a linear phase evolution. This can be observed in the measurement results depicted in Figure 5.22. While the phase is almost flat, above all for the lowest frequencies, the field intensity presents a peaked response, however being more flat between 4 and 8 GHz.

(a)

(b)
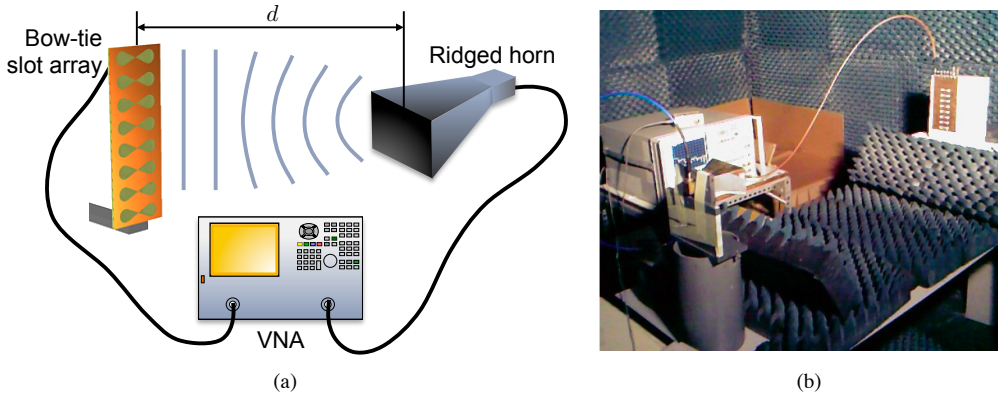
Figure 5.21: Measurement setup for the validation of the arrayed experimental system for microwave imaging. (a) Schematic view of the experimental system, (b) detail of the measurement setup.

(a)

(b)
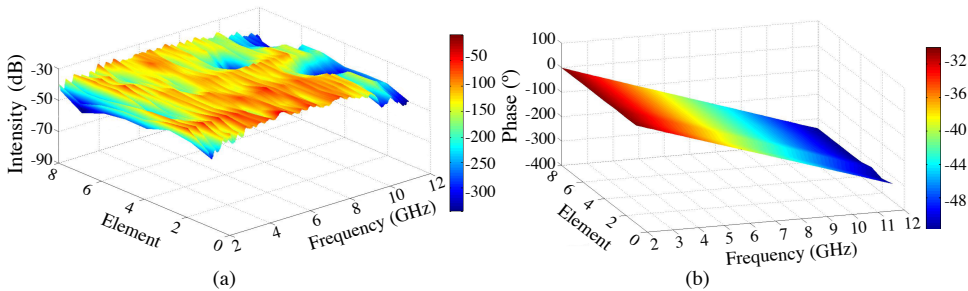
Figure 5.22: Measurement of the far field ($d = 1.5$ m) of a ridged horn with the 8-element bow-tie slot array. (a) Field intensity, (b) Field phase.

The second experiment is devoted to compare the performance of the array with respect to a single moving probe. To do so, the same setup used in the first experiment was considered. Now the distance d is reduced to 20 mm in order to sense the near-field of the ridged horn. The first measurement is taken with the 8-element array and the second with a single bow-tie slot. In the second measurement, the bow-tie slot is moved and a measurement is taken at the same positions as with the array. Figure 5.23 shows the comparison between both measurements at 4 GHz after normalizing to the maximum value in order to cancel the longer feeding lines of the array with respect to those of the single probe. The results show an increasing disagreement

above all for the elements 6, 7 and 8. These elements are the closest to the SMA connectors and thus the corresponding feeding lines are the most meandered ones. This could be one of the reasons influencing the results. Nevertheless, other issues regarding the manual manufacturing of this first prototype may deteriorate the similarity between elements and should be taken into account in the subsequent array versions. Firstly, the via holes at the element ports could not be metallized due to the size of the ground plane and were riveted manually. Secondly, the microstrip feeding lines were very long and thin, and thus the photolithographic process should be performed very carefully in order to prevent damaging the lines. In order to improve the results, a calibration to cancel the different behavior of the elements can be always done.
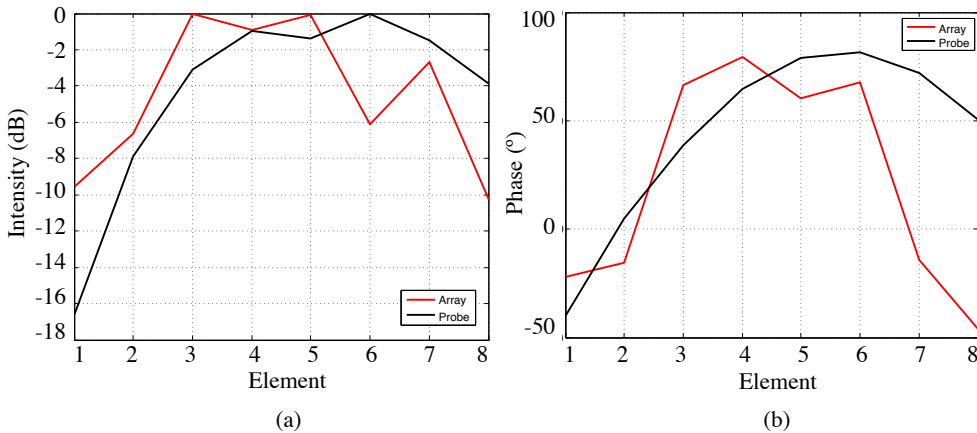
Figure 5.23: Measurement of the far field ($d = 1.5$ m) of a ridged horn with the 8-element bow-tie slot array at 4 GHz. (a) Field intensity, (b) field phase.

Due to reliability problems experienced by the wire bond machine the multiplexing system was not finished by the end of this thesis. Thus, no further evaluation of the system could be presented herein.

5.4 Concluding remarks

This chapter addressed the experimental work carried out during the thesis. The main goal was to demonstrate the robustness of the algorithms to experimental issues, such as noise and multipath corruption, while the detection capability shown in the previous chapter was preserved. To do so, the chapter was organized in three main parts. The first, explained the main parts and characteristics of an experimental system for microwave imaging; the second collected all the experimental work regarding the 2D circular system; while the third dealt with the 3D cylindrical system. For each system, different phantoms, background media and acquisition methods (i.e. arrayed or virtual) were tested. At the end of the third part, an arrayed acquisition system devoted to reduce the measurement time is presented.

In the first part of the chapter, the design requirements for a microwave imaging system were stated taking into account the specific algorithm requirements and considering the actual

state of the art. In order to produce measurements subject to be processed with the algorithm, the system had to be designed to resemble the simulation environment as much as possible. Hence dipole like antennas with a uniform behavior over the frequency band were required. This included linear polarization (negligible cross-polarization) and omnidirectional radiation pattern over the desired frequency band. Planar elliptical dipoles met the previous needs and hence were used for the measurements. The acquisition based on a real cylindrical array of antennas, in spite of allowing real time measurements, face a number of problems such as more manufacturing complexity, coupling between elements and limitations on the element size. On the other way round, the virtual array approach offered the flexibility to change and upgrade the system configuration easily. Hence both types of systems were considered depending on the desired performance at each moment. Nevertheless, the second strategy was chosen for the first prototypes aimed to validate the algorithms.

In the second and third part of the chapter, the experimental acquisition setup was successively improved to be able to measure increasingly realistic phantoms. Starting from a virtual 2D circular acquisition system in air, several modifications were tested (i.e. a matching liquid tank, more degrees of freedom, antenna arrays) to finish with a pre-clinical arrayed system proposal. As a result of this work several remarks can be highlighted:

- One of the major drawbacks was the excessive screening time due to the VNA measurement time plus the movement of the motors. This was specially limiting for the 3D cylindrical arrangement that had a total run time of 66 hours (slightly less than 3 days), while for the 2D system was only 1 hour. Despite the system was not envisaged as a clinical system, such a prolonged duration was not convenient due to VNA drifts, changes of temperature or phantom degradation, and made the system tuning tests very tedious. To reduce the measurement duration, the number of antennas was optimized. One of the most cumbersome decisions was regarding the cylindrical array length l_z. We observed the more complex the phantom or the less accurate the system, the greater the need of redundancy (more antenna levels). Thus, the number of antennas was always a compromise between performance and measurement duration.

- Another important remark was regarding the noise, system sensitivity and safety. The theoretical sensitivity analysis showed that this was not a limiting issue for the detection scenarios studied in this thesis. Concerning the noise, the simulations concluded that for realistic breast tumor detection scenario, the minimum required SNR is -10 dB (taking the differential field as signal). Such a small value is thanks to the antenna gain given by the large amount of antennas in the array. From an absolute field measurement (instead of differential) and considering an input power of 0 dBm, the minimum VNA sensitivity is -60 dBm, which is feasible since the typical VNA sensitivity is -85 dBm. Concerning safety, the SAR levels produced by a illumination of 0 dBm are far below the limits established by the actual standard. Beyond theory, the measured data contains additive noise and undesired reflections that were not taken into account in the previous chapters. The measurement results presented herein demonstrated that the algorithm is robust to this issues and the repeatability is good enough to allow a calibration based on the subtraction of a reference empty measurement (without the presence of the object).

- One of the practical issues influencing more significantly the results when matching liquid was used, was the movement of the antennas producing non predictable disturbances in the liquid. The better results obtained with the arrayed version of the system, clearly demonstrate this point.

6

CONCLUSIONS

THIS PhD thesis was focused on microwave medical imaging for diagnostic purposes. In more than 30 years of research, the microwave medical imaging field has developed significantly, but it has not yet achieved the maturity level required to reach the clinical stage. This fact is certainly distressing and directly leads to the question whether we are doing the right things or we are doing the things right. In this sense, the thesis followed the path of diffraction tomography that was almost abandoned for the research community to pursue quantitative methods when the computational requirements were not a limitation anymore. In general, iterative schemes face important problems when proceed to experimental world due to data acquisition issues related to multipath or noise corruption, or convergence problems due to the difficulty to model the whole system in the direct problem. At the same time, radar-based approaches suffer from skin effects, inaccurate knowledge of phase velocity and detection problems in case of small contrasts. Hence MC tomographic algorithm seemed to be an intermediate solution with characteristics of both approaches. It renounces quantitative performance for a major robustness.

In the following lines, the main conclusions of the thesis are outlined. Next, a more personal opinion written from the experience gathered during the 4 years of the development of this thesis is included. Finally the future research lines envisaged for this area of expertise are presented.

6.1 Main conclusions of the thesis

Multi-view and multi-frequency

The MC tomographic algorithm was proposed, formulated and assessed in this thesis for both 2D circular and 3D cylindrical acquisition geometries. The two major contributions in terms of the algorithm, are from one hand, the extension of the previous 2D diffraction tomographic methods to a full 3D performance, and from the other hand, the magnitude multi-frequency combination strategy overcoming the well-known residual phase errors associated to Born-based algorithms. This provided qualitative contrast images with an enhanced robustness in terms of frequency selective artifacts with similar resolution to that of the higher frequency image. This robustness was also demonstrated with experimental measurements, reporting good detection rates. In general, lower frequencies contribute to the reconstruction of the smoother parts (breast fatty volume, fibroglandular large masses, etc.), while higher frequencies retrieve the contours of the object constituents. The combination of frequencies in the 0.5-4 GHz band reported good results for the majority of scenarios studied in this thesis.

Moreover, the redundancy given by multi-view and multi-frequency scans, allows reducing the number of antennas below the Nyquist sampling criteria. Nevertheless, when dealing with experimental data, these improvements do not seem to be as remarkable as with simulations.

Medically relevant assessment

This thesis was focused into breast cancer and brain stroke detection. Both represent significant medical challenges which can benefit from the microwave technology to improve the current diagnosis process. In order to evaluate the performance of the MC algorithm to detect lesions, a model as realistic as possible is required. To this aim, MRI-derived voxeled breast and brain models are freely available, and were used in this thesis for the final assessment. Apart from the host body, the lesion must be medically relevant in terms of size, placement and shape. The first and the second terms were considered in this study and particularized for the early stage detection, where probably microwave imaging offers more advantages with respect to the current imaging methods (harmless, economical, etc.). However there is still much work to do with respect to the third issue. While several tens of different lesions are identified and classified in radiology, only a little work was done in dielectric characterization. Thus the majority of papers, including the present thesis, represent the tumor as a homogeneous sphere of a certain radius, which is not realistic.

Imaging results evaluation

The performance of the MC tomographic algorithm was obviously dependent on the phantom complexity. Even using the same phantom, the results depended strongly on the frequency choice or the measurement quality (noise, interferences, multipath, etc.). Thus the imaging results were difficult to evaluate. To this aim, this thesis combined the qualitative visual evaluation and the quantitative evaluation using 4 metrics that quantify the target response and the detection accuracy. Using canonical scenarios, the performance of the algorithm in terms of minimum detectable target size (2 mm in radius), resolution or minimum number of antennas could be established. In these case, the use of more antennas than the established by the sampling criteria was not translated to an

image improvement. Nevertheless, this conclusions could not be directly extrapolated to realistic phantoms or measurements, where more redundancy contributes to a better quality. Thus, in complex cases, the number of acquisition points is always a compromise between quality and time.

The main challenges in breast cancer detection were due to the skin layer and the existence of glandular tissue in contact or surrounding the tumor. Accordingly, skin produced important reflections due to its large dielectric contrast with respect to that of the matching medium (matched to the adipose-dominated breast tissue). Thus, skin subtraction techniques were proposed reporting better results. Concerning existence of fibroglandular tissue in the vicinity of the tumor, when both tissues were separated, there was not difficulty in their detection. However when the tumor was completely embedded in fibroglandular tissue, it could be still sensed but the geometrical reconstruction was not accurate. A large amount of fibroglandular tissue (dense breast) was also a challenging issue for the modified-Born method pursued in this thesis. In this case, the low scattering assumption was not fulfilled producing image artifacts. When the absolute imaging failed, differential imaging was proposed. Differential imaging consists on subtracting two measurements presenting a small change into the target.

Brain stroke detection was a very challenging application given the layered structure with really different contrasts combined with the existence of highly lossy liquids inside the brain. It was demonstrated that in a realistic scenario, only the differential approach succeed in detecting a blood mass inside the deepest part of the brain.

Considering the feasibility of the skin subtraction and differential methods, they are still only valid in a theoretical framework. While skin surface detection methods are widely developed, there is not much research on its application to skin subtraction. In a the numerical framework, the subtraction is always possible, however with measured data several challenges arise related to the accuracy in the scenario modeling in the direct problem. Accordingly, if the skin simulation is not accurate enough, the subtraction between the simulation and the measured data will fail. This problem is common with the differential imaging approach. In fact the skin subtraction can be viewed as a differential process. Regarding the differential method, the main problem is to obtain two images with the same conditions in different time instants. It is only feasible in case of a continuous monitoring scenario, such as in the event of a brain stroke.

Experimental results

The experimental work performed in this thesis was aimed to validate the robustness of the algorithm to measurement issues such as noise, interferences or multipath. In any case, the system is not envisaged as a clinical prototype, since it was out of the scope of this thesis. The actual experimental setup was designed to mimic the simulation environment (omnidirectional pattern, linear polarization, broadband) prioritizing the system flexibility. Thus a virtual array approach was used in the majority the setups. Only at the end of the document, an arrayed setup was proposed as a clinic-oriented system. In spite of being more flexible, with no antenna size limitations and no coupling between elements, the virtual approach faced several drawbacks such as long acquisition time and problems with the matching liquid motion. Despite the aforementioned issues, remarkable results were reported by the studied scenarios. To the best of our knowledge, in the literature several tissue mimicking phantom recipes have been reported, however only a few include tomographic reconstructions of these phantoms. In this thesis, a realistic

breast phantom was built and a 2 cm in diameter tumor was detected. Image quality improvements may be reached using a more stable acquisition system. In view of the results, it can be concluded that the primarily objective of the thesis, that was to develop a robust microwave imaging algorithm, was fulfilled.

Towards robust quantitative performance

A short study was devoted to test the potentiality of MC tomography to produce quantitative reconstructions. The so-called FDL technique performed a frequency stepped iterative scheme based on the MC tomographic method. At the current stage of development, it was able to reconstruct quantitatively the real part of the permittivity of a realistic voxeled phantom.

6.2 Personal opinion

The interest in medical microwave imaging, at least among the electromagnetic community, is obvious given the 30 years of almost uninterrupted research. The established imaging methods suffer from important weaknesses for many health problems and microwave imaging could provide additional and new information about the lesion. Despite the high potentialities initially given to microwave imaging, their development has not yet achieved the maturity level required for their implementation in current clinical systems and the research remained enclosed in electromagnetic field except a few exceptions.

Hence to the question if microwave has space in medicine, the answer is difficult. The potential of microwaves in medicine is smaller than previously expected in the early ages of this technology. The contrast between layers and the inhomogeneity of biological organs is very important and causes strong scattering. In case of breast, the initial use of simplified 2D phantoms (mainly due to computational limitations) masked the major actual challenges. The location of the tumor inside fibroglandular tissue, which has a really small contrast with respect to the tumor, and the high contrast between the skin and the adipose dominated breast tissue are high barriers to overcome. Recently, the idea of having a unique and perfect imaging method for every lesion is losing steam. Microwave imaging could offer an alternative or complementary detection method to the rest of screening methods, which is the dielectric properties of tissues. So, it might be effective in cases where MRI or mammography fail. Outstanding but still initial research is devoted to study the synergies between microwave imaging and other imaging methods in the so-called hybrid methods.

Regarding the current research, the intensive simulation efforts are sometimes questioned. The danger is to commit the same error of the past again and omit important issues influencing the results. As an example, functional changes associated to the living tissues possibly have some effect on the dielectric properties that may difficult or help to the detection. Hence, the research community agreed on the need to proceed to clinical measurements. To this aim, a collaborative network supported by the COST action TD131 was created in order to accelerate technological, pre-clinical and commercial evaluation progress in the area of medical microwave imaging for diagnosis and therapeutic applications [135].

Another issue that may benefit from a collaborative work would be the comparison between the different reconstruction algorithms performance. However, it is certainly difficult, since every approach has its own requirements in terms of frequency band, number and shape of the

acquisition array, etc. Establishing a common scenario might be not possible. This was one of the conclusions extracted from a initial collaborative work between several European and Canadian universities including: Malardalen University (Sweden), Supélec (France): University of Bristol (UK), Universitat Politècnica de Catalunya (Spain), University of Calgary (Canada) and University of Manitoba (Canada). The aim was to define a common framework to compare the performance of the algorithms developed for each university around the breast cancer detection topic. As a result, 4 different scenarios were defined, see section 4.1.3. Other initiatives, such as the breast repository of the University of Wisconsin [85], certainly paved the way towards this aim. But there is still a lot of work to do.

Thus, the key factor for success seems to be the acceptance of microwave modality by medical doctors. But, what doctors want to see? Are they interested in the quantitative value of the permittivity or just in the qualitative contrast? Is the image resolution, and thus the accurate shape reconstruction, a crucial point? In order to find out more to realize in which characteristics researchers have to focus, we must cross the frontier of clinic.

6.3 Future research lines

The following lines describe the work that can be performed as a continuation of the research presented in this thesis.

Formulation and implementation of the MC tomographic algorithm for hemispheric geometries
 The hemispheric acquisition surface adapts better to the shape of the breast and the head. In case of the breast, for certain breast typologies it may be feasible to avoid the matching liquid and use a radome to fill the space between the breast and the array or even consider an aspiration system such as the one mentioned before. The challenge regarding this approach is mainly the need of sensing both θ and ϕ field polarizations. Thus the antennas must have two linear and orthogonal polarizations or must be rotated $90°$.

Need for more accurate electrical characterization of lesions
 Research on breast cancer detection using microwaves will certainly benefit for a more accurate electrical and geometrical representation of the different kinds of tumors. Currently spherical homogeneous tumors are considered, which is far from the reality. Actually, malignant tumors are lumps with an irregular shape (not round) with a pebbly surface. However, this is probably a really difficult information to obtain, since it requires a quick measurement just after the excision subject to a very restrictive medical protocols.

Finish the arrayed experimental prototype
 The validation of the MC tomographic method will be faster, more comfortable and more accurate with an arrayed experimental prototype. This is still not a clinical-ready prototype but having the possibility to perform a complete measurement with a few minutes, will possibly open the door to initial clinical measurements.

Perform initial clinical tests
 While the numerical simulations are essential for the initial assessment of the algorithm, they are a necessary but not a sufficient condition to demonstrate its screening capability. Thus the trend is to proceed to clinical tests to ensure trustworthiness in the proposed algorithm or system.

Establish a fruitful collaborative work between research groups

A collaborative work between the research groups involved in microwave imaging for medical applications along the same lines as the initial work performed between the European and Canadian universities or the recent COST initiative, is crucial for the development of microwave imaging.

A

SCATTERING BY A DIELECTRIC CYLINDER

The analytic calculation of the scattering produced by infinite dielectric cylinders in 2D is relatively simple and allows to estimate the scattered fields by objects with circular contours that can be assumed uniform in the z-direction, such as arms or legs. Let us consider the case of a cylindrical incident waves generated by a current filament I parallel to a centered dielectric cylinder of radius a and relative permittivity $\epsilon'_c(f)$ immersed in a background medium of relative permittivity $\epsilon'_b(f)$. The source S is situated at a distance $|\vec{r}_{TC}|$ and at an azimuth angle ϕ_T of the cylinder C and the fields are measured at a point R situated at a distance $|\vec{r}_{CR}|$ and angle ϕ_R, as shows Figure A.1.
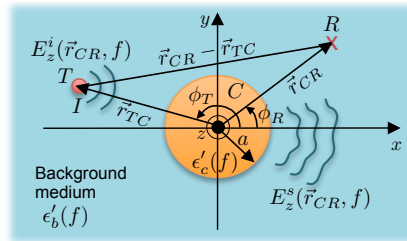
Figure A.1: Dielectric cylinder illuminated by a cylindrical wave.

In this case the scalar wave equation (TM mode) in cylindrical coordinates can be used, leading to solutions of the form $E = R(|\vec{r}|) \cdot \Phi(\phi)$ [64], where the radial functions, $R(|\vec{r}|)$, are the Bessel functions and the angular functions are harmonic functions. Commonly used solutions to Bessel's equation are: Bessel functions of first kind, $J_n(k|\vec{r}|)$, and Hankel functions of second kind, $H_n^{(2)}(k|\vec{r}|)$, which represent outward-travelling waves if $|\vec{r}| \to \infty$.

The incident field produced by a current filament situated along z-axis at a distance $|\vec{r}_{TC}|$ to

the origin of coordinates is:

$$E_z^i(\vec{r}_{CR}, f) = -\frac{\pi f \mu_0 I}{2} H_0^{(2)}(k_b |\vec{r}_{CR} - \vec{r}_{TC}|)$$ (A.1)

By using the addition theorem for the Hankel functions, the cylindrical wave can be expressed as the combination of centered cylindrical modes, as follows:

$$E_z^i(\vec{r}_{CR}, f) = -\frac{\pi f \mu_0 I}{2} \begin{cases} \sum_{n=-\infty}^{\infty} J_n(k_b |\vec{r}_{TC}|) H_n^{(2)}(k_b |\vec{r}_{CR}|) e^{jn(\phi_R - \phi_T)} & |\vec{r}_{CR}| > |\vec{r}_{TC}| \\ \sum_{n=-\infty}^{\infty} J_n(k_b |\vec{r}_{CR}|) H_n^{(2)}(k_b |\vec{r}_{TC}|) e^{jn(\phi_R - \phi_T)} & a < |\vec{r}_{CR}| < |\vec{r}_{TC}| \\ \sum_{n=-\infty}^{\infty} J_n(k_c |\vec{r}_{CR}|) \frac{J_n(k_b a)}{J_n(k_c a)} H_n^{(2)}(k_b |\vec{r}_{TC}|) e^{jn(\phi_R - \phi_T)} & |\vec{r}_{CR}| < a < |\vec{r}_{TC}| \end{cases}$$

$$J_n(k_b |\vec{r}_{TC}|) H_n^{(2)}(k_b |\vec{r}_{CR}|) = J_n(k_b |\vec{r}_{CR}|) H_n^{(2)}(k_b |\vec{r}_{TC}|) \Big|_{|\vec{r}_{CR}| = |\vec{r}_{TC}|}$$

$$J_n(k_c |\vec{r}_{CR}|) = J_n(k_c |\vec{r}_{CR}|) \frac{J_n(k_b a)}{J_n(k_c a)} \Big|_{|\vec{r}_{CR}| = a}$$ (A.2)

The scattered field by a cylinder can be the expressed as:

$$E_z^s(\vec{r}_{CR}, f) = -\frac{\pi f \mu_0 I}{2} \begin{cases} \sum_{n=-\infty}^{\infty} c_n H_n^{(2)}(k_b |\vec{r}_{TC}|) H_n^{(2)}(k_b |\vec{r}_{CR}|) e^{jn(\phi_R - \phi_T)} & |\vec{r}_{CR}| > a \\ \sum_{n=-\infty}^{\infty} c_n J_n(k_c |\vec{r}_{CR}|) \frac{H_n^{(2)}(k_b a)}{J_n(k_c a)} H_n^{(2)}(k_b |\vec{r}_{TC}|) e^{jn(\phi_R - \phi_T)} & |\vec{r}_{CR}| < a \end{cases}$$

$$H_n^{(2)}(k_b |\vec{r}_{CR}|) = J_n(k_c |\vec{r}_{CR}|) \frac{H_n^{(2)}(k_b a)}{J_n(k_c a)} \Big|_{|\vec{r}_{CR}| = a}$$ (A.3)

Finally, the total field can be calculated as the superposition between the incident and the scattered fields, hence:

$$E_z(\vec{r}_{CR}, f) = -\frac{\pi f \mu_0 I}{2} \begin{cases} \sum_{n=-\infty}^{\infty} H_n^{(2)}(k_b |\vec{r}_{CR}|) \left(J_n(k_b |\vec{r}_{TC}|) + c_n H_n^{(2)}(k_b |\vec{r}_{TC}|) \right) e^{jn(\phi_R - \phi_T)} & |\vec{r}_{CR}| > |\vec{r}_{TC}| \\ \sum_{n=-\infty}^{\infty} H_n^{(2)}(k_b |\vec{r}_{TC}|) \left(J_n(k_b |\vec{r}_{CR}|) + c_n H_n^{(2)}(k_b |\vec{r}_{CR}|) \right) e^{jn(\phi_R - \phi_T)} & a < |\vec{r}_{CR}| < |\vec{r}_{TC}| \\ \sum_{n=-\infty}^{\infty} \frac{H_n^{(2)}(k_b |\vec{r}_{TC}|)}{J_n(k_c a)} \left(J_n(k_b a) + c_n H_n^{(2)}(k_b a) \right) J_n(k_c |\vec{r}_{CR}|) e^{jn(\phi_R - \phi_T)} & |\vec{r}_{CR}| < a < |\vec{r}_{TC}| \end{cases}$$

$$H_n^{(2)}(k_b |\vec{r}_{CR}|) \left(J_n(k_b |\vec{r}_{TC}|) + c_n H_n^{(2)}(k_b |\vec{r}_{TC}|) \right) = H_n^{(2)}(k_b |\vec{r}_{TC}|) \left(J_n(k_b |\vec{r}_{CR}|) + c_n \, H_n^{(2)}(k_b |\vec{r}_{CR}|) \right) \Big|_{|\vec{r}_{CR}| = |\vec{r}_{TC}|}$$

$$H_n^{(2)}(k_b |\vec{r}_{TC}|) \left(J_n(k_b |\vec{r}_{CR}|) + c_n H_n^{(2)}(k_b |\vec{r}_{CR}|) \right) = \frac{H_n^{(2)}(k_b |\vec{r}_{TC}|)}{J_n(k_c a)} \left(J_n(k_b a) + c_n H_n^{(2)}(k_b a) \right) J_n(k_c |\vec{r}_{CR}|) \Big|_{|\vec{r}_{CR}| = a}$$
(A.4)

At the cylinder, the boundary condition on the continuity of the tangential fields must be met: $E_z|_b = E_z|_c$, $E_\perp|_b = E_\perp|_c$. From the previous condition

$$c_n = -\frac{J_n(k_b a)}{H_n^{(2)}(k_b a)} \left[\frac{\dfrac{\epsilon_c J_n'(k_c a)}{\epsilon_b k_c a J_n(k_c a)} - \dfrac{J_n'(k_b a}{k_b a J_n(k_b a)}}{\dfrac{\epsilon_c J_n'(k_c a)}{\epsilon_b k_c a J_n(k_c a)} - \dfrac{H_n^{(2)'}(k_b a)}{k_b a H_n^{(2)}(k_b a)}} \right] \tag{A.5}$$

where $B_n'(x) = B_{n-1} - \frac{n}{x} B_n$, $B_n(x)$ denotes any Bessel function.

Note that the plane wave incidence is a particular case of the cylindrical wave incidence where $|\vec{r}_{TC}| \to \infty$. Also the following procedure can be easily extended for an arbitrary number of layers of the dielectric object.

B

PLANE WAVE SYNTHESIS

This appendix is aimed to the derivation of the analytic expressions of the current coefficients $I_z(\vec{r}'_{ij}, f; \hat{r})$ to be applied to each probe, placed at $\vec{r}'_{ij}$, of a circular (2D) or cylindrical (3D) array, that when acting as a transmitter produces a plane wave directed to $\hat{r}$.

B.1   Plane wave synthesis on 2D circular geometries

Figure B.1 shows the geometry for the 2D plane wave synthesis problem. It consists of a circular array of radius a inside a background medium of relative permittivity $\epsilon'_b(f)$. The ith-array element, placed at $\vec{r}'_i = a\cos\phi'_i \cdot \hat{x} + a\sin\phi'_i \cdot \hat{y}$ is excited with a current $I_z(\phi'_i, f; \phi)$ that will be calculated in this section to obtain a plane wave directed to $\hat{r} = \cos\phi \cdot \hat{x} + \sin\phi \cdot \hat{y}$ inside the circular region of radius R.

A plane wave propagating towards $\hat{\phi}$ can be expressed in terms of cylindrical modes as follows [136]:

$$E^{pw}(\vec{r}, f; \hat{r}) = e^{-jk_b(f)\hat{r}\cdot\vec{r}} = \sum_{n=-\infty}^{\infty} j^{-n} J_n(k_b R) e^{jn(\phi-\varphi)} \tag{B.1}$$

J_n are the incident modes modeled by the Bessel's function of first kind. Alternatively, the incident field can be also expressed using the integral equation 3.1 particularized for the 2D Green's function (equation 2.26):

$$E(\vec{r}'_i, f; \vec{r}) = -\frac{\pi f \mu_0}{2} \int_{v'} J(\vec{r}'_i, f) H_0^{(2)}(k_b|\vec{r} - \vec{r}'_i|) \, d\vec{v}' \tag{B.2}$$

Particularizing for a circular array of ideal vertically-polarized probes (line sources), the electric field B.2 can be written as the superposition of the fields of each probe [136].

$$E(\vec{r}'_i, f; \hat{r}) = -\frac{\pi f \mu_0}{2} \sum_{i=0}^{N_\phi} I_z(\phi'_i, f; \phi) H_0^{(2)}(k_b a) \tag{B.3}$$

131
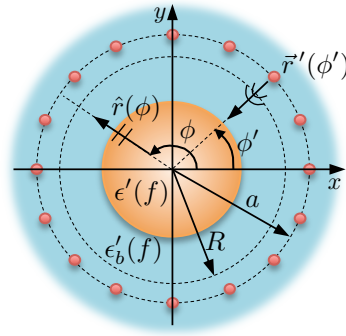
Figure B.1: Plane wave synthesis in a circle of radius R centered in a circular array of radius a composed by N_ϕ angularly equispaced probes immersed in a background medium of relative permittivity $\epsilon'_b(f)$.

Expanding $H_0^{(2)}(k_b a)$ in cylindrical modes using the addition theorem for the Bessel's functions [64]

$$H_0^{(2)}(k_b a) = \sum_{n=-\infty}^{\infty} H_n^{(2)}(k_b a) J_n(k_b R) e^{jn(\phi'_i - \varphi)} \quad R < a \tag{B.4}$$

replacing B.4 in B.3

$$E(\phi'_i, f; \phi) = -\frac{\pi f \mu_0}{2} \sum_{i=0}^{N_\phi} I_z(\phi'_i, f; \phi) \sum_{n=-\infty}^{\infty} H_n^{(2)}(k_b a) J_n(k_b R) e^{jn(\phi'_i - \varphi)} \tag{B.5}$$

Equating expression B.1 and B.5, the current coefficients are obtained:

$$I_z(\phi'_i, f; \phi) = -\frac{1}{\pi^2 f \mu_0 a} \sum_{|n|>0}^{k_b a} \frac{j^{-n}}{H_n^{(2)}(k_b a)} e^{jn(\phi - \phi'_i)} \tag{B.6}$$

B.2 Plane wave synthesis on 3D cylindrical geometries

The derivation of the current coefficients to synthesize a plane wave in 3D geometries is much more cumbersome than in 2D circular geometries. Thus, alternatively to the direct process performed in 2D, an indirect procedure is proposed here based on the radiation pattern measurement with a compact system [137]. In such a system, the measurement probe is not in far field conditions with respect to the antenna under test (AUT), whereas the radiation pattern measurement assumes far-field conditions or plane wave propagation. If instead of a single probe, an array is used, a plane wave directed to $\hat{r} = \sin\theta\cos\phi \cdot \hat{x} + \sin\theta\sin\phi \cdot \hat{y} + \cos\theta \cdot \hat{z}$ can be synthesized by exciting each element, placed at $\vec{r}'_{ij} = a\cos\phi'_{ij} \cdot \hat{x} + a\sin\phi'_{ij} \cdot \hat{y} + z'_{ij} \cdot \hat{z}$, with the proper weights, $w(\vec{r}'_{ij}, f; \hat{r})$. Figure B.2 shows the geometry for the plane wave synthesis problem with a cylindrical array of radius a inside a background medium of relative permittivity $\epsilon'_b(f)$.
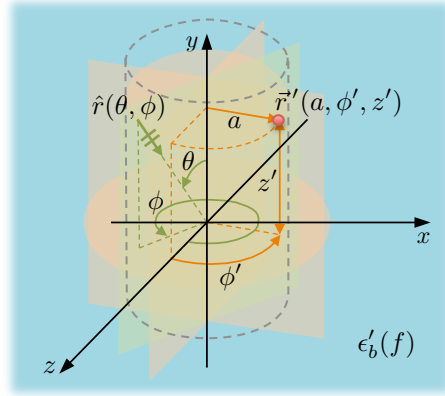
Figure B.2: Plane wave synthesis in a cylindrical array of radius a with a background medium of relative permittivity $\epsilon'_b(f)$.

The indirect method proposes to place the AUT inside the cylindrical array and check that the effects produced by the weights applied to each array's element on the AUT are effectively that of a $\hat{e}$-polarized plane wave defined as:

$$\vec{E}^{pw}(\vec{r}, f) = e^{-jk_b(f)\hat{r}\vec{r}} \cdot \hat{e} \tag{B.7}$$

where $k_b\hat{r} = k_{b,x}\hat{x} + k_{b,y}\hat{y} + k_{b,z}\hat{z} = k_b \sin\theta \cos\phi \cdot \hat{x} + k_b \sin\theta \sin\phi \cdot \hat{y} + k_b \cos\theta \cdot \hat{z}; \quad \hat{e} \cdot k_b\hat{r} = 0$

This procedure proposes the comparison of two scenarios

(a) The AUT is placed in the antenna array that is weighted by the $w(\vec{r}'_{ij}, f; \hat{r})$ coefficients and the open-circuit voltage, v_{ca}, at the AUT is measured.

(b) The far field, $\vec{E}(\vec{r}, f)$, from an AUT is measured when the AUT is excited with an unitary input current $I(0)$

The equation defining scenario (a) is

$$v_{oc}(\vec{r}'_{ij}, f) = -\frac{1}{I(0)} \int_{v'} \vec{J}(\vec{r}'_{ij}, f) e^{-jk_b\hat{r}\vec{r}'_{ij}} \, d_{v'} = -\int_{v'} \vec{J}(\vec{r}'_{ij}, f) e^{-jk_b\hat{r}\vec{r}'_{ij}} \, d_{v'} \tag{B.8}$$

where $\vec{J}(\vec{r}'_{ij}, f)$ is the current distribution at the AUT when acting as a transmitter and with a input current $I(0)$. If the array is virtual, that is, a single probe is moved in an number of positions on the surface of the cylinder, the response of the AUT to the whole array is

$$v_{oc}(\theta, \phi) = \int_0^{2\pi} \int_{-\infty}^{\infty} w(z'_{ij}, \phi'_{ij}; \theta, \phi) v_p(z'_{ij}, \phi'_{ij}) \, d\phi'_{ij} dz'_{ij} \tag{B.9}$$

where $v_p(z'_{ij}, \phi'_{ij})$ is the voltage measured at the AUT when a probe located at z'_{ij}, ϕ'_{ij} on the cylinder is transmitting.

The equation corresponding to scenario (b) is obtained using the integral equation 3.1 particularized for the 3D Green's function (equation 2.25) for large distances:

$$\vec{E}(\vec{r}, f) = -\frac{jf\mu_0}{2} \frac{e^{-jk_b\vec{r}}}{r} \int_{v'} \vec{J}(\vec{r}', f) e^{jk_b\hat{r}\vec{r}'_{ij}} \, d_{v'} \tag{B.10}$$

If the weights w generate a plane wave, the open-circuit voltage of scenario (a) and the far field measured in scenario (b) are proportional along the direction of the plane wave generated by the array:

$$\vec{E}(\vec{r}, f) = v_{oc} \frac{e^{-jk_b \vec{r}}}{r} \tag{B.11}$$

Introducing B.9 into B.11:

$$\begin{bmatrix} E_\theta(\theta, \phi, f) \\ E_\phi(\theta, \phi, f) \end{bmatrix} = \frac{e^{-jk_b \vec{r}}}{r} \int_0^{2\pi} \int_{-\infty}^{\infty} w(z'_{ij}, \phi'_{ij}; \theta, \phi) \begin{bmatrix} v_1(\phi'_{ij}, z'_{ij}, f) \\ v_2(\phi'_{ij}, z'_{ij}, f) \end{bmatrix} d\phi'_{ij} dz'_{ij} \tag{B.12}$$

Note that, in principle, to obtain both θ and ϕ polarizations of the field, two probes are needed, one vertical (v_1) an the other horizontal (v_2). This can be achieved by simply rotating 90° a linear polarized antenna such as a dipole or a horn. In this case w is a matrix containing the weights to apply to probes 1 and 2 to create $\hat{\theta}$ and $\hat{\phi}$-polarized plane waves respectively. The weights depend on the radiation pattern of the probe. For an ideal electrical probe, the coefficients can be calculated as follows.

A plane wave field can be also expressed as an expansion in cylindrical modes:

$$E_\theta(\theta, \phi; f) = -2k_{b,\rho} \frac{e^{-jk_b r}}{r} \sum_{|n|>0}^{k_{b,\rho} a} b_n(k_{b,z}) j^{n+1} e^{jn\phi}$$

$$E_\phi(\theta, \phi; f) = 2k_{b,\rho} \frac{e^{-jk_b r}}{r} \sum_{|n|>0}^{k_{b,\rho} a} a_n(k_{b,z}) j^{n+1} e^{jn\phi} \tag{B.13}$$

where $k_{b,\rho} = k_b \sin\theta$, $k_{b,z} = k_b \cos\theta$ and $k_{b,\rho}^2 + k_{b,z}^2 = 1$. The summation must be extended to $n < |k_{b,\rho} \cdot a|$ to produce a plane wave in the whole internal volume of the cylinder. If the interest is to produce a plane wave in a smaller volume of radius R, then the summation should be $n < |k_{b,\rho} \cdot R|$.

The coefficients a_n and b_n can be obtained according to the formulation proposed by [138], based on obtaining the AUT's cylindrical modal coefficients. Let us consider the situation depicted in Figure B.3. The AUT is situated at the coordinate system defined by (x, y, z), where z corresponds to the cylinder main axis. A probe is placed at the position $(\rho'' = a, \phi'', z'')$ inside the volume v'' expressed in the double primed-coordinate system[1]. To the volume V defined by the cylinder Σ_1, the Lorentz reciprocity theorem in integral form is applied [138]. Making the following assumptions

(a) No double interactions between the probe and the AUT.

(b) The scattered fields by the probe are negligible in front of the fields radiated by the AUT.

(c) The products between scattered fields are negligible in front of the rest of the terms.

the reciprocity theorem leads to:

$$\iint_{\Sigma_1} \left[(\vec{E}_a \times \vec{H}_p - \vec{E}_p \times \vec{H}_a) \right] d\vec{S} = -v_{oc}(\rho'' = a, \phi'', z'') \tag{B.14}$$

---

[1]Note the difference between the coordinates of the probe in the reference coordinate system ($\rho' = a, \theta', z'$), the coordinates of the probe in the new double primed-coordinate system ($\rho'' = a, \theta'', z''$), and the direction of the plane wave (θ, ϕ).
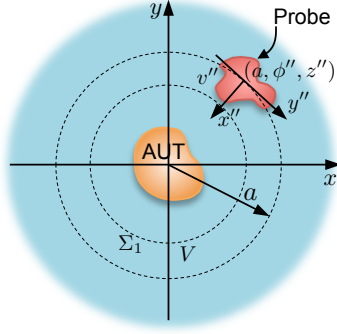
Figure B.3: The AUT is situated at the coordinate system defined by (x, y, z), where z corresponds to the cylinder main axis. A probe is placed at the position $(\rho'' = a, \phi'', z'')$ inside the volume v''.

Where $\vec{E}_a$, $\vec{H}_a$, $\vec{E}_p$ and $\vec{H}_p$ are the fields produced by the AUT (a) and the probe (p) respectively. Their cylindrical wave expansion over Σ_1 can be written in the form[2]:

$$\vec{E}_a(\rho, \phi, z) = - \sum_{n=-\infty}^{\infty} \int_{-\infty}^{\infty} \left[a_n(k_{b,z})\vec{M}_n(k_{b,z}) + b_n(k_{b,z})\vec{N}_n(k_{b,z}) \right] dk_{b,z}$$

$$\vec{H}_a(\rho, \phi, z) = -\frac{j}{\eta} \sum_{n=-\infty}^{\infty} \int_{-\infty}^{\infty} \left[a_n(k_{b,z})\vec{N}_n(k_{b,z}) + b_n(k_{b,z})\vec{M}_n(k_{b,z}) \right] dk_{b,z}$$

$$\vec{E}_p(\rho'', \phi'', z'') = - \sum_{m=-\infty}^{\infty} \int_{-\infty}^{\infty} \left[c_m(k_{b,z}'')\vec{M}_m''(k_{b,z}'') + d_m(k_{b,z}'')\vec{N}_m''(k_{b,z}'') \right] dk_{b,z}''$$

$$\vec{H}_p(\rho'', \phi', z'') = -\frac{j}{\eta} \sum_{m=-\infty}^{\infty} \int_{-\infty}^{\infty} \left[c_m(k_{b,z}'')\vec{N}_m''(k_{b,z}'') + d_m(k_{b,z}'')\vec{M}_m''(k_{b,z}'') \right] dk_{b,z}'' \qquad \text{(B.15)}$$

$$\vec{M}_n(k_{b,z}) = \left[\hat{\rho}\frac{jn}{\rho_1} - \hat{\phi}\frac{\partial}{\partial\rho_1}(\cdot) \right] H_n^{(2)}(k_{b,\rho}\rho_1)e^{jn\phi}e^{-jk_{b,z}z}$$

$$\vec{N}_n(k_{b,z}) = \left[\hat{\rho}\frac{jk_{b,z}}{k_b}\frac{\partial}{\partial\rho_1}(\cdot) - \hat{\phi}\frac{nk_{b,z}}{k_b\rho_1} + \hat{z}\frac{k_{b,\rho}^2}{k_b}(\cdot) \right] H_n^{(2)}(k_{b,\rho}\rho_1)e^{jn\phi}e^{-jk_{b,z}z}$$

being η is the wave impedance defined as $\eta = \sqrt{\frac{\mu_0}{\epsilon_b}}$.

To evaluate B.14, all the fields must be referred to the same coordinate system. Hence, the double primed-coordinate system is expressed in the reference coordinate system by means of the Graf's addition theorem for Bessel functions [139].

$$\vec{M}_m'(k_{b,z}) = e^{jk_{b,z}''(z-z')} \sum_l \left[-\hat{\rho}\frac{jl}{\rho_1} - \hat{\phi}\frac{\partial}{\partial\rho_1}(\cdot) \right] H_{m+l}^{(2)}(k_{b,\rho}''a)e^{jl(\phi-\phi_{ij}')} J_l(k_{b,\rho}''\rho_1)$$

$$\vec{N}_m'(k_{b,z}) = e^{jk_{b,z}''(z-z')} \sum_l \left[-\hat{\rho}\frac{-jk_{b,z}''}{k_b}\frac{\partial}{\partial\rho_1}(\cdot) - \hat{\phi}\frac{lk_{b,z}''}{k_b\rho_1} + \hat{z}\frac{k_{b,\rho}''^2}{k_b} \right] \cdot \qquad \text{(B.16)}$$
$$H_{m+l}^{(2)}(k_{b,\rho}''a)e^{jl(\phi-\phi_{ij}')} J_l(k_{b,\rho}''\rho_1)$$

---

[2]From this point the frequency dependence is not indicated and thus assumed

By solving equation B.14 for B.15 and B.16 leads to:

$$a_n(k_{b,z}) = -\frac{k_b\eta}{16\pi^2 k_{b,\rho}^2} \frac{\tilde{v}_1(n,k_{b,z})b_n^{(2)}(-k_{b,z}) - \tilde{v}_2(n,k_{b,z})b_n^{(1)}(-k_{b,z})}{\Delta(n,k_{b,z})}$$

$$b_n(k_{b,z}) = -\frac{k_b\eta}{16\pi^2 k_{b,\rho}^2} \frac{\tilde{v}_2(n,k_{b,z})a_n^{(1)}(-k_{b,z}) - \tilde{v}_1(n,k_{b,z})a_n^{(2)}(-k_{b,z})}{\Delta(n,k_{b,z})}$$

(B.17)

where $\Delta(n,k_{b,z}) = a_n^{(1)}(-k_{b,z})b_n^{(2)}(-k_{b,z}) - a_n^{(2)}(-k_{b,z})b_n^{(2)}(-k_{b,z})$ and

$$a_n^{(1),(2)}(-k_{b,z}) = \sum_{m=-\infty}^{\infty} c_m^{(1),(2)}(-k_{b,z})H_{m+n}^{(2)}(k_{b,\rho}a)$$

$$b_n^{(1),(2)}(-k_{b,z}) = \sum_{m=-\infty}^{\infty} d_m^{(1),(2)}(-k_{b,z})H_{m+n}^{(2)}(k_{b,\rho}a)$$

(B.18)

being $\tilde{v}_1$ and $\tilde{v}_2$ are the Fourier transforms of the open-circuit voltage of probes 1 and 2 in terms of the probe coefficients $c_m^{(1)}$, $c_m^{(2)}$, $d_m^{(1)}$ and $d_m^{(2)}$ defined as:

$$\tilde{v}_{oc}(\rho'_{ij} = a, n, k_{b,z}) = \frac{1}{2\pi}\int_0^{2\pi}\int_{-\infty}^{\infty} v_{oc}(\rho'_{ij} = a, \phi'_{ij}, z'_{ij})e^{-jn\phi'_{ij}}e^{jk_{b,z}z'_{ij}}\,d\phi'_{ij}dz'_{ij}$$

(B.19)

Introducing equations B.17 into B.13 an identifying terms with B.12, the expression for the w coefficients is obtained.

$$w(z'_{ij},\theta'_{ij};\theta,\phi) = \frac{\eta}{16\pi^3\sin\theta}e^{jk_{b,z}z'_{ij}}\sum_{|n|>0}^{k_{b,\rho}a} j^{n+1}\frac{1}{\Delta(n,k_{b,z})}e^{jn(\phi-\phi'_{ij})}\begin{bmatrix} -a_n^{(2)} & a_n^{(1)} \\ -jb_n^{(2)} & jb_n^{(1)} \end{bmatrix}$$

(B.20)

The probe coefficients of equation B.18, $c_m^{(1)}$, $c_m^{(2)}$, $d_m^{(1)}$ and $d_m^{(2)}$, depend on the radiation pattern of the probe. For the sake of simplicity, the coefficients will be derived for the case of an ideal electric probe. That is the reason why dipole like antennas are used in the experimental system. Equating the modal fields expressed as equation B.13 and the asymptotic expressions of the far-field:

$$E_\theta(r,\theta,\phi) = j\frac{1}{2\pi}k_{b,x}\frac{e^{-jk_b r}}{r}A_\theta(k_{b,y},k_{b,z})$$

$$E_\phi(r,\theta,\phi) = j\frac{1}{2\pi}k_{b,x}\frac{e^{-jk_b r}}{r}A_\phi(k_{b,y},k_{b,z})$$

(B.21)

then,

$$d_m(k_{b,z}) = -\frac{1}{8\pi^2}j^{-m}\int_0^{2\pi}\cos\phi A_\theta(k_{b,y},k_{b,z})e^{-jm\phi}\,d\phi$$

$$c_m(k_{b,z}) = -\frac{1}{8\pi^2}j^{-(m+1)}\int_0^{2\pi}\cos\phi A_\phi(k_{b,y},k_{b,z})e^{-jm\phi}\,d\phi$$

(B.22)

The angular spectrum of plane waves, A_θ and A_ϕ, in absence of magnetic currents can be expressed as:

$$\vec{A}_E = \eta\bar{X}_1\vec{B}_J$$

$$\vec{B}_J(k_{b,y},k_{b,z}) = \int_{v'}\vec{J}e^{jk_b\hat{r}\vec{r}'_{ij}}\,dv'$$

(B.23)

$$\bar{X}_1 = -\frac{k_b}{2k_{b,z}} \begin{bmatrix} 1 - \frac{k_{b,x}^2}{k_b^2} & -\frac{k_{b,x}k_{b,y}}{k_b^2} & -\frac{k_{b,x}k_{b,z}}{k_b^2} \\ -\frac{k_{b,x}k_{b,y}}{k_b^2} & 1 - \frac{k_{b,y}^2}{k_b^2} & -\frac{k_{b,y}k_{b,z}}{k_b^2} \\ -\frac{k_{b,x}k_{b,z}}{k_b^2} & -\frac{k_{b,y}k_{b,z}}{k_b^2} & 1 - \frac{k_{b,z}^2}{k_b^2} \end{bmatrix}$$

Particularizing for a $\hat{\theta}$-polarized ideal probe with a current of the form $\vec{J}(x', y', z') = \hat{z}\,\delta(x')\delta(y')$, and expressing the angular plane wave spectrum in spherical coordinates:

$$A_\theta(k_{b,y}, k_{b,z}) = \frac{\eta}{2\cos\phi}$$

$$A_\phi(k_{b,y}, k_{b,z}) = 0 \tag{B.24}$$

Introducing equation B.24 to B.22

$$c_m^{(1)}(k_{b,\rho}, k_{b,z}) = 0$$

$$d_n^{(1)}(k_{b,\rho}, k_{b,z}) = \begin{cases} -\frac{\eta}{8\pi} & n = 0 \\ 0 & n \neq 0 \end{cases} \tag{B.25}$$

Finally, introducing B.25 to B.18

$$a_n^{(1)}(k_{b,\rho}, k_{b,z}) = 0$$

$$b_n^{(1)}(k_{b,\rho}, k_{b,z}) = \frac{\eta}{8\pi} H_n^{(2)}(k_{b,\rho}a) \tag{B.26}$$

Applying the same for a $\hat{\phi}$-polarized ideal probe of the form $\vec{J}(x', y', z') = \hat{y}\,\delta(x')\delta(z')$,

$$A_\theta(k_{b,y}, k_{b,z}) = -\frac{\eta}{2}\frac{\cos\theta\sin\phi}{\sin\theta\cos\phi}$$

$$A_\phi(k_{b,y}, k_{b,z}) = -\frac{\eta}{2\sin\theta}$$

$$c_n^{(2)}(k_{b,\rho}, k_{b,z}) = \begin{cases} \frac{\eta k_b}{16\pi k_{b,\rho}} & |n| = 1 \\ 0 & |n| \neq 1 \end{cases}$$

$$d_n^{(2)}(k_{b,\rho}, k_{b,z}) = \begin{cases} -\frac{\eta k_{b,z}}{16\pi k_{b,\rho}} & |n| = 1 \\ 0 & |n| \neq 1 \end{cases} \tag{B.27}$$

$$a_n^{(2)}(k_{b,\rho}, k_{b,z}) = -\frac{\eta k_b}{8\pi k_{b,\rho}} H_n^{(2)\prime}(k_{b,\rho}a)$$

$$b_n^{(2)}(k_{b,\rho}, k_{b,z}) = \frac{\eta k_{b,z} n}{8\pi k_{b,\rho}^2 a} H_n^{(2)}(k_{b,\rho}a)$$

Once the probe coefficients have been calculated, let us go back to the expression B.12 and calculate the weights w that, eventually, can be identified as the current coefficients I.

$$w(z'_{ij}, \phi'_{ij}; \theta, \phi) = \frac{1}{2\pi^2} e^{jk_{b,z}z'_{ij}} \sum_{|n|>0}^{k_{b,\rho}a} j^{n+1} e^{jn(\phi - \phi'_{ij})} \begin{bmatrix} \frac{1}{\sin\theta\, H_n^{(2)}(k_{b,\rho}a)} & 0 \\ -j\frac{k_{b,z}n}{k_{b,\rho}a H_n^{(2)\prime}(k_{b,\rho}a)} & j\frac{1}{H_n^{(2)\prime}(k_{b,\rho}a)} \end{bmatrix}$$
$$\tag{B.28}$$

From the previous equation, it can be observed that to produce a vertically polarized plane wave, only vertical currents are needed and can be expressed as:

$$I_z(z'_{ij}, \phi'_{ij}, f; \theta, \phi) = -\frac{1}{2\pi^2} e^{jk_{b,z}z'_{ij}} \sum_{|n|>0}^{k_{b,\rho}a} j^{n+1} e^{jn(\phi-\phi'_{ij})} \frac{1}{\sin\theta H_n^{(2)}(k_{b,\rho}a)} \frac{\delta(\rho'_{ij}-\rho)}{\rho'_{ij}} \hat{z}$$

(B.29)

while to produce a $\hat{\phi}$-polarized plane wave, both horizontal and vertical currents are required.

$$I_\phi(z'_{ij}, \phi'_{ij}, f; \theta, \phi) = -\frac{1}{2\pi^2} e^{jk_{b,z}z'_{ij}} \sum_{|n|>0}^{k_{b,\rho}a} j^{n+1} e^{jn(\phi-\phi'_{ij})}.$$

$$\left[-j \frac{k_{b,z}n}{k_{b,\rho}^2 a H_n^{(2)\prime}(k_{b,\rho}a)} \hat{z} + j \frac{1}{H_n^{(2)\prime}(k_{b,\rho}a)} \hat{\phi} \right] \frac{\delta(\rho'_{ij}-\rho)}{\rho'_{ij}}$$

(B.30)
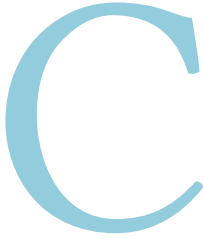
C
METRICS TO EVALUATE THE DETECTION CAPABILITY

This Appendix explains the metrics used along this thesis to evaluate the performance of the algorithms in terms of detection accuracy [140].

The first two metrics evaluate the tumor response compared to other neighboring tissues. The signal to cluter ratio (SCR) compares the maximum target response to the maximum clutter response in the same reconstructed image and is expressed in dB.

$$\text{SCR} = \frac{\text{Max. in target}}{\text{Max. clutter}} \tag{C.1}$$

In case of breast tumor detection, the target would be the tumor and the clutter any image artifact within the reconstruction domain. Thus, the SCR measures the image quality. The signal to mean ratio (SMR) compares the maximum target response with the mean response of the different tissues across the imaged body in the same reconstruction. It is also measured in dB. In case of breast cancer detection, the mean response of the tissues in the imaged body is calculated as the mean contrast value of all the pixels within the breast volume.

$$\text{SMR} = \frac{\text{Max. in target}}{\text{Mean in body}} \tag{C.2}$$

This metric is expected to be higher for canonical scenarios, where the target is embedded in homogeneous tissues. However for realistic breast phantoms, the target (tumor) is surrounded by fibroglandular tissues having a response of the same order of magnitude as the target.

The second group of metrics evaluate how accurate is the target positioning. To do so, two different metrics are defined. The first is the full width half maximum (FWHM). It measures the distance between the peak response of the reconstructed target and the point where this

response has dropped to the half. It is expressed in mm and gives an idea of the algorithm accuracy in retrieving the target size. The last metric called positioning accuracy (PA) measures the distance in mm between the peak response of the reconstructed target and the center of the original target.

The previous metrics are useful to evaluate the performance of the algorithm above all for the canonical scenarios. To evaluate the realistic voxeled reconstructions, since the target (tumor) response presents very similar contrasts to that of the surrounding tissues (fibroglandular tissue), the previous metrics, and above all the SCR, are not fair enough to evaluate the algorithm performance. Thus in order to ensure that the spot identified as target is effectively produced by the target and not by another tissue, the full to healthy ratio (FHR) is introduced. It calculates the relation between the summation of the contrast values of all the voxels contained in a sphere of the same size as the target for the full reconstruction (RF), and the summation of the contrast values in the same sphere for the healthy reconstruction (RH).

$$\text{FHR} = \frac{\text{RF}}{\text{RH}} \tag{C.3}$$

$$\text{RF} = \frac{\iiint c_{full}(\vec{r}) \cdot M(\vec{r}) \, d_{\vec{v}}}{\iiint c_{full}(\vec{r}) \, d_{\vec{v}}} \tag{C.4}$$

$$\text{RH} = \frac{\iiint c_{healthy}(\vec{r}) \cdot M(\vec{r}) \, d_{\vec{v}}}{\iiint c_{healthy}(\vec{r}) \, d_{\vec{v}}} \tag{C.5}$$

where $M(\vec{r})$ is a mask containing zeros at every point of the reconstructed space except inside a sphere of the same radius as the target. At these particular points, the mask contains ones.

D
SENSITIVITY, NOISE AND SAFETY ASSESSMENT

This Appendix is focused to the sensitivity and noise analysis in order to determine theoretically if the algorithm can cope with the experimental data. Moreover, the maximum level of SAR inside a breast phantom is calculated in order to ensure that the safety exposure levels are not exceeded.

D.1 Sensitivity analysis

The sensitivity study consists in determining the minimum level of received power, P_R that will arrive to the receiving antenna given a known input power P_i, as depicted in Figure D.1.
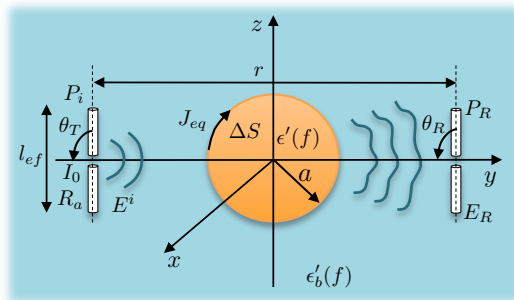
Figure D.1: Diagram of the setup used for the sensitivity study.

Let us establish a typical VNA sensitivity of -85 dBm, meaning that:

$$\frac{P_R}{P_i} = 10^{-8.5} \tag{D.1}$$

where $P_i = I_0^2 R_a$ being R_a the antenna resistance which is 73 Ω for a dipole and I_0 the input current at the antenna. The received power can be calculated as follows

$$P_R = \frac{|V_{ca}|^2}{4R_a} = \frac{l_{ef}^2 |E_R|^2}{4R_a} \tag{D.2}$$

where l_{ef} is the effective length of the antenna that is approximately 36 mm and $|E_R|$ is the field intensity at the receiving antenna that responds to the following expression if we assume a that the antenna is a half-wavelength dipole receiving by the direction of maximum radiation ($\theta_R = 90°$).

$$E_R = j60\frac{e^{-jkr}}{r}J_{eq}\Delta S\frac{\cos{(\pi/2\cos\theta_R)}}{\sin\theta_R} \tag{D.3}$$

J_{eq} is the current density induced on the object and $\Delta S = \pi a^2$ is the area of the object that is assumed to be spherical.

$$J_{eq} = j2\pi f(\epsilon - \epsilon_b)E \simeq J_{eq} = j2\pi f(\epsilon - \epsilon_b)E^i \tag{D.4}$$

In equation D.4 Born approximation has been applied ($E \simeq E^i$). E^i is the incident field generated by the transmitting half-wavelength expressed as

$$E^i = j60\frac{e^{-jkr}}{r}I_0\frac{\cos{(\pi/2\cos\theta_T)}}{\sin\theta_T} \tag{D.5}$$

where again $\theta_T = 90°$.

Going back to equation D.1, the minimum permittivity contrast expressed as $(\epsilon' - \epsilon_b') = \epsilon_b'c(\vec{r}, f)$ can be calculated leading to

$$\epsilon_b' \cdot c(\vec{r}, f) = \frac{1}{\pi a^2 \epsilon_0}\sqrt{\frac{P_R/P_I \cdot R_a \cdot r^4}{l_{ef}^2 \cdot 60^4 \cdot f^2 \cdot \pi^2}} \tag{D.6}$$

for a distance between the antennas of $r = 150$ mm and a frequency of $\epsilon_b'c(\vec{r}, f) = 0.0013$. Such a small permitted contrast indicates that the sensitivity will not be the limiting issue in the measurements. Accordingly, in the worst scenario, the contrast between tumors and the surrounding tissue was reported to be of the order of 0.02. Nevertheless, the previous calculation considered a situation where the antennas were transmitting and receiving by the direction of maximum radiation. Otherwise, the minimum contrast will be larger. As an example if $\theta_T = 220°$ and $\theta_R = 50°$, which is an extreme measurement situation, then $\epsilon_b'c(\vec{r}, f) = 0.0035$.

D.2   Noise analysis

In the experimental measurements, the desired signal will be contaminated by noise. In this section the theoretical permitted noise floor to obtain a correct reconstruction will be calculated

in terms of SNR. The results will depend on the complexity of the scenario and particularly to the contrast between the object to be detected and the surrounding. Let us focus on a realistic simulation such as as the 3D voxeled mostly fatty breast (section 4.2.3.1). Since it is one of the most complex scenarios studied in this thesis, it will be also one of the most restrictive.

The strength of the desired signal (S) is calculated from the simulated scattered field corresponding to the mostly fatty breast as

$$S = \frac{1}{N_z^2 N_\phi^2 N_f} \sum_{i=0}^{N_\phi} \sum_{j=0}^{N_\phi} \sum_{k=0}^{N_z} \sum_{l=0}^{N_z} \sum_{m=0}^{N_f} |E^s(z'_{T_{ij}}, \phi'_{T_{ij}}, f_m, z'_{R_{kl}}, \phi'_{R_{kl}})|^2 \tag{D.7}$$

A matrix of unitary power additive white Gaussian noise is reconstructed using the MC tomographic algorithm with the same conditions as the mostly fatty breast ($c_{n_0}(\vec{r}, f_n)$). Since the reconstruction algorithm is linear except the final magnitude combination, the noise power can be modified after the reconstruction as long as the magnitude combination is not performed. The dielectric contrast with noise can be obtained as

$$c(\vec{r}, f_n) = c_s(\vec{r}, f_n) + c_{n_0}(\vec{r}, f_n) \cdot \sqrt{\frac{S}{SNR}} \tag{D.8}$$

being $c_s(\vec{r}, f_n)$ the reconstructed dielectric contrast of the mostly fatty breast without noise at a frequency f_n and SNR the desired signal to noise ratio. Finally the magnitude combination is performed and $c_{MC}(\vec{r})$ is represented in Figure D.2.
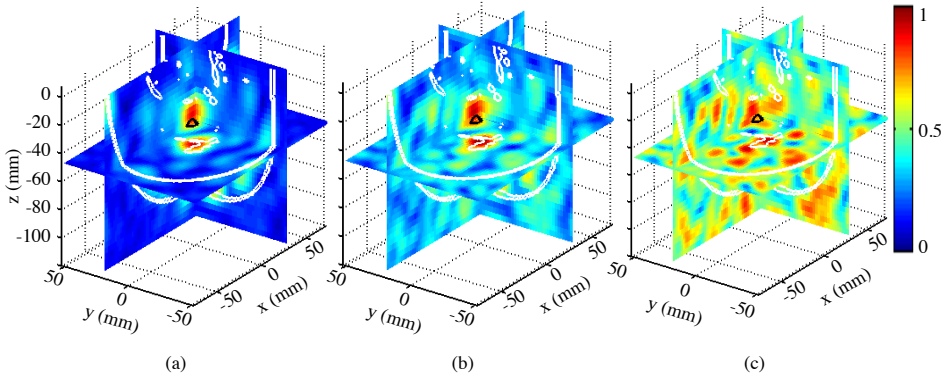
Figure D.2: MC reconstructions of a noisy simulation of the mostly fatty breast [85]. (a) SNR=0 dB, (b) SNR=-10 dB, (c) SNR=-20 dB.

It can be observed that the minimum permitted SNR is -10 dB. Such a small value could be explained thanks to the antenna gain given by the large amount of antennas that configure the acquisition system ($N_z^2 \times N_\phi^2 \times N_f$). Moreover this value is obtained with P_s equal to the power of the differential field (full measurement - skin measurement). If instead of the differential field, the absolute field (full mesurement) is used in equation D.8, the minimum SNR increases up to 50 dB. This means that the sensitivity of the VNA must be larger than -60 dBm (for an input power of 0 dBm) to obtain a reconstruction free of noise corruption. As said, the VNA with a typical sensitivity of -85 dBm is suitable for the measurements.

D.3   Safety levels with respect to human exposure

Another issue to be considered in systems interacting with human body is the compliance of the safety limits for the exposure to radio frequency waves. This limits are included in the International Commission on Non-Ionizing Radiation Protection (ICNIRP Guidelines) and the Institute of Electrical and Electronic Engineers (IEEE and ANSI Standard C95.1-2005) [141]. The purpose of the regulations is to provide the exposure limits to protect against adverse effects to human health induced by exposure to electromagnetic fields over the frequency range from 3 kHz to 300 GHz. The limits are intended to apply to all people with the exception of patients undergoing a procedure for medical diagnosis or treatment. The standard establishes the maximum levels of SAR depending on the localization and the exposure range according to: general public or controlled environments and localized or whole-body exposure. The most restrictive level is that of a general public whole-body exposure, while the less restrictive is for a localized exposure in a controlled environment. The SAR is a quantity used to quantify the compliance with safety standards that measures the time derivative of the incremental energy (dW) absorbed by an incremental mass (dm) contained in a volume element (dV) of density ρ.

$$SAR = \frac{d}{dt}\left(\frac{dW}{dm}\right) = \frac{d}{dt}\left(\frac{dW}{\rho dV}\right) \quad [\text{W/kg}] \tag{D.9}$$

SAR can be also related to the electric field at a point by

$$SAR = \frac{\sigma |E|^2}{\rho} \tag{D.10}$$

where σ is the conductivity of the tissue in S/m, ρ is the mass density in kg/m^3 and E is the rms electric field strength in V/m. Table D.1 shows the SAR levels for the aforementioned scenarios.

Localization	SAR public env.	SAR controlled env.
Whole-body exposure	0.08	0.4
Localized exposure	2	10
Localized exposure (extremities and pinnae)	4	20

Table D.1: SAR levels in W/kg for frequencies between 100 kHz and 3 GHz.

The SAR levels in a simplified breast phantom are simulated using CST. The illuminating signal is generated by a dipole situated at a distance of 40 mm from the breast skin with an input power of 0 dBm. The breast phantom consists of a sphere of 50 mm in radius composed by a uniform breast fatty tissue, a 2-mm thick skin layer and a spherical tumor of 15 mm in radius. The phantom is immersed in oil. Figure D.3 shows the simulation setup and Table D.2 summarizes the complex permittivity and mass density of the breast constituents. The simulation was performed at a frequency of 2 GHz.

Figure D.4 shows the SAR results along y axis. The values correspond to an average over 10 g of tissue as indicated in the standard. The maximum SAR is measured at the area of the breast

Component	ϵ'	σ	Mass density $[\text{kg/m}^3]$
Background	2.33	0	920
Skin	39	1.3	1100
Fat	5	0.1	1100
Tumor	55	1.6	1100
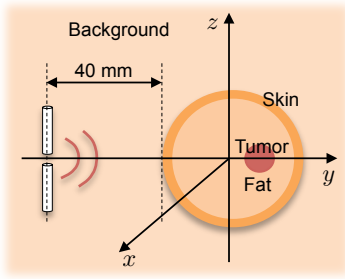
Figure D.3: Geometry of the SAR simulation setup.

Table D.2: Complex permittivities and mass density of the phantom used for the SAR simulation at 2 GHz.

closer to the dipole. The maximum SAR using an imput power of 0 dBm is below $1\,\text{mW/kg}$, far below the $10\,\text{W/kg}$ specified by the standard.
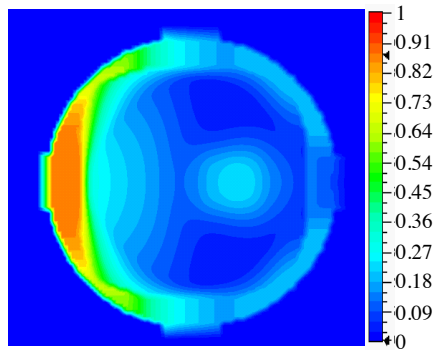
Figure D.4: Simulation results of the SAR in the breast phantom expressed in mW/kg.

E

Design of an Arrayed Cylindrical Acquisition System for Microwave Imaging

This appendix includes the design of an arrayed experimental system as depicted in Figure E.1. According to the state of the art on microwave imaging systems for medical applications, the main requirements for the design of an acquisition system based on two rotating arrays are listed below.

- Non-bulky, compact, portable and low cost acquisition system. A narrow array is desirable to avoid significant shadowing when an array passes behind the other during the rotation.

- Small size of the single element since the separation between elements must satisfy the Nyquist sampling criteria.

- Broadband antenna with a matching below -10 dB between 3-10 GHz (operating in air).

- Linear polarization, small cross-polarization level and low-coupling between elements.

- Compact feeding network avoiding cables from getting tangled.

E.1   Antenna Array

The bow-tie slot is the antenna typology that matched the previous requirements better. Unlike the electric dipole, the slot, allows the integration of the feeding network in the same antenna substrate, making the system much more compact. Moreover the radiation pattern is dipole-
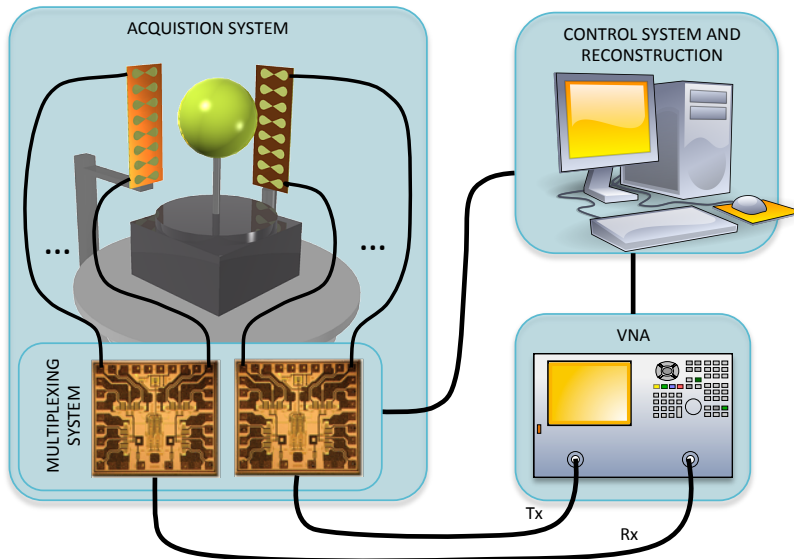
Figure E.1: Block diagram of the arrayed experimental system for microwave imaging for medical applications.

like, as required for the algorithm, and afford an easy and cheap manufacturing.

The bow-tie slot array is composed by two layers. The top layer contains $N_z = 8$ bow-tie horizontal radiating apertures on a metallic plane separated $\Delta_z = 20$ mm. The bottom layer contains the feeding lines. The substrate is ROGERS 4003 ($\epsilon' = 3.55$) of 0.5 mm in thickness.

E.1.1 Design of the bow-tie slot

The bow-tie antenna principle comes from the idea of designing frequency independent antenna. It could be theoretically accomplished by avoiding any dependence on lengths (and hence wavelengths) as occurs with the half-wavelength dipole. The infinitely long bow-tie antenna is sorely defined by the angle between two triangular metal pieces. In practical terms, the bow-tie antenna results from clipping the former structure after some distance. This antenna will have a similar radiation pattern to the dipole antenna, vertical polarization and much better bandwidth than a thin-wire dipole antenna.

The same reasoning is valid for bow-tie slots since they are dual antennas. The implications of duality with respect to the previous array arrangement (vertical dipoles) is that the electric and magnetic fields are interchanged and thus, the slots must be rotated 90° (horizontal slots). This is an advantage given the requirement of a maximum separation between elements of 20 mm. Figure E.2 and Table E.1 shows the main parameters of the designed bow-tie slot. Note that the edges of the bow-tie are rounded to improve the return loss and flatten the input impedance.

Figure E.3(a) shows the comparison between the simulated and measured return loss (S_{11}). The design and simulation of the single element was performed using Ansys HFSS simulation software. It can be observed that the matching is always below -5 dB between 3 and 10 GHz and
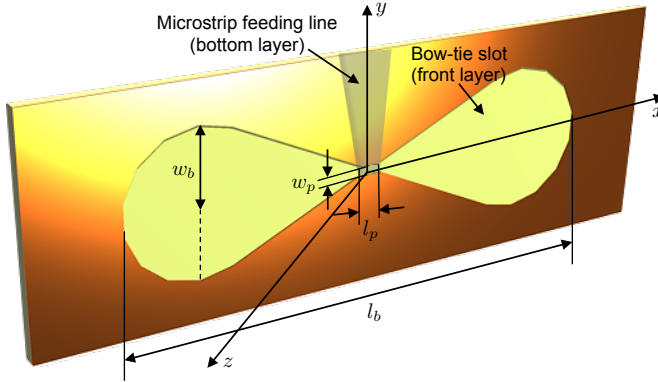
Figure E.2: Detail of the bow-tie slot.

Parameter	Value
l_b	37.5 mm
l_p	0.5 mm
w_f	0.27 mm
w_b	10 mm

Table E.1: Main parameters of the bow-tie slot.

below -10 dB between 4.5 and 8.5 dB. Figure E.3(b) corresponds to the evolution of the simulated resistance and reactance, showing an average resistance of 100 Ω. Figures E.3(c) and E.3(d) present the copolar and crosspolar components of the XZ and YZ planes of the radiation pattern. As expected, the direction of maximum radiation is the z-axis and the crosspolar component is negligible (lower than -45 dB), meaning that the polarization is linear.

E.1.2 Design of the feeding network

Once the single element is designed, the array is created by stacking 8 identical bow-tie slots. The slots are placed with its main axis along $\hat{x}$-direction and separated a distance of 20 mm along $\hat{y}$-direction. The feeding network is implemented with microstrip technology and is placed on the bottom layer of the substrate. The feeding lines are tapered in order to match the 50Ω of the SMA connector and the 100Ω at the antenna port. At the antenna port, the microstrip line is short circuited with the ground plane through the dielectric substrate with a metallized hole. At the other end, the feeding line is excited with a coaxial cable of 50Ω connected with a SMA connector. When considering the whole array structure for sensing purposes, the feeding lines must be designed to ensure the same conditions at each antenna of the array. This means negligible phase shift between the lines, low coupling and low attenuation. Figure E.4 shows a detail of the top and the bottom layer of the bow-tie slot array with the feeding network. Note that the lines corresponding to the antennas nearby the SMA connectors are meandered to ensure the same length with the lines corresponding to the more distant antennas. Figure E.5 shows the simulated attenuation and phase evolution of the 8 feeding lines over the frequency using Advanced Design System (ADS) from Agilent. In terms of module, the evolution is flat for all the antenna elements and presents a smooth variation over the frequency range. In terms of phase, the variation is moderate and bounded to a maximum phase shift of $10°$ ($\lambda/36$).

The first step towards the assessment of the whole array is to simulate the 8-element bow-tie slot array. Figure E.6(a) shows the coupling between the array elements 4 and 5 (S_{45}) and Figure E.6(b) between 5 and 6 (S_{56}). It can be observed that the coupling is always lower than -10 dB.
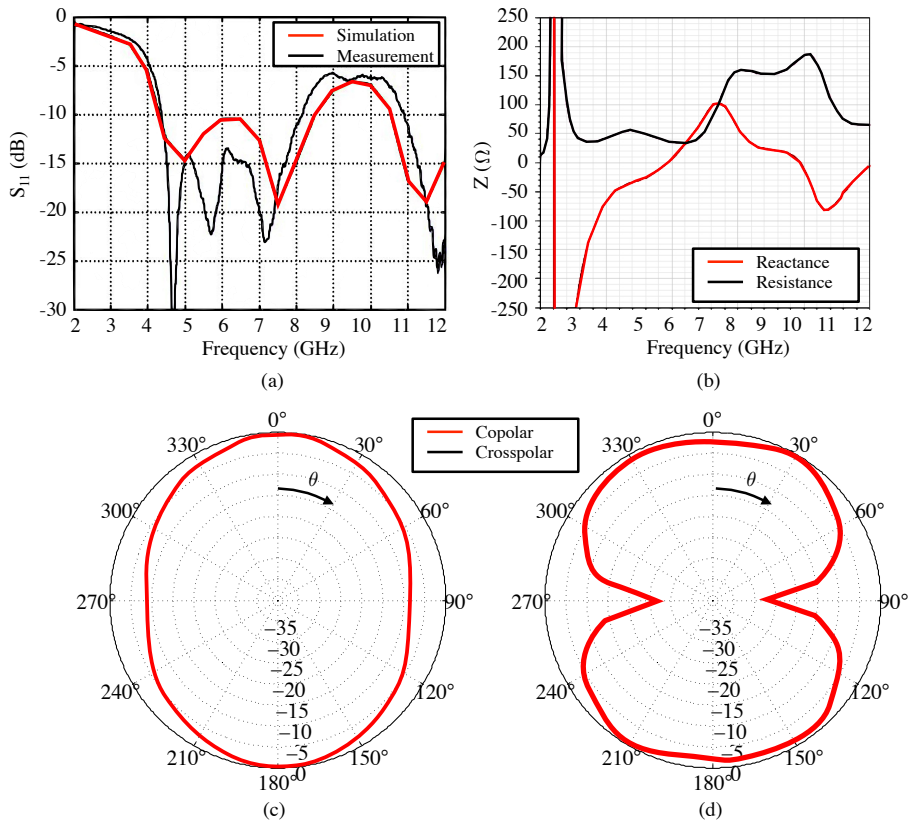
Figure E.3: Evolution of the bow-tie antenna parameters over the frequency. (a) Return loss, (b) Impedance, (c) XZ plane of the radiation pattern, (d) YZ plane of the radiation pattern.
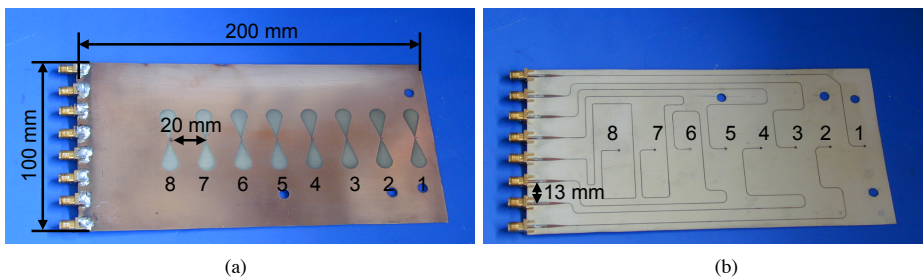
Figure E.4: Detail of the 8-element bow-tie slot array. (a) Front layer, (b) bottom layer.

E.1.3 Design of the multiplexing system

The multiplexing or switching system is composed by two main parts: the switching module and the control module. The switching module, Figure E.7, consists of a ROGERS 4003 substrate with CPW feeding lines that connect the 8 antenna ports of the array to the single-pole 8-throw
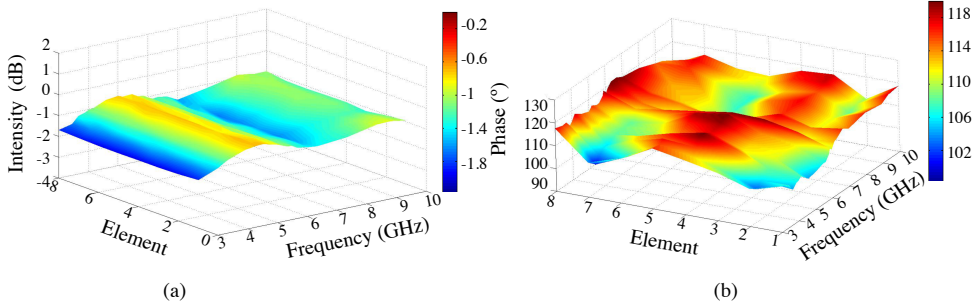
Figure E.5: Simulation results of the array feeding network. (a) Field intensity, (b) field phase.
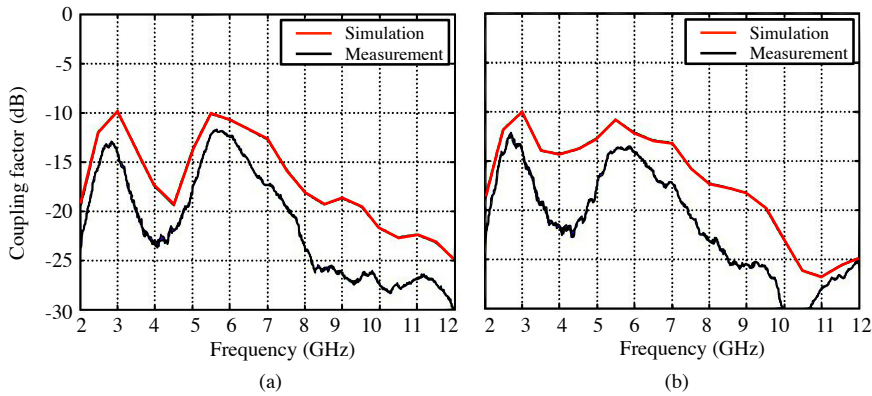
Figure E.6: Coupling factor of the 8-element bow-tie slot array. (a) S_{45}, (b) S_{56}.

(SP8T) switch. Since the circuit has only one layer, the CPW technique can be used. For this application, CPW is always preferable rather than microstrip since it presents less losses due to radiation. The CPWs were designed to have the same length to avoid phase shifts. Also a row of via holes was made at each side of the CPW to ensure the same voltage at both metallic faces of the substrate. The switch is a broadband non-reflective GaAs MESFET SP8T switch covering DC to 10 GHz [142]. It offers high isolation (typical 32 dB at 10 GHz) and low insertion loss (typical 2 dB at 4 GHz) and operates using negative bias of -5V. It must be connected via 0.025 mm diameter wire bonds. Due to size limitations imposed by the wire bond machine, the SP8T has to be mounted on a small substrate of 20 mm side (namely carrier in Figure E.7). The carrier is then fitted in a special hole performed in the switching module substrate. The cut lines are finally connected with wire bonds.

The control module consists of a printed circuit board that generates the control DC signals and the negative bias for the switching module. The control DC signals are generated according the signal coming from a USB port. To this port a computer is connected to control the whole system using Matlab. The control module is fed with DC signal of 12V. Two DB9 connectors deliver the generated control signals to the transmitting and receiving switching units respectively. Figure E.8 show a photograph of the control module printed circuit board.

(a)

(b)
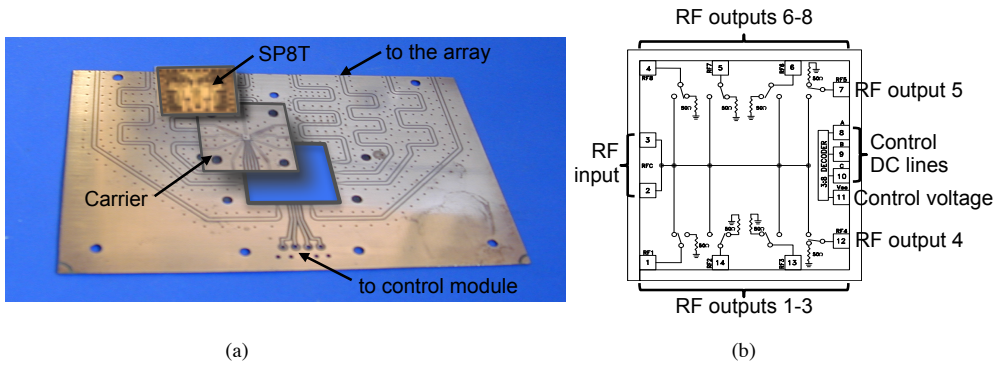
Figure E.7: Switching module. (a) Schematic view of the switching module, (b) SP8T functional diagram.
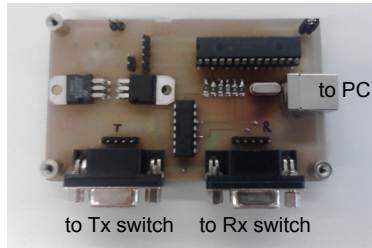
Figure E.8: Detail of the control module.

152

F

Tissue mimicking phantom manufacturing

This appendix includes the recipe used to create the glandular and tumor tissues for the realistic breast phantom considered in the 3D cylindrical measurements. The procedure to obtain the mixtures has been extracted from [130]. The ingredients and the weight percentage needed are summarized in Table F.1.

	Tumor	Gland
Water	74.627	45.654
Oil	7.679	43.526
Surfactant	0.711	0.338
Formaldehyde	0.313	0.358
p-tuloic acid	0.078	0
Agar-agar	13.357	0
Propylene glycol	0	2.839
Gelatin	0	7.286

Table F.1: Material weight percentage for tumor and gland.

F.1 Glandular tissue

The following are the steps for the fibroglandular tissue:

1. In a beaker at room temperature, add the propylene glycol and the deionized water by the amount mentioned in Table F.1. .

2. Slowly add, while stirring, the gelatin.

3. Cover the beaker with polyethylene food wrap and insert small hole in the top. Hold in place with a rubber band.

4. Place the beaker in a larger, metal or Pyrex container of hot water which in turn is placed on a heat source.

5. Heat the water until the gelatin mixture reaches 90°C and becomes transparent. Remove bubbles at the meniscus. This is the molten gelatin.

6. Remove the molten gelatin from the hot water bath and immerse partially in cold water bath.

7. As molten gelatin is cooling, heat the safflower oil to 50°C in a larger beaker.

8. Add the 50°C molten gelatin to the 50°C safflower oil and mix vigorously with a table spoon that is bent at a right angle to minimize disturbances on the surface.

9. Add "Mistol" (liquid surfactant) and continue stirring until the emulsion is nearly white and a separation of oil does not occur when stirring is stopped.

10. Cool in cold water bath to 40°C and slowly add, while stirring, the formalin (37% formaldehyde solution).

11. Cool the emulsion to 34°C and pour into molds for further cooling and congealing. Congealing temperature is approximately 26°C.

12. Cross-linking between formaldehyde and gelatin takes about 8 hours.

F.2 Tumor

For the tumor, the procedure is as follows:

1. Mix oil and surfactant by the amount mentioned in Table F.1.

2. Mix formaldehyde and p-toluic acid in a separate beaker and shake it to get a uniform light blue solution.

3. Heat up the water and add oil-surfactant while stirring the solution.

4. Add formaldehyde-p-toluic acid to the solution and stir continuously.

5. Add agar-agar pinch by pinch (1 tbsp per time). Mix to make a uniform solution.

F.3   Considerations

- The ingredients that have more impact on the material dielectric properties are the oil and the water.

- Once the chemicals are mixed, it can take 1-2 days to solidify. After this time they will keep their shape.

- To ensure the maximum shelf-life, the phantoms should be protected from moisture loss by thin plastic wraps or by placing them in air-tight containers.

- If they are not properly stored, the phantoms can become dehydrated with significant change of dielectric properties [128].

Figure F.1 show the measured dielectric properties of the manufactured phantom materials vs. the Debye estimate of dielectric properties of real breast tissue extracted from [130]. In these figures, the upper region belongs to very dense fibroglandular tissue and malignant tumors. The low water content tissue phantoms, followed by the transitional region containing 31-84% fat are in the lower regions. The lower region is for adipose or fatty tissues.
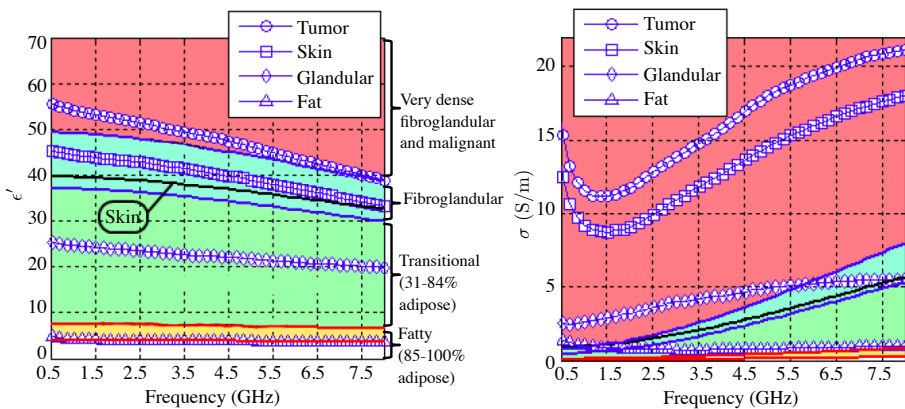
Figure F.1: Relative permittivity and conductivity of glandular tissue and tumor materials compared with the distribution of real tissue permittivity [130].

Nomenclature

Latin Letters

a	Radius of the region of interest	m
$\vec{B}$	Magnetic displacement field	tesla
c	Dielectric contrast	
c_0	Speed of light in vacuum, $c_0 \simeq 3 \cdot 10^9$	m/s
$\tilde{C}$	Spectrum of the dielectric contrast	
$\vec{B}$	Electric displacement field	C/m^2
$\vec{E}^i$	Incident electric field	V/m
$\vec{E}^i$	Total electric field	V/m
$\vec{E}^s$	Scattered electric field	V/m
$\tilde{E}$	Spectrum of the electric field	
f	Frequency	Hz
$\vec{H}$	Magnetic field	A/m
$\vec{J}$	Current density	A/m^2
j	Imaginary unit, $j = \sqrt{-1}$	
$\tilde{J}$	Spectrum of the electric current	
k	Wavenumber	
μ	Magnetic permeability	H/m
N	Number of	
$\vec{r}$	Position vector	

Greek Letters

Δ	Increment	
ϵ	Electric permittivity	F/m
ϵ^*	Complex relative permittivity	
ϵ''	Imaginary part of the complex relative permittivity	
ϵ'	Real part of the complex relative permittivity or dielectric constant	
ϵ_0	Permittivity of the vacuum, $\epsilon_0 = 1/(36\pi) \cdot 10^{-9}$	F/m
ϵ_b	Permittivity of the background medium	
ϵ_{eq}	Complex equivalent permittivity	

μ_0	Permeability of the vacuum, $\mu_0 = 4\pi \cdot 10^{-7}$	H/m
ϕ	Azimuthal angle	rad
ρ	Volumetric charge distribution	C/m^3
σ	Conductivity	S/m
σ_b	Conductivity of the background medium	S/m
ϕ	Polar angle	rad
ω	Angular frequency	rad/s

Superscripts

i	Incident
′	Relative to the antenna position
s	Scattered

Subscripts

0	Initial value
i	Iteration number
m	Measured
R	Relative to the receiver
T	Relative to the transmitter

Glossary

biopsy excision of a small piece of tissue for diagnostic examination.

dense breast tissue in terms of radiology, high breast density means more fibroglandular tissue and less adipose or fatty tissue.

false-negative a test result that indicates that the abnormality or disease being investigated is not present when in fact it is.

false-positive a test result that indicates that the abnormality or disease being investigated is present when in fact is not.

ionizing radiation radiation with enough energy so that during an interaction with an atom, it can remove tightly bound electrons from the orbit of an atom, causing the atom to become charged or ionized. Ionizing radiation is generally harmful and potentially lethal to live but can have health benefits in radiation therapy for the treatment of cancer and thyrotoxicosis in controlled doses. Its most common impact is the induction of cancer with a latent period of years or decades after exposure. High doses can cause visually dramatic radiation burns, and/or rapid fatality through acute radiation syndrome.

magnetic resonance imaging (MRI) imaging technique that uses radiofrequency (RF) waves in the presence of a strong magnetic field. The magnetic field is used to align the protons of the tissues, and the RF pulse is used to cause a change in their direction as it is absorbed by the protons. Different tissues relax at different rates emitting a measurable RF pulse, which is the basis of the imaging process.

malignancy a tumor that has the potential to become lethal through destructive growth or by having the ability to invade surrounding tissue and metastasize.

mammography technique for imaging breast tissues with x-rays.

MEEP free EM simulation code based on FDTD developed by MIT.

metastasis this term describes cancer that has spread from the affected organ to other areas of the body including soft tissues (lymph nodes, skin) or organs such as liver, lungs or bone.

nodal status indicates the presence or absence of cancer cells in glands or lymph nodes.

non-invasive medical procedure is strictly defined as non-invasive when no break in the skin is created and there is no contact with the mucosa, or skin break, or internal body cavity beyond a natural or artificial body orifice.

phantom model of the human body used in computerized analysis.

positron emission tomography (PET) nuclear medical imaging technique that produces an image of the functional processes in the body. The system detects pairs of gamma rays emitted indirectly by a positron-emitting radionuclide (tracer), which is injected into the body.

SAR Specific absorption rate is a measure of the rate at which energy is absorbed by the body when exposed to a RF field.

screening mammography x-ray based breast imaging in an asymptomatic population with the aim of detecting breast tumors at an early stage.

self-examination monthly physical examination of the breasts with the intent of finding lumps that could be an early indication of cancer.

sensitivity ratio of malignant tumors detected to the total number of patients with malignant tumors.

specificity ratio of patients correctly classified as having benign tumors to the total number of patients with benign tumors.

spillover part of the power radiated into the liquid that misses the imaged body.

ultrasounds (US) imaging technique in which high-frequency sound waves are bounced off tissues and internal organs. The echoes produce an image called sonogram.

Acronyms

2D two-dimensional.

3D three-dimensional.

AUT antenna under test.

CAD computer-aided design.

CPW coplanar waveguide.

CSF cerebrospinal fluid.

CT computed tomography.

CVD cardiovascular disease.

EEG electroencephalography.

EM electromagnetic.

EU European Union.

FDL Frequency Differential Linearized.

FDTD finite difference time domain.

FEM finite element method.

FFT fast Fourier transform.

FHR full to healthy ratio.

FWHM full width half maximum.

MC Magnitude Combined.

MEG magnetoencephalography.

MIT Massachusetts Institute of Technology.

MoM method of moments.

MRI magnetic resonance imaging.

MSE mean squared error.

PA positioning accuracy.

PEM positron emission mammography.

PET positron emission tomography.

PML perfect magnetic layer.

SAR specific absorption rate.

SCR signal to cluter ratio.

SMA subminiature version A.

SMR signal to mean ratio.

SNR signal to noise ratio.

SP8T single-pole 8-throw.

SPECT single-photon emission computed tomography.

TDA Time Domain Inversion Algorithm.

TRL Thru Reflect Line.

US ultrasounds.

USPTSF U.S. Preventive Services Task Force.

VNA vector network analyzer.

LIST OF FIGURES

LIST OF TABLES

Bibliography

[1] Anonymous, "Looking back on the millennium in medicine," *New England Journal of Medicine*, vol. 342, no. 1, pp. 42–49, 2000. [Online]. Available: http://www.nejm.org/doi/full/10.1056/NEJM200001063420108 (Cited on page 2.)

[2] S. Y. Semenov and D. R. Corfield, "Microwave tomography for brain imaging: Feasibility assessment for stroke detection," *International Journal of Antennas and Propagation*, vol. 2008, p. 8 pages, 2008. [Online]. Available: http://dx.doi.org/10.1155/2008/254830 (Cited on page 5.)

[3] J. Lin, "Frequency optimization for microwave imaging of biological tissues," *Proceedings of the IEEE*, vol. 73, no. 2, pp. 374 – 375, feb. 1985. (Cited on pages 5, 49, and 164.)

[4] S. Gabriel, R. W. Lau, and C. Gabriel, "The dielectric properties of biological tissues: Ii. measurements in the frequency range 10 hz to 20 ghz," *Phys. Med. Biol.*, vol. 41, no. 11, p. 2251, 1996. (Cited on pages 5, 24, 25, 30, and 167.)

[5] D. Andreuccetti, R. Fossi, and C. Petrucci. (1997-2012) Calculation of the dielectric properties of body tissues in the frequency range 10 hz - 100 ghz. IFAC-CNR. Florence (Italy). [Online]. Available: http://niremf.ifac.cnr.it/tissprop/ (Cited on pages 5, 25, 30, 31, 74, 78, 80, 84, 85, 87, 165, and 167.)

[6] C. Gilmore, P. Mojabi, A. Zakaria, S. Pistorius, and J. LoVetri, "On super-resolution with an experimental microwave tomography system," *Antennas and Wireless Propagation Letters, IEEE*, vol. 9, pp. 393–396, 2010. (Cited on page 5.)

[7] C. Li, J. Cummings, J. Lam, E. Graves, and W. Wu, "Radar remote monitoring of vital signs," *Microwave Magazine, IEEE*, vol. 10, no. 1, pp. 47–56, 2009. (Cited on page 7.)

[8] J. Rius, C. Pichot, L. Jofre, J. Bolomey, N. Joachimowicz, A. Broquetas, and M. Ferrando, "Planar and cylindrical active microwave temperature imaging: Numerical simulations," *Medical Imaging, IEEE Transactions on*, vol. 11, no. 4, pp. 457 –469, dec 1992. (Cited on pages 7 and 18.)

[9] L. Jofre, M. Hawley, A. Broquetas, E. de los Reyes, M. Ferrando, and A. Elias-Fuste, "Medical imaging with a microwave tomographic scanner," *Biomedical Engineering, IEEE Transactions on*, vol. 37, no. 3, pp. 303 –312, march 1990. (Cited on pages 7, 12, 13, 15, 42, 93, and 98.)

[10] S. Semenov, R. Svenson, V. Posukh, A. Nazarov, Y. Sizov, A. Bulyshev, A. Souvorov, W. Chen, J. Kasell, and G. Tatsis, "Dielectrical spectroscopy of canine myocardium dur-

ing acute ischemia and hypoxia at frequency spectrum from 100 kHz to 6 GHz," *Medical Imaging, IEEE Transactions on*, vol. 21, no. 6, pp. 703 –707, june 2002. (Cited on page 7.)

[11] J. Lin and M. Clarke, "Microwave imaging of cerebral edema," *Proceedings of the IEEE*, vol. 70, no. 5, pp. 523–524, 1982. (Cited on page 7.)

[12] X. Li, M. Jalilvand, L. Zwirello, and T. Zwick, "Synthetic aperture-based uwb imaging system for detection of urine accumulation in human bladder," in *Ultra-Wideband (ICUWB), 2011 IEEE International Conference on*, 2011, pp. 351–354. (Cited on page 7.)

[13] S. Semenov and D. R. Corfield, "Microwave tomography for brain imaging: Feasibility assessment for stroke detection," *International Journal of Antennas and Propagation*, vol. 2008, p. 8 pages, 2008. (Cited on pages 7, 25, and 30.)

[14] A. Fhager and M. Persson, "Stroke detection and diagnosis with a microwave helmet," in *Antennas and Propagation (EUCAP), 2012 6th European Conference on*, 2012, pp. 1796–1798. (Cited on pages 7 and 17.)

[15] P. Meaney, D. Goodwin, A. Golnabi, T. Zhou, M. Pallone, S. Geimer, G. Burke, and K. Paulsen, "Clinical microwave tomographic imaging of the calcaneus: A first-in-human case study of two subjects," *Biomedical Engineering, IEEE Transactions on*, vol. 59, no. 12, pp. 3304–3313, 2012. (Cited on page 7.)

[16] E. Fear, X. Li, S. Hagness, and M. Stuchly, "Confocal microwave imaging for breast cancer detection: localization of tumors in three dimensions," *Biomedical Engineering, IEEE Transactions on*, vol. 49, no. 8, pp. 812 –822, aug. 2002. (Cited on pages 7, 13, and 93.)

[17] M. Klemm, I. Craddock, J. Leendertz, A. Preece, and R. Benjamin, "Radar-based breast cancer detection using a hemispherical antenna array - experimental results," *Antennas and Propagation, IEEE Transactions on*, vol. 57, no. 6, pp. 1692–1704, 2009. (Cited on pages 7, 16, 93, and 98.)

[18] P. Meaney, M. Fanning, T. Raynolds, C. Fox, Q. Fang, C. Kogel, S. Poplack, and K. Paulsen, "Initial clinical experience with microwave breast imaging in women with normal mammography," *Acad. Radiol.*, vol. 14, pp. 207–218, 2007. (Cited on pages 7, 16, and 27.)

[19] E. Zastrow, S. Hagness, B. Van Veen, and J. Medow, "Time-multiplexed beamforming for noninvasive microwave hyperthermia treatment," *Biomedical Engineering, IEEE Transactions on*, vol. 58, no. 6, pp. 1574–1584, 2011. (Cited on page 7.)

[20] M. Lubner, C. Brace, J. Hinshaw, and F. Lee, "Microwave tumor ablation: Mechanism of action, clinical results and devices," *Journal of Vascular and Interventional Radiology*, vol. 21, p. S192ÐS203, 2010. (Cited on page 7.)

[21] C. Rappaport, "Treating cardiac disease with catheter-based tissue heating," *Microwave Magazine, IEEE*, vol. 3, no. 1, pp. 57–64, 2002. (Cited on page 7.)

[22] M. Nichols, N. Townsend, R. Luengo-Fernandez, J. Leal, A. Gray, P. Scarborough, and M. Rayner, *European cardiovascular disease statistics 2012*. European Heart Network, Brussels and European Society of Cardiology, Sophia Antipolis, 2012. (Cited on pages 7, 10, and 163.)

[23] (2012, February) El cáncer en España.com. Sociedad Española de Oncología Médica (SEOM). [Online]. Available: www.seom.org (Cited on page 8.)

[24] (2012, September) Incidencia del cáncer de mama. Asociación española contra el cáncer (aecc). [Online]. Available: www.aecc.es (Cited on page 8.)

[25] (2011, October) Programa de detecció precoç del càncer de mama. Institut Català d'Oncologia (ICO). [Online]. Available: www20.gencat.cat/portal/site/salut (Cited on page 8.)

[26] National Cancer Policy Board Institute of Medicine and Division of Earth and Life Studies National Research Council, *Mammography and Beyond: Developing Technologies for the Early Detection of Breast Cancer*, Committee on Technologies for the Early Detection of Breast Cancer, S. J. Nass, I. C. Henderson, and J. C. Lashof, Eds. The National Academies Press, 2001. [Online]. Available: http://www.nap.edu/openbook.php?record_id=10030 (Cited on pages 8 and 10.)

[27] U.S. Preventive Services Task Force, "Screening for breast cancer: U.S. preventive services task force recommendation statement," *Ann. Internal Medicine*, vol. 151, no. 10, pp. 716–726, 2009. (Cited on page 8.)

[28] A. Berrington de González and S. Darby, "Risk of cancer from diagnostic x-rays: estimates for the uk and 14 other countries," *Lancet*, vol. 363, no. 9406, pp. 345–351, 2004. (Cited on page 8.)

[29] W. Berg, L. Gutierrez, M. NessAiver, W. Carter, M. Bhargavan, R. Lewis, and O. Ioffe, "Diagnostic accuracy of mammography, clinical examination, u.s., and mr imaging in pre-operative assessment of breast cancer," *Radiology*, vol. 233, pp. 830–848, 2004. (Cited on pages 9, 10, and 167.)

[30] E. L. Rosen, W. B. Eubank, and A. D. Mankoff, "FDG PET, PET/CT, and breast cancer imaging," *Radiographics*, vol. 27, pp. 215–229, 2007. (Cited on page 10.)

[31] A. Marrugata, J. Arboix, L. Garcia-Eroles, T. Salas, J. Vila, R. Castell, C. Tresserras, and R. Elosua, "EstimaciÛn de la incidencia poblacional y la mortalidad de la enfermedad cerebrovascular establecida isquŐmica y hemorrĞgica en 2002," *Rev Esp Cardiol.*, vol. 60, no. 6, pp. 573–580, 2007. (Cited on pages 11 and 163.)

[32] I. Karanasiou, "Combined functional data from multispectral non-ionizing and non-invasive brain imaging," in *Information Technology and Applications in Biomedicine, 2009. ITAB 2009. 9th International Conference on*, 2009, pp. 1–4. (Cited on page 11.)

[33] A. Anderson, "Microwave holography," *Electrical Engineers, Proceedings of the Institution of*, vol. 124, no. 11, pp. 946 –962, november 1977. (Cited on page 12.)

[34] L. Larsen, J. Jacobi, I. M. Theory, and T. Society, *Medical Applications of Microwave Imaging*. IEEE Press, 1986. (Cited on pages 12 and 15.)

[35] R. Mueller, M. Kaveh, and G. Wade, "Reconstructive tomography and applications to ultrasonics," *Proceedings of the IEEE*, vol. 67, no. 4, pp. 567 – 587, april 1979. (Cited on page 12.)

[36] L. Larsen and J. Jacobi, "Microwave scattering parameter imaging of an isolated canine kidney," *Medical Physics*, vol. 6, pp. 70–78, 1979. (Cited on page 12.)

[37] J.-C. Bolomey and F. E. Gardiol, *Engineering Applications of the Modulated Scatterer Technique*, A. House, Ed. Artech House, 2001. (Cited on pages 12 and 13.)

[38] M. Slaney, A. Kak, and L. Larsen, "Limitations of imaging with first-order diffraction tomography," *Microwave Theory and Techniques, IEEE Transactions on*, vol. 32, no. 8, pp. 860 – 874, aug 1984. (Cited on pages 12, 15, 38, 52, and 53.)

[39] A. Datta and B. Bandyopadhyay, "Nonlinear extension to a moment method iterative reconstruction algorithm for microwave tomography," *Proceedings of the IEEE*, vol. 74, no. 4, pp. 604 – 606, april 1986. (Cited on page 12.)

[40] W. Guo and T. Guo, "Three-dimensional dielectric imaging by microwave inverse scattering with resolution unlimited by wavelength," in *Electrical Insulation and Dielectric Phenomena, 1989. Annual Report., Conference on*, oct-2 nov 1989, pp. 65 –74. (Cited on page 12.)

[41] N. Joachimowicz, C. Pichot, and J. Hugonin, "Inverse scattering: an iterative numerical method for electromagnetic imaging," *Antennas and Propagation, IEEE Transactions on*, vol. 39, no. 12, pp. 1742 –1753, dec 1991. (Cited on pages 12 and 15.)

[42] P. Meaney, M. Fanning, D. Li, S. P. Poplack, and K. Paulsen, "A clinical prototype for active microwave imaging of the breast," *Microwave Theory and Techniques, IEEE Transactions on*, vol. 48, no. 11, pp. 1841–1853, 2000. (Cited on pages 13, 16, 27, 42, 93, and 98.)

[43] P. Meaney, Q. Fang, and K. Paulsen, "Data collection strategies and their impact on 3D microwave imaging of the breast," in *Antennas and Propagation Society International Symposium, 2005 IEEE*, vol. 1B, 2005, pp. 183 –186 vol. 1B. (Cited on pages 13 and 37.)

[44] L. Jofre, A. Broquetas, J. Romeu, S. Blanch, A. Toda, X. Fabregas, and A. Cardama, "UWB tomographic radar imaging of penetrable and impenetrable objects," *Proceedings of the IEEE*, vol. 97, no. 2, pp. 451 –464, feb. 2009. (Cited on pages 13 and 14.)

[45] M. Pastorino, *Microwave Imaging.* Hoboken, N.J., 2010. (Cited on page 14.)

[46] E. Bond, X. Li, S. Hagness, and B. Van Veen, "Microwave imaging via space-time beamforming for early detection of breast cancer," *Antennas and Propagation, IEEE Transactions on*, vol. 51, no. 8, pp. 1690 – 1705, aug. 2003. (Cited on page 14.)

[47] M. Klemm, J. A. Leendertz, D. Gibbins, I. J. Craddock, A. Preece, and R. Benjamin, "Microwave radar-based breast cancer detection: Imaging in inhomogeneous breast phantoms," *Antennas and Wireless Propagation Letters, IEEE*, vol. 8, pp. 1349–1352, 2009. (Cited on pages 14, 92, and 93.)

[48] T. Williams, E. Fear, and D. Westwick, "Tissue sensing adaptive radar for breast cancer detection-investigations of an improved skin-sensing method," *Microwave Theory and Techniques, IEEE Transactions on*, vol. 54, no. 4, pp. 1308 – 1314, june 2006. (Cited on page 14.)

[49] P. Kosmas and C. Rappaport, "Time reversal with the fdtd method for microwave breast cancer detection," *Microwave Theory and Techniques, IEEE Transactions on*, vol. 53, no. 7, pp. 2317 – 2323, july 2005. (Cited on page 14.)

[50] M. El-Shenawee and E. Miller, "Spherical harmonics microwave algorithm for shape and location reconstruction of breast cancer tumor," *Medical Imaging, IEEE Transactions on*, vol. 25, no. 10, pp. 1258 –1271, oct. 2006. (Cited on page 15.)

[51] A. Ishimaru, *Wave propagation and scattering in random media.* Academic Press, New York, 1978. (Cited on pages 15 and 33.)

[52] S. Semenov, A. Bulyshev, A. Abubakar, V. Posukh, Y. Sizov, A. Souvorov, P. van den Berg, and T. Williams, "Microwave-tomographic imaging of the high dielectric-contrast objects using different image-reconstruction approaches," *Microwave Theory and Techniques, IEEE Transactions on*, vol. 53, no. 7, pp. 2284 – 2294, July 2005. (Cited on page 15.)

[53] P. Mojabi and J. LoVetri, "Microwave biomedical imaging using the multiplicative regularized gauss-newton inversion," *Antennas and Wireless Propagation Letters, IEEE*, vol. 8, pp. 645 –648, 2009. (Cited on page 15.)

[54] W. Chew and Y. Wang, "Reconstruction of two-dimensional permittivity distribution using the distorted born iterative method," *Medical Imaging, IEEE Transactions on*, vol. 9, no. 2, pp. 218 –225, jun 1990. (Cited on page 15.)

[55] A. Abubakar, P. van den Berg, and J. Mallorqui, "Imaging of biomedical data using a multiplicative regularized contrast source inversion method," *Microwave Theory and Techniques, IEEE Transactions on*, vol. 50, no. 7, pp. 1761–1771, Jul 2002. (Cited on page 15.)

[56] A. Sabouni, S. Noghanian, and S. Pistorius, "A global optimization technique for microwave imaging of the inhomogeneous and dispersive breast," *Electrical and Computer Engineering, Canadian Journal of*, vol. 35, no. 1, pp. 15 –24, winter 2010. (Cited on page 15.)

[57] S. Poplack, T. Tosteson, W. Wells, B. Pogue, P. Meaney, A. Hartov, C. Kogel, S. Soho, J. Gibson, and P. K.D., "Electromagnetic breast imaging: results of a pilot study in women with abnormal mammograms," *Radiology. 2007 May;243(2):350-9. Epub 2007 Mar 30.*, vol. 243, pp. 350–359, 2007. (Cited on pages 16, 27, and 163.)

[58] T. Grzegorczyk, P. Meaney, P. Kaufman, R. di Florio-Alexander, and K. Paulsen, "Fast 3-d tomographic microwave imaging for breast cancer detection," *Medical Imaging, IEEE Transactions on*, vol. 31, no. 8, pp. 1584 –1592, aug. 2012. (Cited on pages 16 and 18.)

[59] M. Klemm, I. Craddock, J. Leendertz, A. Preece, and R. Benjamin, "Experimental and clinical results of breast cancer detection using uwb microwave radar," in *Antennas and Propagation Society International Symposium, 2008. AP-S 2008. IEEE*, July 2008, pp. 1–4. (Cited on page 17.)

[60] M. Klemm, D. Gibbins, J. Leendertz, T. Horseman, A. Preece, R. Benjamin, and I. Craddock, "Development and testing of a 60-element uwb conformal array for breast cancer imaging," in *Antennas and Propagation (EUCAP), Proceedings of the 5th European Conference on*, April 2011, pp. 3077–3079. (Cited on pages 17 and 93.)

[61] T. Henriksson, M. Klemm, D. Gibbins, J. Leendertz, T. Horseman, A. Preece, R. Benjamin, and I. Craddock, "Clinical trials of a multistatic uwb radar for breast imaging," in *Antennas and Propagation Conference (LAPC), 2011 Loughborough*, nov. 2011, pp. 1 –4. (Cited on pages 17, 18, and 163.)

[62] A. Fhager and M. Persson, "A microwave measurement system for stroke detection," in *Antennas and Propagation Conference (LAPC), 2011 Loughborough*, 2011, pp. 1–2. (Cited on pages 17 and 30.)

[63] R. Amineh, M. Ravan, A. Khalatpour, and N. Nikolova, "Three-dimensional near-field microwave holography using reflected and transmitted signals," *Antennas and Propagation, IEEE Transactions on*, vol. 59, no. 12, pp. 4777 –4789, dec. 2011. (Cited on pages 18 and 93.)

[64] R. F. Harrington, *Time-Harmonic Electromagnetic Fields*. McGraw-Hill, 1961. (Cited on pages 22, 33, 49, 127, and 132.)

[65] C. Balanis, *Advanced engineering electromagnetics*, J. Willey and Sons, Eds., 1989. (Cited on page 22.)

[66] A. Von Hippel, *Dielectric materials and applications*, A. House, Ed., 1954. (Cited on pages 23, 101, 106, 110, and 168.)

[67] C. Gabriel, S. Gabriel, and E. Corthout, "The dielectric properties of biological tissues: I. literature survey," *Phys. Med. Biol.*, vol. 41, pp. 2231–2249, 1996. (Cited on pages 23, 24, 25, 30, and 167.)

[68] ——, "The dielectric properties of biological tissues: Iii. parameric models for the dielectric spectrum of tissues," *Phys. Med. Biol.*, vol. 41, pp. 2271–2293, 1996. (Cited on pages 24, 25, 30, and 167.)

[69] M. Lazebnik, L. McCartney, D. Popovic, C. B. Watkins, M. J. Lindstrom, J. Harter, S. Sewall, A. Magliocco, J. H. Booske, M. Okoniewski, and S. C. Hagness, "A large-scale study of the ultrawideband microwave dielectric properties of normal, benign and malignant breast tissues obtained from cancer surgeries," *Phys. Med. Biol.*, vol. 52, no. 20, pp. 6093–6115, 2007. (Cited on pages 24, 25, 27, 28, 61, 72, 74, 76, 78, 84, and 167.)

[70] M. Castro-Giráldez, P. Fito, and P. Fito, "Application of microwaves dielectric spectroscopy for controlling pork meat (longissimus dorsi) salting process," *Journal of Food Engineering*, vol. 97, no. 4, pp. 484 – 490, 2010. [Online]. Available: http://www.sciencedirect.com/science/article/pii/S026087740900572X (Cited on pages 24 and 163.)

[71] K. Foster and H. Schwan, "Dielectrc properties of tissues and biological materials: a critical review," *Crit. rev. biomed*, vol. 17, pp. 25–104, 1989. (Cited on page 24.)

[72] R. Halter, T. Zhou, P. Meaney, A. Hartov, R. Barth, K. Rosenkranz, W. Wells, C. Kogel, A. Borsic, E. Rizzo, and K. Paulsen, "The correlation of in vivo and ex vivo tissue dielectric properties to validate electromagnetic breast imaging: initial clinical experience." *Physiol Meas.*, vol. 30, pp. 121–136, 2009. (Cited on pages 24 and 27.)

[73] M. Lazebnik, L. McCartney, D. Popovic, C. B. Watkins, M. J. Lindstrom, J. Harter, S. Sewall, A. Magliocco, J. H. Booske, M. Okoniewski, and S. C. Hagness, "A large-scale study of the ultrawideband microwave dielectric properties of normal breast tissue obtained from cancer surgeries," *Phys. Med. Biol.*, vol. 52, no. 10, pp. 2637–2656, 2007. (Cited on pages 24, 27, 28, 61, 72, and 76.)

[74] N. Nikolova, "Microwave imaging for breast cancer," *Microwave Magazine, IEEE*, vol. 12, no. 7, pp. 78–94, 2011. (Cited on page 25.)

[75] W. Joines, Y. Zhang, C. Li, and R. Jrirtle, "The measured properties of normal and malignant human tissues from 50 to 9000 mhz," *Med. Phys.*, vol. 21, no. 4, pp. 547–550, 1994. (Cited on pages 25 and 27.)

[76] A. Suroviec, S. Stuchly, J. Barr, and A. Swarup, "Dielectric properties of breast carcinoma an the surrounding tissues," *IEEE Transactions on Biomedical Engineering*, vol. 35, no. 4, pp. 257–263, 1988. (Cited on pages 25 and 27.)

[77] N. Howlader, A. Noone, M. Krapcho, N. Neyman, R. Aminou, W. Waldron, S. Altekruse, C. Kosary, J. Ruhl, Z. Tatalovich, H. Cho, A. Mariotto, M. Eisner, D. Lewis, H. Chen, E. Feuer, K. Cronin, and B. Edwards. (2011) Seer cancer statistics review, 1975-2008. National Cancer Institute. [Online]. Available: http://seer.cancer.gov/csr/1975_2008/ (Cited on page 26.)

[78] (2013) Breast cancer. American Cancer Society. [Online]. Available: http://www.cancer. org/cancer/breastcancer/detailedguide/breast-cancer-survival-by-stage (Cited on page 26.)

[79] A. M. Campbell and D. V. Land, "Dielectric properties of female human breast tissue measured in vitro at 3.2 ghz," *Physics in Medicine and Biology*, vol. 37, no. 1, 1992. (Cited on page 27.)

[80] D. Woten and M. El-Shenawee, "Broadband dual linear polarized antenna for statistical detection of breast cancer," *IEEE Transactions on Antennas and Propagation*, vol. 56, no. 11, pp. 3576–3580, 2008. (Cited on page 27.)

[81] M. Zhao, J. Shea, S. Hagness, D. Van der Weide, B. Van Veen, and T. Varghese, "Numerical study of microwave scattering in breast tissue via coupled dielectric and elastic contrasts," *Antennas and Wireless Propagation Letters, IEEE*, vol. 7, pp. 247–250, 2008. (Cited on page 27.)

[82] B. Xie, J. Weaver, P. Meaney, and P. K.D., "Magnetic resonance microwave absorption imaging: Feasibility of signal detection," *Med. Phys.*, vol. 36, no. 11, pp. 5190–5197, 2009. (Cited on page 27.)

[83] A. Mashal, J. Booske, and S. Hagness, "Toward contrast-enhanced microwave-induced thermoacoustic imaging of breast cancer: an experimental study on the effects of microbubbles on simple thermoacoustic targets," *Phys. Med. Biol.*, vol. 54, pp. 641–650, 2009. (Cited on page 27.)

[84] A. Mashal, B. Sitharaman, X. Li, P. Avti, A. Sahakian, J. Booske, and S. Hagness, "Toward carbon-nanotube-based theranostic agents for microwave detection and treatment of breast cancer: Enhanced dielectric and heating response of tissue-mimicking materials," *Biomedical Engineering, IEEE Transactions on*, vol. 57, no. 8, pp. 1831–1834, 2010. (Cited on page 27.)

[85] E. Zastrow, S. Davis, M. Lazebnik, F. Kelcz, B. Van Veen, and S. Hagness. (2012, July) Database of 3d grid-based numerical breast phantoms for use in computational electromagnetics simulations. University of Wisconsin Computational Electromagnetics Laboratory. [Online]. Available: http://uwcem.ece.wisc.edu/ (Cited on pages 27, 28, 72, 82, 84, 125, 143, and 166.)

[86] G. Schmid, G. Neubauer, and P. R. Mazal, "Dielectric properties of the human brain measured less than 10 hours post mortem," *Bioelectromagnetics*, vol. 24, no. 6, pp. 423–430, 2003. (Cited on page 30.)

[87] M. Tofighi and A. Daryoush, "Characterization of the complex permittivity of brain tissues up to 50 ghz utilizing a two-port microstrip test fixture," *Microwave Theory and Techniques, IEEE Transactions on*, vol. 50, no. 10, pp. 2217–2225, 2002. (Cited on page 30.)

[88] A. Christ, W. Kainz, E. Hahn, M. Honegger, K .and Zefferer, E. Neufeld, W. Rascher, R. Janka, W. Bautz, J. Chen, B. Kiefer, P. Schmitt, H. Hollenbach, J. Shen, M. Oberle, D. Szczerba, A. Kam, G. J.W., and N. Kuster, "The virtual family Ð development of surface-

based anatomical models of two adults and two children for dosimetric simulations," *Physics in Medicine and Biology*, vol. 55, no. 2, p. N23ÐN38, 2010. (Cited on pages 30, 31, and 85.)

[89] A. Cardama, L. Jofre, J. Rius, J. Romeu, S. Blanch, and M. Ferrando, *Antennas.*   Edicions UPC, 1998. (Cited on page 32.)

[90] K. Yee, "Numerical solution of initial boundary value problems involving maxwell's equations in isotropic media," *Antennas and Propagation, IEEE Transactions on*, vol. 14, no. 3, pp. 302–307, 1966. (Cited on page 35.)

[91] A. F. Oskooi, D. Roundy, M. Ibanescu, P. Bermel, J. D. Joannopoulos, and S. G. Johnson, "MEEP: A flexible free-software package for electromagnetic simulations by the FDTD method," *Computer Physics Communications*, vol. 181, p. 687Ð702, 2010. (Cited on pages 35 and 60.)

[92] A. Broquetas, J. Romeu, J. Rius, A. Elias-Fuste, A. Cardama, and L. Jofre, "Cylindrical geometry: a further step in active microwave tomography," *Microwave Theory and Techniques, IEEE Transactions on*, vol. 39, no. 5, pp. 836–844, 1991. (Cited on page 37.)

[93] J. Rius, M. Ferrando, L. Jofre, E. de los Reyes, A. Elias, and A. Broquetas, "Microwave tomography: an algorithm for cylindrical geometries," *Electronics Letters*, vol. 23, no. 11, pp. 564–565, 1987. (Cited on pages 37 and 55.)

[94] A. Broquetas, "Tomografía de microondas en geometría cilindrica para aplicaciones biomédicas," Ph.D. dissertation, Universitat Politècnica de Catalunya. Escola Tècnica Superior d'Enginyers de Telecomunicació de Barcelona, 1989. (Cited on pages 42 and 114.)

[95] J. Sill and E. Fear, "Tissue sensing adaptive radar for breast cancer detection - experimental investigation of simple tumor models," *Microwave Theory and Techniques, IEEE Transactions on*, vol. 53, no. 11, pp. 3312–3319, 2005. (Cited on pages 42 and 93.)

[96] J. Shea, P. Kosmas, S. Hagness, and B. van Veen, "Three-dimensional microwave imaging of realistic numerical breast phantoms via a multiple-frequency inverse scattering technique," *Medical Physics,*, vol. 37, p. 4210Ð4226, 2012. (Cited on pages 49 and 54.)

[97] L. Jofre, A. Toda, J. Montana, P. Carrascosa, J. Romeu, S. Blanch, and A. Cardama, "UWB short-range bifocusing tomographic imaging," *Instrumentation and Measurement, IEEE Transactions on*, vol. 57, no. 11, pp. 2414 –2420, nov. 2008. (Cited on page 49.)

[98] J. Romeu and L. Jofre, "Truncation errors in cylindrical near to far field transform. a plane wave synthesis approach," in *Microwave Conference, 1992. 22nd European*, vol. 1, 5-9 1992, pp. 659 –663. (Cited on page 51.)

[99] T. Grzegorczyk, P. Meaney, S. Jeon, S. Geimer, and K. Paulsen, "Importance of phase unwrapping for the reconstruction of microwave tomographic images," *Biomedical Optics Express*, vol. 2, p. 315Ð330, 2011. (Cited on page 54.)

[100] D. Roundy. (2005-2009) Meep. Massachusetts Institute of Technology. [Online]. Available: http://ab-initio.mit.edu/wiki/index.php/Meep (Cited on page 60.)

[101] J. Bourqui, E. Fear, and M. Okoniewski, "Versatile ultrawideband sensor for near-field microwave imaging," in *Antennas and Propagation (EuCAP), 2010 Proceedings of the Fourth European Conference on*, 2010, pp. 1–5. (Cited on pages 62 and 93.)

[102] E. Fear, S. Hagness, P. Meaney, M. Okoniewski, and M. Stuchly, "Enhancing breast tumor detection with near-field imaging," *Microwave Magazine, IEEE*, vol. 3, no. 1, pp. 48–56, 2002. (Cited on pages 65 and 98.)

[103] M. Sarafianou, D. Gibbins, and I. Craddock, "A novel 3-d breast surface reconstruction algorithm for a multi-static radar-based breast imaging system," in *Antennas and Propagation Conference (LAPC), 2011 Loughborough*, 2011, pp. 1–4. (Cited on page 67.)

[104] Y. Nishina, S. Miura, Y. Kuwahara, H. Sakahara, and H. Ogura, "Clinical setup of microwave mammography: Phase 2," in *Antennas and Propagation (ISAP), 2012 International Symposium on*, 2012, pp. 483–486. (Cited on page 93.)

[105] M. Elsdon, D. Smith, M. Leach, and S. J. Foti, "Experimental investigation of breast tumor imaging using indirect microwave holography," *Microwave and Optical Technology Letters*, vol. 48, no. 3, pp. 480–482, 2006. [Online]. Available: http://dx.doi.org/10.1002/mop.21384 (Cited on page 93.)

[106] N. Petrovic, T. Gunnarsson, N. Joachimowicz, and M. Otterskog, "Robot controlled data acquisition system for microwave imaging," in *Antennas and Propagation, 2009. EuCAP 2009. 3rd European Conference on*, March 2009, pp. 3356–3360. (Cited on page 94.)

[107] C. Yu, M. Yuan, J. Stang, E. Bresslour, R. George, G. Ybarra, W. Joines, and Q.-H. Liu, "Active microwave imaging ii: 3-d system prototype and image reconstruction from experimental data," *Microwave Theory and Techniques, IEEE Transactions on*, vol. 56, no. 4, pp. 991–1000, 2008. (Cited on page 94.)

[108] S. Semenov, R. Svenson, A. Bulyshev, A. Souvorov, A. Nazarov, Y. Sizov, A. Pavlovsky, V. Borisov, B. Voinov, G. Simonova, A. Starostin, V. Posukh, G. Tatsis, and V. Baranov, "Three-dimensional microwave tomography: experimental prototype of the system and vector born reconstruction method," *Biomedical Engineering, IEEE Transactions on*, vol. 46, no. 8, pp. 937–946, 1999. (Cited on page 94.)

[109] Rt-5 motorized rotary stage. Newmark Systems Inc. [Online]. Available: http://www.newmarksystems.com/rotary-positioners/rt-5-motorized-rotary-stage/ (Cited on page 94.)

[110] *ZSH 57 to 107. 2-Phase Hybrid Stepper Motor*, Phytron-Elektronik Gmb. (Cited on page 94.)

[111] M. Guardiola, "Anàlisi i implementació de tècniques de formació d'imatge i localització ultra-wideband," Master's thesis, Universitat Politècnica de Catalunya, 2008. (Cited on page 95.)

[112] C. Yu, M. Yuan, J. Stang, E. Bresslour, R. George, G. Ybarra, W. Joines, and Q. H. Liu, "Active microwave imaging II: 3-D system prototype and image reconstruction from experimental data," *Microwave Theory and Techniques, IEEE Transactions on*, vol. 56, no. 4, pp. 991–1000, April 2008. (Cited on page 95.)

[113] W. Huang and A. Kishk, "Compact dielectric resonator antenna for microwave breast cancer detection," *Microwaves, Antennas Propagation, IET*, vol. 3, no. 4, pp. 638–644, 2009. (Cited on page 95.)

[114] M. Al-Joumayly, S. Aguilar, N. Behdad, and S. Hagness, "Dual-band miniaturized patch antennas for microwave breast imaging," *Antennas and Wireless Propagation Letters, IEEE*, vol. 9, pp. 268–271, 2010. (Cited on page 95.)

[115] D. Gibbins, M. Klemm, I. Craddock, J. Leendertz, A. Preece, and R. Benjamin, "A comparison of a wide-slot and a stacked patch antenna for the purpose of breast cancer detection," *Antennas and Propagation, IEEE Transactions on*, vol. 58, no. 3, pp. 665–674, 2010. (Cited on page 95.)

[116] J. Bourqui, M. Okoniewski, and E. Fear, "Balanced antipodal vivaldi antenna with dielectric director for near-field microwave imaging," *Antennas and Propagation, IEEE Transactions on*, vol. 58, no. 7, pp. 2318–2326, 2010. (Cited on page 95.)

[117] X. Li, S. Hagness, M. Choi, and D. Van der Weide, "Numerical and experimental investigation of an ultrawideband ridged pyramidal horn antenna with curved launching plane for pulse radiation," *Antennas and Wireless Propagation Letters, IEEE*, vol. 2, no. 1, pp. 259–262, 2003. (Cited on page 95.)

[118] R. K. Amineh, M. Ravan, A. Trehan, and N. Nikolova, "Near-field microwave imaging based on aperture raster scanning with tem horn antennas," *Antennas and Propagation, IEEE Transactions on*, vol. 59, no. 3, pp. 928–940, 2009. (Cited on page 95.)

[119] A. Guy, "Analyses of electromagnetic fields induced in biological tissues by thermographic studies on equivalent phantom models," *Microwave Theory and Techniques, IEEE Transactions on*, vol. 16, no. 2, pp. 205–214, 1968. (Cited on page 96.)

[120] M. G. Bini, A. Ignesti, L. Millanta, R. Olmi, N. Rubino, and R. Vanni, "The polyacrylamide as a phantom material for electromagnetic hyperthermia studies," *Biomedical Engineering, IEEE Transactions on*, vol. BME-31, no. 3, pp. 317–322, 1984. (Cited on page 96.)

[121] J. J. W. Lagendijk and P. Nilsson, "Hyperthermia dough: a fat and bone equivalent phantom to test microwave/radiofrequency hyperthermia heating systems," *Phys. Med. Biol.*, vol. 30, pp. 709–712, 1985. (Cited on page 96.)

[122] C. Marchal, M. Nadi, A. J. Tosser, C. Roussey, and M. L. Gaulard, "Dielectric properties of gelatin phantoms used for simulations of biological tissues between 10 and 50 mhz," *Int. J. Hyperthermia*, vol. 5, p. 725Đ732, 1989. (Cited on page 96.)

[123] T. Sunaga, H. Ikehira, S. Furukawa, M. Tamura, E. Yoshitome, T. Obata, H. Shinkai, S. Tanada, H. Murata, and Y. Sasaki, "Development of a dielectric equivalent gel for better impedance matching for human skin," *Bioelectromagnetics*, vol. 24, p. 214Đ217, 2003. (Cited on page 96.)

[124] S. Bindu, A. Lonappan, V. Thomas, C. Aanandan, and K. Mathew, "Dielectric studies of corn syrup for applications in microwave breast imaging," *Progress In Electromagnetics Research*, vol. 59, pp. 175–186, 2006. (Cited on page 96.)

[125] T. Henriksson, N. Joachimowicz, C. Conessa, and J.-C. Bolomey, "Quantitative microwave imaging for breast cancer detection using a planar 2.45 ghz system," *Instrumentation and Measurement, IEEE Transactions on*, vol. 59, no. 10, pp. 2691–2699, 2010. (Cited on page 96.)

[126] A. Surowiec, A. M. Shrivastava P N, and P. Z, "Utilization of a multilayer polyacry-lamide phantom for evaluation of hyperthermia applicators," *Int. J. Hyperthermia*, vol. 8, p. 795Ð807, 1992. (Cited on page 97.)

[127] J. Chang, M. Fanning, P. Meaney, and K. Paulsen, "A conductive plastic for simulating bi-ological tissue at microwave frequencies," *Electromagnetic Compatibility, IEEE Transactions on*, vol. 42, no. 1, pp. 76–81, 2000. (Cited on page 97.)

[128] M. Lazebnik, E. Madsen, G. Frank, and S. Hagness, "Tissue-mimicking phantom materials for narrowband and ultrawideband microwave applications," *Phys. Med. Biol.*, vol. 50, no. 18, pp. 4245–4258, 2005. (Cited on pages 97 and 155.)

[129] E. Porter, J. Fakhoury, R. Oprisor, M. Coates, and M. Popovic, "Improved tissue phantoms for experimental validation of microwave breast cancer detection," in *Antennas and Propa-gation (EuCAP), 2010 Proceedings of the Fourth European Conference on*, 2010, pp. 1–5. (Cited on page 97.)

[130] M. Ostadrahimi, R. Reopelle, S. Noghanian, S. Pistorius, A. Vahedi, and F. Safari, "A het-erogeneous breast phantom for microwave breast imaging," in *Engineering in Medicine and Biology Society, 2009. EMBC 2009. Annual International Conference of the IEEE*, 2009, pp. 2727–2730. (Cited on pages 97, 113, 153, 155, and 166.)

[131] M. Miyakawa, K. Orikasa, M. Bertero, P. Boccacci, F. Conte, and M. Piana, "Experimen-tal validation of a linear model for data reduction in chirp-pulse microwave ct," *Medical Imaging, IEEE Transactions on*, vol. 21, no. 4, pp. 385–395, 2002. (Cited on page 98.)

[132] E. Porter, A. Santorelli, M. Coates, and M. Popovic, "An experimental system for time-domain microwave breast imaging," in *Antennas and Propagation (EUCAP), Proceedings of the 5th European Conference on*, 2011, pp. 2906–2910. (Cited on page 98.)

[133] A. Fhager, P. Hashemzadeh, and M. Persson, "Reconstruction quality and spectral con-tent of an electromagnetic time-domain inversion algorithm," *Biomedical Engineering, IEEE Transactions on*, vol. 53, no. 8, pp. 1594–1604, 2006. (Cited on page 100.)

[134] M. Gustafsson and S. He, "An optimization approach to two-dimensional time domain electromagnetic inverse problems," *Radio Science*, vol. 35, pp. 525–536, 2000. (Cited on page 104.)

[135] BMBS COST action td1301. development of a european-based collaborative network to accelerate technological, clinical and commercialisation progress in the area of medical microwave imaging. [Online]. Available: http://www.cost.eu/TD1301 (Cited on page 124.)

[136] D. Hill, "A circular array for plane-wave synthesis," *Electromagnetic Compatibility, IEEE Transactions on*, vol. 30, no. 1, pp. 3–8, 1988. (Cited on page 131.)

[137] J. Romeu, "FormulaciŬn espectral de la radiaciŬn. aplicaciŬn al caso cilindrico," Ph.D. dissertation, Universitat PolitŔcnica de Catalunya, 1991. (Cited on page 132.)

[138] J. Leach, W. and D. Paris, "Probe compensated near-field measurements on a cylinder," *Antennas and Propagation, IEEE Transactions on*, vol. 21, no. 4, pp. 435 – 445, jul 1973. (Cited on page 134.)

[139] M. Abramowitz, *Handbook of Mathematical Functions with Formulas, Graphs, and Mathematical Tables*, M. Abramowitz and I. Stegun, Eds.   Dover Publications, New York, 1972. (Cited on page 135.)

[140] R. C. Conceicao, R. M. Capote, B. L. Oliveira, P. Almeida, M. Glavin, E. Jones, and M. O'Halloran, "Novel multimodal pem-uwb approach for breast cancer detection: Initial study for tumour detection and consequent classification," in *Antennas and Propagation (EuCAP), 2013 7th European Conference on*, 2013, pp. 630–634. (Cited on page 139.)

[141] *IEEE Standard For safety levels with respect to human exposure to radio frequency electromagnetic fields, 3 kHz to 300 GHz*, IEEE International commitee on electromagnetic safety (SCC39) Std., 2005. (Cited on page 144.)

[142] *HMC322 GaAs MMIC SP8T non-reflective switch, DC-10 GHz*, Hittite. (Cited on page 151.)

List of Publications

Journal Articles

[J1] **M. Guardiola**, S. Capdevila, J. Romeu, and L. Jofre, "3-D microwave magnitude combined tomography for breast cancer detection using realistic breast models," *Antennas and Wireless Propagation Letters, IEEE*, vol. 11, pp. 1622 –1625, 2012. (Cited on pages 7, 18, and 27.)

[J2] **M. Guardiola**, B. Monsalve, I. Calafell, G. Roqueta, and J. Romeu, "Practical guidelines for students on the fabrication and measurement of homemade standard antennas," *Antennas and Propagation Magazine*, vol. 54, no. 1, pp. 177–194, 2012. (Cited on pages 183 and 165.)

[J3] **M. Guardiola**, L. Jofre, S. Capdevila, S. Blanch, and J. Romeu, "3D UWB magnitude-combined tomographic imaging for biomedical applications. algorithm validation," *Radioengineering*, vol. 18, pp. 1–7, 2011. (Cited on pages 18, 42, 93, and 91.)

Conference Articles

[CA1] **M. Guardiola**, S. Capdevila, and L. Jofre, "Robust differential multi-frequency microwave imaging for breast cancer detection," in *Antennas and Propagation (EuCAP), 2013 7th European Conference on*, 2013, pp. 622–623. (Cited on pages 71 and 69.)

[CA2] S. Capdevila, G. Roqueta, **M. Guardiola**, L. Jofre, J. Romeu, and J. Bolomey, "Water infiltration detection in civil engineering structures using rfid," in *Antennas and Propagation (EUCAP), 2012 6th European Conference on*, 2012, pp. 2505–2509.

[CA3] **M. Guardiola**, L. Jofre, S. Capdevila, and J. Romeu, "UWB brain differential imaging capabilities," in *Antennas and Propagation (EUCAP), 2012 6th European Conference on*, 2012, pp. 1780–1783. (Cited on pages 87 and 83.)

[CA4] **M. Guardiola**, L. Jofre, and J. Romeu, "UWB magnitude combined realistic breast model imaging capabilities," in *Antennas and Propagation Society International Symposium (AP-SURSI), 2012 IEEE*, 2012, pp. 1–2. (Cited on pages 82, 183, 80, and 164.)

[CA5] L. Jofre, S. Capdevila, **M. Guardiola**, and G. Roqueta, "Robust differential multifrequency microwave biomedical imaging," in *32nd Progress in Electromagnetics Research Symposium (PIERS)*, 2012.

[CA6] **M. Guardiola**, A. Fhager, L. Jofre, and M. Persson, "Circular microwave tomographic imaging. experimental comparison between quantitative and qualitative algorithms," in *Antennas and Propagation (EUCAP), Proceedings of the 5th European Conference on*, 2011, pp. 2800–2804. (Cited on pages 100, 102, and 98.)

[CA7] **M. Guardiola**, G. Roqueta, S. Capdevila, J. Romeu, and L. Jofre, "Semi-embedded RFID sensor networks for imaging application," in *5th International Conference on Electromagnetic Near-field Characterization and Imaging (ICONIC)*, 2011. (Cited on pages 183 and 165.)

[CA8] **M. Guardiola**, L. Jofre, S. Capdevila, S. Blanch, and J. Romeu, "Toward 3d uwb tomographie imaging system for breast tumor detection," in *Antennas and Propagation (EuCAP), 2010 Proceedings of the Fourth European Conference on*, 2010, pp. 1–5. (Cited on pages 76 and 74.)

[CA9] **M. Guardiola**, L. Jofre, F. Gedda, S. Capdevila, J. Romeu, and S. Blanch, "3D arrayed microwave tomographic system for medical imaging," in *Wireless Information Technology and Systems (ICWITS), 2010 IEEE International Conference on*, 2010, pp. 1–4. (Cited on pages 115 and 113.)

[CA10] **M. Guardiola**, L. Jofre, and J. Romeu, "3D UWB tomography for medical imaging applications," in *Antennas and Propagation Society International Symposium (APSURSI), 2010 IEEE*, 2010, pp. 1–4. (Cited on pages 80 and 77.)

[CA11] E. Nova, J. Abril, **M. Guardiola**, S. Capdevila, A. Broquetas, J. Romeu, and L. Jofre, "Terahertz subsurface imaging system," in *Antennas and Propagation (EuCAP), 2010 Proceedings of the Fourth European Conference on*, 2010, pp. 1–5.

[CA12] **M. Guardiola**, S. Capdevila, S. Blanch, J. Romeu, and L. Jofre, "UWB high-contrast robust tomographic imaging for medical applications," in *Electromagnetics in Advanced Applications, 2009. ICEAA '09. International Conference on*, 2009, pp. 560–563.

[CA13] **M. Guardiola**, S. Capdevila, and L. Jofre, "UWB bifocusing tomography for breast tumor detection," in *Antennas and Propagation, 2009. EuCAP 2009. 3rd European Conference on*, 2009, pp. 1855–1859.

[CA14] E. Nova, J. Abril, **M. Guardiola**, S. Capdevila, A. Broquetas, J. Romeu, and L. Jofre, "Terahertz tomographic imaging technologies," in *XXIV Simposium Nacional de la Unión Científica Internacional de Radio (URSI)*, 2009.

[CA15] S. Capdevila, M. Jofre, J. Rodriguez, **M. Guardiola**, A. Papio, F. De Flaviis, and L. Jofre, "UWB MST MEMS-based near-field imaging system," in *Antennas and Propagation Society International Symposium, 2008. AP-S 2008. IEEE*, 2008, pp. 1–4.

Awards and Mentions

Part of the work developed during this thesis has lead to the following awards and mentions at international conferences:

- **Honorable Mention** at the Student Paper Contest of the *IEEE Antennas and Propagation Society International Symposium 2012. APSURSI 2012* held in Chicago, USA in July 2012 for the paper "UWB Magnitude Combined Realistic Breast Model Imaging Capabilities" [CA4]

- **First Student Prize** at the *5th International Conference on Electromagnetic Near-field Characterization and Imaging (ICONIC 2011)* held in Rouen, France in December 2011 for the paper "Semi-embedded RFID Sensor Networks for Imaging Applications" [CA7]

- **First Prize** at the Antenna Design Contest of the *Antennas and Propagation Society International Symposium 2010. APSURSI 2010* held in Toronto, Canada in July 2010 for the paper "Practical Guidelines for Students on the Fabrication and Measurement of Home-made Standard Antennas" [J2]

Master Thesis Supervised

During the development of this thesis, two master thesis have been supervised:

- **Roselena Rubino**, "Numerical MRI-Based Breast Model for Microwave Imaging", Master Thesis, Universitat Politècnica de Catalunya (UPC), January 2012

- **Fabrizio Gedda**, "UWB Linear Array for 3D Microwave Imaging", Master Thesis, Universitat Politècnica de Catalunya (UPC) - Politecnico di Torino, September 2010

Participation in R&D Projects

- **CONSOLIDER CSD2008-68** project entitled "Terahertz Technology for Electromagnetic Sensing Applications (TERASENSE)" from 2008 to 2013

- **CICYT TEC2010-20841-C04-02** project entitled "Design, simulation and measurement of millimeter wave antennas for communications and imaging" supported by the Spanish Interministerial Commission on Science and Technology (CICYT) from 2010 to 2012

- **FPU Fellowship** Supported by the Formación de Profesorado Universitario (FPU) fellowship program from the Spanish Ministerio de Educación y Ciencia (MEC) from August 2009 to March 2013

- **CICYT TEC2007-66698-C04-01** project entitled "Sistemas Multiantenas Reconfigurables para Comunicaciones y Sensores" supported by the Spanish Interministerial Commission on Science and Technology (CICYT) from 2007 to 2010

- **FICOSA** project entitled "Advanced Materials Antenna Development for Automotive and Spatial Applications" from 2008 to 2009